ADVANCED STEEL CONSTRUCTION

An International Journal

Volume 22 Number 1

February 2026

CONTENTS

Technical Papers

Website: *http://www.hkisc.org*
ISSN 1816-112X
Science Citation Index Expanded, Materials Science Citation Index and ISI Alerting
Cover: Guangzhou Baiyun International Airport T3, China. Photo@ Chen Hui-Min
e-copy of IJASC is free to download at "www.ascjournal.com" in internet and mobile apps.

ADVANCED STEEL CONSTRUCTION

VOL.22, NO.1 (2026)

ADVANCED STEEL CONSTRUCTION

an International Journal

ISSN 1816-112X

Volume 22 Number 1 *February 2026*

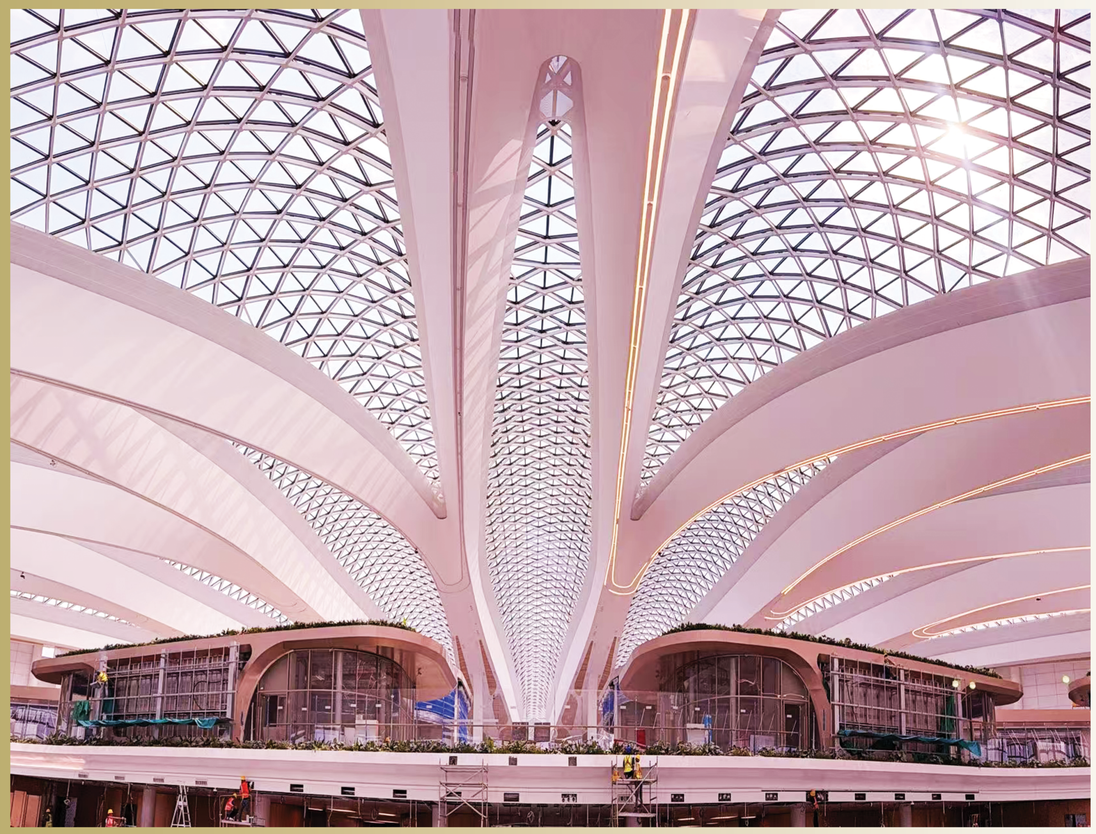

ISSN 1816-112X

Science Citation Index Expanded, Materials Science Citation Index and ISI Alerting

Advanced Steel Construction
an international journal

Cover: Guangzhou Baiyun International Airport T3, China. Photo@ Chen Hui-Min
e-copy of IJASC is free to download at "www.ascjournal.com" in internet and mobile apps.

General Information
Advanced Steel Construction, an international journal

Aims and scope

The International Journal of Advanced Steel Construction provides a platform for the publication and rapid dissemination of original and up-to-date research and technological developments in steel construction, design and analysis. Scope of research papers published in this journal includes but is not limited to theoretical and experimental research on elements, assemblages, systems, material, design philosophy and codification, standards, fabrication, projects of innovative nature and computer techniques. The journal is specifically tailored to channel the exchange of technological know-how between researchers and practitioners. Contributions from all aspects related to the recent developments of advanced steel construction are welcome.

Subscription inquiries and change of address. Address all subscription inquiries and correspondence to Member Records, IJASC. Notify an address change as soon as possible. All communications should include both old and new addresses with zip codes and be accompanied by a mailing label from a recent issue. Allow six weeks for all changes to become effective.

The Hong Kong Institute of Steel Construction
HKISC
c/o Prof. SL Chan,
Unit 209B, Photonics Centre, No. 2 Science Park East Avenue,
Hong Kong Science Park, Shatin, N.T., Hong Kong, China.
Tel: 852- 3595 6150 Fax: 852- 3619 7238
Email: ceslchan@connect.polyu.hk Website: *http://www.hkisc.org/*
ISSN 1816-112X
Science Citation Index Expanded, Materials Science Citation Index and ISI Alerting

ISSN 1816-112X

Science Citation Index Expanded, Materials Science Citation Index and ISI Alerting

Advanced Steel Construction
an international journal

VOLUME 22 NUMBER 1 February 2026

Technical Papers

Advanced Steel Construction – Vol. 22 No. 1 (2026) 1–7
DOI:10.18057/IJASC.2026.22.1.1

HYSTERETIC BEHAVIOR OF ORTHOGONAL-INSTALLED DOUBLE CORRUGATED STEEL PLATE SHEAR WALL

Yan-Sheng Song [1], Zhuo-Yuan Jiang [1,*], Yu-Rong Dai [2] and Chun-Gang Wang [1]

[1] *School of Civil Engineering, Shenyang Jianzhu University, Shenyang 110168, China*
[2] *China Construction Fourth Bureau First construction Co., Ltd., Guangzhou 510000, China*
* *(Corresponding author: E-mail: jiangzy0922@163.com)*

ABSTRACT

To enhance the weak-axis performance of double corrugated steel plate shear walls (DCSPSWs), this study introduces an innovative orthogonal-installed double corrugated steel plate shear wall (OD-CSPSW). The proposed system comprises two orthogonally interlocked corrugated plates connected via through-bolts and integrated into a steel frame using fish-tail plate connections. A large-scale general-purpose finite element (FE) software, ABAQUS 6.14, was employed. Following validation against experimental benchmarks, 15 OD-CSPSW models were analyzed, and the effects of the corrugation angle and arrangement method on the hysteretic behavior of OD-CSPSWs were investigated. Additionally, two specimens of the co-directional DCSPSWs were designed as the control group. The results indicate that the OD-CSPSW demonstrates better hysteretic behavior compared to the co-directional DCSPSW. Specifically, the OD-CSPSW with a corrugation angle of 45° demonstrates the best overall stiffness and resistance to out-of-plane buckling, while also possessing a high energy dissipation capacity. According to the coverage method, the shear wall exhibits the highest initial stiffness when fully coverage, though its load-bearing capacity degrades more rapidly. For non-fully coverage, the energy dissipation capability of a vertically-centered shear wall outperforms a horizontally-centered one. It is recommended that when designing the OD-CSPSW, the corrugation angle should be set to 45° with full coverage, and if non-fully coverage is necessary, a vertically-centered arrangement should be selected.

ARTICLE HISTORY

Received: 30 December 2024
Revised: 3 June 2025
Accepted: 4 June 2025

KEYWORDS

Double steel corrugated plate wall;
Wave angles;
Coverage;
Hysteretic behavior;
FE analysis

1. Introduction

In recent years, the Corrugated Steel Plate Shear Wall (CSPSW) has emerged as a novel seismic-resistant structural component. The distinctive folded geometry of these systems has been proven effective in enhancing out-of-plane stability, improving elastic buckling strength, increasing energy dissipation capacity, and simplifying the construction process [1-3]. These advantages enable the CSPSW to play a crucial role in the structural stability and safety of high-rise buildings [4-8].

To evaluate the hysteretic performance of the CSPSW, Breman and Bruneau [9-11] conducted low-cycle reversed loading tests on shear walls made of flat steel plates and corrugated steel plates. Their comparative analysis of failure mechanisms and energy dissipation characteristics revealed that the CSPSW achieved better energy dissipation capacity and greater peak load resistance than the flat steel plate shear walls.

Furthermore, Ghodratian-Kashan et al. [12-15] focused on the performance evaluation and optimization design of corrugated steel plate shear walls including double-corrugated and single-corrugated types under cyclic loading. Through experiments and numerical simulations, they explored the influence of different connection designs and geometric parameters (e.g. plate thickness, aspect ratio, and corrugation direction) on the hysteretic behavior and seismic performance of the shear walls.

To mitigate local buckling instabilities prevalent in the conventional corrugated steel plate shear wall, researchers globally have proposed innovative configurations of double-corrugated steel plate shear wall (DC-SPSW). This design integrates two trapezoidal corrugated steel plates arranged in mirrored configurations along the horizontal/vertical axis, forming a composite system that capitalizes on the anisotropic properties of corrugated plates. When placed horizontally, the wall can avoid vertical loads through the "accordion effect" and mainly resist shear forces, whereas when placed vertically, it can effectively share vertical loads.

To address the weak-axis limitations of the DC-SPSW, this study proposes an orthogonal-installed Double Corrugated Steel Plate Shear Wall (OD-CSPSW). This configuration offers high bending stiffness in both the strong and weak axes, providing better deformation resistance and load-bearing capacity under both vertical and horizontal loads. Compared to single corrugated steel plate shear walls or traditional flat steel plate shear walls, the OD-CSPSW shows improvements in load-bearing capacity, energy dissipation, and hysteretic behavior.

Prior studies [17-26] have rarely investigated the application of orthogonally installed double corrugated steel plates in shear walls. To address this gap, this study designs 15 novel orthogonal double corrugated steel plate shear wall (OD-CSPSW) models, considering the distinctive characteristics of both horizontal and vertical placements of the corrugated steel plates. Building on prior studies [16], this paper further examines the influence of corrugation angle and arrangement method on the hysteretic behavior of the OD-CSPSW. Based on the findings from the parametric analysis, design recommendations are provided.

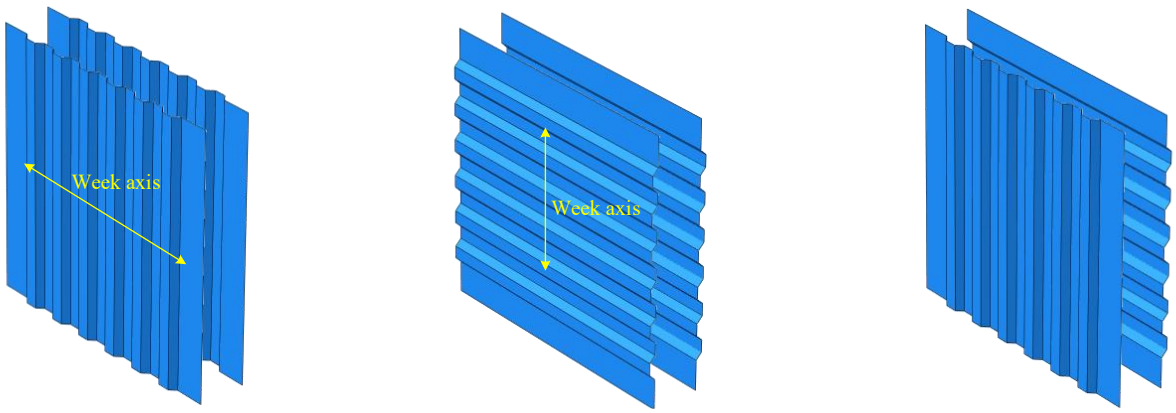

(a) VD-CSPSW (b) TD-CSPSW (c) OD-CSPSW

Fig. 1 Configuration of the insert steel plate

2. Configuration of the OD-CSPSW

The orthogonal double corrugated steel plate shear wall (OD-CSPSW) specimens investigated in this work, as illustrated in Fig. 1, comprise two orthogonally interlocked corrugated steel plates mechanically fastened at corrugation troughs using through-bolts and anchored to a two-story single-span steel frame via fish-tail plate connections. This unique orthogonal out-of-plane corrugated configuration achieves an effect similar to that of a flat steel plate shear wall with longitudinal and transverse stiffeners, enabling comparable shear resistance and seismic energy dissipation while eliminating the need for welded stiffeners. By replacing welded stiffeners with bolted corrugation interconnections, the OD-CSPSW achieves a reduction in weld volume, thereby mitigating weld-related failure risks inherent in conventional stiffened shear walls and simplifying on-site assembly processes. Compared to VD/TD-CSPSW, as shown in Fig. 1(a) and (b), OD-CSPSW combines the advantages of both, balancing load-bearing capabilities in two axial directions within the plane, and exhibits high potential for application.

3. FE models

3.1. Model calibration

A numerical analysis was conducted using the large-scale general-purpose FE software ABAQUS 6.14. To validate the numerical model, quasi-static test data of a two-story steel frame-steel plate shear wall structure from reference [16] were used for calibration. As shown in Fig. 2, the frame columns were selected as HW 200mm×200mm×8mm×12mm, the side beams as HN 250mm×200mm×12mm×14mm, the middle beams as HN 175mm×175mm×8mm×10mm, and the embedded steel plates were 2mm thick. The material of the frame was chosen as Q355B, and the embedded flat steel plates were made of Q235B, with a bilinear constitutive model.

Tie constraints were enforced between the top/bottom edges of the embedded steel plates and the outer frame. Similarly, the nodes at the left and right edges of the embedded steel plates were tied to the corresponding nodes at the contact surface in the outer frame. Both the outer frame and the embedded plates were modeled using shell elements (S4R) in the simulation, and an implicit dynamic analysis was performed. The column top was coupled at a point on the centroid line of the cross-section of the top beam of the frame, serving as the loading point.

The model was subjected to horizontal cyclic loading, with the loading protocol depicted in Fig. 3. Initially, load control was applied, with the following loading levels: 100 kN, 200 kN, 300 kN, 400 kN, 500 kN, 550 kN, 600 kN, and 650 kN, each level being cycled once. Afterward, displacement control was applied. The loading protocol comprised two phases: (1) eight stages (0.25%–2.0% drift) covering serviceability to ultimate limit states, aligned with the test program [16], and (2) six post-yield stages (2.5%–5.0% drift) to replicate the experimental program's planned loading-to-failure sequence. This approach ensured direct comparability of failure modes between FE simulations and physical tests.

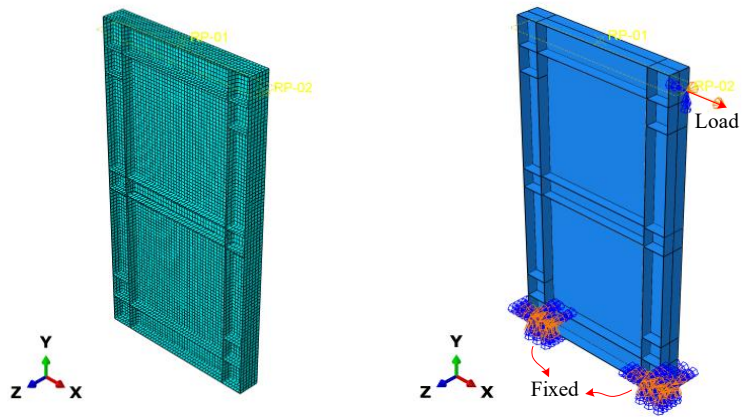

(a) Meshing (b) Boundary condition

Fig. 2 The establishment of FE model

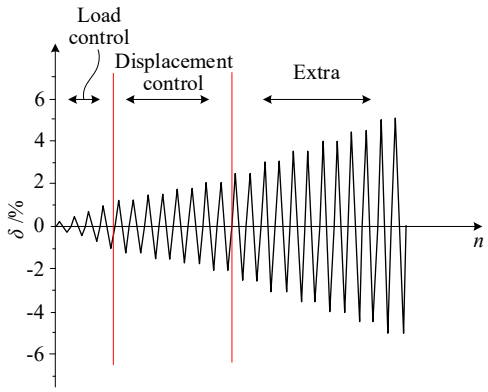

Fig. 3 Loading protocol

Fig. 4 shows a comparison between the FE and experimental hysteretic curves, skeleton curves, and stiffness degradation curves. It can be seen that the hysteretic curves obtained from numerical simulation and experiments exhibit a high degree of similarity in the shape of the hysteretic loops formed at each level. Both curves present a well-defined shape, displaying characteristics of both a spindle and a bow, with comparable enclosed areas within the loops. Based on the trend of the skeleton curve, it can be observed that the initial changes for both are consistent, with similar initial stiffness, a close plastic hinge point, and a similar development trend in the later stages. The numerical values are also close, with the largest error occurring at a displacement of 65 mm. At this point, the peak load in the experiment was 796.11 kN, while the finite element simulation value was 842.39 kN, showing a 5.8% overestimation. This discrepancy arises from the idealized boundary conditions in the FE model (e.g., perfect nodal ties and uniform material properties), which neglected experimental complexities such as additional constraints and localized imperfections that reduced the physical specimen's capacity. Additionally, the trend of the stiffness degradation curve in the finite element simulation is consistent with the experimental data, with the values being quite close. Therefore, the numerical analysis method used in this study accurately predicted the hysteretic behavior of the corrugated steel plate shear wall, and can be further applied to analyze the effects of corrugation angle and arrangement method on the hysteretic performance of corrugated steel plate shear walls.

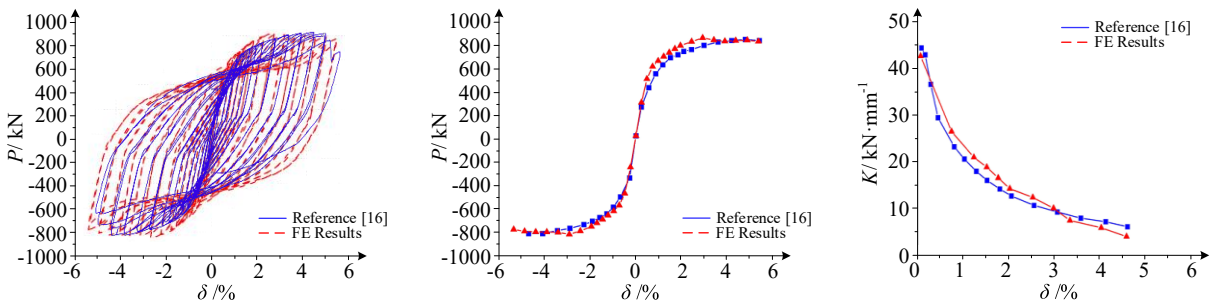

(a) Hysteretic curves (b) Skeleton curves (c) Stiffness degradation curves

Fig. 4 Comparison of hysteresis curves between test and FE results

3.2. FE models establish of the OD-CSPSW

To investigate the hysteretic behavior of orthogonal double corrugated steel plates, models for the transverse double corrugated steel plate shear wall (TD-CSPSW) and vertical double corrugated steel plate shear wall (VD-CSPSW) were designed. As shown in Fig. 5, to study the effect of the corrugation angle, three corrugation angles (30°, 45°, 90°) for the OD-CSPSW were considered based on their significant influence on the out-of-plane buckling resistance, shear stiffness, and energy dissipation capacity of the CSPSW [16,24]. Additionally, to explore material efficiency by reducing steel usage and enabling utility installations in non-fully covered regions, and to evaluate the impact of aspect ratio on seismic performance, five arrangement methods were considered: fully coverage (F), vertically-centered coverage (VC), horizontally-centered coverage (HC), vertically-split arrangement (VS), and horizontally-split coverage (HS). The latter four methods were non-fully coverage, with the aspect ratio of the embedded steel plates adjusted from 1.0 to 0.8. The coverage methods are shown in Fig. 6.

Based on the model validated through FE simulation, the arranged steel plates were replaced with the models mentioned above during assembly. The material constitutive relations for the steel plates, plate-frame interaction, boundary conditions, and loading conditions for the specimens were adjusted according to the control group, and the shear wall specimens were subjected to cyclic loading. A total of 17 cases as shown in Table 1 were analyzed for parametric studies, further investigating the hysteretic behavior of the orthogonal double corrugated steel plate shear walls.

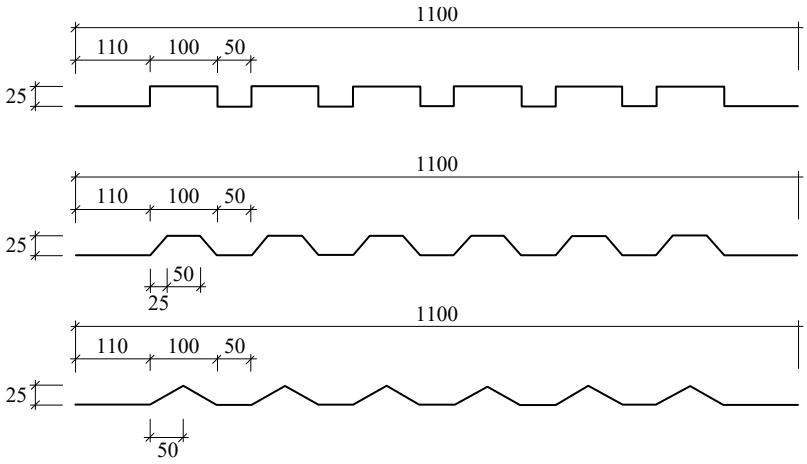

Fig. 5 Section dimensions of the steel plates

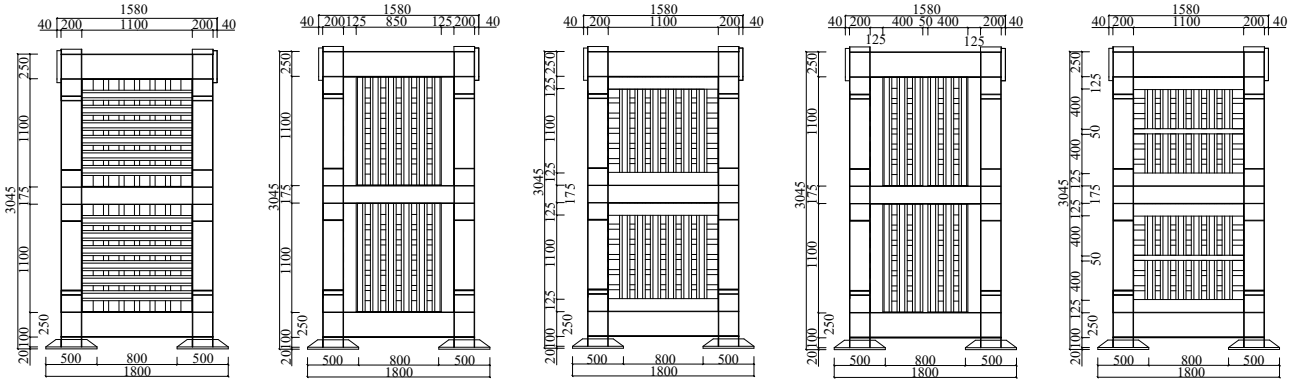

(a) F (b) VC (c) HC (d) VS (e) HS

Fig. 6 Arrangement modes and sizes of the steel plates (Unit: mm)

Table 1
Parameters of shear wall models

Models	Directions of corrugation	Corrugation angle	Coverage methods
OD-CSPSW-45-F	Orthogonal	45°	F
TD-CSPSW-45-F	Transverse	45°	F
VD-CSPSW-45-F	Vertical	45°	F
OD-CSPSW-90-F	Orthogonal	90°	F
OD-CSPSW-30-F	Orthogonal	30°	F
OD-CSPSW-90-VC	Orthogonal	90°	VC
OD-CSPSW-45-VC	Orthogonal	45°	VC
OD-CSPSW-30-VC	Orthogonal	30°	VC
OD-CSPSW-90-HC	Orthogonal	90°	HC
OD-CSPSW-45-HC	Orthogonal	45°	HC
OD-CSPSW-30-HC	Orthogonal	30°	HC
OD-CSPSW-90-VS	Orthogonal	90°	VS

OD-CSPSW-45-VS	Orthogonal	45°	VS
OD-CSPSW-30-VS	Orthogonal	30°	VS
OD-CSPSW-90-HS	Orthogonal	90°	HS
OD-CSPSW-45-HS	Orthogonal	45°	HS
OD-CSPSW-30-HS	Orthogonal	30°	HS

4. Analysis of FE results

4.1. Influence of the corrugation direction

Fig. 7 shows the stress distribution contours of the double corrugated steel plate shear walls (OD-CSPSW-45-F, TD-CSPSW-45-F, and VD-CSPSW-45-F) under failure conditions for different corrugation directions. Notably, transverse and vertical corrugation cases exhibit nearly identical failure modes. In both cases, a corrugated tensile band forms around the edges of the flat steel plate regions, with only the direction of the residual deformation differing. In contrast, the orthogonally configured OD-CSPSW-45-F demonstrates a fundamentally distinct failure mechanism: no diagonal tensile bands emerge, and residual deformations deviate from the conventional "X"-shaped pattern. Instead, the orthogonal corrugation interlocks promote uniform out-of-plane integrity, resulting in a concentric "O"-shaped bulge propagating radially from the plate center. This unique deformation mode correlates with a stress gradient where the annular "O"-shaped zone experiences lower von Mises stresses than its peripheral regions, suggesting enhanced stress redistribution capabilities through bidirectional corrugation synergy.

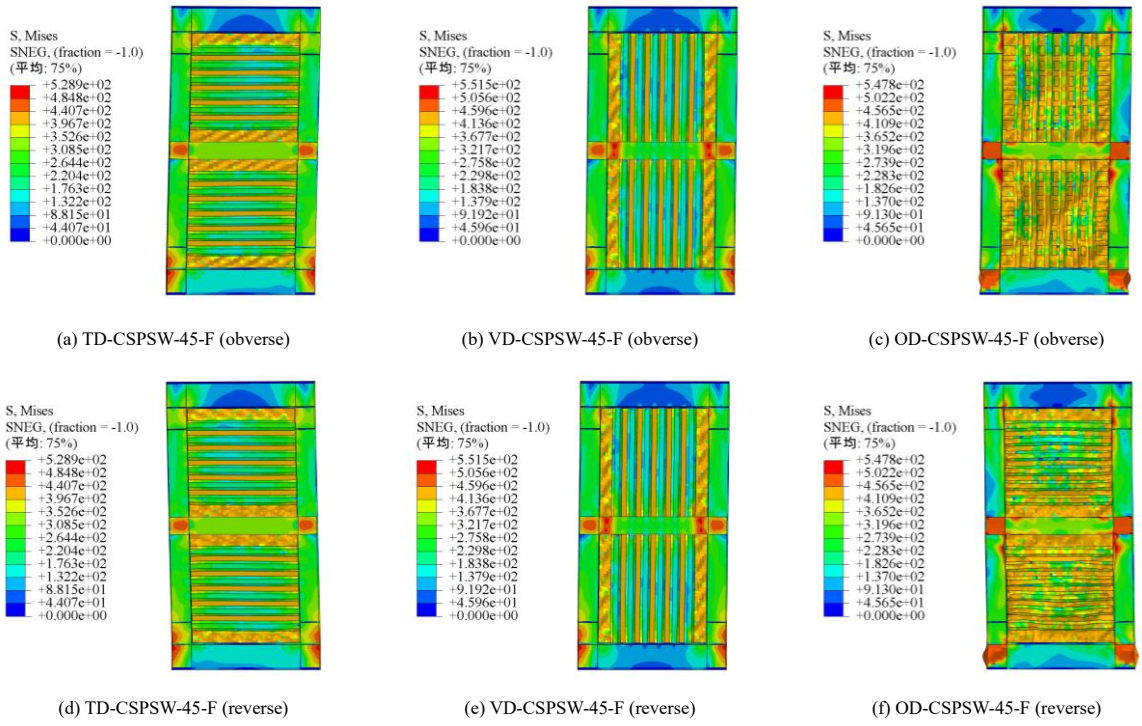

(a) TD-CSPSW-45-F (obverse) (b) VD-CSPSW-45-F (obverse) (c) OD-CSPSW-45-F (obverse)

(d) TD-CSPSW-45-F (reverse) (e) VD-CSPSW-45-F (reverse) (f) OD-CSPSW-45-F (reverse)

Fig. 7 Stress nephogram of failure state for example with different ripple directions (Unit: MPa)

Fig. 8 compares the hysteretic curves and cumulative energy dissipation capacities of double corrugated steel plate shear walls (OD-CSPSW-45-F, TD-CSPSW-45-F, and VD-CSPSW-45-F) under varying corrugation orientations. The results show that both VD-CSPSW-45-F and TD-CSPSW-45-F exhibit comparable cumulative energy dissipation, approximately 60,000 kN·m. In contrast, the cumulative energy dissipation of the OD-CSPSW-45-F model reaches nearly 220,000 kN·m, which is more than 3.5 times that of the VD and TD configurations. It can be concluded that the OD-CSPSW-45-F case exhibits the best energy dissipation capacity. This is due to the orthogonal installation of the embedded steel plates, which strengthens the original single-directional double corrugated steel plate shear wall's performance in the weak axis direction. As a result, the orthogonal double corrugated steel plate shear wall demonstrates high bending stiffness in both the strong and weak axis directions, meaning that the wall shows superior deformation resistance and load-bearing capacity when subjected to both vertical and horizontal loads.

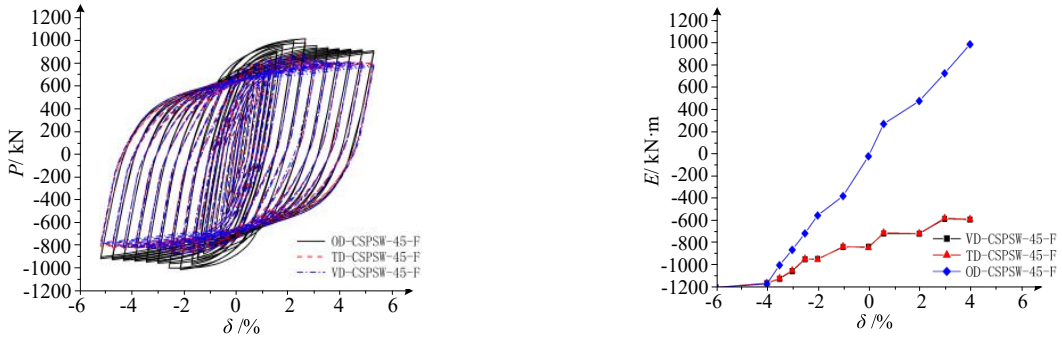

(a) Hysteretic curves (b) Energy dissipation curves

Fig. 8 Examples of hysteresis curves and energy dissipation capacity curves of different ripple directions

4.2. Influence of the corrugation angle

Fig. 9 depicts the stress distribution and failure mechanisms of orthogonal double corrugated steel plate shear walls (OD-CSPSW-90-F, OD-CSPSW-45-F, OD-CSPSW-30-F) under ultimate lateral drift (5%). For OD-CSPSW-90-F, the peak von Mises stress reached 539.20 MPa, accompanied by a maximum out-of-plane displacement of 96.07 mm. Similar to conventional shear walls, this configuration developed diagonal tension zones along the plate edges, with residual deformations forming a symmetrical "X" pattern. This is likely because the orthogonally distributed out-of-plane corrugations hinder the uniform development of the diagonal tensile bands, leading to a reduced "X" shaped stress distribution on the embedded steel plates.

In contrast, OD-CSPSW-30-F exhibited marginally higher peak stress (540.20 MPa) and greater out-of-plane displacement (106.30 mm). The embedded steel plates also display diagonal tensile bands and "X" shaped residual deformation. However, the "X" shape is less symmetrical than in the control group in [16] or the OD-CSPSW-90-F case. The "X" intersection of the upper steel plate is displaced downward, while the intersection of the lower steel plate shifts diagonally upwards to the right. Additionally, the stress at the column base and the node between the middle beam and the column is relatively high for the OD-CSPSW-30-F. For the OD-CSPSW-30-F case, the maximum stress is 540.20 MPa, and the maximum out-of-plane displacement is 106.30 mm. From the perspective of out-of-plane deformation, the OD-CSPSW-45-F exhibits the smallest deformation, followed by OD-CSPSW-90-F, and OD-CSPSW-30-F shows the largest out-of-plane deformation.

For the OD-CSPSW-45-F, the embedded steel plate's deformation predominantly localized along diagonal directions, manifesting as a diagonal wave-shaped buckling pattern. This contrasts with the orthogonally staggered 90° corrugations, whose geometric configuration mimics the mechanical function of bidirectional stiffeners (longitudinal and transverse). By restricting lateral displacement through corrugation interlocking, this orthogonal arrangement suppresses out-of-plane buckling instabilities, achieving a reduction in peak out-of-plane displacement compared to conventional stiffened shear walls. Consequently, the resultant wave-shaped deformations in OD-CSPSW-90-F are less pronounced and more uniformly distributed than those observed in non-orthogonal configurations.

The OD-CSPSW-90-F case shows an "O"-shaped out-of-plane bulge at the center of the embedded steel plate, and the bulge and its range for the lower steel plate are greater than those of the upper steel plate. The OD-CSPSW-30-F case also concentrates out-of-plane deformation along the diagonal, forming an asymmetric "X"-shaped bulge, and the intersection points of the "X" shape exhibit sharp out-of-plane deformation. This indicates that the triangular corrugated cross-section is disadvantageous for preventing out-of-plane buckling of the embedded steel plates.

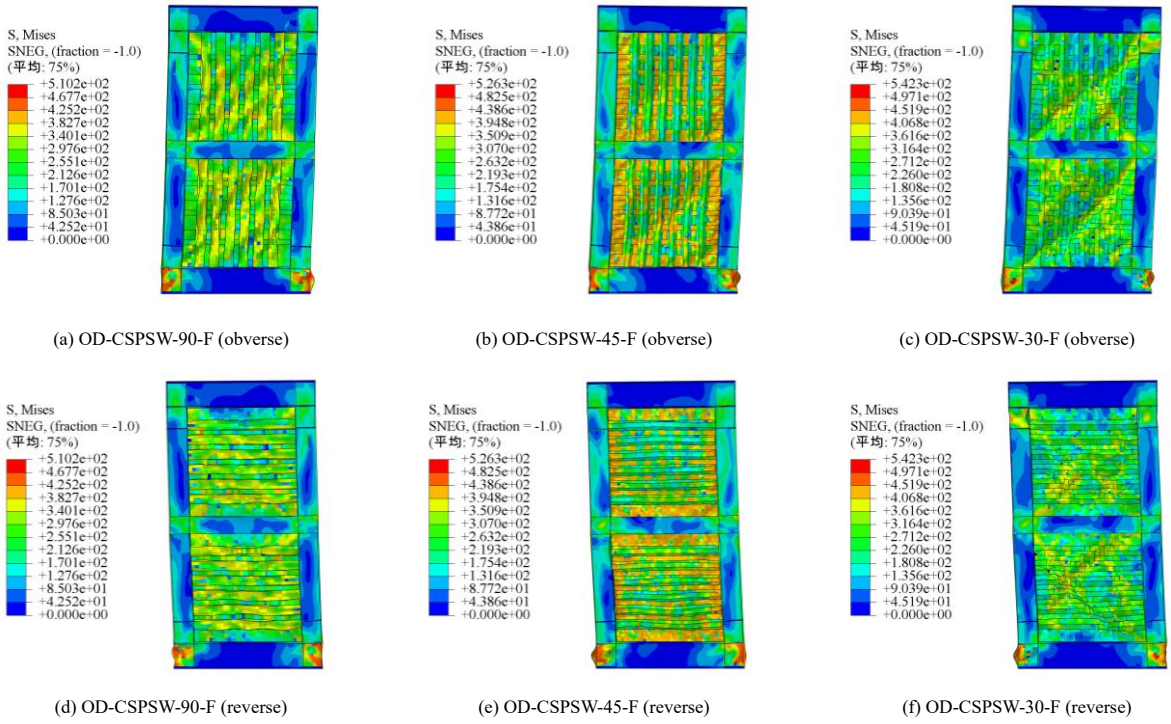

(a) OD-CSPSW-90-F (obverse) (b) OD-CSPSW-45-F (obverse) (c) OD-CSPSW-30-F (obverse)

(d) OD-CSPSW-90-F (reverse) (e) OD-CSPSW-45-F (reverse) (f) OD-CSPSW-30-F (reverse)

Fig. 9 The stress cloud diagram of the failure state of the example with different twist angles (Unit: MPa)

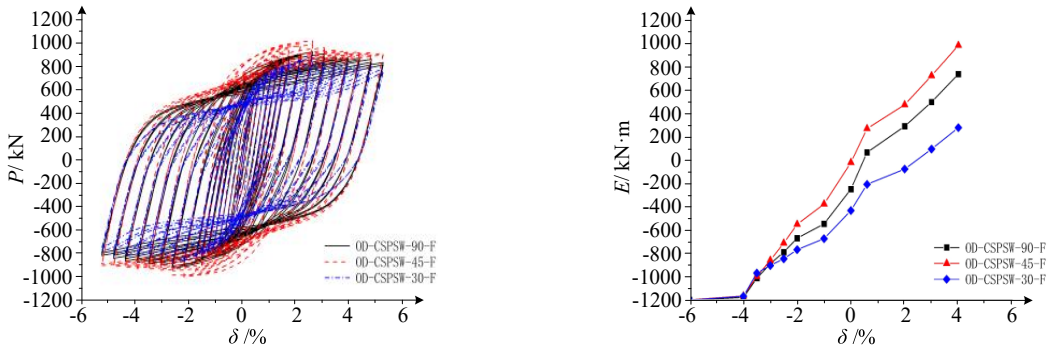

(a) Hysteretic curves (b) Energy dissipation curves

Fig. 10 Examples of hysteresis curve and energy dissipation capacity curve of different bending angles

Under cyclic loading, the lateral load-displacement hysteretic curves of the models are shown in Fig. 10. All models with different corrugation angles demonstrate stable hysteretic performance. The comparison reveals that the hysteretic curves for OD-CSPSW-90-F and OD-CSPSW-45-F are fully enclosed, with OD-CSPSW-45-F displaying the highest loop completeness. In contrast, the hysteretic curves for OD-CSPSW-30-F exhibit significant pinching. Therefore, the energy dissipation capacity ranks as OD-CSPSW-45-F > OD-CSPSW-90-F > OD-CSPSW-30-F, despite the apparent discrepancy in

cumulative energy values (1938.2, 2183.6, and 1478.8 kN·m, respectively), which may require further validation. The equivalent viscous damping coefficients are 0.36, 0.38, and 0.30, respectively.

Combining the analysis of the failure states, it can be concluded that the OD-CSPSW-45-F model benefits from the orthogonal superposition of 45° corrugated steel plates, which enhances its out-of-plane integrity and improves its seismic performance. In contrast, the OD-CSPSW-90-F and OD-CSPSW-30-F models exhibit gradual post-peak strength degradation despite inelastic buckling of the infill plates. This behavior stems from the sustained load-bearing capacity of the diagonal tension fields formed after yielding: even as partial unloading occurs due to out-of-plane deformations, stress redistribution through these diagonal tensile mechanisms enables progressive failure rather than abrupt collapse. The OD-CSPSW-45-F's absence of such tension bands further underscores its distinct failure mechanism, where bidirectional corrugation synergy replaces localized tension fields with uniform stress dispersion.

4.3. Influence of the coverage method

Under cyclic loading with VC as shown in Fig. 11(a), the lateral load-lateral displacement hysteretic curves for the specimens OD-CSPSW-45-VC, OD-CSPSW-30-VC, and OD-CSPSW-90-VC exhibit good hysteretic performance, with all curves showing a full and closed shape. Evaluation of loop fullness and peak load magnitudes revealed marginally superior energy dissipation capacities in OD-CSPSW-45-VC and OD-CSPSW-30-VC compared to OD-CSPSW-90-VC. Distinct failure modes emerged across configurations: OD-CSPSW-90-VC and OD-CSPSW-30-VC developed prominent "H"-shaped residual deformations with incomplete annular out-of-plane buckling patterns, particularly pronounced in OD-CSPSW-30-VC where buckling localized eccentrically (peak displacement = 106.30 mm). In contrast, OD-CSPSW-45-VC exhibited preferential bidirectional outward flexural buckling along diagonal axes. Mechanistically, asymmetric outward bending in OD-CSPSW-45-VC promoted distributed plasticity and delayed strain localization, while symmetric "H"-shaped or eccentric annular buckling in OD-CSPSW-90/30-VC accelerated localized yielding. This asymmetric deformation mode enhanced energy dissipation through controlled plastic hinge formation, establishing the performance hierarchy: OD-CSPSW-45-VC surpassed OD-CSPSW-30-VC, which outperformed OD-CSPSW-90-VC in cumulative energy dissipation efficiency.

Under the condition of HC as described in Fig. 11(b), the specimens OD-CSPSW-45-HC, OD-CSPSW-30-HC, and OD-CSPSW-90-HC exhibit good hysteretic curves during lateral load-displacement cyclic loading, with full and similar shapes. Preliminary analysis indicates that OD-CSPSW-45-HC and OD-CSPSW-30-HC perform slightly better than OD-CSPSW-90-HC in energy dissipation. Further observation of the failure modes reveals that all specimens show vertical outward buckling of the embedded steel plates, and the back of the OD-CSPSW-90-HC specimen exhibits significant "H"-shaped residual deformation and localized circular out-of-plane bulging in the upper steel plates. It can be inferred that the "H"-shaped residual deformation and bulging phenomena are detrimental to energy dissipation, whereas the vertical outward buckling is an early manifestation of circular bulging. Overall, the corrugation angle has a minimal impact on the hysteretic curve in arrangement method 2, though further parameter analyses may reveal more details.

Under the condition of VS as described in Fig. 11(c), the hysteretic curve performance of specimens OD-CSPSW-90-VS, OD-CSPSW-45-VS, and OD-CSPSW-30-VS shows minimal difference. The hysteretic curves of the three groups maintain high fullness and exhibit similar deformation trends. Although the effect of the corrugation angle on the hysteretic performance is not very significant, the lower steel plates of OD-CSPSW-30-VS show notable outward buckling. Analysis of the out-of-plane deformation level reveals the order of deformation severity as OD-CSPSW-90-VS, OD-CSPSW-45-VS, and OD-CSPSW-30-VS in descending order of severity.

Under the condition of HS as shown in Fig. 11(d), the specimens OD-CSPSW-45-HS, OD-CSPSW-30-HS, and OD-CSPSW-90-HS also demonstrate full hysteretic curves, with similar hysteretic performance and consistent curve shapes. In terms of energy dissipation, OD-CSPSW-45-HS and OD-CSPSW-30-HS perform slightly better than OD-CSPSW-90-HS, although the differences are not significant. Observation of the failure modes reveals that OD-CSPSW-45-HS and OD-CSPSW-30-HS show more pronounced outward buckling in the lower embedded steel plates. It can be inferred that under arrangement method 4, the energy dissipation performance ranks from high to low as follows: OD-CSPSW-45-HS, OD-CSPSW-30-HS, and OD-CSPSW-90-HS.

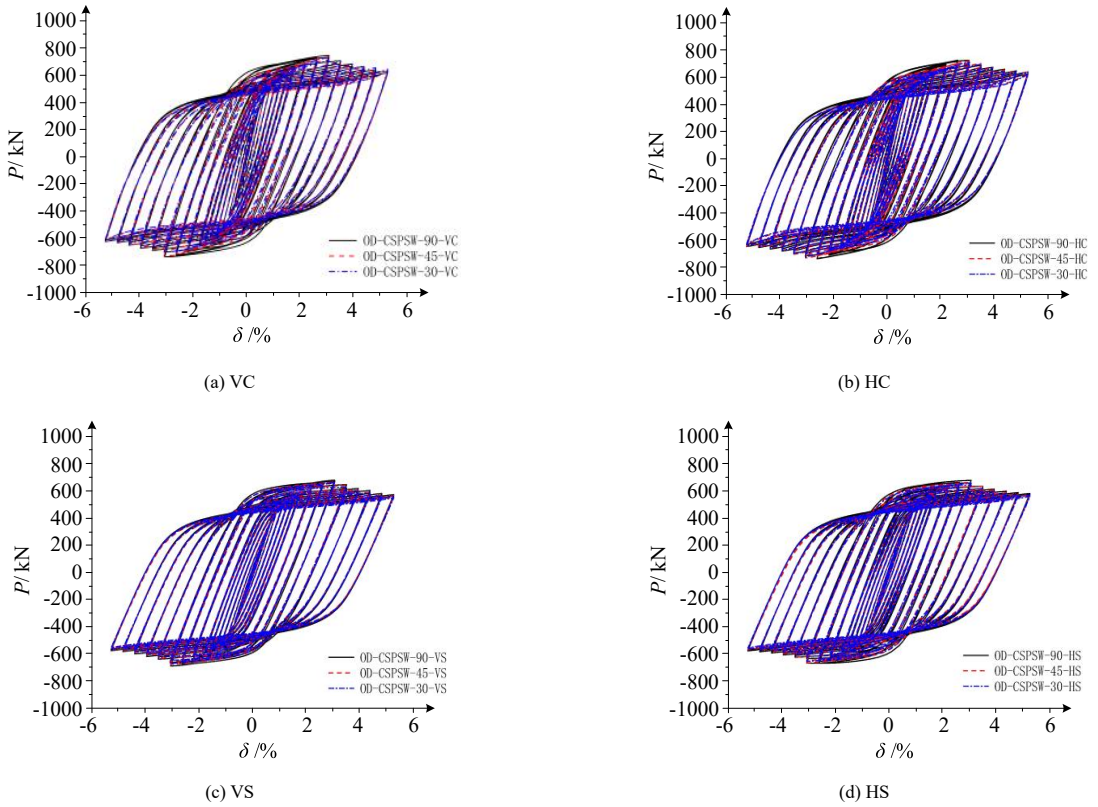

(a) VC (b) HC

(c) VS (d) HS

Fig. 11 Hysteresis curves under different arrangements

5. Conclusions

This study employs the finite element software ABAQUS to simulate the cyclic loading of 17 DCSPSW and investigates the effects of corrugation direction, corrugation angle, and arrangement method on their mechanical performance. The following conclusions were drawn:

(1) The unidirectional double corrugated steel plate shear wall and the orthogonal double corrugated steel plate shear wall exhibit significant differences in lateral resistance performance. While the unidirectional double corrugated steel plate shear wall improved the lateral stiffness of the embedded

steel plate in the early stages, its load-bearing capacity decreased due to severe out-of-plane deformation in the later stages. In contrast, the orthogonal double corrugated steel plate shear wall demonstrates clear advantages in both ultimate load-bearing capacity and energy dissipation capacity. Its structural design more effectively delays out-of-plane deformation, thereby enhancing overall stability and energy dissipation.

(2) The initial lateral stiffness of the orthogonal double corrugated steel plate shear wall decreases sequentially as the corrugation angle increases from 30° to 90°. When factors such as lateral stiffness, out-of-plane buckling resistance, and energy dissipation capacity are considered, the steel plate with a 45° corrugation angle offers a more balanced overall performance. It not only exhibits good initial lateral stiffness but also demonstrates strong resistance to out-of-plane buckling. In terms of energy dissipation capacity, the 45° corrugated steel plate outperforms other corrugation angles, with its hysteretic curve being full and energy dissipation being uniform, showing stable hysteretic performance.

(3) The hysteretic performance of the orthogonal double corrugated steel plate shear wall is also significantly influenced by the arrangement method and the area of the embedded steel plates. Orthogonal double corrugated steel plates with larger areas exhibit stronger energy dissipation capacity, higher initial stiffness, and greater peak load. In the fully-covered arrangement, the initial stiffness is the highest, but the load-bearing capacity degrades more rapidly. In non-fully-covered cases, the energy dissipation capacity of the vertically-centered arrangement is better than that of the split arrangement, while the horizontally-centered arrangement shows the opposite trend. Overall, the energy dissipation of the vertically-centered single plates is better than that of the horizontally-centered arrangement, but for split arrangements, the energy dissipation of the horizontally-centered embedded steel plates is better than that of the vertically-centered ones.

(4) The orthogonal double corrugated steel plate shear wall demonstrates superior energy dissipation capacity and load-bearing stability under various conditions of corrugation angle, arrangement method, and embedded steel plate area. The corrugation angle plays a key role in improving stiffness and ductility, with the 45° corrugation angle performing best in terms of overall integrity and anti-buckling capability. Furthermore, the rational configuration of the arrangement method and plate area can significantly enhance the mechanical performance. By optimizing these factors comprehensively, excellent hysteretic performance and stable lateral stiffness of the steel plate shear walls can be achieved in practical applications.

While the OD-CSPSW with 45° corrugation and full coverage demonstrates superior performance, its real-world implementation faces challenges. The orthogonal interlocking configuration demands precise fabrication and alignment during installation, potentially increasing labor costs. Additionally, full coverage requires more material than non-fully covered arrangements, though this trade-off may be justified in seismically active regions due to enhanced energy dissipation. To mitigate these challenges, prefabricated modular panels and standardized bolted connections (e.g., pre-assembled fish-tail plates) are recommended to reduce on-site complexity. Future studies should further explore cost-benefit analyses and lightweight optimization strategies for broader applicability.

Declaration of competing interest

The authors declare that they have no known competing financial interests or personal relationships that could have appeared to influence the work reported in this paper.

Acknowledgments

This study was financially supported by the China Construction Shares Technology Research and Development Project (CSCEC-2010-Z-01-02, CSCEC-2010-C-05).

References

[1] Zand SMD, Kalatjari V, Attari NK A. Cyclic performance of new steel plate shear wall reinforced by trapezoidal corrugated plate [J]. Journal of Architectural Journal,2017,35(1):11-11 Journal of Civil Engineering, Institute of Technology,2023.

[2] Bahrebar Milad, Lim James B.P., Clifton George Charles. Response assessment and prediction of low yield point steel plate shear walls with curved corrugated web plates and reduced beam sections[J]. Structures,2020,28.

[3] Bahrebar Milad, Kabir M Z, Zirakian T, et al. Structural Performance Assessment of Trapezoidally-Corrugated and Centrally-Perforated Steel Plate Shear Walls[J]. Journal of Constructional Steel Research, 2016(122):584-594.

[4] Jin H.J., Sun F.F., Li G.Q.. Simplified inelastic global buckling theory of non-buckling corrugated steel shear walls for seismic energy dissipation[J]. Thin-Walled Structures,2021,159.

[5] Fadhil H, Ibrahim I, Mahmood M. Effect of Corrugation Angle and Direction on the Performance of Corrugated Steel Plate Shear Walls[J]. Civil Engineering Journal, 2018,4(11):2667-2679.

[6] Yu C, Yu G. Experimental Investigation of Cold-Formed Steel Framed Shear Wall Using Corrugated Steel Sheathing with Circular Holes[J]. Journal of Structural Engineering, 2016, 142(12):04016126:8.

[7] Rajeev A, Jacob B, Muhamed S. Evaluation and Comparison of Behavior of Trapezoidally Corrugated Steel Plate Shear Walls[J]. International Research Journal of Engineering and Technology, 2016,3(9):318-327.

[8] Dou C, Jiang Z, Pi Y, et al. Elastic Shear Buckling of Sinusoidally Corrugated Steel Plate Shear Wall[J]. Engineering Structures, 2016(121):136-146.

[9] Hosseinzadeh L, Emami F, Mofid M. Experimental study on Performance of corrugated steel shear walls under Different trapezoidal plate Angles [J]. High-rise and Special Building Structure Design,2017,26(17):e1390.

[10] J. W. Berman, M. Bruneau. Experimental Invetigation of Light-Gauge Steel Plate Shear Walls[J]. Journal of Structural Engineering, 2005, 131(2):259-267.

[11] J. W. Berman, M. Bruneau. Experimental Investigation of Light-Gauge Steel Plate Shear Walls for The Seismic Retrofit of Building[R]. Tech. Rep. No. Mceer-03-0001:Multidisciplinary center for earthquake engineering research, Univ. at Buffalo, N. Y., 2003.

[12] Ghodratian-Kashan, SM,Maleki S. Experimental investigation of double corrugated steel plate shear walls [J]. Journal of Architectural Journal,2017,35(1):11-11 .

[13] Ghodratian-Kashan, SM,Maleki S. Experimental and Numerical Study of Beam-Only-Connected Corrugated Steel Plate Shear Walls[J]. Journal of Earthquake Engineering,2023:1-23.

[14] Ghodratian-Kashan, SM,Maleki S. Numerical study of Double corrugated steel plate shear Wall [J]. Journal of Civil Engineering and Construction,2021,10(1):44-58.

[15] Ghodratian-Kashan, SM,Maleki S. Experimental study on Double corrugated steel plate shear wall [J]. Journal of Building Steel Research,2022,190:107138.

[16] Qiuhong Zhao, Jing Qiu, Bochao Hao, et al. Lateral resistance of vertical corrugated steel plate shear walls with Two Sides Connected [J]. Journal of Tianjin University (Natural Science and Engineering Technology),2019,52(S2):46-53.

[17] Boli Zhu, Jingzhong Tong, Jinxun Zhang, et al. Shear properties and design of orthogonal double corrugated plate shear walls [J]. Thin-wall Structures,2023,187:110759.

[18] Fadhil H, Ibrahim I, Mahmood M. Effect of Corrugation Angle and Direction on the Performance of Corrugated Steel Plate Shear Walls[J]. Civil Engineering Journal, 2018,4(11):2667-2679.

[19] Y Boli, Zhu Jingzhong, Tong Jinxun Zhang, et al. Shear properties and Design of orthogonal double corrugated plate shear walls [J]. Thin-wall Structures,2023,187:110759.

[20] Dou C ,Pi Y ,Gao W .Shear resistance and post-buckling behavior of corrugated panels in steel plate shear walls[J].Thin-Walled Structures,2018,131816-826.

[21] Jingzhong Tong, Jinxun Zhang, Wenhua Pan. Ultimate shear resistance and ultimate performance of double corrugated plate shear wall [J]. Journal of Construction Steel Research,2020,165:105895.

[22] Fang J ,Bao W ,Ren F , et al.Experimental study of hysteretic behavior of semi-rigid frame with a corrugated plate[J].Journal of Constructional Steel Research,2020,174.

[23] Yadollahi Y,Pakar I,Bayat M. Performance Evaluation and comparison of corrugated steel plate shear walls [J]. Latin American Journal of Solids and Structures,2015, 12:763-786.

[24] S.M. Ghodratian-Kashan ,S. Maleki .Experimental investigation of double corrugated steel plate shear walls[J].Journal of Constructional Steel Research,2022,190.

[25] S.M. Ghodratian-Kashan ,S. Maleki . Cyclic Performance of Corrugated Steel Plate Shear Walls with Beam-Only-Connected Infill Plates[J]. Advances in Civil Engineering, 2021, 2021(1): 5542613.

[26] S.M. Ghodratian-Kashan ,S. Maleki .Experimental and Numerical Study of Beam-Only-Connected Corrugated Steel Plate Shear Walls[J].Journal of Earthquake Engineering,2024,28(6):1769-1791.

Advanced Steel Construction – Vol. 22 No. 1 (2026) 8–16
DOI:10.18057/IJASC.2026.22.1.2

PLASTIC ENHANCEMENT OF COLD-FORMED THIN-WALLED STEEL FOR PREFABRICATED SUPPORT AND HANGER

Zong-Lai Peng [1], Yi-Pei Zeng [1], Ning Xu [1], Xian-Hui Yi [1], Fu-Li Liu [1], Wei Xiong [1] and Yong Cai [2, *]

[1] *China Construction Fifth Bureau Installation Engineering Co., LTD, Shenzhen 518118, China*
[2] *School of Civil Engineering, Central South University, Changsha 410075, China*
** (Corresponding author: E-mail: 18803314336@163.com)*

ABSTRACT

In prefabricated support and hanger, the study of corner strength in cold-formed thin-walled steel (CFTWS) is crucial. Corners are prone to stress concentration, increasing local buckling and connection failure risks. This study analyzes the stress in the corner parts and derives the yield strength using the linear hardening model and the Von-Mises yield criterion. Based on the Prandtl-Reuss flow rule and strain superposition principle in plastic mechanics, a theoretical analysis of corner material hardening during the cold-bending process is conducted. Experiments and ABAQUS simulations are carried out to prove the effectiveness of the theoretical model. The findings reveal that the cold bending effect is relatively significant. The yield strength of the corner parts is about 79-86 MPa higher than that of the flat parts, which is equivalent to an increase of 23% to 25%. Due to the relatively low degree of anisotropy and smaller thickness measurement errors in thicker CFTWS, the theoretical formula has higher calculation accuracy for steel plates with greater thickness. In addition, in the same batch of steel produced by the same cold bending process, the yield strength of CFTWS slightly decreases with the increase of thickness.

ARTICLE HISTORY

Received: 14 March 2025
Revised: 27 June 2025
Accepted: 2 July 2025

KEYWORDS

Prefabricated support and hanger;
Cold-formed thin-walled steel;
Yield strength;
Linear hardening model;
Corner parts

1. Introduction

As prefabricated construction is advancing and popularizing swiftly on a global scale, the construction industry is undergoing a technological revolution aimed at improving construction efficiency, reducing costs, and minimizing environmental impact. The core advantage of prefabricated construction lies in its modular and factory-based production characteristics, which not only accelerate construction progress but also help achieve standardization of building quality and performance [1-4]. In prefabricated support and hanger, examining the corner strength of CFTWS is vital. Corners are susceptible to stress concentration, heightening the risk of local buckling and connection failures. Studying this aspect aids in comprehending stress distribution, thereby facilitating optimized structural design and augmenting load-bearing capacity and stability.

Fig. 1 shows common prefabricated support and hanger used in subway and housing construction. CFTWS, with its ability to achieve complex cross-sectional shapes during processing, perfectly fits the customized needs of prefabricated support and suspension systems. The lightweight, high-strength, and good processing performance of this material make it an ideal choice for prefabricated support and hanger [5-7], meeting the modern construction requirements for rapid construction and high load-bearing capacity. However, to further enhance its performance in practical applications, in-depth research on the plastic strengthening of CFTWS is particularly necessary.

Fig. 1 CFTWS in prefabricated support and hanger

While cold bending is taking place, the steel endures plastic deformation, which leads to changes in the material's crystal lattice structure, thereby requiring greater stress to continue plastic deformation under subsequent loading. This effect is referred to as strain hardening or plastic strengthening, which increases the material's yield strength. In CFTWS, research on plastic strengthening involves the material's yield criteria and plastic stress-strain relationships [8-10]. This paper aims to explore the research on plastic strengthening in this field, discussing it from three aspects: theoretical research, numerical simulation, and experimental research, to highlight its key role in static design and application.

Up to now, some studies on plastic strengthening and residual stress during the cold bending of metals have mainly focused on carbon steel sections [11-13] and stainless steel sections [14-16], with some representative work among them. Wang et al. [17] studied the link between cold deformation and mechanical parameters of 316L austenitic stainless steel. Their work found that cold working somewhat raises the material's yield stress but doesn't significantly affect the reduction factor. Byun et al. [18] studied the true strain hardening and plastic instability characteristics of steel at different test temperatures. The strength decreased with increasing temperature in both annealed and cold-worked states, while plasticity reached a peak below room temperature. In high-temperature conditions, work-hardened samples failed via instantaneous necking once their yield stress surpassed the plastic instability stress. Ghosh et al. [19] explored how plastic deformation from cold rolling or surface processing affects the chloride - induced stress corrosion cracking susceptibility of 304L austenitic stainless steel at ambient temperature. Test materials underwent solution annealing, cold rolling, and surface processing to create varying material strain and stress levels. The results showed that cracks in the cold-worked samples propagated along slip lines and cracked earlier than the solution-annealed samples. Kim et al. [20] compared steel's deformation mechanisms and mechanical properties at different temperatures. The 293 K tensile curve showed a smooth elastic-plastic transition with continuous work hardening. In contrast, the 123 K curve exhibited yield point extension, strain softening, followed by sudden strain hardening and fracture.

As early as 1997, Macdonald et al. [21] used standard hardness testing

methods to determine the local yield strength at the cold-formed corners. Compared with the design specification methods, using hardness measurement to estimate material strength achieved the main goal of collecting detailed mapping of the distribution of yield stress increases due to cold working. It was also pointed out that the yield values from hardness testing can be used to conservatively estimate the increase in yield stress of cold-formed sections.

In the past decade or so, cold bending technology has increasingly gained attention due to its unique advantages, stimulating the research enthusiasm of many scholars who have turned their research focus to the field of CFTWS. With the popularization and maturation of cold bending processes, its potential for application in the fields of construction and engineering has gradually been explored, attracting in-depth academic exploration of its performance and applications. Ungureanu et al. [22] based on some of the latest surveys and collected literature data, took inventory and classified local plastic mechanisms, providing the ultimate load-bearing capacity of some of the most commonly used cold-bent steel structure sections. Yao et al. [23] developed a finite-element-based method to predict residual stress and equivalent strain distribution in cold-bent steel hollow profiles. This method effectively simulates these distributions, which are hard to measure in labs. Later, simplified models for residual stress and equivalent strain in cold-bent steel elliptical hollow sections were proposed [24]. These models aid in defining component initial states for nonlinear finite element analysis, helping future research assess cold-working effects on component behavior. Luo et al. [25] examined how material strength, plate thickness, sampling position, and heating temperature affect the post - fire mechanical properties of CFTWS. Their study found that exposure to 800°C could reduce yield strength by 40%. However, cold-worked strain hardening can still increase yield strength by 20%. Kim et al. [26] investigated the mechanical properties of cold-bent and heat-treated pipe elbows by conducting tensile tests on simulated samples. The study found that despite heat treatment to eliminate residual stress, the strength of cold-worked material is higher than that of the parent material, while plasticity is lower. The increase in strength and the decrease in plasticity are proportional to the strain level applied during the cold working process. Korsun et al. [27] noted the mechanical properties' non - uniform section - wide distribution in the profile, as hardening in the bending corners and adjacent areas boosts metal strength. Analysis of thin steel plate samples with and without hardening effects showed that the maximum stress in non-hardened samples was more than 30% higher than that in hardened samples, and the maximum displacement in the hardened state was more than triple. Gao et al. [28] performed finite-element parametric analyses using manually calculated residual stress and plastic strain, probing cold bending's impact on steel columns' response. Compared to cases ignoring cold-bending effects, models with isotropic hardening raise the apparent yield stress and column load-bearing capacity.

However, most existing studies on CFTWS focus on the overall performance and processing of the material. These studies lack an in-depth analysis of the plastic strengthening characteristics of the corners, which limits the full utilization of the potential of CFTWS in prefabricated support and hanger. The corners, as key areas for connection and load-bearing in support and hanger, are crucial for improving the stability and load-bearing capacity. Research on the plastic strengthening of CFTWS for prefabricated support and hanger is of significant theoretical and practical importance in the field of statics. This will not only provide theoretical support for the design of prefabricated support and hanger but also promote the performance optimization and innovative design of CFTWS in a wider range of engineering applications, thus providing new perspectives and solutions for the application of CFTWS in the field of prefabricated construction.

The layout of this paper is presented as follows: Section 2 provides a theoretical analysis of cold bending process, focusing on the elastoplastic constitutive relationship. In Section 3, we conduct an examination of the stress distribution at the corners of CFTWS sections and develop a formula for calculating the yield strength at these corners using the Von-Mises yield criterion. Section 4 conducts tensile tests on two types of CFTWS, including the corner parts and flat plate parts, comparing the experimentally measured yield strength with theoretical values. Section 5 combines the constitutive relationships obtained from the experiments with ABAQUS software for analysis, comparing the obtained failure modes with the experiments. Finally, some conclusions are summarized in Section 6.

2. Theoretical analysis of cold bending process

Forming thin-walled steel sections via cold bending mainly involves elastic-plastic deformation of the steel plates. As a numerical computational method for analyzing the elastic and plastic deformations of materials under external forces, the elastoplastic finite element method serves as a theoretical tool for analyzing the cold bending forming process. Unlike elastic deformation, the plastic deformation during the cold bending process is irreversible, and the superposition principle no longer applies. In the plastic development zone, when the stress exceeds the yield limit, irreversible changes begin to occur within the material's microstructure, complicating the stress-strain relationship, which no longer conforms to Hooke's law. During plastic deformation, the stress-strain relationship of the material depends not only on the current stress and strain states but is also significantly influenced by the loading history. This means that even at the same stress level, different loading paths and histories can lead to different strain responses.

According to plasticity theory, the stress-strain tensor can be split into spherical and deviatoric parts. The spherical tensor represents the average effect of the stress tensor, that is, the hydrostatic pressure, which is related to volume changes in the material and does not cause shape changes. Yield criteria are usually defined based on the deviatoric tensor to determine whether the material has entered the plastic state.

For isotropic materials, the internal structure is uniform and identical in all directions. Therefore, the yield behavior of such materials is not affected by the orientation of the coordinate axes; that is, no matter the direction of the stress, as long as the stress magnitude and combination are the same, the material's response will be the same. In this case, the yield function of the material can be represented by three principal stresses（$\sigma_1 \geq \sigma_2 \geq \sigma_3$）, as the principal stresses represent the maximum, intermediate, and minimum stresses in three orthogonal directions. Thus, the yield function

$$f(\sigma_1,\sigma_2,\sigma_3)=0 \tag{1}$$

As shown in Fig. 2, since the yield curve under the Von-Mises condition is the circumcircle of the Tresca hexagon, the yield function can be derived as follows

$$\frac{1}{2}\left[(\sigma_1-\sigma_2)^2+(\sigma_2-\sigma_3)^2+(\sigma_3-\sigma_1)^2\right]=k^2 \tag{2}$$

Where, k is a constant associated with the base material. It can be determined through a simple tension test, as the yield criterion is applicable to various stress states. During simple tension, we have

$$k=\sigma_s \tag{3}$$

Where, σ_s represents the yield stress of the base material.

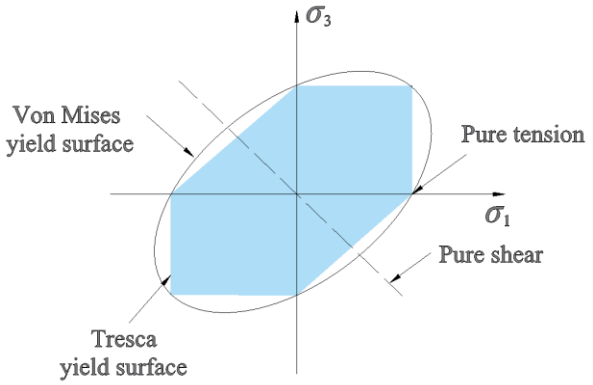

Fig. 2 The connection between Von-Mises criterion and Tresca criterion

According to the calculation formula for stress intensity, it has the following relationship with the octahedral shear stress:

$$\bar{\sigma}=\frac{3\sqrt{2}}{2}\tau_{oct} \tag{4}$$

Where, τ_{oct} represents the octahedral shear stress, and its calculation formula is:

$$\tau_{oct}=\frac{1}{3}\sqrt{(\sigma_1-\sigma_2)^2+(\sigma_2-\sigma_3)^2+(\sigma_3-\sigma_1)^2} \tag{5}$$

According to the Von-Mises condition [29], when the stress intensity reaches a certain value, the material begins to enter the plastic state.

$$\bar{\sigma} = k \tag{6}$$

Combining Eqs. (3) and (6), we can obtain

$$\bar{\sigma} = \sigma_s \tag{7}$$

The Von-Mises yield criterion indicates that when the equivalent stress equals the tensile yield limit, the material starts to plastically deform. Between the elastic and plastic zones of the material, as well as between the loading and unloading zones, there exists a transition zone (neutral zone). Within this zone, the material exhibits both elastic and plastic characteristics. To ensure the continuity of stress and strain in the neutral zone, the plastic relationship should automatically revert to the elastic relationship within the neutral zone. Incremental theory can guarantee this continuity, but total theory cannot. However, under conditions of small deformations and simple loading, the two theories are consistent, meaning that the total relationship can be derived from the incremental relationship. For cold bending forming, there is a neutral zone that needs to ensure its continuity, and since nonlinear finite elements mainly use plastic incremental theory, it is reasonable to use incremental theory in the cold bending forming process.

According to the Prandtl-Reuss flow rule,

$$\mathrm{d}\varepsilon_{ij}^{\mathrm{p}} = \mathrm{d}\lambda S_{ij},\ \mathrm{d}\lambda \geq 0 \tag{8}$$

Where, $\mathrm{d}\lambda$ represents the proportionality factor, which is related to the position of the material point and the level of load, hence the equation above is a nonlinear relationship. $\mathrm{d}\varepsilon_{ij}^{\mathrm{p}}$ denotes the increment of plastic strain, and S_{ij} represents the deviatoric stress tensor, satisfying

$$S_{ij} = \frac{\partial p_{\mathrm{f}}}{\partial \sigma_{ij}} \tag{9}$$

Where, p_{f} represents the loading function, and σ_{ij} represents the stress components.

According to the principle of superposition of strains, the total strain increment during the cold bending forming process is composed of the elastic strain increment and the plastic strain increment, that is:

$$\mathrm{d}\varepsilon_{ij} = \mathrm{d}\varepsilon_{ij}^{\mathrm{e}} + \mathrm{d}\varepsilon_{ij}^{\mathrm{p}} \tag{10}$$

In elastoplastic deformation, the stress increment caused by the elastic strain increment obeys Hooke's law and can be expressed as

$$\mathrm{d}\sigma_{ij}^{e} = D^{\mathrm{e}}\mathrm{d}\varepsilon_{ij}^{e} \tag{11}$$

Where, D^{e} represents the elastic modulus matrix.

Stress and strain satisfy the following expression:

$$\mathrm{d}\sigma_{ij} = D^{\mathrm{ep}}\mathrm{d}\varepsilon_{ij} \tag{12}$$

Where, D^{ep} represents the elastoplastic matrix. And the following relationship holds:

$$D^{\mathrm{ep}} = D^{\mathrm{e}} - D^{\mathrm{p}} \tag{13}$$

$$D^{\mathrm{p}} = \frac{D^{\mathrm{e}}}{\Omega} - \frac{\partial p_{\mathrm{f}}}{\partial \sigma_{ij}}\left(D^{\mathrm{e}}\frac{\partial p_{\mathrm{f}}}{\partial \sigma_{ij}}\right)^{\mathrm{T}} \tag{14}$$

$$\Omega = \left(\frac{\partial p_{\mathrm{f}}}{\partial \sigma_{ij}}\right)^{\mathrm{T}} D^{\mathrm{e}}\frac{\partial p_{\mathrm{f}}}{\partial \sigma_{ij}} - \frac{\partial p_{\mathrm{f}}}{\partial K}\left(\frac{\partial K}{\partial \varepsilon_{ij}^{\mathrm{p}}}\right)^{\mathrm{T}}\frac{\partial p_{\mathrm{f}}}{\partial \sigma_{ij}} - \left(\frac{\partial p_{\mathrm{f}}}{\partial \varepsilon_{ij}^{\mathrm{p}}}\right)^{\mathrm{T}}\frac{\partial p_{\mathrm{f}}}{\partial \sigma_{ij}} \tag{15}$$

Where, Ω is a coefficient matrix related to plastic behavior, and K is a parameter associated with material hardening.

3. Corner yield stress

To simplify the model and facilitate theoretical analysis, the following basic assumptions are introduced:

(1) Plane strain assumption [30], meaning that the strain component perpendicular to the analysis plane is zero.

(2) Linear hardening assumption [31], meaning that the post-yield behavior of the material is considered linear, i.e., after the yield point, the material's stress increases proportionally with strain until the ultimate strength is reached.

(3) Incompressibility assumption [32] in plastic deformation.

(4) Ignoring residual stress [33], time-dependent effects [34], and Bauschinger effects [35].

(5) The elastic strain is much smaller compared to the plastic strain and can be neglected.

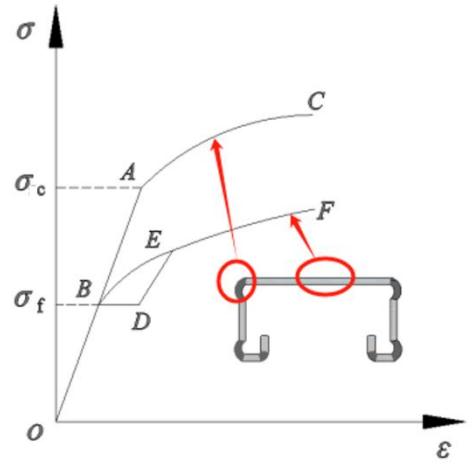

Fig. 3 Stress-strain curves of various parts of CFTWS sections

CFTWS sections are divided into two parts: the corner part and the flat plate part, as shown in Fig. 3.

Cold bending causes plastic deformation, leading to work hardening and higher material yield strength [36]. If shear stress is neglected [37-39], the stress analysis problem can be considered as an axisymmetric problem, as shown in Fig. 4.

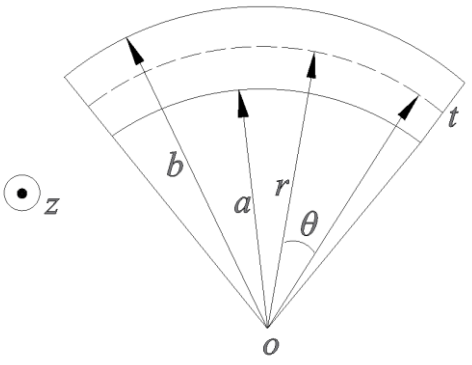

Fig. 4 Axisymmetric bending of the corner section

In Fig. 4, a represents the distance from the inner surface of the cylinder to the center, b represents the distance from the outer surface of the cylinder to the center, r is the displacement in the radial direction, and θ is the tangential displacement.

According to the Von-Mises criterion, the yield stress at each point in the corner is equal to the effective stress. Since shear stress in multiaxial stress states increases material deformation, thereby increasing effective stress, neglecting shear stress underestimates the actual stress state that the material withstands. Therefore, the calculated effective stress will be less than the actual

value, making the theoretical analysis conservative.

$$\frac{\sigma_\theta-\sigma_r}{2\mu\varepsilon_\theta}=\frac{\sigma_\theta-\sigma_z}{\mu\varepsilon_\theta}=\frac{\sigma_z-\sigma_r}{\mu\varepsilon_\theta}=1 \tag{16}$$

Where, σ_θ, σ_r, σ_z represent the strains along the circumferential, radial, and axial axes, respectively, ε_θ is the strain in the circumferential direction. μ is the material's strength parameter, and the following equation is also valid.

$$\bar{\sigma}=\frac{3}{2}\mu\bar{\varepsilon} \tag{17}$$

Where, $\bar{\sigma}$ and $\bar{\varepsilon}$ represent the effective stress and effective strain, respectively, and the following two relations hold true [40]

$$\bar{\sigma}=\sqrt{\frac{1}{2}[(\sigma_\theta-\sigma_r)^2+(\sigma_\theta-\sigma_z)^2+(\sigma_z-\sigma_r)^2]},\bar{\varepsilon}=\sqrt{\frac{2}{3}(\varepsilon_r^{\,2}+\varepsilon_\theta^{\,2}+\varepsilon_z^{\,2})} \tag{18}$$

Substituting Eq. (16) into Eq. (18) yields:

$$\bar{\sigma}=\begin{cases}\sqrt{3}\mu\varepsilon_\theta,\varepsilon_\theta\geq 0\\ -\sqrt{3}\mu\varepsilon_\theta,\varepsilon_\theta<0\end{cases} \tag{19}$$

In pure bending, there is no shear stress on the cross-section, and the plane section assumption can be used [41]. For any point on the corner part of the section, let the distance to the neutral axis be r, and r_0 be the radius of curvature of the length-unchanged surface. Since strain is proportional to distance, this relationship can be described by the following function:

$$r=r_0e^{\varepsilon_\theta} \tag{20}$$

Taking the element of the corner part for force analysis, the stress components in the cylindrical coordinate system are depicted in Fig. 5.

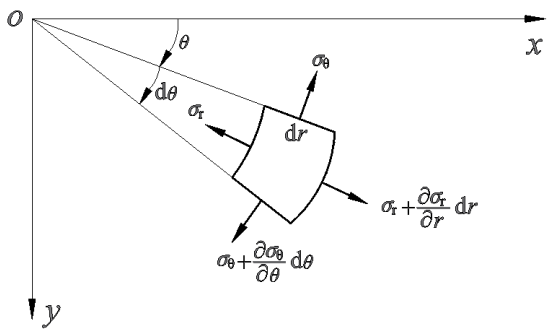

Fig. 5 Stress analysis of the corner element

From the equilibrium differential equation of the element, we get:

$$\frac{\partial\sigma_r}{\partial r}+\frac{\sigma_r-\sigma_\theta}{r}=0 \tag{21}$$

Assuming that the pressure q is acting in the radial direction on the inner surface. According to the force boundary conditions:

$$\sigma_r=\begin{cases}0,\ r=b\\ -q,\ r=a\end{cases} \tag{22}$$

Taking the limit of uniform strain as

$$\Delta=2\delta_{10}-\delta_5 \tag{23}$$

Where, δ_{10} and δ_5 represent the elongation ratios for gauge lengths of 10 times and 5 times the diameter, respectively.

Although some studies focus on advanced analysis methods to delve into the nonlinear behavior of structures under complex loading conditions [42-44]. The linear hardening model is a theoretical model that describes the stress-strain relationship of a material during plastic deformation. In this model, the expression can be written as

$$\bar{\sigma}=\alpha_0\bar{\varepsilon}+\sigma_s,\ \alpha_0=\frac{(1+\Delta)\sigma_b-\sigma_s}{\ln(1+\Delta)} \tag{24}$$

Where, σ_b is the tensile strength of the base metal flat section, which is the maximum stress that the material can withstand in a tensile experiment. α_0 is the slope of the linear hardening model.

The material in the corner section can be assessed for its yield strength under bending conditions using the Von-Mises yield criterion. The yield stress in the elastic region near the neutral surface does not increase due to bending. The yield stress distribution in the corner section is shown in Fig. 6.

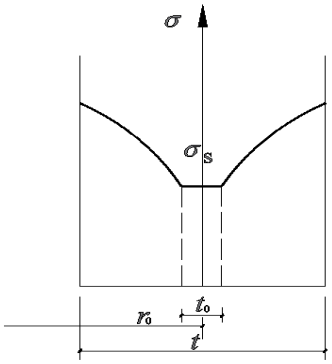

Fig. 6 Distribution of yield stress in the corner section

The yield strength of the corner section of CFTWS is

$$\sigma_c=\frac{2}{b^2-a^2}\left[\int_a^{r_0-\frac{t'}{2}}\bar{\sigma}r\mathrm{d}r+\int_{r_0-\frac{t'}{2}}^{r_0+\frac{t'}{2}}\sigma_s r\mathrm{d}r+\int_{r_0+\frac{t'}{2}}^{b}\bar{\sigma}r\mathrm{d}r\right] \tag{25}$$

Considering the continuity of the radial stress at $r=r_0$, we have:

$$r_0=\sqrt{ab} \tag{26}$$

When the thickness $t_0=0$ of the elastic zone in Fig. 6 under bending, integrating Eq. (25) by parts yields:

$$\sigma_c=\sigma_s+\frac{t}{2a+t}\cdot\frac{(1+\Delta)\sigma_b-\sigma_s}{\sqrt{3}\ln(1+\Delta)} \tag{27}$$

4. Experimental verification

To assess the yield strength and tensile strength of CFTWS in the corner sections, this section conducted tensile tests on two types of CFTWS (41.3mm×41mm×2.0mm and 41.3mm×72mm×2.75mm), including the corner sections and flat plate sections. The corner and flat plate specimens were extracted from the steel profile by milling. Sampling was done according to the "Metallic materials-Method of test at room temperature" (GB/T228-2002) [45].

All specimens were made from the same batch of Q345B grade hot-rolled steel plates that were cold-bent, and the double-limb combined specimens were made by combining single-limb specimens, so only the single-limb specimens were sampled. In the prefabricated support and hanger, the top view plan of the common perforated and non-perforated specimens are shown in Fig. 7.

Specimens are sampled from CFTWS profiles without holes. Sampling positions were at the right-angle and flat plate sections, with the sampling positions and specimen numbers shown in Fig. 8. For specimens with gauge widths of 7.5mm, 10mm, and 15mm, wire cutting was used for processing as

shown in Fig. 9, three specimens were taken for testing at each position.

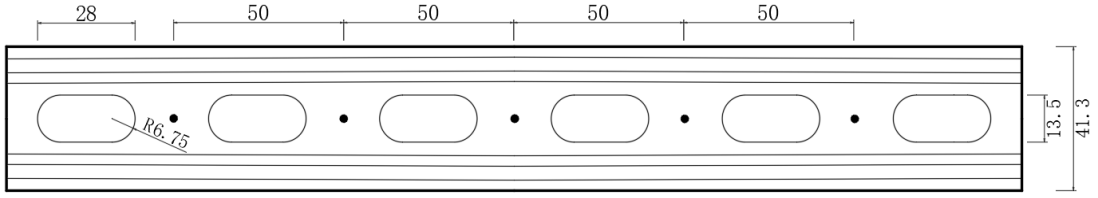

(a) The top view plan of perforated components (mm)

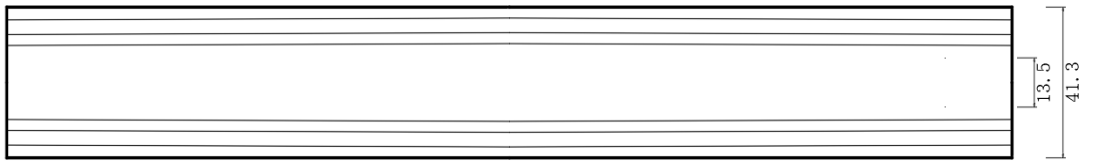

(b) The top view plan of a poreless component (mm)

Fig. 7 The geometric dimensions of the single-limb specimen

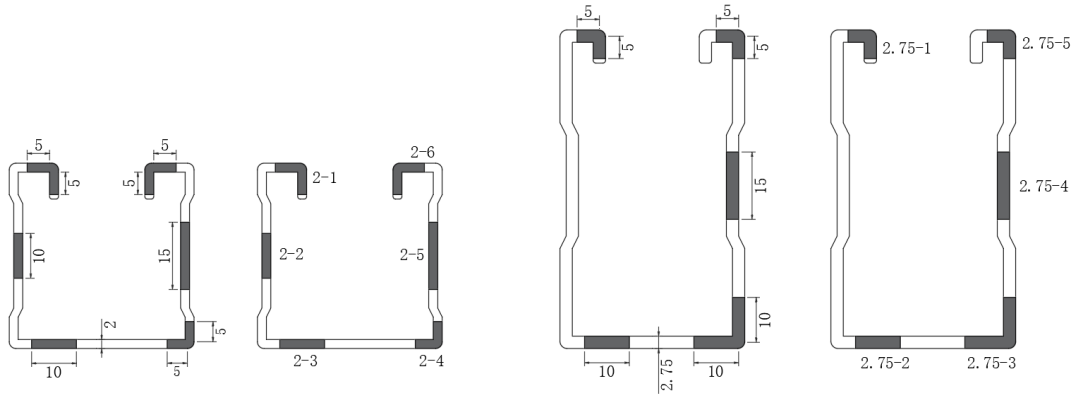

(a) 41.3mm×41mm×2.0mm (b) 41.3mm×72mm×2.75mm

Fig. 8 Sampling positions and numbers for specimens of different cross-sections

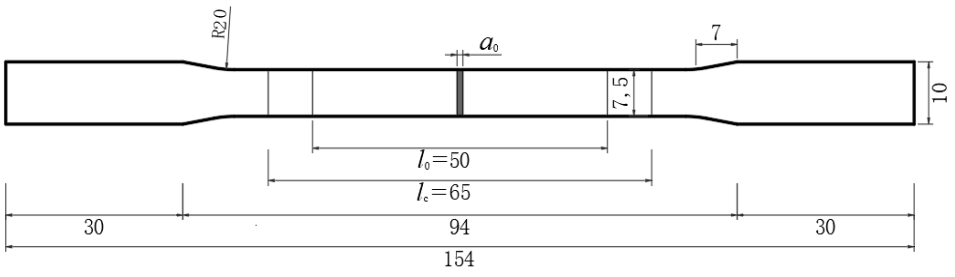

(a) 7.5 mm gauge length width

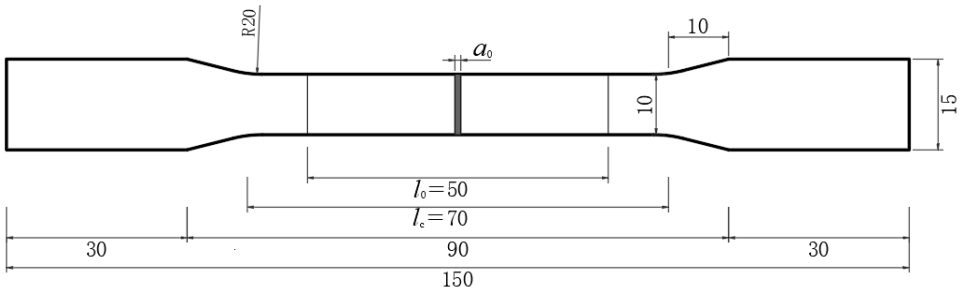

(b) 10 mm gauge length width

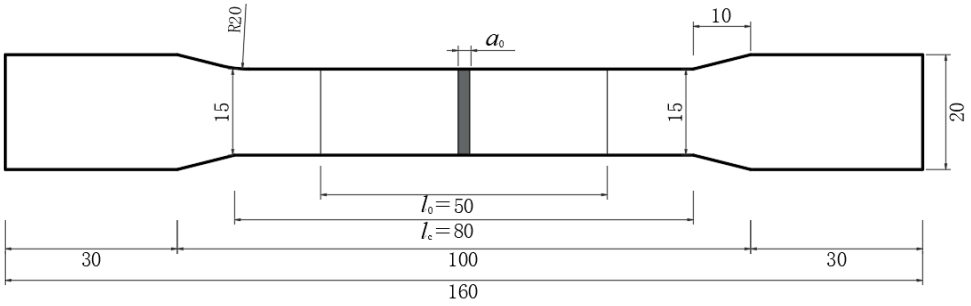

(c) 15 mm gauge length width

Fig. 9 Processing dimensions of different tensile specimens

In Fig. 9, a_0 is the original thickness, l_0 is the original gauge length (l_0=5.56$\sqrt{S_0}$), S_0 is the original cross-sectional area of the parallel length.

Before the start of the experiment, dots are marked on the prepared specimen at intervals of 10mm. They will serve as references for measuring the length after fracture. Material property tests were conducted using a 30t microcomputer-controlled electro-hydraulic servo universal testing machine, some representative specimens used in the experiment are shown in Fig. 10.

Fig. 10 Specimens taken from different positions

The tensile deformation of the specimen was measured using an extensometer with a gauge length of 50mm to determine the elastic modulus, as shown in Fig. 11. Further insights into the functional mechanisms of extensometers are available in reference [46].

Fig. 11 Using an extensometer to measure tensile deformation

Before material yielding, the loading speed was set at 1.0 mm/min to observe the material's elastic behavior and stress-strain relationship. After material yielding, the loading speed was appropriately increased to 2mm/min to observe the material's plastic flow and hardening behavior. The increase in loading speed was controlled within a range that does not cause dynamic effects (such as vibration or impact), as these effects could affect the accuracy of the experimental results. As shown in Fig. 12, after the specimen is broken, the length of the fully deformed region is measured using a vernier caliper to calculate the elongation of the specimen.

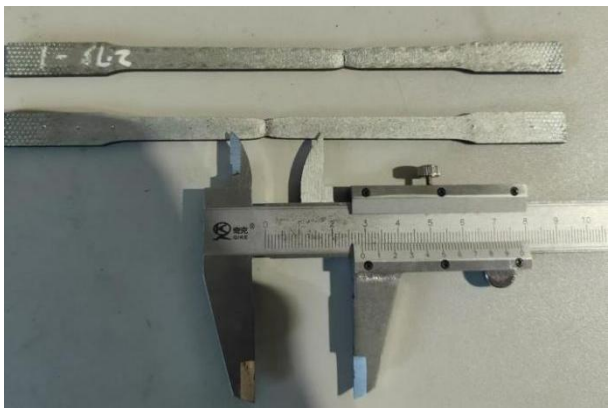

Fig. 12 Measurement of steel elongation

The dimensions a and b are measured using a radius gauge, and the average of a and b-t is calculated as the thickness a value of the specimen. Since the tensile yield strength of the steel profile is essentially equal to its compressive yield strength, if the verification formula is applicable to the tensile yield strength, then the formula is also applicable to the compressive yield strength. The parameters of the CFTWS are shown in Table 1. After three measurements, the data are averaged if all are valid. The comparison of the corner yield strength is shown in Table 2.

Table 1
Parameters of the CFTWS

Thickness	Parameter	Symbol	Value
2.0mm	The strain at a gauge length that is 5 times the diameter	δ_5	39.1%
	The strain at a gauge length that is 10 times the diameter	δ_{10}	32.6%
	The yield strength of the flat plate	σ_s	348MPa
2.75mm	The strain at a gauge length that is 5 times the diameter	δ_5	36.2%
	The strain at a gauge length that is 10 times the diameter	δ_{10}	30.4%
	The yield strength of the flat plate	σ_s	345MPa

Table 2
Comparison of theoretical and experimental yield strengths at the corner

Thickness	a/t	Experimental value	Eq.(27)	Relative error
2.0mm	1.81	448.0MPa	433.9MPa	3.25%
2.75mm	1.65	428.2MPa	423.6MPa	1.10%

Table 2 shows that the theoretical analysis aligns well with the experiments. The yield strength measured using specimens of two different thicknesses has an error range of less than 5%. Moreover, the theoretical calculation results obtained are slightly smaller than the experimental results, which is more conservative. Applying the theoretical formulas from this study in practical engineering can ensure a certain safety margin.

It can be seen that the cold bending effect has a significant impact on the steel. The yield strength of the corner part is about 79-86 MPa higher than that

of the flat part. For the CFTWS used in the prefabricated support and hanger, the yield strength of the corner part can be increased by 23% to 25% compared to the flat part, which has good utilization value. The theoretical formulas have higher precision when the steel plate thickness is larger. On one hand, the degree of anisotropy of thick steel plates is relatively low [47], which can better meet the assumptions in the theoretical formulas, thereby making the theoretical calculation results closer to the experimental values. On the other hand, the error in measuring the value of for thick steel plates is smaller, which in turn improves the accuracy of the calculation results.

In addition, it can be observed that in the same batch of steel produced by the same cold bending process, the yield strength of CFTWS sections slightly decreases with the increase of thickness, and thinner steel plates exhibit higher yield strength. This is because when the steel plate thickness is thinner, the degree of deformation the material undergoes during the cold bending process is greater, making it more prone to work hardening, which significantly increases the yield strength. When thin steel plates are bent, the stress distribution on their cross-section is more concentrated, and the deformation per unit area is greater, leading to more dislocations moving and accumulating in the crystal lattice, hindering further plastic deformation, and thereby significantly enhancing the material's strength.

5. Numerical simulation

Taking the tensile specimen corresponding to position 2-1 as an example, the geometric model shown in Fig. 9 (a) is established using the ABAQUS software. In the "Property" module, the material properties of Q345 CFTWS are defined, including the elastic modulus (210 GPa), Poisson's ratio (0.3), etc. The plastic parameters are inputted based on the curve shown in Fig. 13, which is obtained from the experiment.

In the "Mesh" module, the solid element type is selected to mesh the model, and the approximate global size is set to 0.5. This size is chosen based on experience from similar simulations. It's fine enough to capture key structural behavior details without excessive computational cost. The 0.5mm mesh balances computational efficiency and result accuracy. No significant changes in key response variables are observed with further refinement, indicating satisfactory convergence for this study. After the meshing of the specimen is completed, it is shown in Fig. 14. The hexahedral mesh quality is good, with regular element shapes, no obvious distortion, and the Jacobian value is close to 1.

In the "Step" module, the options "Large deformation" and "Nonlinear geometry" are selected to simulate the yielding behavior of the material. In the "Interaction" module, two reference points are established at the centroid positions of the cross-sections at both ends of the specimen, and the sections are coupled with the reference points through the coupling command. In the "Load" module's "Boundary Condition Manager" tab, a fixed constraint is applied to one end of the specimen to simulate the fixture's clamping. A displacement is applied to the reference point at the other end to simulate the stretching process in the tensile experiment, until the specimen fails and the process stops. The job is submitted in the Job module, and after the calculation is completed, the stress distribution and the development of the plastic zone of the specimen are viewed.

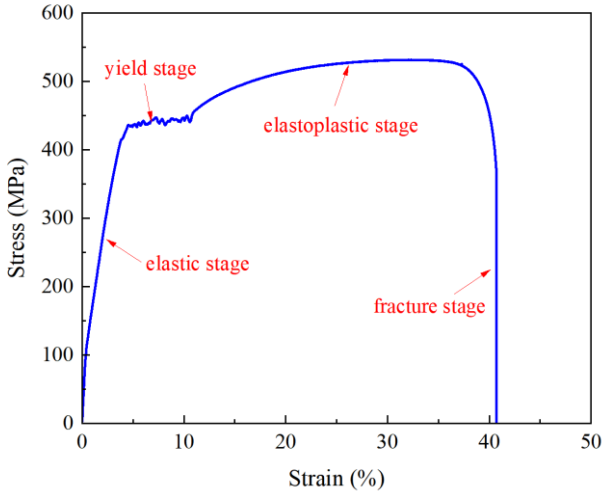

Fig. 13 The stress-strain curve of the steel at position 2-1

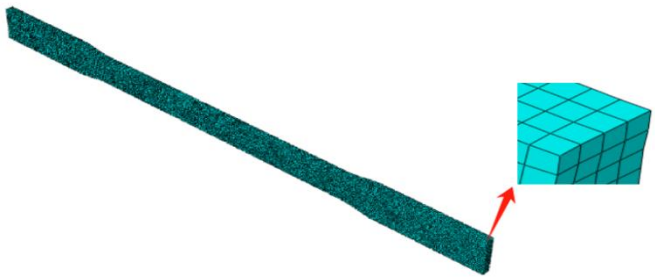

Fig. 14 The meshing of the specimen

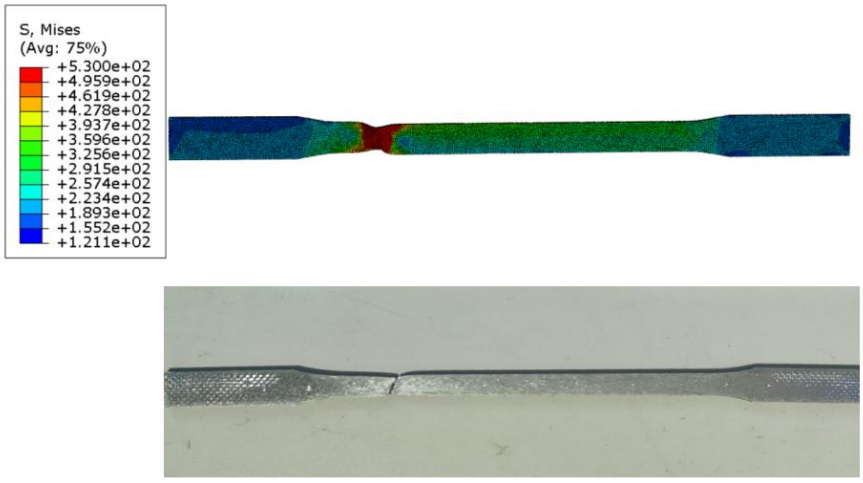

Fig. 15 Comparison between ABAQUS simulation and experiment at position 2-1

The numerical simulation in Fig. 15 shows the stress data during corner material failure aligns with Fig. 13, especially for maximum tensile stress, indirectly proving the theory's feasibility. Additionally, the failure state of the specimen obtained through ABAQUS calculation is basically consistent with the experimental failure state. The high degree of coincidence between the two validates the correctness and effectiveness of the research findings in this study.

In line with the previous research approach, position 2.75-1 was selected for validation. The comparison results are shown in Fig. 16. After changing the thickness of the CFTWS, the failure mode experiments and ABAQUS simulations still show high consistency. This addition further validates the accuracy of the theoretical model across different locations, demonstrating the robustness of this study.

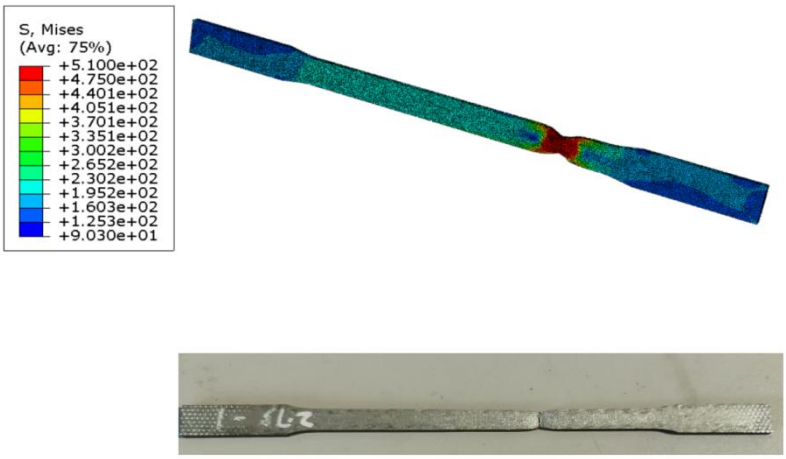

Fig. 16 Comparison between ABAQUS simulation and experiment at position 2.75-1

6. Conclusions

This paper derives the yield strength calculation formula for the corner parts of CFTWS used in prefabricated support and hanger by employing a linear strengthening model. The stress analysis is conducted and the corresponding mechanical model is established based on the idea that the yield stress at each point of the corner part is equal to the effective stress at that point during the cold forming process. The validity of the theory is verified by experimental data and finite element results. The key findings are as follows:

(1) The theoretical formula in this study has a clear physical meaning and good calculation accuracy. Compared with the experimental results, the calculation error of the yield strength for the corner parts is within 5%.

(2) The CFTWS is significantly affected by the cold forming effect. The yield strength of the corner parts is about 23% to 25% higher than that of the flat parts, which has good utilization value.

(3) Due to the influence of theoretical assumptions and actual thickness measurement, the theoretical formula of this study has higher calculation accuracy when the steel plate thickness is larger.

(4) Under the same conditions, the yield strength of thin steel plates is more sensitive to the cold forming process. Because the deformation per unit area is greater during bending, more dislocations move and accumulate in the lattice, making it easier for the yield strength to increase.

The next step of the research will employ the power-law strengthening model to study the yield strength of the cross-section, taking into account the influence of initial imperfections. A yield strength modification coefficient considering the cold forming strengthening effect will be proposed, and it is suggested that relevant content be added to the specifications to expand the scope of application of the theory.

References

[1] Luo T, Xue X, Wang Y, et al. A systematic overview of prefabricated construction policies in China[J]. Journal of Cleaner Production, 2021, 280: 124371.
[2] Zhong R Y, Peng Y, Xue F, et al. Prefabricated construction enabled by the Internet-of-Things[J]. Automation in Construction, 2017, 76: 59-70.
[3] Tam V W Y, Tam C M, Zeng S X, et al. Towards adoption of prefabrication in construction[J]. Building and environment, 2007, 42(10): 3642-3654.
[4] Navaratnam S, Satheeskumar A, Zhang G, et al. The challenges confronting the growth of sustainable prefabricated building construction in Australia: Construction industry views[J]. Journal of Building Engineering, 2022, 48: 103935.
[5] Adanur Ö, Varol F. Investigation of the effect of friction force on the energy absorption characteristics of thin-walled structures loaded with axial impact force[J]. Materials Today Communications, 2023, 36: 106420.
[6] Wang X T Z, PLi L J L, NSu X P W, et al. Restoring force model of phosphogypsum-filled cold-formed thin-walled square steel tube composite wall[J]. Materials Today Communications, 2024, 65.
[7] Magnucka-Blandzi E, Magnucki K. Buckling and optimal design of cold-formed thin-walled beams: Review of selected problems[J]. Thin-Walled Structures, 2011, 49(5): 554-561.
[8] Kawasaki M, Lee H J, Jang J, et al. Strengthening of metals through severe plastic deformation[J]. Reviews on Advanced Materials Science, 2017, 48(1).
[9] Zhuravlev G M, Gvozdev A E, Cheglov A E, et al. Maximum plastic strengthening in tool steels[J]. Steel in Translation, 2017, 47: 399-411.
[10] Wang Z, Shi S, Yu J, et al. Enhanced cryogenic tensile properties through cryogenic cyclic plastic strengthening in a metastable austenitic stainless steel[J]. Scripta Materialia, 2023, 222: 115024.
[11] Key P W, Hancock G J. A theoretical investigation of the column behaviour of cold-formed square hollow sections[J]. Thin-Walled Structures, 1993, 16(1-4): 31-64.
[12] Chen M T, Young B. Material properties and structural behavior of cold-formed steel elliptical hollow section stub columns[J]. Thin-Walled Structures, 2019, 134: 111-126.
[13] Tong L, Hou G, Chen Y, et al. Experimental investigation on longitudinal residual stresses for cold-formed thick-walled square hollow sections[J]. Journal of Constructional Steel Research, 2012, 73: 105-116.
[14] Young B, Lui W M. Behavior of cold-formed high strength stainless steel sections[J]. Journal of Structural Engineering, 2005, 131(11): 1738-1745.
[15] Zheng B, Shu G, Jiang Q. Experimental study on residual stresses in cold rolled austenitic stainless steel hollow sections[J]. Journal of Constructional Steel Research, 2019, 152: 94-104.
[16] Cruise R B, Gardner L. Residual stress analysis of structural stainless steel sections[J]. Journal of constructional steel research, 2008, 64(3): 352-366.
[17] Wang S, Xue H, Cui Y, et al. Effect of Different Cold Working Plastic Hardening on Mechanical Properties of 316L Austenitic Stainless Steel[J]. Procedia Structural Integrity, 2018, 13: 1940-1946.
[18] Byun T S, Hashimoto N, Farrell K. Temperature dependence of strain hardening and plastic instability behaviors in austenitic stainless steels[J]. Acta Materialia, 2004, 52(13): 3889-3899.
[19] Ghosh S, Kain V. Effect of surface machining and cold working on the ambient temperature chloride stress corrosion cracking susceptibility of AISI 304L stainless steel[J]. Materials Science and Engineering: A, 2010, 527(3): 679-683.
[20] Kim J S, Kim J K. Martensitic-transformation-driven strain-softening in the cryogenic deformation of austenitic stainless steel[J]. Materials Science and Engineering: A, 2024: 147681.
[21] Macdonald M, Taylor G T, Rhodes J. The effect of cold forming on the yield strength of thin gauge steel—hardness test approach[J]. Thin-Walled Structures, 1997, 29(1-4): 243-256.
[22] Ungureanu V, Kotełko M, Mania R J, et al. Plastic mechanisms database for thin-walled cold-formed steel members in compression and bending[J]. Thin-Walled Structures, 2010, 48(10-11): 818-826.
[23] Yao Y, Quach W M, Young B. Finite element-based method for residual stresses and plastic strains in cold-formed steel hollow sections[J]. Engineering Structures, 2019, 188: 24-42.
[24] Yao Y, Quach W M, Young B. Simplified models for residual stresses and equivalent plastic strains in cold-formed steel elliptical hollow sections[J]. Thin-Walled Structures, 2020, 154: 106835.
[25] Luo K, Li H, Yang J, et al. Research on post-fire mechanical properties of thin-walled cold-formed steel and its influence on the Σ-shaped columns after fire exposure[J]. Thin-Walled Structures, 2024, 204: 112315.
[26] Kim J W, Lee M Y, Lee S Y. Estimation of Tensile Properties of Pipe Bends Manufactured by Cold-Bending[J]. Transactions of the Korean Society of Mechanical Engineers A, 2012, 36(9): 1059-1064.
[27] Korsun N, Prostakishina D. Modeling thin-walled elements with regard to steel hardening[C]//E3S Web of Conferences. EDP Sciences, 2021, 263: 02044.
[28] Gao T, Moen C D. The cold work of forming effect in steel structural members[J]. SDSS' Rio 2010 stability and ductility of steel structures, 2010: 1017-1024.
[29] Roy A M, Guha S. A data-driven physics-constrained deep learning computational framework for solving von Mises plasticity[J]. Engineering Applications of Artificial Intelligence, 2023, 122: 106049.
[30] Barber J R. Plane strain and plane stress[M]//Elasticity. Cham: Springer International

Publishing, 2023: 41-49.
[31] Han J, Matsubara S, Moriguchi S, et al. Variational crack phase-field model for ductile fracture with elastic and plastic damage variables[J]. Computer Methods in Applied Mechanics and Engineering, 2022, 400: 115577.
[32] Bechir H, Mendil F, Yaya K. Extension and inflation of a thick-cylindrical tube made of isotropic compressible of Mooney-Rivlin materials: modeling and finite element simulations[J]. Acta Mechanica, 2023, 234(11): 5461-5475.
[33] Zhang Y, Cai J, Mi C, et al. Effect of surface residual stress and surface layer stiffness on mechanical properties of nanowires[J]. Acta Mechanica, 2022: 1-25.
[34] Zhang X, Li Y, Lei J, et al. Time-dependent effects of microplastics on soil bacteriome[J]. Journal of Hazardous Materials, 2023, 447: 130762.
[35] Lee E H, Rubin M B. Eulerian constitutive equations for the coupled influences of anisotropic yielding, the Bauschinger effect and the strength-differential effect for plane stress[J]. International Journal of Solids and Structures, 2022, 241: 111475.
[36] Patra A K, Kapoor R, Mandal S, et al. Influence of strain rate on the work hardening, strain induced martensite formation, strain partitioning, and variant selection in a medium-Mn steel[J]. Materials Science and Engineering: A, 2024, 902: 146593.
[37] Camotim D, Basaglia C. On the behaviour, failure and direct strength design of thin-walled steel structural systems[J]. Thin-Walled Structures, 2014, 81: 50-66.
[38] Liu S W, Liu Y P, Chan S L. Direct analysis by an arbitrarily-located-plastic-hinge element—Part 1: Planar analysis[J]. Journal of Constructional Steel Research, 2014, 103: 303-315.
[39] Rasmussen K J R, Hancock G J. Design of cold-formed stainless steel tubular members. II: Beams[J]. Journal of Structural Engineering, 1993, 119(8): 2368-2386.
[40] Ban H, Yao Y. The coupling effects of strain gradient and damage on Mode I crack tip stress fields[J]. Theoretical and Applied Fracture Mechanics, 2023, 126: 103989.
[41] Qin F, Wei X, Lu Y, et al. Flexural behaviour of high strength engineered cementitious composites (ECC)-reinforced concrete composite beams[J]. Case Studies in Construction Materials, 2023, 18: e02002.
[42] Liu S W, Liu Y P, Chan S L. Direct analysis by an arbitrarily-located-plastic-hinge element—Part 2: Spatial analysis[J]. Journal of Constructional Steel Research, 2014, 103: 316-326.
[43] Liu S W, Liu Y P, Chan S L. Advanced analysis of hybrid steel and concrete frames:Part 1: Cross-section analysis technique and second-order analysis[J]. Journal of Constructional Steel Research, 2012, 70: 326-336.
[44] Liu S W, Liu Y P, Chan S L. Advanced analysis of hybrid steel and concrete frames: Part 2: Refined plastic hinge and advanced analysis[J]. Journal of Constructional Steel Research, 2012, 70: 337-349.
[45] Metallic materials-Method of test at room temperature: GB/T228-2002[S]. Beijing: China Standards Press, 2002. (in Chinese)
[46] Alias M A, Ismail M F, Sa'ad M S M, et al. A high-precision extensometer system for ground displacement measurement using fiber Bragg grating[J]. IEEE Sensors Journal, 2022, 22(9): 8509-8521.
[47] Meyers M A, Chawla K K. Mechanical behavior of materials[M]. Cambridge university press, 2008.

Advanced Steel Construction – Vol. 22 No. 1 (2026) 17–36
DOI:10.18057/IJASC.2026.22.1.3

SEISMIC PERFORMANCE ANALYSIS OF THE INTEGRATED MODEL FOR LARGE STADIUM STEEL STRUCTURE CANOPY

Chen-Xiao Zhang [1, 2], Chun-Jie Yu [1], Ren-Cai Jin [2], Cong-Ying Gan [1], Dong-Yun Jia [1], Foysal Bin Shakil [1] and Song Jin [1, *]

[1] *College of Architecture and Engineering, Anhui University of Technology, Maanshan 243002, China*
[2] *Technology Center, China MCC17 group Co. Ltd., Maanshan 243000, China*
** (Corresponding author: E-mail: jinsong_342601@163.com)*

ABSTRACT

Traditional seismic design method of steel canopy structures usually assumes that the lower support structure to be rigid. However, in practical engineering, the steel canopy and the lower support structure interact as an integrated system. With the innovation in design method of steel canopy structures, the seismic design of traditional large cantilever steel structure faces higher requirements. In this study, the integrated model of a large stadium steel canopy and its lower support structure is used as a reference. To consider the influence of the lower support structure, two simplified preliminary analysis models are established separately. Time history analysis is performed on all three models to evaluate simplified calculation methods for the lower support structure under seismic excitation. A series of studies are conducted to identify the causes of the discrepancies in the dynamic response among models. The study examines the effects of stiffness in-homogeneity in the lower support structure, revealing significant directional variations in stiffness across three axes. Furthermore, by analyzing peak acceleration and frequency variations between input and output for ground motion in the lower support structure, the results demonstrate that the structure's amplification and filtering effects of the lower support structure on ground motion are key contributors to in dynamic response variability. Results indicated that the seismic performance of large cantilever steel canopy structures should be evaluated using an integrated model to ensure more reliable seismic design outcomes.

ARTICLE HISTORY

Received: 27 December 2024
Revised: 24 June 2025
Accepted: 26 June 2025

KEYWORDS

Large cantilever steel canopy structures;
Seismic performance;
Lower support structure;
Ground motion;
Integrated model

1. Introduction

China is located within the seismically active zone between the Pacific Rim Seismic Belt and the Eurasian Seismic Belt, where the frequent occurrence of shallow-source earthquakes often results in severe earthquake disasters. Recent earthquake damage investigations reveal that steel canopy structures in stadiums constitute a vulnerable part in seismic design [1]. In addition to its primary functional role, the large-span spatial steel structure typically serves as a post-earthquake temporary rescue command center or aid station. Therefore, the seismic performance requirements for the spatial structure differ from those of ordinary residential buildings, necessitating compliance with region-specific seismic design codes [2]. Zhang [3, 4] and Liang [5] conducted a time-history analysis of a large-span spatial structure, studying the dynamic response and internal force distribution of the model. Lu [6] investigated the seismic performance and seismic response of large-span string trusses under rare earthquakes. The results indicate that the large-span string truss structure exhibits good seismic performance under rare earthquakes, but the weak areas of the structure still exist. Xiao [7] et al. conducted the whole process of stability analysis and the static elasto-plastic analysis under rare earthquakes on the spatial grids of an exhibition hall with vertical force transmission, indicating that the inter-story drift is minimal under multiple and rare earthquakes, and the structure's resistant lateral rigidity is substantial. Tong [8] analyzed the seismic performance and ultimate bearing capacity of three special-shaped multi-towers connected high-rise structures, quantifying the degradation patterns of both bearing capacity and stiffness under varying seismic intensities. Wang [9] proposed a new direction-dependent evolution lag coherence model for the seismic ground motions in non-stationary horizontal space. Jian [10] et al. compared the seismic responses of adjacent bridges with and without control systems, identifying critical parameters governing spatially varying ground motion effects. Rodda [11] et al demonstrated that spatial variations in vertical ground motion could significantly influence the dynamic response of large-span structures (e.g., bridges and pipelines). Bi [12] et al. quantified the structural effects of spatial ground motion variations by decomposing responses into dynamic, quasi-static, and total components. Hao [13] et al. investigated the behavior of symmetrical buildings under spatially varying base excitation and discussed the adequacy of seismic code provisions for accidental eccentricity.

Ground motions are random and dispersive, and the selection of ground motions affects the dynamic response results when using time history analysis to analyze the seismic performance of structures. Therefore, the rational selection of ground motion is imperative. Watson-Lamprey [14] et al. proposed a time series selection method for nonlinear analysis to obtain the average response of a nonlinear system rather than based on amplitude, period, and type of response spectrum. Katsanos [15] et al. demonstrated that the current seismic code framework is overly simplistic and emphasized significant inherent uncertainties in ground motion selection. Ao [16] et al. established the efficacy of multivariate regression-based selection for seismic risk assessment. Bradley [17] developed an algorithm integrating recorded and simulated motions for response history analysis. Wang[18] introduced a new algorithm for selecting and modifying ground motions, which exhibited high computational efficiency and demonstrates significant potential in enhancing seismic performance in nonlinear civil systems. Sinković [19] et al. investigated the effect that the type of target response spectrum and the number of ground motions have on the response of buildings, which indicating that these two influences were limited. For probabilistic seismic hazard analysis, Kowsari [20] et al. proposed a deviation information criterion to select the most suitable ground motion. Eftekhari [21] et al. validated data envelopment analysis (DEA) for evaluating ground motion prediction equation efficiency in site-specific studies. Gao [22] et al. demonstrated that fuzzy optimization theory can be used for the selection of ground motion recordings in structural dynamic analysis.

The support structure has a significant influence on the seismic performance of large-span spatial steel structures. Typically composed of a steel structure and a composite or concrete structure, these systems are commonly designed using decoupled models. However, integrated analysis more realistically captures their synergistic behavior. Junwu Dai's comparative analysis between simulated damage and field observations of [23] double-story mesh shell for a large-span stadium indicated that the dynamic amplification effect of the lower frame exacerbate damage to the upper grid. This underscores the necessity of employing coupled models for seismic analysis of spatial structures with concrete supports. Xue [24] systematically reviewed damping ratio determination methods and outlined future research directions for integrated systems. Nie [25-27] et al. investigated the effect of lower support structures on the seismic performance of the overall structure, which indicated that the coupling effect between the lower support structure and the single-layer cylindrical reticulated shell reduces the natural vibration frequency of the structure and significantly compromises the overall stiffness of the structure. Wang [28] introduced a simplified calculation method for the stiffness of supported structures. The comparison of the three calculation methods in terms of period, vibration pattern, and unit stresses revealed that the concrete support adversely affects the integrated model performance of the large-span space latticed structure model, which confirming the imperative for unified modeling. Yu [29] et al. analyzed two typical damage modes of steel reticulated dome structures with lower support structures to propose a failure criterion for the ultimate load-carrying capacity of a single-story steel reticulated dome's structure. The hybrid frame simulations done by Zheng [30] et al. identified maximum inter-story drifts predominantly in the lower support structure during frequent earthquakes, shifting to the upper structures under rare earthquakes. Meng [31] quantified discrepancies in portal frame analysis: decoupled models overestimated mid-span displacements and member stress ratios by 15-22% versus integrated benchmarks. Xia [32]

developed a MATLAB-based integrated modeling platform demonstrating optimal inter-story drift control and post-seismic recoverability in staggered-truss high-rises. Han [33] et al. established foundational principles for seismic design by investigating errors induced by neglecting lower support interactions in large-span reticulated domes.

In summary, conventional seismic analysis of steel canopy structures exhibits critical safety limitations due to the neglect of substructure interactions. While integrated modeling (coupling upper steel canopy with lower concrete supports) provides higher fidelity, its prohibitive computational cost and lack of established design precedents necessitate alternative approaches. This study therefore systematically investigates the seismic performance and global stability of large-span stadium canopies, with the dual objectives of developing rational simplified analytical models and establishing specialized assessment methodologies.

The case study focuses on a central stadium featuring a saddle-shaped steel canopy, shown in Fig. 1, comprising large-span spatial tube trusses with composed of ring truss, radial truss, tension cable, and facade structure. In this paper, the integrated analysis model (upper steel structure coupled with lower concrete support structure) and two simplified analysis models (separation of the upper steel structure from the lower concrete support structure) are established. By comparing and analyzing the seismic responses of the three models, a simplified method for seismic calculation for steel canopy structures is explored, which provides a reference for the preliminary design of the structure. The three-direction stiffness of the lower support structure as well as the peak and frequency changes caused by ground motion are calculated in this study. The effects of stiffness inhomogeneity for the lower support structure as well as the amplification and filtering effects of ground motion acceleration on the dynamic response of the three models are analyzed.

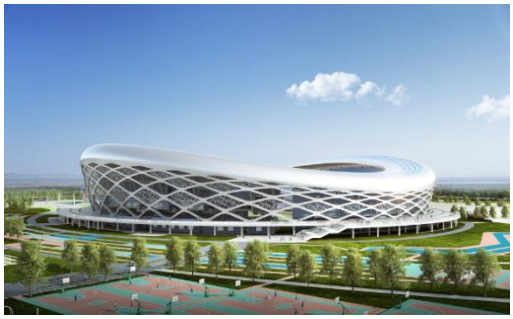

(a) Exterior of steel canopy structure stadium

(b) Interior of steel canopy structure stadium

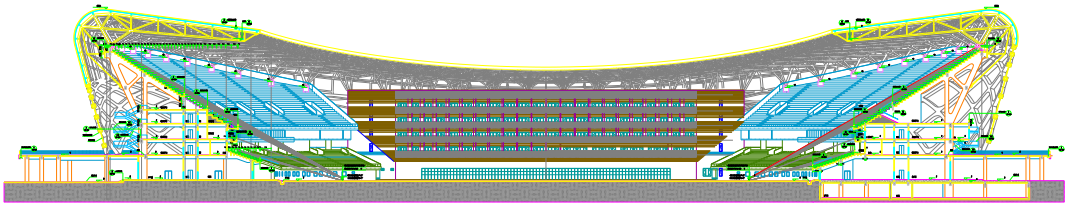

(c) East-west sectional view

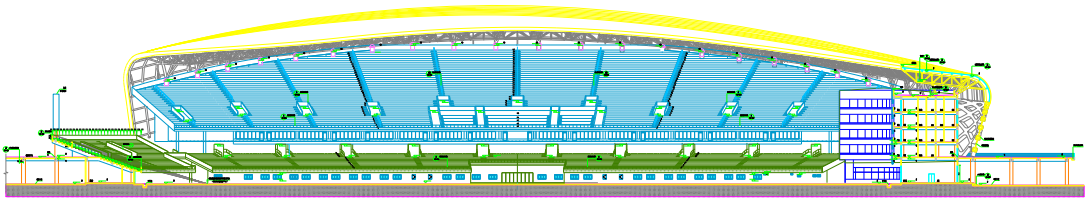

(d) North-south sectional view

Fig. 1 Steel canopy structure stadium architectural drawing

2. Model building, modal analysis and ground motion selection

2.1. Modeling of three calculations

In conventional seismic design of steel canopy structures, the lower support structure is typically idealized as rigid with perfect coupling to the steel canopy structure. To investigate dynamic characteristics of the steel canopy structure and interaction effects between the upper and lower structures, three finite element models were established using ANSYS APDL. First, separate models of the steel canopy (large-span cantilevered space-truss system) and the lower diagonally braced concrete combined trusses were developed. Subsequently, the top of each truss of the lower structure is coupled with the upper pipe truss support to shape the integrated model. Integrated model A, considering the coupling of the lower support structure with the steel canopy structure, is shown in Fig. 2(a) and Model B is a simplified separated model of the steel canopy structure, assuming that the lower support structure is rigid, as shown in Fig. 2(b). The average ground motion response of the lower support columns is applied to the upper steel canopy structure. Model C of the simplified lower support structure is created, as shown in Fig. 2(c). Models B and C are simplified computational models with lower computational costs.

The selection of Models B and C as simplified decoupled approaches is justified by three key rationales aligned with engineering practice and computational efficiency:

1. Model B: Canopy isolated analysis model (high-efficiency focus on the upper steel structure)

a) Objectives and advantages

The core purpose of this model is to isolate and evaluate the seismic response characteristics of the steel canopy, significantly reducing computational costs. It entirely ignores the dynamic calculations of the lower support structure, treating it as an infinite rigid body, and applies site ground motions only to the supports of the upper canopy.

b) Theoretical foundations

Based on the rigid base input hypothesis and static condensation method [34], its validity requires that the lower support structure has higher stiffness than the upper canopy or its dominant frequencies are far from those of the canopy (confirmability via preliminary integrated modal analysis, as shown in Fig. 5).

c) Engineering practices

This model is widely adopted in preliminary design and optimization phases of large stadium structures [35-38], as well as for rapid special performance evaluations of key components or nodes [39]. It allows engineers to efficiently focus on the canopy's performance under limited computational resources or clarifying its inherent response characteristics by parametric studies—though its natural frequencies may deviate from those of the integrated model.

2. Model C: Synergistic effect analysis model (balancing computational efficiency and interaction between the canopy and the lower support structure)

a) Objectives and advantages

This model assesses the influence of lower support structure flexibility and its dynamic response to ground motions on seismic force transfer to the steel canopy structure, while maintaining computational efficiency. It simulates the main dynamic response characteristics by significantly simplifying the lower

support structure complexity (e.g., using equivalent lumped masses, simplified beam-column models, or condensation models), taking key node values (e.g., average displacements or accelerations at all support column tops) as inputs for the upper canopy.

b) Theoretical foundations

Adopting model condensation techniques such as the Guyan condensation method, dynamic condensation method [40], establishing simple equivalent single-degree-of-freedom (SDOF) or multi-degree-of-freedom (MDOF) systems to capture the lower support structure's main dynamic characteristics in transmitting ground motions. The use of average response inputs relies on the transfer function consistency approximation under uniform support conditions [41].

c) Engineering practices

When preliminary evaluation of lower support flexibility is required but integrated modeling proves computationally prohibitive, this simplified model serves as an engineering-accepted compromise [42]. It is particularly suitable for large-scale seismic scheme screening, parametric sensitivity studies (e.g., the impact of column stiffness changes on canopy response), or rapid analysis under specific load combinations. Compared to Model B, it more reasonably reflects key dynamic interaction effects between the upper and lower structures, supporting mid-design adjustments and optimizations for canopy components sensitive to synergistic effects while significantly enhancing computational efficiency.

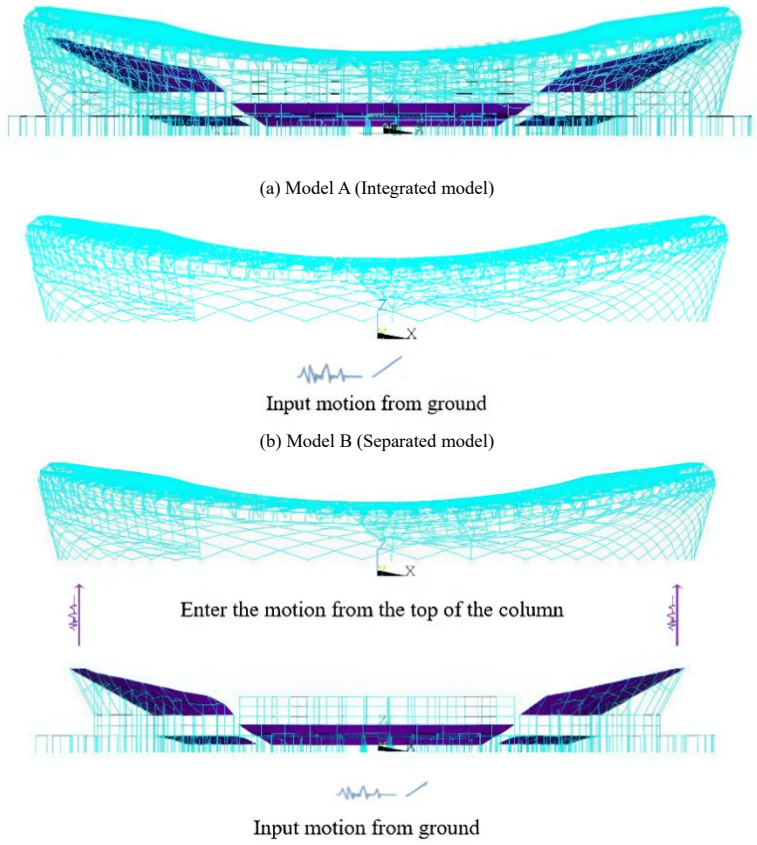

(a) Model A (Integrated model)

(b) Model B (Separated model)

(c) Model C (Separated model)

Fig. 2 Three finite element analysis models for steel canopies

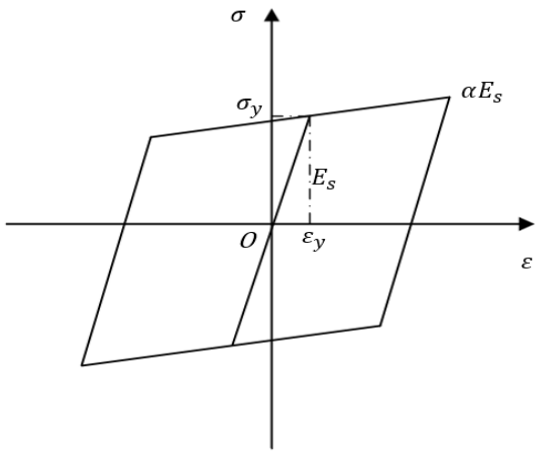

Fig. 3 Steel constitutive model

The constitutive model of steel in the finite element is in accordance with Eq. 1, and the simplified form of the model is shown in Fig. 3.

$$\sigma_s = \begin{cases} E_y \cdot \varepsilon_s & \varepsilon_s \le \varepsilon_y \\ E_y \cdot \varepsilon_y + 0.01E_y \cdot (\varepsilon_s - \varepsilon_y) & \varepsilon_s > \varepsilon_y \end{cases} \quad (1)$$

where σ_s is the stress of steel, ε_s is the strain of steel, ε_y is the yield strain of steel, E_y is the elastic modulus of steel.

The bi-linear constitutive model (Equation 1) adopted in this study assumes a post-yield stiffness ratio of 0.01, with this simplification supported by the following engineering rationales and code-compliant justifications:

1. Rationales for simplification

a) Code compatibility

Mainstream seismic design codes [43-44] require that structural systems form plastic energy dissipation mechanisms under severe earthquakes. A post-yield stiffness ratio of 0.01 accurately simulates the quasi-ideal plastic behavior of steel during the yield plateau, complying with code-specified simplifications for plastic hinge characterization.

b) Computational efficiency

For nonlinear time-history analyses of large spatial steel canopies, the bilinear model mitigates convergence issues inherent in complex hardening models (e.g., Chaboche's law), significantly enhancing analytical feasibility [45].

2. Limitations under large deformations and mitigation measures

a) Sources of potential errors

When components enter large-strain regimes, the strain-hardening behavior of actual steel may lead to an underestimation of bearing capacity by the simplified model [46]. However, this impact is offset by other safety provisions.

b) System redundancy compensation

The cross-grid structure of the canopy exhibits an internal force redistribution capacity, ensuring that local overestimation of plastic deformation do not lead to structural failure [43].

2.2. Modal analysis of steel canopy

The modal analysis is used to obtain the results of the structure's intrinsic frequency, period, vibration shapes of each mode, and the mass of participation corresponding to each vibration shape. Provide a reference for subsequent time history analysis. The proper definition of damping in a structure's dynamic analysis is critical to the accuracy of the computational results. In this study, Rayleigh damping is used.

In Rayleigh damping, assuming that the damping matrix is linear in the stiffness matrix and the mass matrix, the Rayleigh damping can be expressed as:

$$C = \alpha M + \beta K \tag{2}$$

Where C is the damping matrix, M is the mass matrix, and K is the stiffness matrix. The relationship between α and β in Rayleigh damping is:

$$\begin{Bmatrix}\alpha\\ \beta\end{Bmatrix} = \frac{2\omega_m\omega_n}{\omega_n^2-\omega_m^2}\begin{bmatrix}\omega_n & -\omega_m\\ -\frac{1}{\omega_n} & \frac{1}{\omega_m}\end{bmatrix}\begin{bmatrix}\xi_m\\ \xi_n\end{bmatrix} \tag{3}$$

ω_m , ω_n are the circular frequencies (*rad/s*) of *m*th and *n*th modes, respectively; α is the mass-proportional damping coefficient; β is the stiffness-proportional damping coefficient. The critical damping ratio is ξ.

(1) Modal analysis of separated steel canopy

The *Lanczos* algorithm was used for the modal analysis of the structure. Since the proportion of mass participation coefficients is concentrated within the top 20 modes, Table 1 presents the self-vibration frequencies, periods, and mass participation coefficients for these dominant modes.

Table 1
Modal information of separated steel canopy

Number of stages	Frequency（Hz）	Periods（s）	Mass participation factor（%）
1	1.33	0.75	19.84
2	1.45	0.69	0.19
3	1.55	0.65	1.28
4	1.73	0.58	21.34
5	1.77	0.56	4.29
6	1.87	0.53	0.93
7	2.06	0.49	8.63
8	2.15	0.47	0.04
9	2.29	0.44	0.01
10	2.36	0.42	2.92
11	2.66	0.38	1.22
12	2.67	0.37	1.45
13	3.15	0.32	0.33
14	3.19	0.31	0.37
15	3.44	0.29	0.56
16	3.52	0.28	0.30
17	3.56	0.28	0.20
18	3.58	0.28	2.07
19	3.71	0.27	0.01
20	3.77	0.27	0.56

From Table 1, it can be seen that the principal mode of vibration of the structure is concentrated in the first 8 modes, with a mass fraction proportion of 85%.

Therefore, the top 8 modes of structural self-vibration mode diagrams are taken and analyzed as shown in Fig. 4.

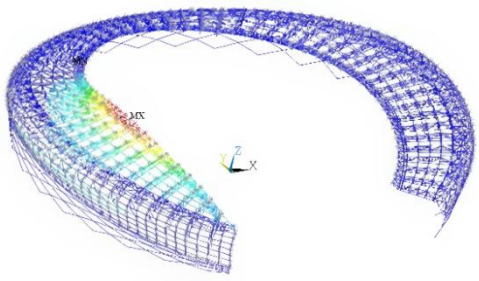

（a） Mode 1

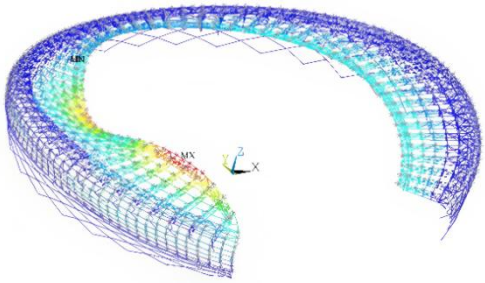

（b） Mode 2

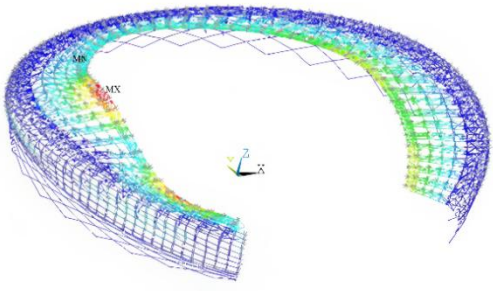

（c） Mode 3

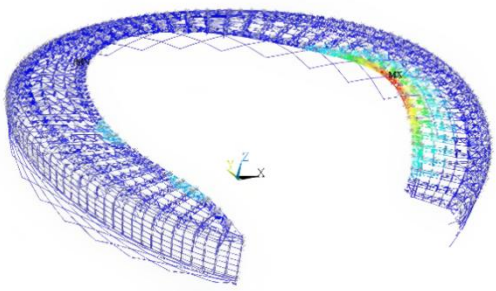

（d） Mode 4

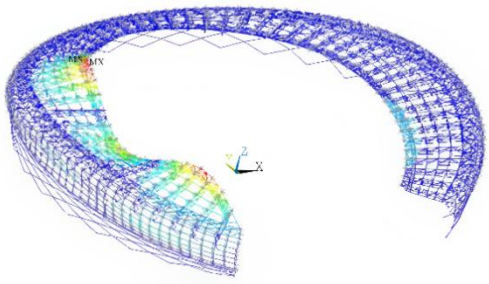

（e） Mode 5

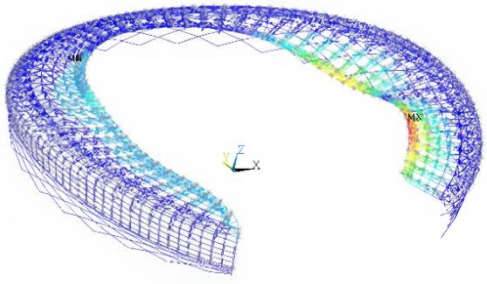

（f） Mode 6

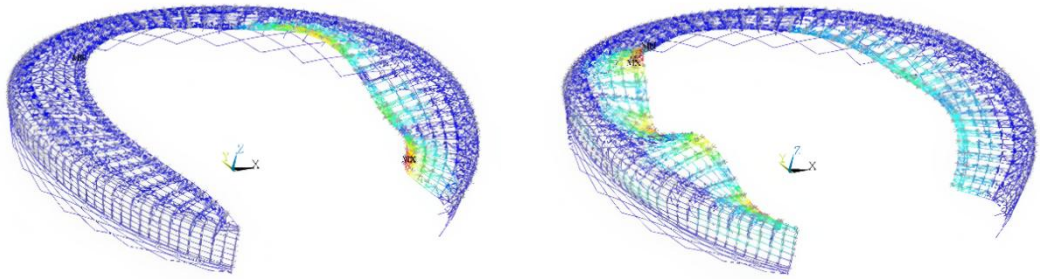

（g） Mode 7　　（h） Mode 8

Fig. 4 Separated steel canopy first 8 modes vibration mode diagram

From the modal information listed in Table 1: 1) the vibration modes with higher mass participation factors are the 4th and 1st modes. As seen in Fig. 4, these two modes mainly exhibit vertical deformation in major areas of the east and west cantilevers. 2) The 7th and 5th stage modes correspond to the third and fourth highest mass participation factors, respectively. They demonstrate vertical deformation at minor openings within eastern and western cantilevers, causing waveform distortions in adjacent regions.3) The remaining vibration modes are primarily characterized by vertical waveform deformation in other eastern and western zones.

(2) Modal analysis of integrated model

The self-vibration frequencies, periods, and mass participation factors for the top 20 modes of the integrated model are shown in Table 2 below.

From Table 2 it can be seen that the first 8 modes of the main vibration mode of the integrated structure, with a mass fraction of 80%, is smaller than the proportion of the first 8 modes of the vibration mode of the independent steel structure. The self-vibration mode of the first 8 modes of the structure is shown in Fig. 5.

Table 2
Modal analysis information of the integrated model

Number of modes	Frequency（Hz）	Periods（s）	Mass participation factor（%）
1	1.10	0.91	9.02
2	1.11	0.90	8.89
3	1.21	0.83	0.57
4	1.23	0.81	0.02
5	1.29	0.77	0.01
6	1.38	0.72	0.06
7	1.42	0.70	3.33
8	1.45	0.69	0.40
9	1.53	0.65	1.50
10	1.54	0.65	0.47
11	1.55	0.64	0.09
12	1.71	0.59	0.01
13	1.79	0.56	0.03
14	1.89	0.53	0.12
15	1.94	0.52	0.01
16	2.10	0.48	0.10
17	2.12	0.47	0.04
18	2.17	0.46	2.62
19	2.21	0.45	0.45
20	2.29	0.44	0.07

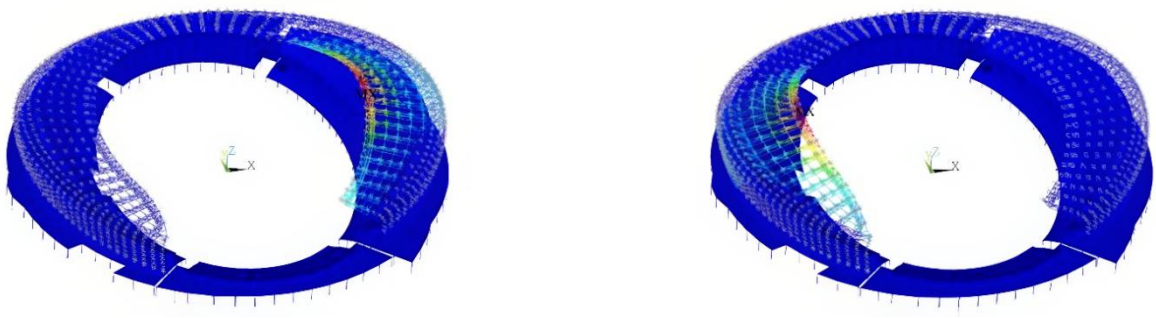

(a) Mode 1　　(b) Mode 2

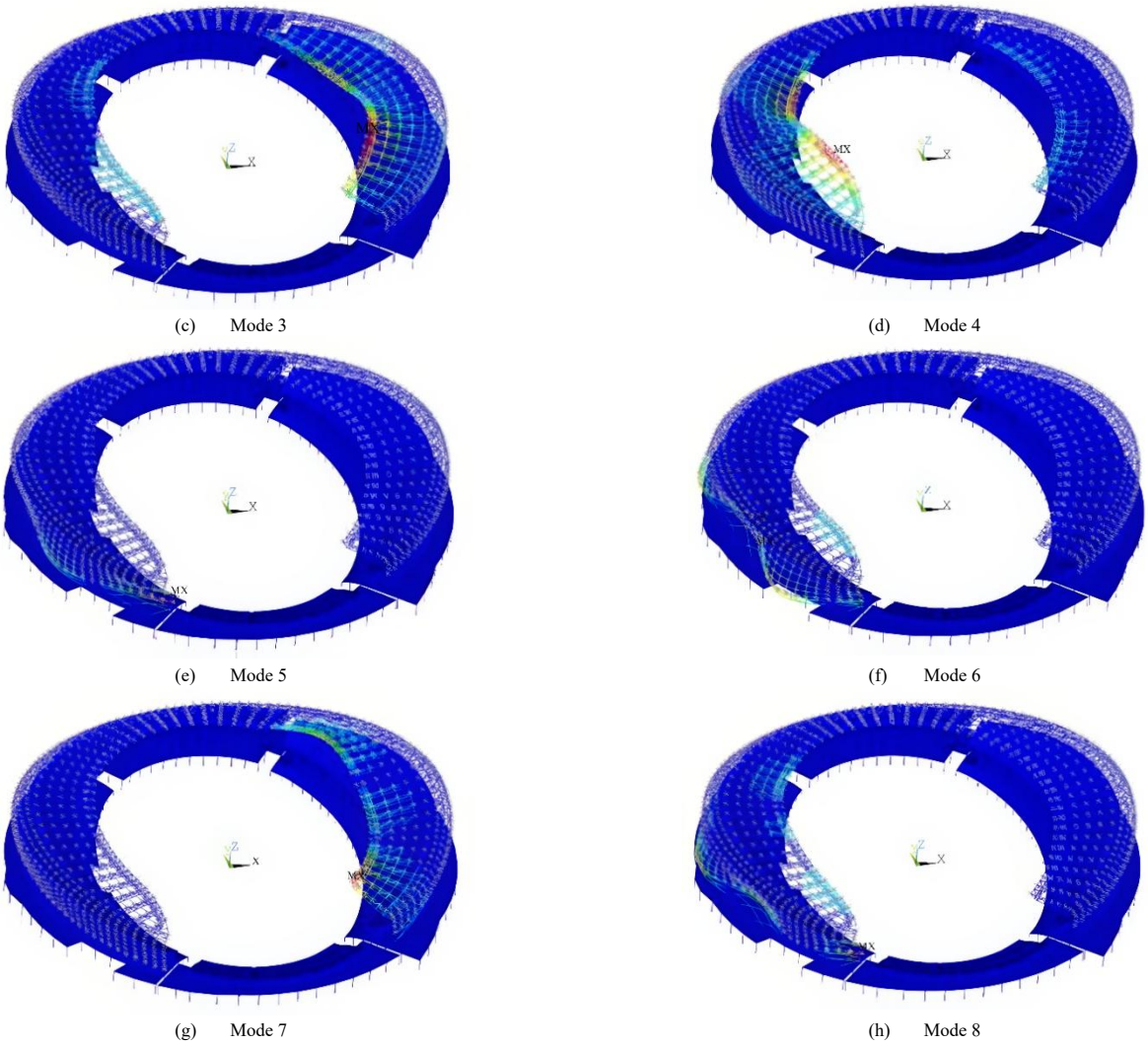

(c) Mode 3 (d) Mode 4

(e) Mode 5 (f) Mode 6

(g) Mode 7 (h) Mode 8

Fig. 5 The first 8 modes vibration mode diagram of the integrated model

From the modal information listed in Table 2, it can be seen that 1) the vibration mode with the highest mass participation factor is the 1st mode, followed by the 2nd mode. As seen in Fig. 5, this two-mode predominantly exhibit vertical deformation in major cantilevered areas of the eastern and western spans. 2) The 7th mode corresponds to the third-highest mass participation factor, displaying vertical deformation at minor openings within eastern cantilevers and inducing waveform distortions in the surrounding areas. 3) The 3rd and 4th mode shows continuous fluctuating vertical deformation in other cantilever areas.

The main vibration modes of the integrated structure and the separated steel canopy are concentrated in the first 8th modes, accounting for 80% and 85% mass participation respectively. While both systems exhibit vertical deformation in major east-west pipe trusses for their first two stage modes, the integrated model's longer self-vibration period period (0.91s vs. 0.75s) indicates that it has less stiffness. Moreover, localized deformation of the facade structure occurs in the vibration mode of the integrated structure. The modal analysis results of these two models are different to some extent.

The physical essence of the natural frequency differences between the integrated and separated models stems from a threefold stiffness enhancement mechanism induced by coupling effects:

1) Stiffness Reconfiguration. The separated model assumes hinged connections (transmitting only vertical forces) between the canopy and stands, neglecting the flexural capacity of nodes. In the integrated model, bidirectional constraints at welded nodes strengthen the off-diagonal terms of the stiffness matrix, directly enhancing the integrated stiffness.

2) Modal Fusion. The independent vibrations in the separated model (vertical bending of the canopy and horizontal sway of the stands) couple into a synergistic lateral displacement mode in the integrated model. The stiffer force-transfer path of this new modal configuration elevates the fundamental frequency.

3) Mass-Stiffness Equilibrium. While the added mass of interface components tends to decrease frequencies, the stiffness reinforcement effect consistently dominates, leading to a higher fundamental frequency in the integrated model. This phenomenon can be analogized to the coupled vibration of a string and a resonance box. The separated model only excites local vibrations of the canopy, whereas the integrated model establishes a complete energy transfer chain, thereby amplifying the fundamental frequency response.

2.3. Ground motion selection

The seismic fortification intensity of this project is 7 degrees, and the fundamental seismic acceleration value is 0.10g. The site is classified as Seismic Group 2, Site Class II, featuring a characteristic period of 0.40s.

Based on the seismic design parameters and structural self-vibration characteristics, seven ground motions were selected for analysis (Table 3). The standard response spectrum curve, the ground motion response spectrum curve, and its average spectrum curve are illustrated in Figure 6. The average spectrum maintains less than 30% deviation from the standard spectrum, satisfying, ASCE7-10[47] Requirements. The seven ground motions listed in Table 3 were rigorously selected to match the seismic site characteristics of the large stadium [43].

1.Soil Type: All records have V_{S30} values (213 - 356 m/s), which encompass the range for Class II medium-stiff soil (V_{S30} = 180 - 375 m/s).

2.Magnitude Range: The moment magnitudes (M_w 6.7 - 7.6) correspond to the site's design basis earthquake (M_w 7.0 ± 0.3) and rare earthquake (M_w 7.5) levels.

3.Risk Coverage: The selection includes scenarios such as near-fault pulse (Northridge), basin effect (Kobe), and deep-source seismicity (Victoria, Mexico). These systematically examine the canopy's structural vulnerabilities across diverse hazard conditions. The names of the later ground motions are simplified to EL, NR, KB, TF, WL, CC and VM.

Table 3
Ground motion records

No.	Name	Date	Station	Magnitude
1	EL Centro	1940	EL Centro Array #9	7.0
2	Northridge	1994	Arleta - Nordhoff Fire Sta	6.6
3	Kobe	1995	Takarazuka	6.9
4	Taft	1952	Taft Lincoln School	7.4
5	Wo Long	2008	051WCW 31.04N 103.18E	8.0
6	CHICHI	1999	TCU122	7.6
7	Victoria Mexico	1980	Cerro Pricto	6.4

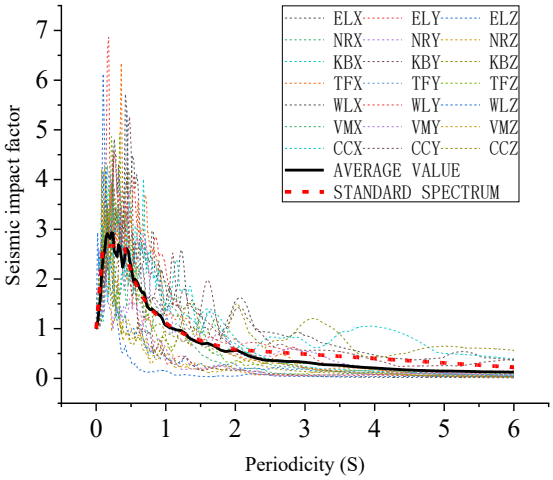

Fig. 6 Spectral curves of seismic effect coefficients for different ground motion

To study the seismic performance of the steel canopy structure and investigate the effects of different types of ground motion and peak acceleration on the structure, time history analysis is employed in this paper. The stress time histories of the critical members and the displacement time histories of the necessary nodes are calculated. The peak ground motion acceleration is adjusted in the X, Y, and Z directions in a 1:0.85:0.65 ratio [43]. Time history analysis was performed using peak acceleration at 50 gal, 100 gal, 200 gal and 300 gal.

3. Steel canopy computational model time-range analysis results comparison

3.1. Maximum value of the dynamic response and comparison methods

To ensure analytical accuracy, Fig. 7 identifies the monitored pipe trusses and measurement point locations. Because the most severe dynamic response of model A is under Taft ground motion, this is used as an example to illustrate the comparative analysis method of the dynamic response for the three models. The structural dynamic response of Model A under 100 gal Taft ground motion is shown in Figs. 8(a) and (b).

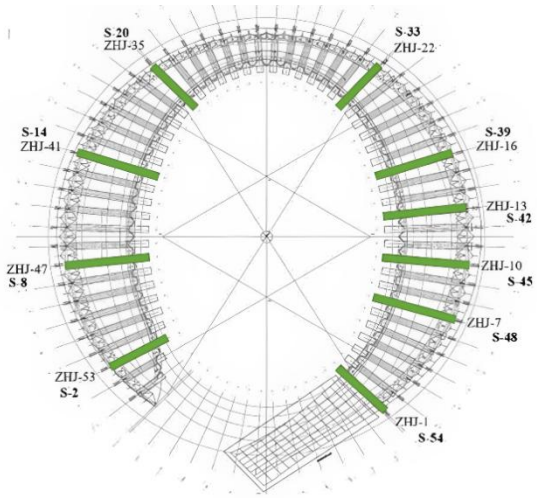

(a) Plan position of pipe trusses

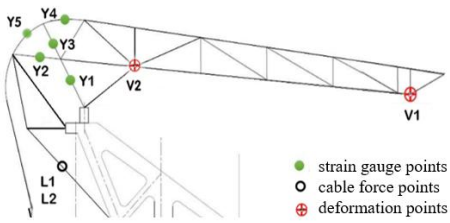

(b) Location of measuring points

Fig. 7 Pipe truss monitoring location

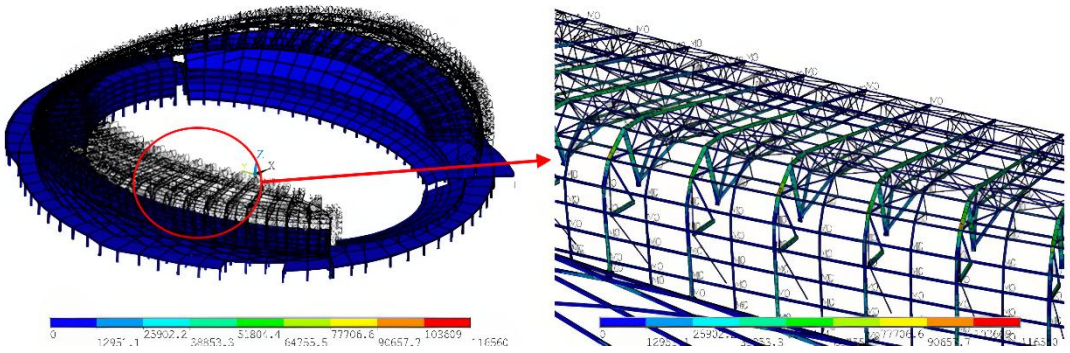

(a)stress chart

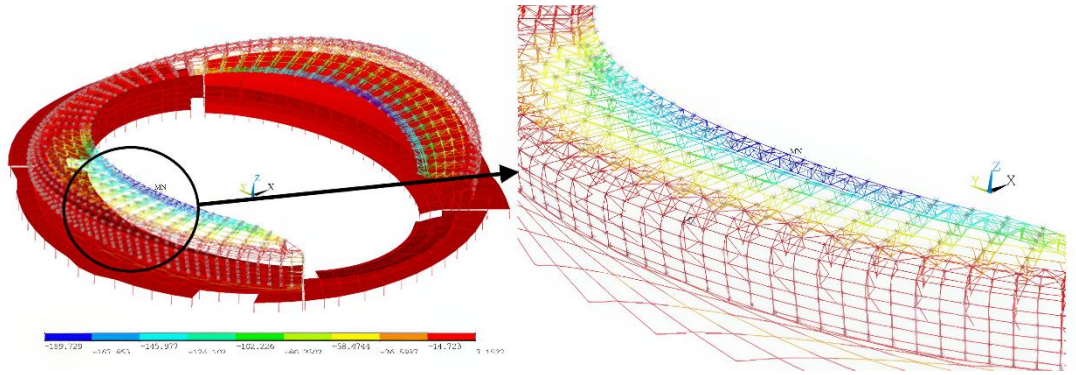

(b) transformation chart

Fig. 8 Structural dynamic response under Taft ground motion for model A 100 gal

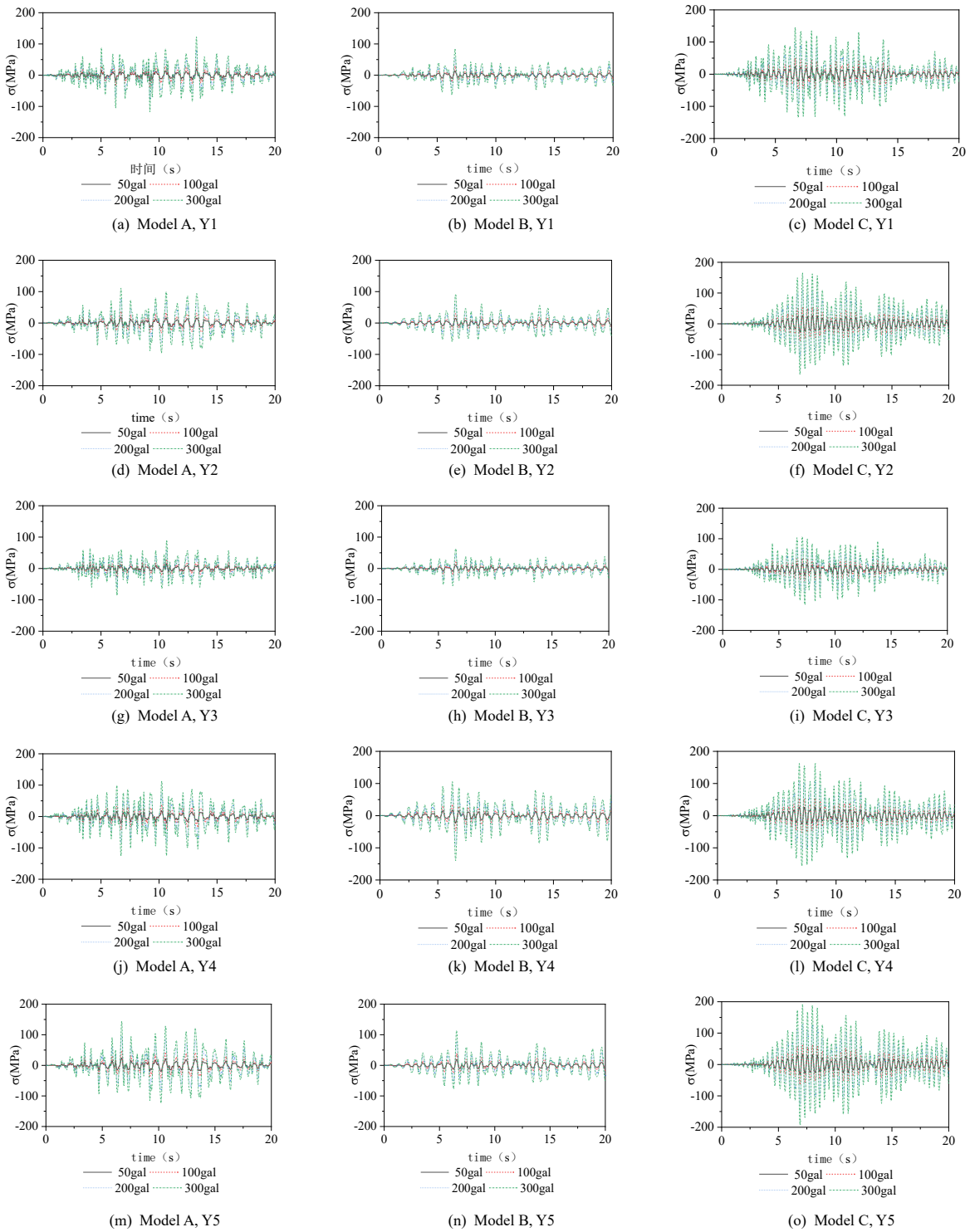

Fig. 9 Stress time history curves of crucial components of ZHJ-47 in three model analyses

Table 4
Maximum stresses and comparison of critical members of ZHJ-47 truss under Taft ground motion with three analytical models (MPa)

Critical members	Peak acceleration（gal）	σA（MPa）	σB（MPa）	σC（MPa）	σB/σA	σC/σA
Y1	50	20.41	14.09	24.33	0.69	1.19
	100	40.81	28.18	48.66	0.69	1.19
	200	81.62	56.36	97.33	0.69	1.19
	300	122.43	84.55	145.99	0.69	1.19
Y2	50	18.56	15.05	27.68	0.81	1.49
	100	37.11	30.11	55.36	0.81	1.49
	200	74.23	60.21	110.73	0.81	1.49
	300	111.34	90.32	166.09	0.81	1.49
Y3	50	14.82	10.51	17.75	0.71	1.20
	100	29.65	21.02	35.50	0.71	1.20
	200	59.29	42.04	70.99	0.71	1.20
	300	88.94	63.06	106.49	0.71	1.20
Y4	50	18.90	17.59	27.07	0.93	1.43
	100	37.81	35.19	54.13	0.93	1.43
	200	75.61	70.38	108.26	0.93	1.43
	300	113.42	105.57	162.35	0.93	1.43
Y5	50	24.06	18.98	32.11	0.79	1.33
	100	48.13	37.96	64.18	0.79	1.33
	200	96.25	75.92	128.36	0.79	1.33
	300	144.38	113.88	192.54	0.79	1.33

Fig. 8 identifies the maximum stress of 116.56 MPa at the critical member near the support, while the maximum deformation of 189.72 mm occurs at the longest cantilevered truss. Taft ground motions with peak accelerations of 50-gal, 100-gal, 200-gal, and 300-gal were input to Models A, B, and C. The maximum stresses and vertical displacements of this pipe truss are used as an example to illustrate the differences between Models B, C, and Model A.

（1）Comparative analysis of peak stresses in critical members of ZHJ-47 pipe truss under Taft ground motion.

The positions of critical members Y1, Y2, Y3, Y4, and Y5 of the ZHJ-47 pipe truss were obtained under Taft ground motion stimulation, as shown in Fig. 7(b). The stress time history curves are shown in Fig. 9. The stress limits for each member were extracted and included in Table 4.

As can be seen from Table 4: 1) For peak ground accelerations ⩽300 gal, peak stresses in all three models exhibit linear growth with increasing acceleration.; 2) The maximum value of C model stress is 192.54 MPa under 300-gal ground motion, equivalent to 65.3% of the design value of steel strength; 3) The stresses in Model B are 0.79 times higher on average than those in Model A. The stresses in Model C are 1.33 times higher on average than Model A. As a result, Model B's calculations are biased toward insecurity, and Model C's calculations are biased toward conservatism compared to the integrated model A.

(2) The displacement time history curve of the cantilevered end of ZHJ-47 pipe truss is obtained under the excitation of Taft ground motion, shown in Fig. 10. Extracted vertical displacement extremes for endpoint V1 are listed in Table 5.

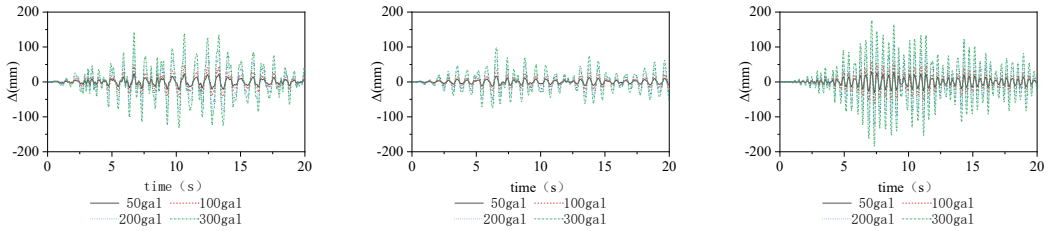

(a) Model A (b) Model B (c) Model C

Fig. 10 Displacement time history curves of ZHJ-47 cantilever point V1 in three model analyses

Table 5
Maximum deflection at the cantilever point and comparison of three models of ZHJ-47 under Taft ground motion（mm）

Peak acceleration（gal）	Δ_A（mm）	Δ_B（mm）	Δ_C（mm）	Δ_B/Δ_A	Δ_C/Δ_A
50	23.89	16.38	29.29	0.69	1.23
100	47.78	32.76	58.58	0.69	1.23
200	95.56	65.52	117.16	0.69	1.23
300	143.34	98.28	175.74	0.69	1.23

Table 5 demonstrates: 1) T Maximum displacements at the cantilever end increase linearly with peak acceleration for all three models, confirming their elastic response range.2) According to the linear interpolation, the maximum deflections are 33.45mm and 105.12mm, respectively, for 8-degree multiple earthquakes of 70 gal and a 7-degree rare earthquake of 220 gal. The results were 1/1184 and 1/377 of the cantilever length, which meets norm requirements.[43] The average deflection of Model B is 0.69 times higher than that of Model A, while Model C averages 1.23 times higher. The results indicate that the calculation results of model B are unreliable, and those of model C are conservative.

Based on the dynamic responses calculated from the three models under Taft ground motion, the steel canopy structure has better seismic performance. To further analyze the differences in seismic performance among the three models, the two trusses with larger spans, ZHJ-10 and ZHJ-47, and the truss with smaller spans, ZHJ-22, were selected. The time history curves under seven kinds of ground motion excitation are obtained. Using the results of model A calculations as a benchmark, the change rule for maximum stresses of critical members Y1 - Y5, and the maximum deflection of the cantilever point V1 in the three models are analyzed to investigate a simplified calculation method for the seismic performance of steel canopy structures.

3.2. Stress comparison analysis of critical members

Based on the calculation results of the three analytical models, the peak stresses of the critical members for the three tube trusses ZHJ-10, 22, and 47 are extracted. The maximum stresses of Model B and Model C were compared with Model A, which is shown in Fig. 11. Analysis reveals:

1) As the peak acceleration increases, most Model B to Model A maximum stress ratios are less than 1.0, indicating that the stresses in the critical members obtained from the analysis of Model B are less than that of Model A. The calculation results are not safe.

2) As the peak acceleration increases, most Model B to Model A maximum stress ratios are more than 1.0, indicating that the stresses in the vital members obtained from the analysis of Model C are more than that of Model A. The calculation results are conservative.

3) The stresses derived from simplified Models B and C respectively provide lower-bound and upper-bound estimates of Model A results, establishing validated reference values for structural preliminary design.

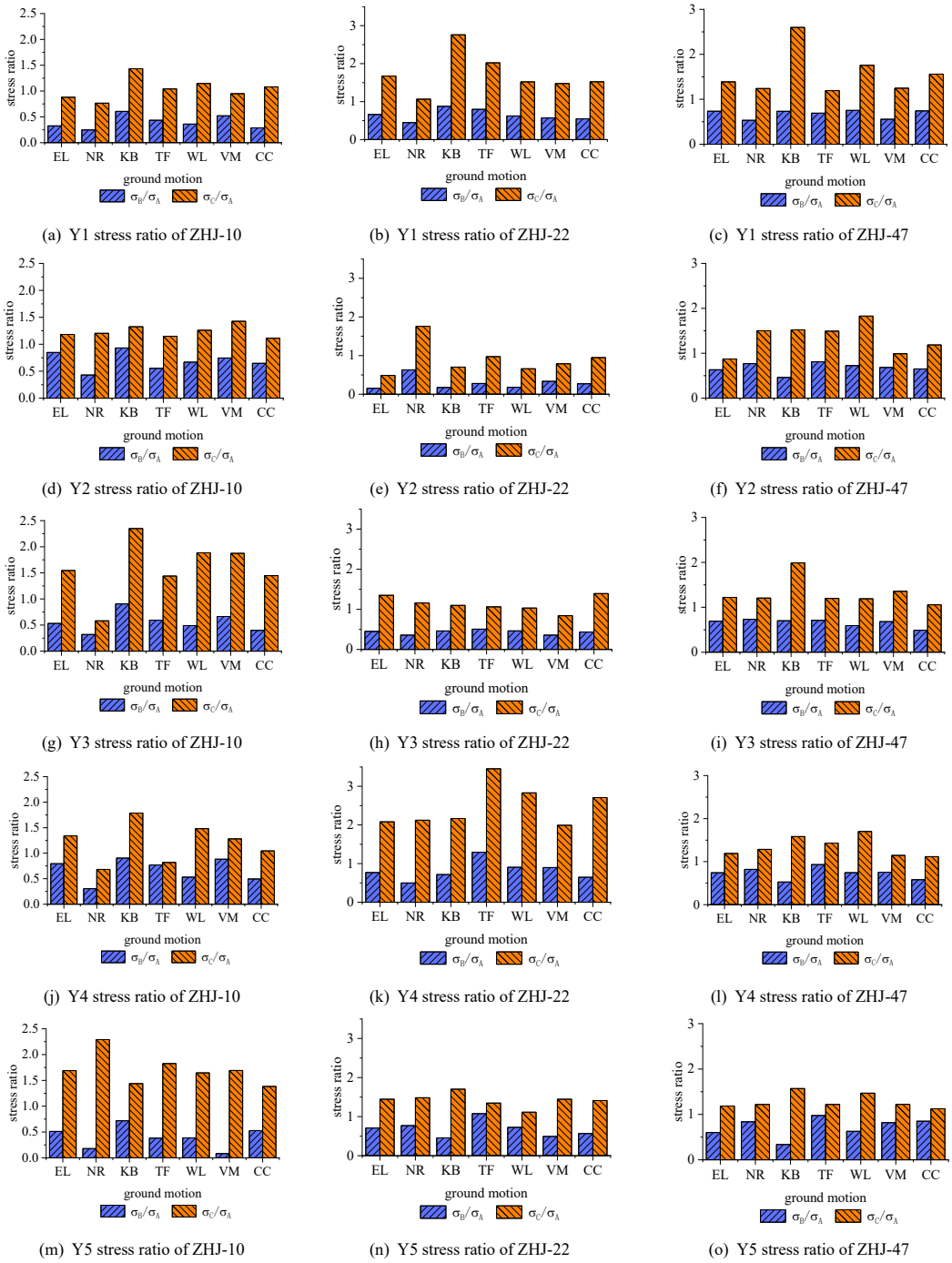

(a) Y1 stress ratio of ZHJ-10 (b) Y1 stress ratio of ZHJ-22 (c) Y1 stress ratio of ZHJ-47

(d) Y2 stress ratio of ZHJ-10 (e) Y2 stress ratio of ZHJ-22 (f) Y2 stress ratio of ZHJ-47

(g) Y3 stress ratio of ZHJ-10 (h) Y3 stress ratio of ZHJ-22 (i) Y3 stress ratio of ZHJ-47

(j) Y4 stress ratio of ZHJ-10 (k) Y4 stress ratio of ZHJ-22 (l) Y4 stress ratio of ZHJ-47

(m) Y5 stress ratio of ZHJ-10 (n) Y5 stress ratio of ZHJ-22 (o) Y5 stress ratio of ZHJ-47

Fig. 11 Maximum stress ratios of critical members in the three analytical models

3.3. Comparative analysis of deflection at the cantilever point

Based on the calculation results of the three analytical models, the peak vertical displacements at the cantilever ends are extracted. The maximum displacements of models B and C are compared with model A. Trend plots of the maximum displacement ratios of model B and C versus model A for the three pipe trusses under seven ground motions are shown in Fig. 12.

It can be seen from Fig. 12 that, as the peak acceleration increases:

1) Most of the maximum displacement ratios of the three tube truss cantilever points in Model B and Model A showed a trend of less than 1.0, indicating that the displacement of the cantilever point obtained from the analysis of Model B is smaller than that of Model A.

2) Most of the maximum displacement ratios of the three pipe truss cantilevering points in Model C and Model A showed a trend of more than 1.0 for most of the models, indicating that the displacement of the cantilever point obtained from the analysis of Model C is larger than that of Model A.

In summary, all three models' dynamic responses satisfy design requirements, validating satisfactory seismic resilience of the steel canopy structure.

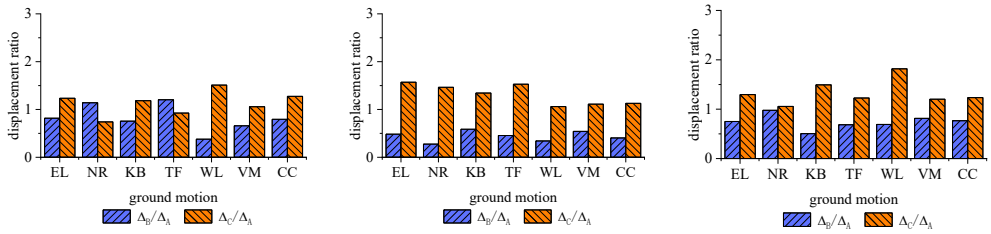

(a) ZHJ-10 (b) ZHJ-22 (c) ZHJ-47

Fig. 12 Maximum vertical displacement ratio of three types of pipe trusses

4. Simplified calculations of the dynamic response of steel canopy structure in elastic stage

Seven ground motions were selected for time history analysis of three computational models at four peak acceleration values (50-gal, 100-gal, 200 gal and 300 gal). Peak stresses at critical members and maximum displacements at cantilever ends were extracted for three typical tube trusses. With the increase in peak ground motion, both stress and displacement exhibit a linear growth trend, indicating that the structure is currently operating within its elastic range. Based on this, a simplified computational method is proposed to investigate the relationship between the computational model and two simplified models. Furthermore, the results of the simplified model calculations can reduce computational costs, which provides a reference for the preliminary design of the integrated structure.

4.1. Simplified calculation method for integrated model stresses

Under the influence of seven ground motions, with an acceleration peak of 100 gal, three computational models are selected to analyze the maximum stress in critical members. They are listed the in Tables. 6, 7, and 8, respectively.

Table 6
Model A critical member stress (MPa)

Truss number	Member number	ground motion						
		EL	NR	KB	TF	WL	VM	CC
ZHJ-10	Y1	34.57	22.72	29.72	42.27	28.41	18.17	30.49
	Y2	53.13	34.03	50.67	52.98	34.65	22.02	34.88
	Y3	17.40	13.24	18.79	27.49	16.02	9.16	20.48
	Y4	23.95	23.72	24.87	39.81	18.56	14.48	30.34
	Y5	20.60	14.78	23.49	37.73	10.43	24.49	26.41
ZHJ-22	Y1	12.47	9.47	11.24	10.63	14.94	8.09	15.48
	Y2	15.02	12.71	15.48	17.71	18.48	7.62	11.94
	Y3	11.63	8.62	14.71	13.40	13.94	7.32	11.17
	Y4	17.02	8.16	21.25	12.55	12.24	8.24	16.09
	Y5	18.71	14.75	26.83	29.38	31.92	27.03	29.07
ZHJ-47	Y1	35.34	30.18	30.26	40.81	25.87	22.18	28.34
	Y2	47.20	30.42	40.66	37.11	25.41	20.94	35.73
	Y3	25.18	19.87	27.26	29.65	28.88	12.55	31.49
	Y4	41.35	29.49	41.35	37.81	28.88	20.71	42.89
	Y5	43.74	31.45	44.08	48.32	42.08	37.69	62.14

Table 7
Model B critical member stress (MPa)

Truss number	Member number	ground motion						
		EL	NR	KB	TF	WL	VM	CC
ZHJ-10	Y1	11.24	5.62	18.02	18.40	10.24	9.47	8.78
	Y2	45.05	14.63	47.20	29.34	23.18	16.40	22.56
	Y3	9.24	4.24	17.02	16.32	7.85	6.08	8.16
	Y4	19.02	7.24	22.48	30.65	9.86	12.78	15.02
	Y5	10.55	2.66	16.86	14.40	4.04	2.00	13.94
ZHJ-22	Y1	8.24	4.24	9.86	8.47	9.32	4.62	8.47
	Y2	2.31	8.01	2.70	4.93	3.31	2.54	3.23
	Y3	5.24	3.08	6.78	6.78	6.47	2.62	4.85
	Y4	13.09	4.08	15.25	16.25	11.09	7.39	10.40
	Y5	13.28	11.36	12.24	31.61	23.18	13.28	16.48
ZHJ-47	Y1	25.95	16.09	22.18	28.18	19.48	12.32	21.02
	Y2	29.88	23.41	18.79	30.11	18.40	14.32	23.25
	Y3	17.40	14.55	19.10	21.02	17.09	8.55	15.40
	Y4	30.65	24.18	21.79	35.19	21.48	15.63	24.87
	Y5	26.33	26.41	14.86	47.12	26.41	30.88	52.86

Table 8
Model C critical member stress (MPa)

Truss number	Member number	ground motion						
		EL	NR	KB	TF	WL	VM	CC
ZHJ-10	Y1	30.42	17.40	42.58	44.04	32.57	17.25	32.96
	Y2	62.87	40.96	67.14	60.79	43.66	31.42	38.85
	Y3	26.87	7.70	44.12	39.58	30.18	17.17	29.65
	Y4	32.11	16.17	44.43	32.57	27.49	18.56	31.72
	Y5	34.80	33.84	33.76	68.88	17.17	41.43	36.54
ZHJ-22	Y1	20.87	10.09	31.03	21.48	22.72	11.94	23.56
	Y2	7.32	22.33	10.86	17.25	12.17	6.01	11.32
	Y3	15.71	10.01	16.17	14.25	14.40	6.16	15.55
	Y4	35.42	17.33	46.05	43.35	34.65	16.40	43.58
	Y5	27.07	21.87	45.66	39.54	35.54	39.08	41.00
ZHJ-47	Y1	49.05	37.42	78.62	48.66	45.43	27.64	44.20
	Y2	41.20	45.66	61.83	55.36	46.43	20.71	42.35
	Y3	30.72	23.91	54.21	35.50	34.34	17.02	33.26
	Y4	49.20	37.88	65.45	54.13	49.13	23.72	47.89
	Y5	51.82	38.38	69.22	58.98	61.79	46.05	69.95

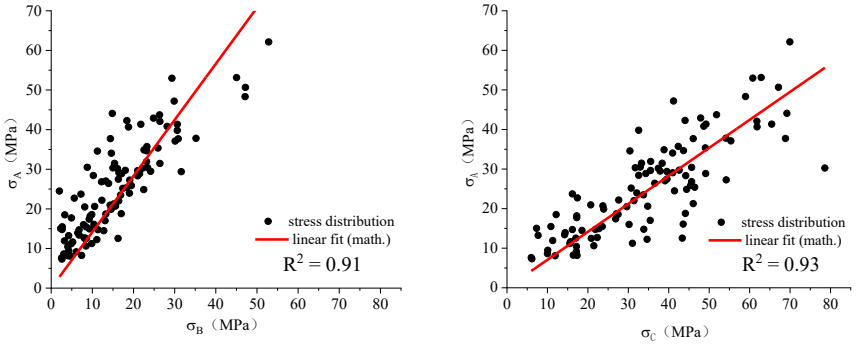

(a) Model B & Model A (b) Model C & Model A

Fig. 13 Stress distribution and linear fitting of models B and C to model A

The stress distributions of the critical components of models B and A, as well as models C and A are shown in the form of scatter plots as shown in Fig. 13. And the proportionality equations of σ_A vs. σ_B and σ_A vs. σ_C are fitted.

As shown in Fig. 13(a), the stress distributions of models B and A are linearly distributed. The slope of the fitted line is 1.42 > 1, which indicates that Model B underestimates stresses versus Model A. R^2 = 0.91 indicates that the fitting accuracy is a bit reasonable.

As shown in Fig. 13(b), the stress distributions of model C and model A are also linearly distributed. The slope of the fitted line is 0.71 < 1, indicating that Model C overestimates stresses versus Model A. R^2 = 0.93 indicates a reasonable fitting accuracy. Therefore, the stress relationship between models B/C and model A can be approximated by the following calculation equation:

$$\sigma_A = 1.42 \times \sigma_B \quad (4)$$

$$\sigma_A = 0.71 \times \sigma_C \quad (5)$$

In the equation, σ_A、 σ_B and σ_C which are obtained from time history analysis under a specific peak acceleration represent the maximum stress values of the members in models A, B, and C, respectively..

Stress ratios σ_A/σ_B and σ_A/σ_C for the critical members of the three pipe trusses in Model A, B, and C are listed in Table 9 and 10, respectively.

As can be seen in Table 9, the σ_A/σ_B data are in the vicinity of the factor 1.42 in the computational equation (4), except for individual data with large deviations. This distribution indicates validity of the fitted equation.

Table 9
Stress ratios in critical members of Model A and Model B

Truss number	Member number	ground motion						
		EL	NR	KB	TF	WL	VM	CC
ZHJ-10	Y1	3.03	4.00	1.64	2.27	2.78	1.92	3.45
	Y2	1.18	2.33	1.08	1.82	1.49	1.35	1.54
	Y3	1.89	3.13	1.10	1.69	2.04	1.52	2.50
	Y4	1.27	3.23	1.11	1.30	1.89	1.14	2.00
	Y5	1.96	5.56	1.39	2.63	2.56	12.50	1.89
ZHJ-22	Y1	1.52	2.22	1.14	1.25	1.61	1.75	1.82
	Y2	6.67	1.59	5.88	3.57	5.56	3.03	3.70
	Y3	2.22	2.78	2.17	1.96	2.17	2.78	2.33
	Y4	1.30	2.00	1.39	0.78	1.10	1.11	1.54

	Y5	1.41	1.30	2.17	0.93	1.37	2.04	1.75
ZHJ-47	Y1	1.37	1.89	1.37	1.45	1.33	1.79	1.35
	Y2	1.59	1.30	2.17	1.23	1.39	1.47	1.54
	Y3	1.45	1.37	1.43	1.41	1.69	1.47	2.04
	Y4	1.35	1.22	1.89	1.08	1.35	1.33	1.72
	Y5	1.67	1.19	2.94	1.02	1.59	1.22	1.18

Table 10
Stress ratios in critical members of model A and model C

Truss number	Member number	ground motion						
		EL	NR	KB	TF	WL	VM	CC
ZHJ-10	Y1	1.14	1.30	0.70	0.96	0.87	1.05	0.93
	Y2	0.85	0.83	0.75	0.87	0.79	0.70	0.90
	Y3	0.65	1.72	0.43	0.69	0.53	0.53	0.69
	Y4	0.75	1.47	0.56	1.22	0.68	0.78	0.95
	Y5	0.59	0.44	0.69	0.55	0.61	0.59	0.72
ZHJ-22	Y1	0.60	0.93	0.36	0.50	0.66	0.68	0.66
	Y2	2.04	0.57	1.43	1.03	1.52	1.27	1.05
	Y3	0.74	0.86	0.91	0.94	0.97	1.19	0.72
	Y4	0.48	0.47	0.46	0.29	0.35	0.50	0.37
	Y5	0.69	0.68	0.59	0.74	0.90	0.69	0.71
ZHJ-47	Y1	0.72	0.81	0.38	0.84	0.57	0.80	0.64
	Y2	1.15	0.67	0.66	0.67	0.55	1.01	0.84
	Y3	0.82	0.83	0.50	0.83	0.84	0.74	0.94
	Y4	0.84	0.78	0.63	0.70	0.59	0.87	0.89
	Y5	0.85	0.82	0.64	0.82	0.68	0.82	0.88

As can be seen from Table 10, except for individual data with large deviations, the σ_A/σ_C data are in the vicinity of the coefficient 0.71 in the calculated equation (5), indicating that the fitted calculated equation is more reasonable. It also indicates validity of the fitted equation.

4.2. Simplified calculation method for integrated model displacement

It is similar to the simplified calculation method for the stresses of the integrated model. Under the influence of seven ground motions, with an acceleration peak of 100 gal, three computational models are selected to analyze the maximum displacement of the cantilever end. They are listed in Table 11, Table. 12, and Table. 13, respectively.

Table 11
Model A critical member displacement (mm)

Truss number	ground motion						
	EL	NR	KB	TF	WL	VM	CC
ZHJ-10	22.63	6.71	26.02	23.40	15.71	13.92	14.12
ZHJ-22	7.07	2.98	9.55	13.12	12.94	5.42	11.06
ZHJ-47	35.66	24.05	33.28	47.78	31.72	19.11	33.60

Table 12
Model B critical member displacement (mm)

Truss number	ground motion						
	EL	NR	KB	TF	WL	VM	CC
ZHJ-10	18.50	7.64	19.68	28.18	5.94	9.18	11.22
ZHJ-22	3.42	0.82	5.60	5.98	4.42	2.94	4.48
ZHJ-47	26.76	23.50	16.82	32.76	21.94	15.58	25.74

Table 13
Model C critical member displacement (mm)

Truss number	ground motion						
	EL	NR	KB	TF	WL	VM	CC
ZHJ-10	27.92	4.96	30.78	21.64	23.7	14.72	18
ZHJ-22	11.12	4.36	12.82	20.06	13.72	6.02	12.48
ZHJ-47	46.24	25.38	49.7	58.58	57.68	22.98	41.48

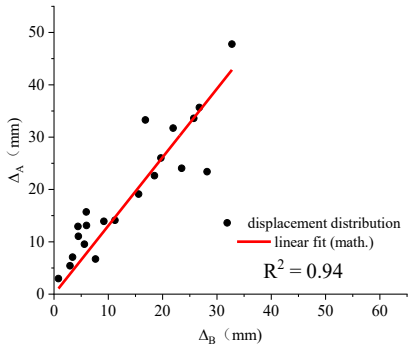

(a) Model B and Model A displacement distributions and linear fitting

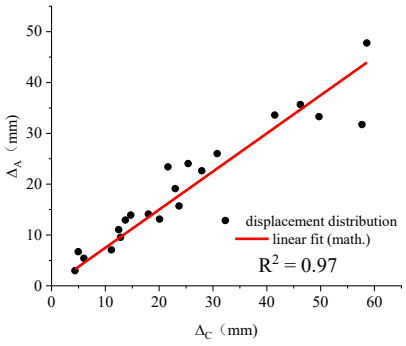

(b) Model C and Model A displacement distributions and linear fitting

Fig. 14 Model B and Model C with Model A displacement distribution and linear fit law, respectively

The displacement distribution of models B and A, as well as models C and A are shown in the form of scatter plots, respectively. It is shown in Fig. 14. And the proportionality equations of σ_A vs. σ_B and σ_A vs. σ_C are fitted.

As can be seen from Fig. 14(a), the displacement distributions of model B and model A are linearly distributed. The slope of the fitted line is 1.31 > 1, which indicates that Model B's displacement is less than Model A. $R^2 = 0.94$ indicates that the fitting accuracy is reasonable.

As can be seen from Fig. 14(b), the displacement distributions of model C and model A are linearly distributed. The slope of the fitted line is 0.75 < 1, which indicates that Model C's displacement is more than Model A. $R^2 = 0.97$ indicates that the fitting accuracy is reasonable. Therefore, the relationship between model B, C and model A can be expressed as follows:

$$\Delta_A = 1.31 \times \Delta_B \quad (6)$$

$$\Delta_A = 0.75 \times \Delta_C \quad (7)$$

In the equation, Δ_A, Δ_B and Δ_C are the maximum displacements at the cantilever end of the pipe truss obtained from time history analysis at a certain peak acceleration.

The displacement ratios of the cantilever end between Model A and Model B, as well as between Model A and Model C, are listed in Table 14 and 15, respectively.

Table 14
Displacement ratio between Model A and Model B cantilevered ends

Truss number	ground motion						
	EL	NR	KB	TF	WL	VM	CC
ZHJ-10	1.22	0.88	1.32	0.83	2.63	1.52	1.27
ZHJ-22	2.08	3.57	1.69	2.17	2.94	1.85	2.44
ZHJ-47	1.33	1.02	1.96	1.45	1.45	1.22	1.30

Table 15
Displacement ratio between Model A and Model C cantilevered ends

Truss number	ground motion						
	EL	NR	KB	TF	WL	VM	CC
ZHJ-10	0.81	1.35	0.85	1.09	0.66	0.94	0.79
ZHJ-22	0.64	0.68	0.75	0.65	0.94	0.90	0.88
ZHJ-47	0.77	0.94	0.67	0.81	0.55	0.83	0.81

As can be seen from Table 14 and 15, the displacement ratios in the Table are close to 1.31 and 0.75 in the displacement calculation equations (6) and (7), except for deviations in individual data. It indicates that the computational equation is fitted well.

To further validate the reliability and applicability of Equations (4)-(7), a comparative verification was conducted using published shaking table test data [48]. The case study adopted a modeling approach analogous to this paper, employing both integrated and separated models for computational analysis. Finite element analyses are performed on Lushan Middle School Gymnasium and Lushan County Gymnasium, utilizing ground motion records from actual seismic stations in earthquake-affected regions. By substituting the stresses and key displacements acquired from the three models (the integrated model and the two separated models) of each gymnasium into the equations, a good agreement was observed between the test data and the formula predictions, confirming that the simplified equations accurately reflect the fundamental behavioral relationships between the integrated and separated models of steel canopies in large stadium structures.

5. Analysis of the lower support structure influencing dynamic response

The comparative analysis of dynamic responses between simplified and integrated steel canopy structure models demonstrates that Model B (considering the lower support structure as rigid) and Model C (inputting average ground motion responses of lower support columns to the upper steel canopy structure) are both different from the calculation results of the integrated model. Therefore, it is necessary to analyze the fundamental mechanisms of the lower support structure's influence on the dynamic response of the steel canopy structure.

This section calculates the three-directional stiffness of the lower support structure at the steel canopy supports and quantifies the peak and frequency changes induced by ground motion passing through the structure. It further examines the effects of lower support structure stiffness in-homogeneity, amplification effect, and filtering effect of ground motion acceleration on the dynamic responses of all three models. The results show that there are differences between the three models.

5.1. Support stiffness in-homogeneity effect

Differences in constructing various frames of the lower support structure cause in-homogeneous stiffness at different steel canopy structure supports. This resulted in an inconsistent dynamic response output to the steel canopy structure at each support under ground motion excitation. Furthermore, it has an impact on the dynamic response of the steel canopy structure, and this phenomenon is referred to as the support stiffness in-homogeneity effect.

A primary cause of support stiffness in-homogeneity stems from construction tolerances during the actual fabrication and installation of support nodes, as well as material and manufacturing variability in support components (e.g., elastic pads, pins, connecting plates).

1) Quantitative Impact of Construction Tolerances

Inevitably, construction deviations occur in the support positioning (planar

location and elevation) and assembly clearances of key components (e.g., clearances between pins and sleeves and gasket thickness between connecting plates). According to the Code for Construction Quality Acceptance of Steel Structure Engineering [49] and related standards [50-51], dimensional tolerances for key nodes in large steel structures typically range from ±3 mm to ±5 mm for installation positions and ±0.5 mm to ±1.0 mm for assembly clearances. Such minor geometric deviations significantly alter the actual constraint conditions of supports (e.g., boundary clearance changes directly affect sliding resistance and rotational restraint) and the effective load-transfer path length (influencing the effective length L_e in axial and bending stiffness formulas), causing the in-service effective horizontal and rotational stiffness to deviate from design values.

2) Quantitative Impact of Material/Manufacturing Variability

Key properties of supports (e.g., the shear modulus G of rubber pads, the elastic modulus E of metal parts, and the friction coefficient μ of sliding materials) exhibit inherent property dispersion due to manufacturing tolerances. For rubber supports: their designed shear modulus G typically allows for manufacturing deviations of ±15% or higher [52]. Since the shear stiffness $K \approx G \cdot A/t$ (where A is the rubber bearing area and t is the net of rubber layers height), such G-value deviations directly lead to stiffness fluctuations exceeding ± 15%. Similarly, minor volatility (e.g., ±1% - 2%) in the dimensional accuracy (e.g., thickness, hole diameter) of metal components during manufacturing will affect their contribution to composite stiffness by altering cross-sectional properties.

Therefore, the main difference between the integrated model A, which considers the coupling effect of the lower support structure, and the simplified analytical models B/C lies in their boundary assumptions: Model B presumes infinitely rigid supports (zero displacement); Model C enforces displacement coincidence at tops of the supporting structure. To illustrate the difference in stiffness of the lower support structure at each pipe truss support, unit forces were applied in three directions at each support. The support numbers are illustrated in Fig. 15. The nodal displacements are used to determine the support stiffness, which is listed in Table 16.

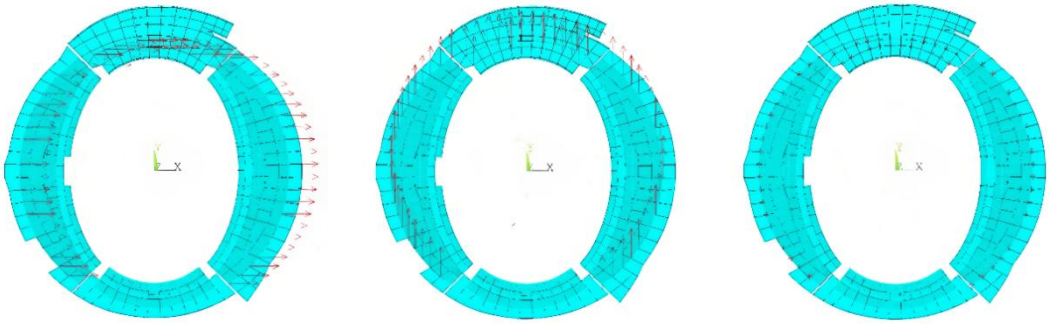

(a) X-direction (b) Y-direction (c) Z-direction

Fig. 15 Apply unit force to lower support structure model

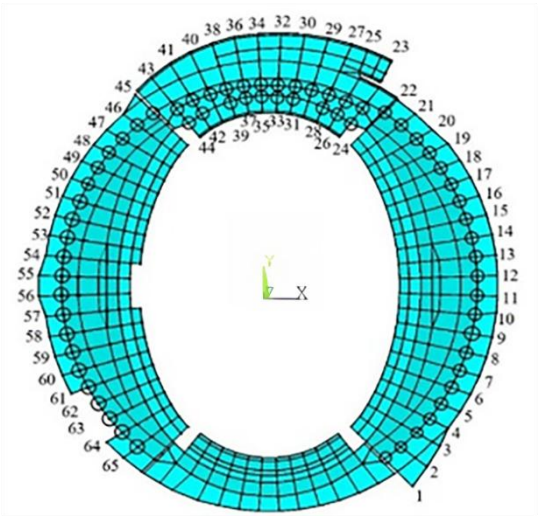

Fig. 16 Location of support columns and corresponding numbers

Table 16
Three- direction stiffness of 65 supports of steel canopy structure (1 x 105kN/m)

Support Number	X-direction	Y-direction	Z-direction	Support Number	X-direction	Y-direction	Z-direction
1	0.99	1.56	1.65	34	1.31	0.54	5.87
2	1.13	1.57	1.84	35	1.33	0.54	7.51
3	1.06	1.43	1.08	36	1.30	0.54	5.87
4	1.12	1.42	1.09	37	1.33	0.54	7.33
5	1.26	1.43	1.34	38	1.31	0.54	6.20
6	1.36	1.44	1.46	39	1.33	0.54	8.81
7	1.45	1.44	1.58	40	1.31	0.53	6.42
8	1.50	1.43	1.59	41	1.32	0.52	6.25
9	1.56	1.43	1.65	42	1.36	0.53	9.11
10	1.65	1.43	1.75	43	1.33	0.51	6.12
11	1.68	1.44	1.79	44	1.39	0.52	8.26
12	1.68	1.44	1.79	45	2.28	5.58	3.86
13	1.64	1.43	1.75	46	2.76	5.74	4.58

14	1.56	1.43	1.65	47	2.75	5.13	3.23
15	1.49	1.43	1.59	48	2.94	5.10	3.51
16	1.45	1.44	1.58	49	3.29	5.15	4.31
17	1.35	1.44	1.46	50	3.53	5.13	4.71
18	1.24	1.43	1.33	51	3.74	5.12	5.21
19	1.11	1.42	1.09	52	3.81	5.06	5.34
20	1.05	1.43	1.07	53	3.95	5.02	5.59
21	1.11	1.57	1.82	54	4.11	5.01	5.80
22	0.98	1.57	1.64	55	4.19	5.02	5.93
23	1.32	0.51	6.05	56	4.20	5.02	5.90
24	1.38	0.52	8.40	57	4.15	5.01	5.86
25	1.31	0.52	5.89	58	4.00	4.99	5.62
26	1.35	0.53	7.65	59	3.75	5.01	5.24
27	1.31	0.53	6.28	60	3.86	5.12	5.24
28	1.34	0.53	8.92	61	3.69	5.13	4.81
29	1.31	0.54	6.50	62	3.47	5.15	4.22
30	1.31	0.54	6.22	63	3.28	5.22	3.71
31	1.33	0.54	8.66	64	3.03	5.25	2.90
32	1.31	0.54	5.88	65	3.15	6.02	3.21
33	1.33	0.55	7.28	-	-	-	-

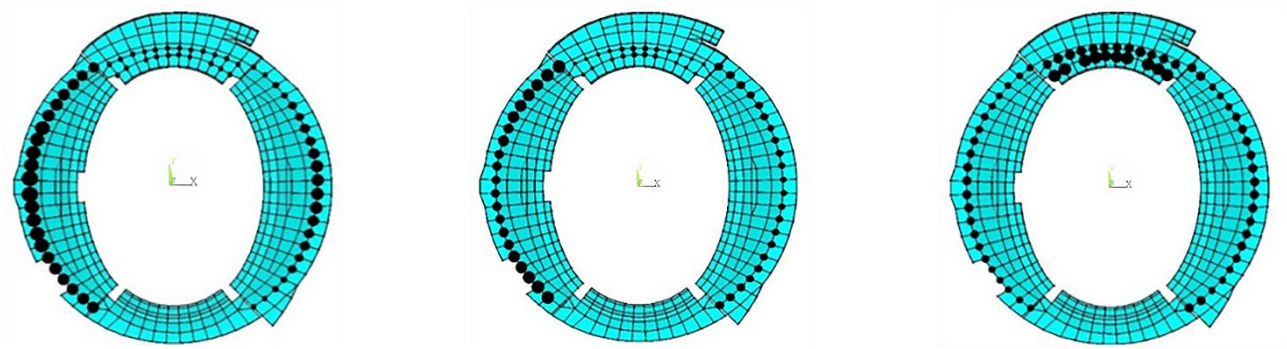

(a) X-direction (b) Y-direction (c) Z-direction

Fig. 17 Three- direction stiffness distribution at the support

To visually show the three-direction stiffness distribution at the support, the stiffness distribution was plotted in Fig. 17. Solid black circles denote support locations, with their areas scaled proportionally to the relative stiffness magnitude. The distribution of stiffness in X, Y and Z directions are shown in Fig. 17 (a), (b) and (c).

As shown in Fig. 17:

1) In the middle part of the east and west sides, the supporting columns of the trusses with the enormous cantilever spans have higher stiffness in the X-direction, while the stiffness shows a decreasing trend toward the columns at two ends..

2) In the middle part of the east and west sides, the supporting columns of the trusses with the smaller cantilever spans have higher stiffness in the Y-direction, while the stiffness shows a decreasing trend toward the columns in the middle.

3) The mid-span columns of east/west sides and the north side support columns have higher Z-direction stiffness.

Given the significant three-directional stiffness differences in lower support columns, the analytical models diverge fundamentally in their boundary assumptions: model B assumes infinite support stiffness; model C considers the displacements at the top of the support as consistent. Both dynamic responses differ from the integrated analytical model A.

To quantitatively assess stiffness inhomogeneity effects, displacement data from 10 radial truss bays are extracted and compared with the field-measured values during canopy construction. Since the measurement points are arranged symmetrically, there are four measurement points (2 cantilever measurement points V1 and two support measurement points V2) for each joint, as shown in Fig. 7. Cantilever nodes displacements are presented in Table 17, while support nodes displacements are detailed in Table 18. Field-measured versus analytical values are comparatively visualized in Fig. 18.

From Table 17, it can be seen that the measured maximum displacement of the cantilever point is -50.0 mm, which is 1/7200 of the span and satisfies the requirement [49-50]. Compared with the finite element analysis value, the maximum error is 29.73%, showing reasonable agreement. From Table 18, it can be seen that the measured value of the node at the support is -16.0mm. Compared with the finite element analysis value, the maximum error is 59.50%. The significantly larger relative error is mainly due to the small absolute displacement magnitudes near supports.

Table 17
Comparison of measured Z-direction displacement of radial truss cantilever point (V1) with finite element value (mm)

Axis line number	Truss number	Field-measured value u_1	Analytical value u_2	Error (%) $(u_2-u_1)/u_1$
S-54	ZHJ-1	-31.00	-32.57	5.06
		-31.00	-33.36	7.61
S-48	ZHJ-7	-38.00	-42.17	10.97
		-37.00	-43.81	18.41

S-45	ZHJ-10	-29.00	-34.64	19.45
		-32.00	-34.06	6.44
S-42	ZHJ-13	-40.00	-43.27	8.18
		-42.00	-45.76	8.95
S-39	ZHJ-16	-45.00	-47.33	5.18
		-43.00	-44.69	3.93
S-33	ZHJ-22	-11.00	-14.27	29.73
		-11.00	-13.42	22.00
S-20	ZHJ-35	-9.00	-11.04	22.67
		-12.00	-13.47	12.25
S-14	ZHJ-41	-35.00	-41.97	19.91
		-41.00	-40.35	-1.59
S-8	ZHJ-47	-41.00	-45.61	11.24
		-46.00	-44.30	-3.70
S-2	ZHJ-53	-50.00	-44.77	-10.46
		-46.00	-43.36	-5.74

Table 18
Comparison of measured Z-direction displacement of node (V2) at radial truss support with finite element value (mm)

Axis line number	Truss number	Field-measured value u_1	Analytical value u_2	Error（%） $(u_2-u_1)/u_1$
S-54	ZHJ-1	-9.00	-6.05	-32.78
		-12.00	-8.71	-27.42
S-48	ZHJ-7	-6.00	-5.26	-12.33
		-4.00	-5.43	35.75
S-45	ZHJ-10	-5.00	-6.73	34.60
		-3.00	-4.28	42.67
S-42	ZHJ-13	-4.00	-5.14	28.50
		-6.00	-6.86	14.33
S-39	ZHJ-16	2.00	2.34	17.00
		-2.00	-3.19	59.50
S-33	ZHJ-22	-1.00	-1.13	13.00
		-2.00	-2.6	30.00
S-20	ZHJ-35	1.00	1.13	13.00
		-1.00	-1.27	27.00
S-14	ZHJ-41	-7.00	-9.05	29.29
		-15.00	-9.62	-35.87
S-8	ZHJ-47	-16.00	-10.27	-35.81
		-13.00	-10.47	-19.46
S-2	ZHJ-53	-12.00	-8.39	-30.08
		-13.00	-8.51	-34.54

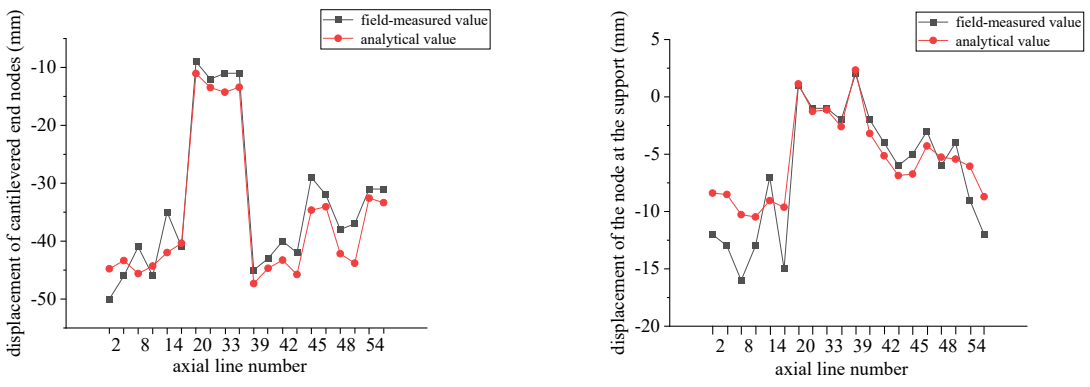

(a) Vertical displacement of cantilever end nodes

(b) Vertical displacement of the node at the support

Fig. 18 Comparison of measured values of displacement of some nodes with FEA values

From Fig. 18, the measured values of displacement and the simulated values from the finite element analysis are basically consistent, indicating that the results of the finite element model analysis are in good agreement with the actual engineering. It verifies the feasibility of the dynamic analysis of the finite

element model presented in this paper and enhances the discussion of stiffness in-homogeneity.

5.2. Acceleration amplification effect

During transmission, ground motion is influenced by factors such as site conditions and the lower structure. To quantify acceleration amplification during energy transfer from lower supports to the steel canopy, seven ground motions are applied to the lower support structure of Model A and Model C. The three-direction output acceleration time histories for each support column top are extracted to obtain the average acceleration response time history curve. For a peak acceleration of 100 gal in the main direction, Table 19 and 20 show the peak ground input acceleration (PGA), peak response frequency acceleration of the supporting columns (PRFA), and acceleration dynamic force amplification factor (DFA) for Model A and Model C, respectively.

It can be seen from Table 19 that, the average values of DAF in the X, Y, and Z directions are 2.05, 2.15 and 1.28, respectively. It indicates that the acceleration amplification effect of the lower support structure in model A is larger in the horizontal X and Y directions but more negligible in the Z direction.

It can be seen from Table 20 that, the average values of DAF in the X, Y, and Z directions are 2.34, 2.08 and 2.25, respectively. It indicates that the acceleration amplification effect of the lower support structure in Model C is larger in three-directions. The amplification factor comparison of the three-direction acceleration for model A and C is shown in Fig. 19.

Table 19
Acceleration amplification effect of the support column obtained from model A calculations

Ground motion	Incentive direction								
	X			Y			Z		
	PGA (gal)	PRFA (gal)	DAF	PGA (gal)	PRFA (gal)	DAF	PGA (gal)	PRFA (gal)	DAF
EL Centro	100	182.88	1.83	85	236.51	2.78	65	77.75	1.20
Northridge	100	239.81	2.40	85	83.51	0.98	65	74.20	1.14
Kobe	100	148.69	1.49	85	247.07	2.91	65	77.61	1.19
Taft	100	206.87	2.07	85	209.53	2.47	65	84.13	1.29
Wo Long	100	260.03	2.60	85	221.65	2.61	65	98.89	1.52
Victoria Mexico	100	174.00	1.74	85	99.33	1.17	65	81.77	1.26
CHICHI	100	221.19	2.21	85	179.31	2.11	65	87.28	1.34

Table 20
Acceleration amplification effect of the support column obtained from Model C calculations

Ground motion	Incentive direction								
	X			Y			Z		
	PGA (gal)	PRFA (gal)	DAF	PGA (gal)	PRFA (gal)	DAF	PGA (gal)	PRFA (gal)	DAF
EL Centro	100	265.96	2.66	85	190.38	2.24	65	167.01	2.57
Northridge	100	265.77	2.66	85	86.51	1.02	65	128.26	1.97
Kobe	100	157.96	1.58	85	302.20	3.56	65	129.83	2.00
Taft	100	266.93	2.67	85	183.46	2.16	65	167.32	2.57
Wo Long	100	246.80	2.47	85	196.72	2.31	65	146.13	2.25
Victoria Mexico	100	182.20	1.82	85	126.00	1.48	65	128.49	1.98
CHICHI	100	250.99	2.51	85	152.66	1.80	65	156.70	2.41

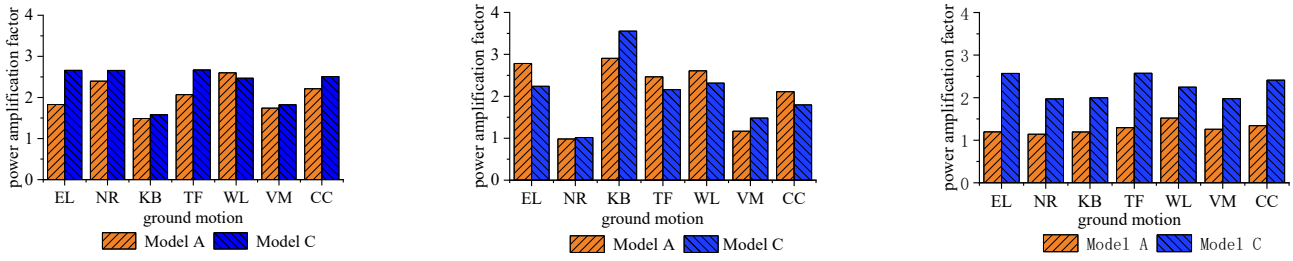

(a) X-direction (b) Y-direction (c) Z-direction

Fig. 19 Amplification factor of the Three-direction

As observed in Fig. 19:

1) For Model A, Northridge and Wolong ground motions amplify X-direction acceleration more significantly, whereas El Centro and Kobe motions amplify Y-direction acceleration more significantly.

2) For Model C, Kobe motion amplifies Y-direction acceleration most prominently.

3) The effect of ground motion on the amplification effect of Z-direction acceleration is similar for both models.

Data from Tables. 19, 20 and Fig. 19 further indicate:

1) The average values of the power amplification factor in the horizontal direction of Models A and C are relatively close.

2) Model C's vertical acceleration dynamic amplification factor is nearly twice as much as that of model A. This discrepancy occurs because model A's integrated steel canopy functions as a three-dimensional metal damper, providing greater horizontal stiffness but lower Z-direction stiffness, thereby enhancing Z-direction damping effectiveness..

Consequently, the lower support structure induces significant three-directional acceleration amplification in both models, with Model C exhibiting approximately twice the Z-direction amplification of Model A. Therefore, when designing the upper steel canopy structure, model B, which does not consider the lower support structure, and model C, which separates the upper and the lower structures, exhibit dynamic response differences compared to the integrated model A. It indicates that the different models exhibit varying dynamic responses.

5.3. Filtering effects

The selective permeability of structures to ground motion leads to significant differences in the effects of ground motion on structures across different frequency bands. The Fourier transform of the ground input acceleration time history and the output acceleration time history at the top of the support column was performed by the Seism Signal software to obtain the principal frequencies of the acceleration time history. The filtering effects of Model A and C for supporting columns under different ground motions are included in Table 21. In this Table, IPF is the principal frequency of the input acceleration time history, and OPF is the principal frequency of the output acceleration time history.

Table 21
Filtering effects (Hz) of supporting columns calculated by Models A and C

Ground motion	Direction of vibration								
	X			Y			Z		
	IPF	OPF (A)	OPF (C)	IPF	OPF (A)	OPF (C)	IPF	OPF (A)	OPF (C)
EL Centro	2.37	3.75	3.10	1.47	4.38	2.08	8.42	4.38	3.10
Northridge	1.07	3.33	3.33	3.22	4.33	1.47	6.98	7.00	3.00
Kobe	0.29	2.00	2.07	2.00	4.27	2.07	2.15	2.20	4.67
Taft	1.42	3.35	2.85	2.98	4.65	2.35	4.40	4.40	4.40
Wo Long	2.34	3.94	3.11	5.47	4.33	2.33	5.91	5.94	3.11
Victoria Mexico	0.98	4.10	3.00	1.76	4.65	2.05	4.64	6.55	4.65
CHICHI	1.47	3.21	3.21	2.54	4.54	2.00	0.49	0.50	3.21
Average value	1.42	3.38	2.95	2.78	4.45	2.05	4.67	4.42	3.73

As can be seen from Table 21:

1) The output average principal frequency OPE of the model A support column in both X and Y directions is larger than the input ground motion principal frequency. At the same time, it is smaller in the Z direction.

2) The output average principal frequency OPE of the model C support columns in the Y and Z directions is smaller than the principal frequency of the input ground motion, except in the X direction.

The lower support structures of models A and C both have some filtering effect on the principal frequency of ground motion. The ratio of the output principal frequency to the input principal frequency for Model A and Model C under seven ground motions is plotted in Fig. 20, showing the difference in filtering effects between the two models.

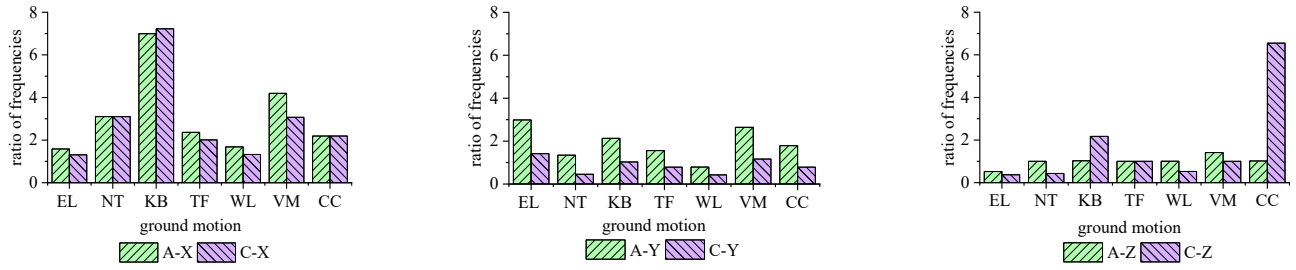

(a) X-direction (b) Y-direction (c) Z-direction

Fig. 20 Filtering effect of lower support structure

As observed in Fig. 20:

1) Due to greater X-direction stiffness in both models' lower support structures, their filtering effects exhibit closer alignment in this direction.

2) In the Y-direction, model A demonstrates higher output-to-input principal frequency ratios than model C, indicating distinct filtering behavior.

3) In the Z-direction, the filtering effect of model C on Kobe and CHICHI ground motions is significantly different from that of model A.

The above analysis indicates a difference in the filtering effects between Model A and Model C. In particular, the Z-direction will influence the principal frequency of ground motion input to the steel canopy structure, which in turn will affect its dynamic response.

These frequency shifts have potentially significant implications for the safety performance of the steel canopy structure, primarily manifested in two damage mechanisms:

1) Resonance Amplification Risks

When the dominant frequency of filtered ground motions shifts close to the natural frequency of key areas in the steel canopy (e.g., cantilever tips), it can excite significant resonance effects. Classical theories indicate [53] that such frequency-domain overlap can lead to the doubling of acceleration and displacement responses, triggering two typical failures:

a) Main structure instability: Amplified inertial forces cause inelastic buckling of compression chords in pipe trusses or brittle shear failure of support anchor bolts [54].

b) Secondary system cascading failure: Excessive support displacements may cause buckling-restrained braces to lose energy-dissipating capacity [55].

2) High-Frequency Fatigue Accumulation

Filtering effects also alter the high-frequency energy distribution of ground motions. Engineering practice confirms that although such high-frequency vibrations do not cause immediate failure, they induce cumulative damage through repeated stress cycles [56], leading to:

a) Joint fatigue cracking: Cyclic stresses concentrated at tubular joint welds initiate micro-cracks, which eventually propagate through the pipe wall [57].

b) Connection functional degradation: High-frequency micro-vibrations cause continuous loosening of metal roof panel bolts, weakening the airtightness and wind resistance of the envelope system.

These mechanisms demonstrate that differences in Z-direction filtering effects between Model A and Model C directly influence the canopy's damage modes. The excessive low-frequency shift in Model C may underestimate resonance risks at cantilever tips, necessitating verification of the true filtered spectrum using the integrated Model A.

6. Conclusions

In this study, the seismic performance of a large stadium steel canopy structure was researched, and the following conclusions were obtained:

1) The results of stress and displacement calculations for integrated model A are intermediate between the two simplified models: model B and model C. To reduce computational resources, the seismic calculation results of simplified models B and C can be used as upper and lower reference values during the preliminary design of the structure.

2) A simplified calculation method is proposed, which can approximate the structural response of the integrated model based on the simplified model calculated data. Simplified calculations of stresses and displacements can be provided for the seismic analysis of the steel canopy structure during the preliminary design stage.

3) The vertical damping filtering effect of the upper steel canopy structure

resulted in a closer vertical acceleration amplification factor of model A and model C. The difference in the vertical acceleration amplification effect is obvious.

4) Comparison of the output average acceleration time history principal frequencies at the top of the lower support structure for Model A and Model C reveals that the filtering effect of the lower support structure is not negligible. An integrated model should be used for accurate calculations.

5) The integrated shape of the lower support structure is like that of a saddle. In the north-south direction, the steel canopy structure is presented as a relatively uniform frame structure. On the east-west sides, it is expressed as a diagonal cantilever structure with disparate scales. This design resulted in substantial differences in the three-direction stiffness at the top of the supporting columns and an uneven distribution of the integrated structural stiffness, which is the main reason for the large differences in the dynamic response of the three models. Integrated analysis is therefore essential for seismic design of large cantilevered steel canopies.

Acknowledgements

This work was financially supported by the Natural Science Foundation of Anhui Province, China (21080850E252) and the Anhui Province Housing and Urban Rural Construction Science and Technology Plan Project(2022-YFO89).

References

[1] Chen W, Chan T.M. Seismic design and parametric study of steel modular frames with distributed seismic resistance. Thin-Walled Structures, 2023, 182(PB).
[2] Guan B, Su M, Lian M. Seismic behavior of combined steel framed tube the lower support structure with replaceable shear links. Journal of Constructional Steel Research, 2020, 167105968-105968.
[3] Zhang A, Fang H, Liu X, et al. Seismic response analysis of large-span steel structures in zone C5 of the terminal building of Beijing Daxing International Airport. Advances in Architectural Steel Structures, 2021, 23(01): 25-30. (in Chinese)
[4] Zhang A, Wang X, Liu X, et al. Study on shaking Tab. test of large-span steel structure of terminal building of Beijing Daxing International Airport with integrated model of scaling. Journal of Building Structures, 2021, 42(03): 1-13. (in Chinese)
[5] Liang C, Zhu Z, Qin K, et al. Research on seismic design of roof steel structure of Beijing new airport terminal building. Steel Structure, 2020, 35(05): 19-26. (in Chinese)
[6] Lu B, Gong J. Seismic response analysis of large-span tensile truss structures under rare earthquakes. Steel Structure, 2019, 34(11): 50-55. (in Chinese)
[7] Xiao W, Wang J, Wan L, et al. Structural analysis of a multi-story steel exhibition hall. Building Structure, 2021, 51(15): 38-43. (in Chinese)
[8] Tong J. Study on seismic performance and ultimate bearing capacity of a shaped multi-tower linked high-rise structure under megathrust earthquake. Building Structure, 2020, 50(13): 101-105. (in Chinese)
[9] Wang D, Wang L, Xu J, et al. A directionally-dependent evolutionary lagged coherency model of nonstationary horizontal spatially variable seismic ground motions for engineering purposes. Soil Dynamics and Earthquake Engineering, 2019, 11758-71.
[10] Jian S, Kaiming B, Kun X, et al. Influence of spatially varying ground motions on the seismic responses of adjacent bridges coupled by a tuned inerter damper. Soil Dynamics and Earthquake Engineering, 2022, 154.
[11] Rodda K. G, Basu D. Spatially correlated vertical ground motion for seismic design. Engineering Structures, 2020, 206(C): 110191-110191.
[12] Bi K, Hao H, Ren W. Response of a frame structure on a canyon site to spatially varying ground motions. Structural Engineering and Mechanics, 2010, 36(1): 111-127.
[13] Hao H and Duan X, Multiple excitation effects on response of symmetric buildings. Engineering Structures, 1996,18(9): 732-740.
[14] Watson-Lamprey J, Abrahamson N. Selection of ground motion time series and limits on scaling. Soil dynamics and earthquake engineering, 2006, 26(5): 477-482.
[15] Katsanos I. E, Sextos G A, Manolis D G. Selection of earthquake ground motion records: A state-of-the-art review from a structural engineering perspective. Soil Dynamics and Earthquake Engineering, 2009, 30(4): 157-169.
[16] Ao D, E J.P. Refined multivariate return period-based ground motion selection and implications for seismic risk assessment. Structural Safety, 2021, 91.
[17] Bradley A B. A ground motion selection algorithm based on the generalized conditional intensity measure approach. Soil Dynamics and Earthquake Engineering, 2012, 4048-61.
[18] Wang G. A ground motion selection and modification method capturing response spectrum characteristics and variability of scenario earthquakes. Soil dynamics and earthquake engineering, 2011, 31(4): 611-625.
[19] Sinković L N, Dolšek M, Žižmond J. Impact of the type of the target response spectrum for ground motion selection and of the number of ground motions on the pushover-based seismic performance assessment of buildings. Engineering Structures, 2018, 175731-742.
[20] Kowsari M, Halldorsson B, Hrafnkelsson B, et al. Selection of earthquake ground motion models using the deviance information criterion. Soil Dynamics and Earthquake Engineering, 2019, 117288-299.
[21] Eftekhari N, Yazdani A, Razmyan S, et al. Data envelopment analysis based procedure for selection and ranking of ground motion prediction equations[J].Soil Dynamics and Earthquake Engineering, 2020, 137.
[22] Gao J, Yao J, Chen L, and Cheng Z. Optimized scheme for ground motion selection based on fuzzy synthesis decision-making. Soil Dynamics and Earthquake Engineering, 2021, 18: 106580.
[23] Dai J, Chen J, Zhang C, et al. Seismic Damage Investigation and Seismic Performance Study of Lushan Middle School Gymnasium. Journal of Performance of Constructed Facilities, 2020, 34(3).
[24] Xue S, Liu Y, Li X, et al. Current status and prospect of research on cooperative work problems of large-span spatial structures. Industrial Building, 2015, 45(01): 1-9.
[25] Nie G. On the buckling of imperfect squarely-reticulated shallow spherical shells supported by elastic media. Thin-Walled Structures, 2003, 41(1): 1-13.
[26] Nie G,Wang W,Du K,et al. A review on the development of seismic theory for large-span spatial structures. World Earthquake Engineering, 2020, 36(02): 21-34. (in Chinese)
[27] Nie G, Zhi X, Shang Y, et al. Study on seismic performance of single-story column-faced mesh shell structure considering lower support effect. Journal of Building Structures, 2020, 41(S1): 10-16. (in Chinese)
[28] Wang Y, Jiang J. Research on the effect of concrete support on the mechanical performance of large-span spatial lattice structures and simplified analysis method. Building Structure, 2019, 49(09): 43-47. (in Chinese)
[29] Yu Z, Zhi X, Fan F, et al. Effect of the lower support structures upon failure behavior of steel reticulated domes subjected to the severe earthquake. Thin-Walled Structures, 2011, 49(9):1160-1170.
[30] Zheng Y, Wang R.Q, et al. Dynamic analysis of anti-dip bedding rock slopes reinforced by pre-stressed cables using discrete element method. Engineering Analysis with Boundary Elements, 2021.
[31] Meng J.X. Comparative Analysis of Space Truss Door Beams Based on Different Calculation Models. Research on Engineering Technology, 2023,8(15): 106-108.（in Chinese）
[32] Xia W.J. Electrochemical Seismic Design and Artificial Intelligence System Modeling of High-Rise Steel Structure Buildings. Journal of Chemistry, 2022.
[33] Han Q.H, Sun M.Y. et al. Ground motion parameters and fragility analysis for single-layer reticulated domes supported by the lower support structures. Earthquake Engineering and Engineering Vibration, 2024, 44(03): 29-40.（in Chinese）
[34] Chopra, A.K. Naeim F. Dynamics of Structures—Theory and Applications to Earthquake Engineering, Third Edition. Earthquake Spectra, 2007, 23(2): 491-492.
[35] M. Birchall. 22-Recent developments in architectural fabric structures in Europe: The des--ign and construction of the London 2012 Olympic Stadium and its context in the European fabric structures market. Fabric Structures in Architecture, 773-817, 2015.
[36] Zhang S, Liu N, Li W and Yan S. Umbrella structure building design method via case-based design and statistical analysis of structural morphological parameters, Journal of Building Engineering, 2022, 45: 103542.
[37] Fan C, Yang K, et al. Design and research on large-span roof structure supported by mega arches of Xiamen Egret stadium. Journal of Building Structures, 2023, 44(09): 27-39.（in Chinese）
[38] Ivan B, Alen H, Vesna J.P. Conceptual design of arena Nikola gazdic stadium split. Proceedings of the Faculty of Civil Engineering, 2019, 9(18): 28-37.
[39] Seismic Design Criteria for Structures, Systems and Components in Nuclear Facilities. ASCE/SEI Standard 43-05, American Society of Civil Engineers (ASCE), Reston, Virginia. 2016.
[40] Guyan R J. Reduction of stiffness and mass matrices. AIAA Journal, 1965, 3(2): 380.
[41] NERHP recommended seismic provisions for new buildings and other structures. FEMA P-750 report prepared by the Building Seismic Safety Council of The National Institute of Building Sciences for the Federal Emergency Management Agency, Washington, D.C; 2009.
[42] Ferrante A, Dubois F, Morenon P. Comparison of Continuous and Discrete Modeling Strategies for the Structural Assessment of a Masonry Vault Under Dynamic Seismic Loading. International Journal of Architectural Heritage, 2024, 18(12): 1873-1885.
[43]Code for Seismic Design of Buildings, GB 50011-2010, China Academy of Building Research, Institute of Engineering Mechanics, China Earthquake Administration, China Architectural Design and Research Group, China National Institute of Standards and Design for Buildings, Beijing Institute of Architectural Design, 2010.
[44] Engineers C O S A. Minimum Design Loads and Associated Criteria for Buildings and Other Structures. American Society of Civil Engineers, 2022.
[45] Lignos G D, Krawinkler H, Whittaker S A. Prediction and validation of sidesway collapse of two scale models of a 4-story steel moment frame. Earthquake Engineering & Structural Dynamics, 2011, 40(7): 807-825.
[46] Kunnath K S, Nghiem Q, El-Tawil S. Modeling and Response Prediction in Performance-Based Seismic Evaluation: Case Studies of Instrumented Steel Moment-Frame Buildings. Earthquake Spectra,2004,20(3):883-915.
[47] Pujari N. N, Ghosh S, Lala S. Bayesian Approach for the Seismic Fragility Estimation of a Containment Shell Based on the Formation of Through-Wall Cracks. ASCE-ASME Journal of Risk and Uncertainty in Engineering Systems, Part A: Civil Engineering, 2015, 2(3).
[48] Zhang C.X. Study on the Failure Mechanism under Strong Earthquake Excitation and Isolation of Space Double-layer Lattice Structure. Institute of Engineering Mechanics, China Earthquake Administration, 2016. (in Chinese)
[49] Standard for acceptance of construction quality of steel structures: GB 50205-2020. China Planning Press, 2020.
[50] Design of steel structures: GB 50017—2017. China Planning Press, 2017.
[51] High strength low alloy structural steels: GB/T 1591-2018. Standards Press of China, 2018.
[52] Rubber bearings—Part 3: Elastomeric seismic-protection isolators for buildings: GB/T 20688.3-2006. Standards Press of China, 2006.
[53] Liu Z, Chen J. Structural dynamics. China Water&Power Press:2012.
[54] ELNASHAI A, SARNO D.L. Earthquake Engineering: From Engineering Seismology to Performance-Based Engineering, Journal of Earthquake Engineering, 2004, 8(6): 963-964.
[55] Kitayama S, Constantinou C.M. Seismic Performance of Buildings with Viscous Damping Systems Designed by the Procedures of ASCE/SEI 7-16. Journal of Structural Engineering, 2018, 144(6).
[56] Cui D, Xie R, Li M, et al. Time-dependent reliability analysis for structures under multilevel loads based on fatigue damage theory. Engineering Failure Analysis, 2024.
[57] Hobbacher F A. The IIW fatigue design recommendations - newly revised and expanded. Welding in the World: Journal of the International Institute of Welding: Journal of the International Institute of Welding, 2007, 51(Suppl.1): 243-254.

Advanced Steel Construction – Vol. 22 No. 1 (2026) 37–47
DOI:10.18057/IJASC.2026.22.1.4

EXPERIMENTAL STUDY ON STATIC PERFORMANCE OF SINGLE-LAYER SADDLE-SHAPED CABLE NET STRUSTURES

Jie Qin [1, 3], Hao Zhang [2], Guo-Jun Sun [2, *], Yu Xue [2], De-Qing You [4] and Jin-Zhi Wu [2]

[1] *University of Emergency Management, Langfang 065201, China*
[2] *Beijing University of Technology, Beijing 100124, China*
[3] *Hebei Key Laboratory of Civil Engineering Catastrophe Control and Disaster Emergency Response, Langfang 065201, China*
[4] *Beijing Building Construction Research Institute Co., Ltd., Beijing, 100039, China*
** (Corresponding author: E-mail: sunguojun@bjut.edu.cn)*

ABSTRACT

This study investigates the single-layer cable-net roof structure of the Xiatian Cultural Park Stadium by conducting a 1:10 scale model experiment to systematically examine the internal forces and deformations under various static loading conditions. The experiment incorporates full-span loading scenarios, and in conjunction with finite element simulations, analyzes and compares the force and deformation responses of the load-bearing cables, ring cables, diagonal cables, anti-wind cables, and back cables. The results demonstrate that, during loading, the cable forces and node displacements in all groups exhibit a linear relationship with the applied load. Among these, the ring cables sustain the highest internal forces, indicating their role as the primary load-bearing elements of the structure. Moreover, the finite element analysis results for static performance show close agreement with the experimental data, with discrepancies remaining within an acceptable range. This consistency verifies the accuracy of the numerical simulation method and confirms the reliability of the experimental results. The findings offer valuable reference data for the structural design and optimization of similar systems.

ARTICLE HISTORY

Received: 3 March 2025
Revised: 8 July 2025
Accepted: 18 July 2025

KEYWORDS

Single-layer cable structure;
Cable net structure;
Scaled model experiment;
Static loading test;
Mechanical performance

1. Introduction

Cable-net structures represent a significant form of tensile architecture, characterized by efficient stress distribution, diverse geometric configurations, effective force transmission, and substantial reductions in steel consumption. These advantages also contribute to the realization of sustainable building objectives, making cable-net systems a widely adopted structural solution in contemporary architecture [1]. Such structures are extensively used in large-span spatial applications. Single-layer cable-net systems typically consist of two sets of cables with opposing curvatures: the downward-curved load-bearing cables primarily support the dead and live loads of the roof, while the upward-curved tension cables function as stabilizing elements, resisting uplift forces induced by wind loads [2]. The elliptical boundary, saddle-shaped single-layer cable-net structure is notable for its elegant form and has seen application both domestically and internationally—for example, in the London Velodrome, Suzhou Olympic Sports Center Swimming Hall, and the National Speed Skating Oval. In recent years, it has undergone rapid development and broader implementation in China [3][4].

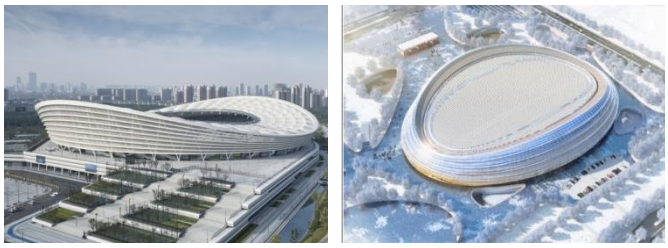

(a) Suzhou Olympic Sports Center Gymnasium

(b) National Speed Skating Oval

Fig. 1 Typical saddle-shaped cable network construction

Current research on reticulated structures, both domestically and internationally, primarily focuses on aspects such as shape finding, construction methods, and mechanical performance. Schek [5] introduced the force-density method to perform preliminary shape finding for cable-net structures. Li et al. [6] employed a modified force-density method to analyze the shape finding of saddle-shaped orthotropic cable networks, applying this method to systems without an inner ring cable and achieving results closely aligned with numerical solutions. Li et al. [7] further proposed an innovative minimum surface finding method for cable-net structures, which significantly improved the iteration speed of the shape-finding process.Cable structures exhibit pronounced nonlinear behavior, distinguishing them from rigid structures. Unlike rigid systems, the performance of cable structures in meeting design requirements is closely tied to their construction processes [8]. A review of engineering cases, both in China and abroad, indicates that construction methods for saddle-shaped cable-net structures can be broadly categorized into three main types. The first method involves the use of auxiliary scaffolding, as seen in the construction of Calgary Stadium in Canada [9]. The cable system is laid atop the scaffolding and then tensioned to complete the cable-net installation. The second method entails overall lifting of the cable net, similar to the construction approach used for radial cable-net structures, exemplified by the Olympic Sports Center in Munich, Germany [10]. The third method is high-altitude assembly, in which stabilizing cables are delivered from outside the construction site to designated elevated positions using a cable-lowering technique. This method was applied in the construction of the cable-net roof at the Suzhou Swimming Pool [11]. Currently, engineers in China predominantly adopt the second method, involving the overall lifting of the cable net followed by sequential tensioning and batch installation. In the absence of established precedents, Gao et al. [12] proposed a construction method consisting of the overall lifting of the load-bearing cables, followed by unified tensioning of the stabilizing cables. This approach incorporates auxiliary measures such as accounting for passive forces in curtain wall cables and releasing the horizontal constraints of the outer ring beam supports. Final calculations confirmed that the shaping effect achieved was ideal. In addition to overall lifting, a few projects have employed high-altitude scaffolding. For example, the double-layer cable net of the Yangzhou Sports Park Swimming and Diving Hall was assembled midair using this method. Installation followed the principle of primarily tensioning the lower cables, with the upper cables serving as secondary supports.

Regarding the construction of cable-net structures, the methods vary depending on factors such as the construction site, hardware facilities, and economic conditions[13]. Consequently, their applicable scopes differ. Regardless of the method employed, it is essential to ensure that the structure remains in a low-stress state for as long as possible, while the duration in a high-stress state should be minimized during the construction process[14][15].The study of the static performance of cable nets primarily focuses on the shape and force changes of the cable net under static loads such as self-weight and snow load. The research on the dynamic performance of cable nets mainly investigates the structural natural frequencies and the response of the structure under dynamic loading. Although the negative curvature and relatively high prestress level make the cable net inherently "stiff," it still exhibits strong nonlinear behavior under load [16]. The stiffness of the structure itself is related to factors such as the deflection of the cable net, the magnitude and distribution of prestress, and the structural span-to-rise ratio. Generally, the control variable

method can be used to determine the extent of the influence of these factors on the cable net. Lu [17], based on a hub-and-spoke type single and double-layer hybrid cable net structure, found that the influence of wind suction on the internal forces and vertical displacement of the structure is greater than that of live loads, while the effect of temperature variations is negligible. Fabio et al. [18] conducted a full-scale static experiment on a single-layer cable net and investigated the effects of three different types of failure on the static performance of the cable net. The experimental results indicated that the failure of the connections between the cables had minimal impact on the static performance of the structure. In contrast, failure at the anchorage points of the cables significantly affected the structure. Furthermore, the damage itself had a greater influence on node displacements than on internal forces. Sun et al. [19] studied the inflection point behavior of a complex single-layer cable net model under horizontal loading, taking into account the effects of different prestress levels and glass stiffness.

This study focuses on the roof structure of the Xiatian Cultural Park Stadium. A 1:10 scaled model of the single-layer, saddle-shaped cable-net structure was designed and constructed for static loading experiments. The effects of different loading levels and load types on cable forces and displacements were examined under three static loading conditions. Based on the experimental findings, a corresponding finite element model was developed using ANSYS software at the same scale. The simulation results were then compared with the experimental data to validate the model, providing practical guidance for the structural design and application of cable-net systems in engineering practice.

2. Introduction of the test model

2.1. Engineering background

As shown in Fig. 2, the subject of this study is the roof structure of the Xiatian Cultural Park Stadium. The roof adopts a single-layer reticulated shell system with one rigid boundary and three flexible boundaries. The span of the structure measures 210 m × 54 m. The overall system comprises crescent-shaped steel ring beams and steel inclined columns serving as boundary conditions. The downward-curved load-bearing cables and upward-curved stabilizing cables are arranged orthogonally to form the single-layer reticulated shell. The structure is connected to the masts through ring cables and boundary cables, while backstay cables are employed for balance. This project introduces an innovative design that builds upon the conventional single-layer reticulated shell system, featuring one rigid boundary and three open, flexible line boundaries. The flexible boundaries are realized through the use of masts and backstay cables, enabling the structure to achieve large spans and wide open spaces. The overall structural form is novel, with a roof that appears light and elegant yet structurally robust. This configuration represents a new type of structural system that has not previously been seen in either domestic or international applications.

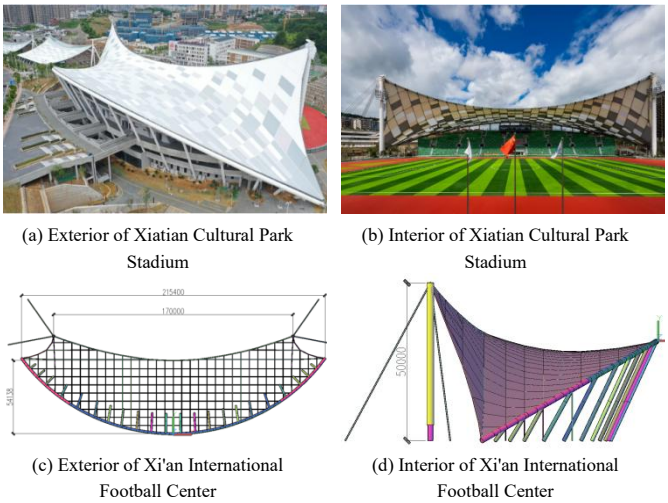

(a) Exterior of Xiatian Cultural Park Stadium

(b) Interior of Xiatian Cultural Park Stadium

(c) Exterior of Xi'an International Football Center

(d) Interior of Xi'an International Football Center

Fig. 2 Roof of Xiatian Cultural Park Stadium

2.2. Similitude law

Due to the large dimensions of the original structure and considering factors such as the testing site limitations, the model design was based on similarity theory, with a geometric scaling ratio of 1:10. The ratios of other physical quantities between the scaled model and the original structure were determined using magnitude analysis [20][21], as shown in Table 1.

Table 1
Similarity ratio between test model and actual structure

Physical property	Physical parameter	Symbol	Similarity ratio
Material Property	Elastic Modulus	S_E	1:1
	Stress	S_σ	1:1
	Poisson's Ratio	S_μ	1:1
	Density	S_ρ	1:1
Geometric Property	Span	S_L	1:10
	Area	S_A	1:100
	Strain	S_ε	1:1
Load Property	Concentration force	S_P	1:100

2.3. Model size and component specifications

As shown in Fig 3, the model is composed of supporting steel structure and single-layer cable net structure. The steel structure members include steel ring beam, steel inclined column, steel mast, steel mast support. The scale is designed according to the geometric scale of 1:10, and the similarity ratio of EA is 1:100. According to the actual materials that can be purchased, the final scale design is similar, such as the following Table 2, which basically meets the similarity ratio requirements. The steel ring beam, steel inclined column, steel mast and its support adopt welded steel pipe, and the material used is Q355B. The steel inclined column support adopts square tube, 150*150*5, and the steel grade is Q235B.

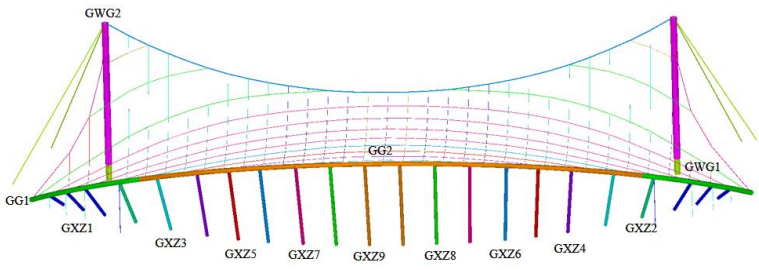

Fig. 3 Schematic diagram of steel members numbering

Table 2
Specifications and dimensions of beam

		Original model			Scale model			
Member type	Section type	Diameter/ mm	Thickness/ mm	Cross-sectional area/ mm²	Diameter/ mm	Thickness/ mm	Cross-sectional area/ mm²	EA similar ratio
GG1	Circular tube	1500	50	227766	152	5.75	2642	1:86
GG2		1500	40	183469	152	3.75	1746	1:105
GWG		2000	80	482534	203	7.75	4754	1:102
GXZ1		1000	30	91420	102	7.75	1157	1:79
GXZ2		1000	70	204518	102	7.75	2295	1:89
GXZ3		1000	80	231221	102	7.75	2295	1:101
GXZ4		1000	60	177186	102	5.75	1739	1:102
GXZ5		1000	40	120637	102	3.75	1157	1:104
GXZ6		1000	60	177186	102	5.75	1739	1:102
GXZ7		1000	65	190930	102	7.75	2295	1:83
GXZ8		1000	60	177186	102	5.75	1739	1:102
GXZ9		1000	50	149226	102	5.75	1739	1:86

As the Fig 4 shown, the single-layer cable network primarily comprises three main components: load-bearing cables(CS), anti-wind cables(KS), diagonal cable(XS), ring cables(HS) and back cables(BS). The EA similarity ratio is 1:100 for the design of drawbars according to the principle of stress similarity, and the following table shows the results of the design of drawbars. As for the material, the actual engineering ropes are all sealed cables, and the model test uses sealed cables and steel cables. the EA similarity ratio is about 1:100, which basically meets the requirements.

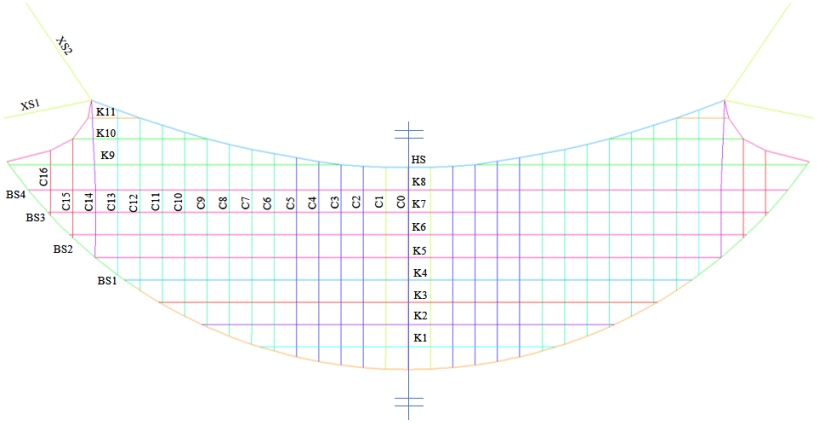

Fig. 4 Schematic diagram of cables numbering

Table 3
Specifications and dimensions of cables

Cables	Original model			Scale model			
	Specifications	Breaking force/kN	E/Mpa	Specifications	Breaking force/kN	E/Mpa	EA similar ratio
Load-bearing cables	Φ40	1580	1.6×10^5	Φ7	49.5	1.5×10^5	1:41
	Φ50	2470	1.6×10^5	Φ7	49.5	1.5×10^5	1:64
	Φ50	2470	1.6×10^5	Φ7	49.5	1.5×10^5	1:64
	Φ55	2170	1.6×10^5	Φ7	49.5	1.5×10^5	1:80
Anti-wind cables	Φ75	5620	1.6×10^5	Φ10	93.8	1.5×10^5	1:73
	Φ80	6390	1.6×10^5	Φ14	184.0	1.5×10^5	1:83
	Φ95	9110	1.6×10^5	Φ14	184.0	1.5×10^5	1:116
Ring cables Side-ring cables	Φ90	8090	1.6×10^5	Φ14	184.0	1.5×10^5	1:104
	Φ90	8090	1.6×10^5	Φ14	184.0	1.5×10^5	1:104
Back cables	Φ95	9110	1.6×10^5	Φ14	184.0	1.5×10^5	1:116
	Φ105	11100	1.6×10^5	Φ20	363.0	1.5×10^5	1:71
Diagonal cables	Φ125	15800	1.6×10^5	Φ26	660.0	1.5×10^5	1:103

3. Test scheme

3.1. Test load conditions

According to the design basis related to the single-layer saddle-shaped cable network structure of the stadium of Xiatian Cultural Park, the dead load, which includes the membrane structure, sound insulation, sunshade ceiling, and other hanging components, is 0.2 kN/m² . The live load is 0.3 kN/m² , the wind

load reference design institute MIDAS model export results, as specified in the Load Code for Building Structures (GB50009-2012) [22]. The load combinations are shown in Table 4. The distribution of load points is shown in Fig. 5.Although only 22 loading points were available, their layout was carefully optimized using a grid-based scheme to achieve a relatively uniform load distribution.

Table 4
Test conditions

Loading cases	Load distributions	Load composition
I	Full-span distribution	1.3×D+1.5×L
II	Full-span distribution	1.3×D+1.5×WP
III	Full-span distribution	1.3×D+1.5×WS

Note:D, L, WP, WS represent dead load, live load, wind pressure load and wind suction load respectively.

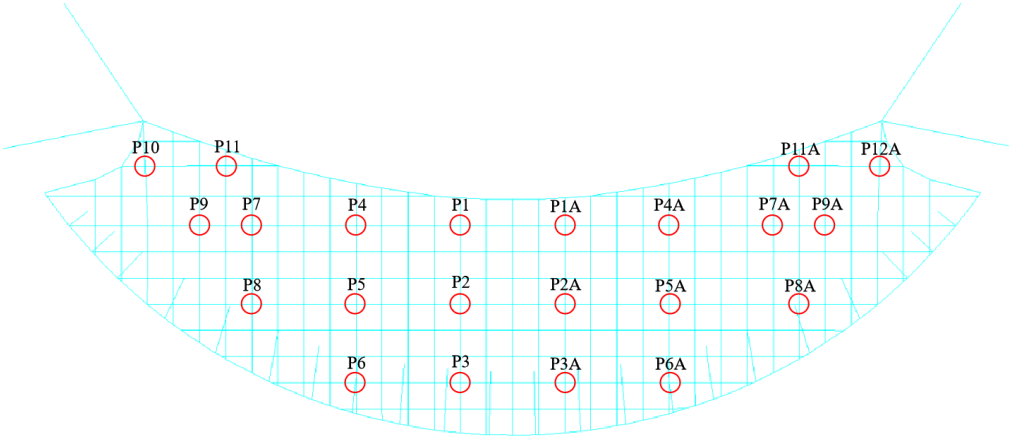

Fig. 5 Schematic diagram of loading points distribution

3.2. Loading method and load point location

During the static loading tests, the applied load required multiple adjustments to achieve the desired experimental conditions. Hence, the electro-servo loading control system was employed to perform the loading process. As shown in theFig 6, this system driven by an electric motor and integrated with servo control technology, enables precise control of load, velocity, and displacement.

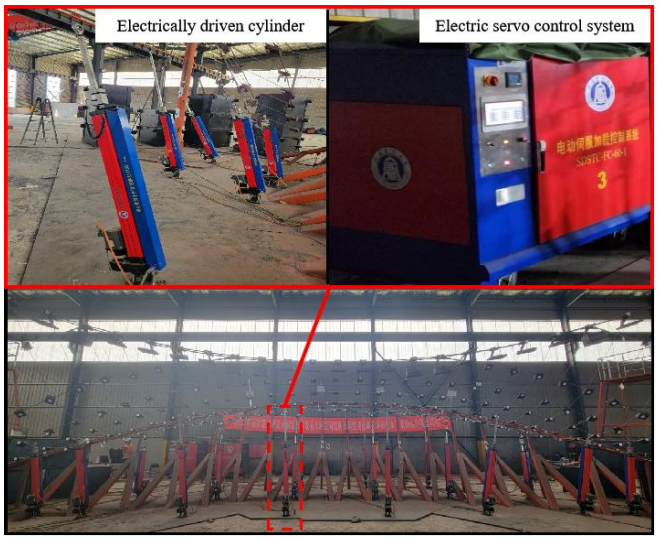

3.3. Measurement equipment and measurement point layout

In the cable force monitoring, S-type load cells and anchor cable force sensors were used. The Midas computational model for the actual engineering project provided the envelope values of internal and reaction forces. In the model test, these forces were scaled to 1/100 of the actual values. For the load-bearing cables, S-type tension and compression sensors with a 2 tons capacity were used, with 3 sensors in total. The anti-wind and edge cables were fitted with S-type tension sensors with a 10 tons capacity, totaling 10 sensors. The diagonal cables were monitored with anchor cable force sensors, each with a 50 tons capacity. During the loading process, a total station paired with laser reflectors was used to monitor structural deformation. The arrangement of the measurement equipment is shown in Fig 7.

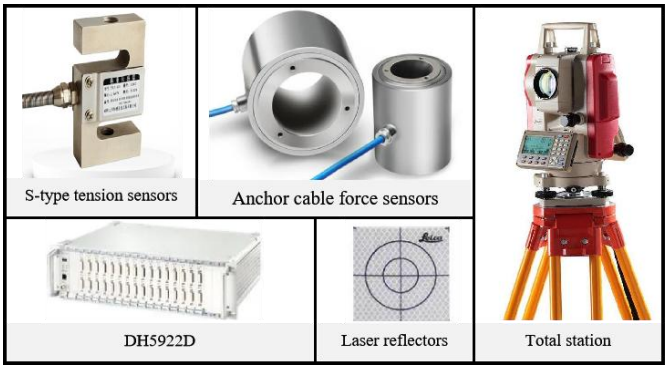

Fig. 7 Measuring equipments

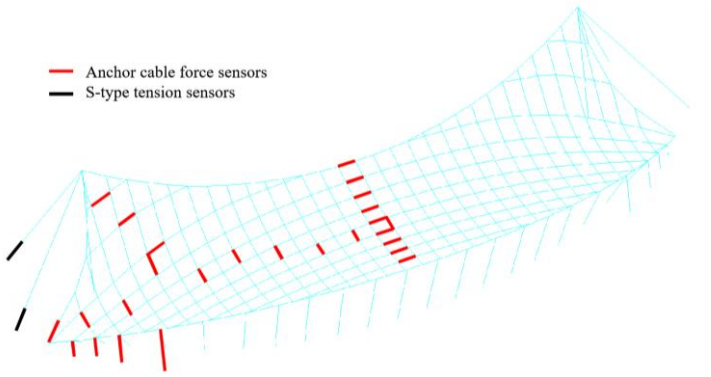

(a) Layout of cable force measurement points

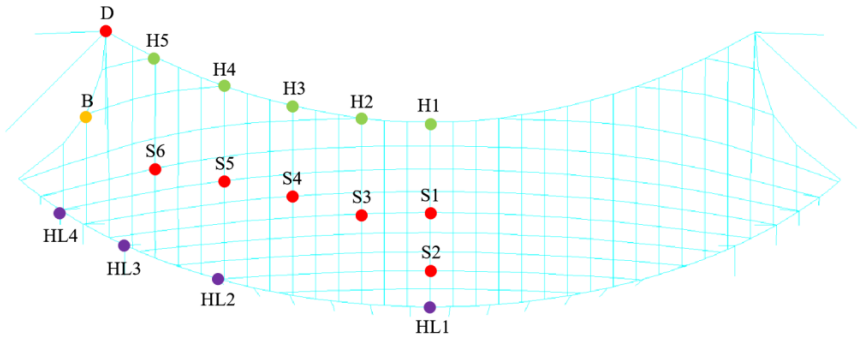

(b) Layout of deformation measurement points

Fig. 8 Layout of measurement points

This experiment included 28 cable force measurement points, as shown in Fig 8(a). A total of 36 displacement measurement points were also arranged. These included 2 at the mast tops, 2 at the edge cables, 4 at the bases of the diagonal cables, 9 on the annular cables, 10 on the cable net, 7 on the ring beam, and 2 at the bottom of the ring beam. The detailed arrangement is shown in Fig 8(b).

4. Test result

Under three loading conditions, the tensile forces and displacements of the single-layer cable net structure were measured. Loading case 1 includes dead load and live load, Loading case 2 includes dead load and wind pressure load, and Loading case 3 includes dead load and wind suction load. The loading levels range from 5, with each level increasing by 20%.

4.1. Case I

4.1.1. Changes in cable force

The variation in cable force at the measurement points under Case I is shown in Fig. 9. As the load increased linearly, the cable forces also exhibited a linear increase. During the incremental loading process, the tension in the HS cables reached its maximum, identifying them as the primary load-bearing components of the structure. The internal force in XS1 was approximately 6% greater than that in XS2, while the internal forces in the four BS cables showed relatively minor differences. Notably, the tension in the load-bearing cables varied with the loading level depending on their specific positions. Most of the tensions in the CS cables increased with the applied load; however, the tensions in CS0, CS4, and CS8 gradually decreased. The variations in the tensions of KS2, KS9, KS10, and KS11 were relatively small, whereas the tensions in the remaining KS cables progressively decreased, with KS9 maintaining a consistently higher tension level.

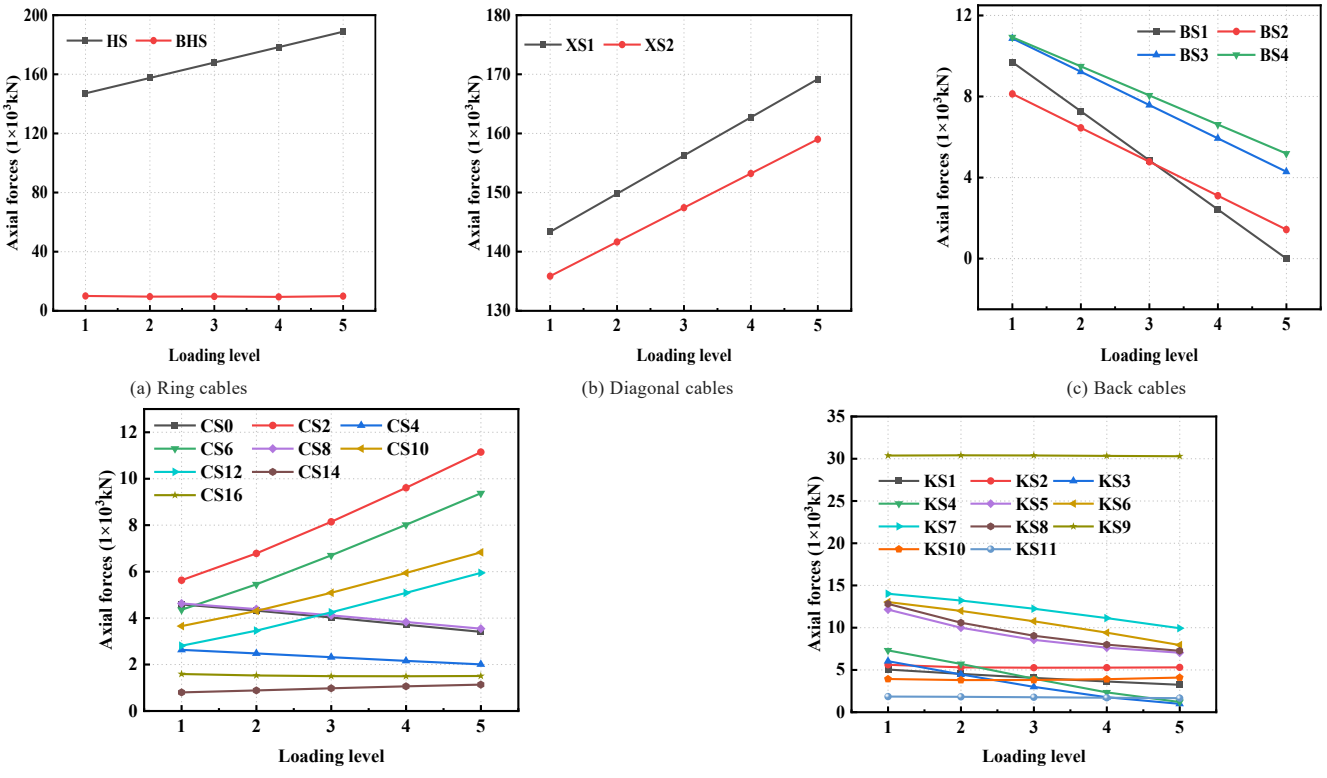

(a) Ring cables (b) Diagonal cables (c) Back cables

(d) Load-bearing cables (e) Anit-wind cables

Fig. 9 Changes in the cable force at the measurement point under Case I

4.1.2. Changes in displacement

The variation in displacement at the measurement points under Case I is shown in Fig. 10. As the load increased, the displacement of the cable net decreased approximately linearly. With the external load increasing from Level 1 to Level 5, the maximum vertical displacement of the structure occurred at measurement point S6 on the cable net, reaching 80 mm. The displacement at the ring beam node HL gradually increased, with a more pronounced upward trend observed at HL1, where the maximum displacement reached 9.95 mm. At the flexible boundary of the cable net, the displacement at measurement point B increased by approximately 13.78 mm, while the displacement at measurement point D, located at the top of the mast, exhibited relatively small variations.

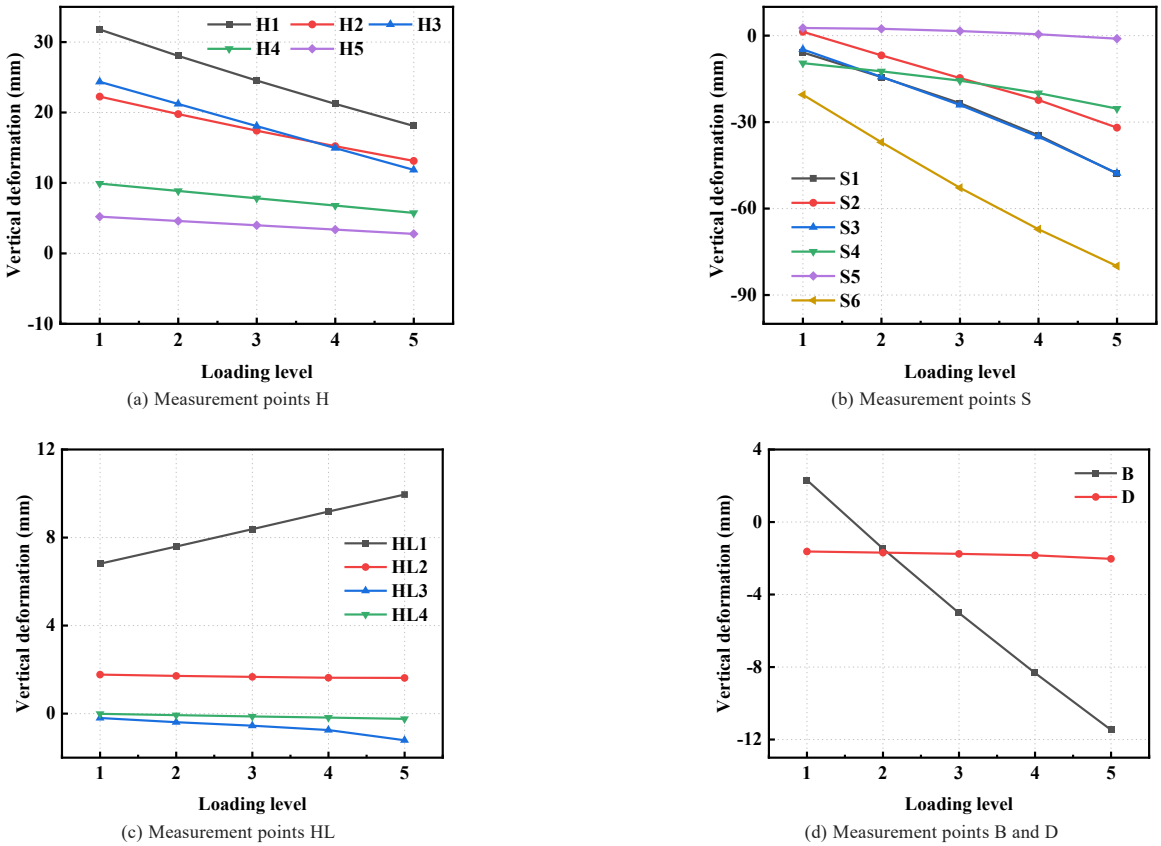

(a) Measurement points H

(b) Measurement points S

(c) Measurement points HL

(d) Measurement points B and D

Fig. 10 Changes in the displacement of the measuring point under Case I

4.2. Case II

4.2.1. Changes in cable force

The variation in cable force at the measurement points under Case II is shown in Fig. 11. As the load increased, the cable forces at the measurement points increased approximately linearly. The variation pattern closely resembles that observed in Case I, with the ring cables continuing to serve as the primary load-bearing components of the structure. The internal force in XS1 consistently exceeds that in XS2, and the differences in force among the four backstay cables remain relatively small. Notably, after the fourth loading level, BS1 and BS2 exhibit signs of force relaxation. While most of the forces in the CS cables increase with the applied load, the forces in CS0, CS4, and CS8 gradually decrease. The force variations in KS2, KS9, KS10, and KS11 are relatively minor, whereas the forces in the remaining KS cables gradually decline, with KS9 maintaining a comparatively higher force level.

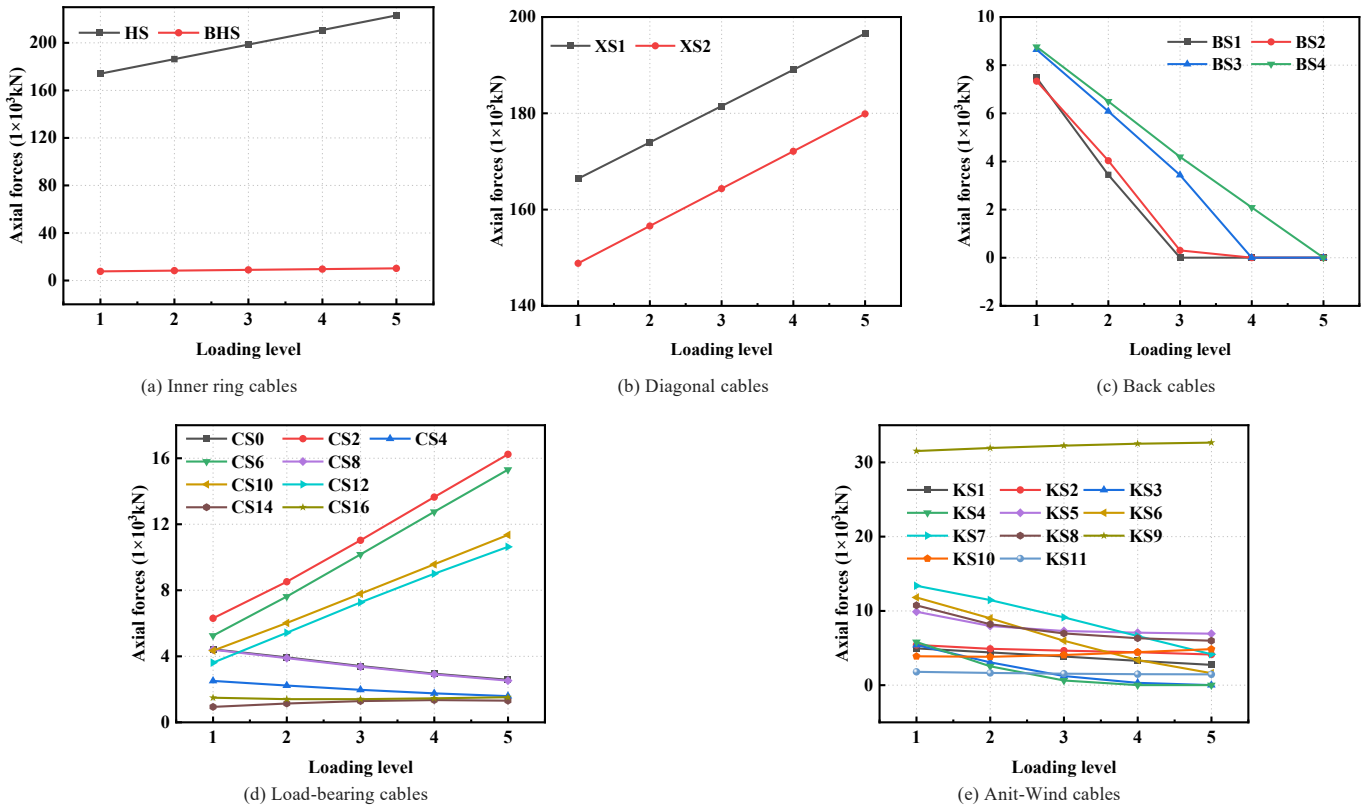

(a) Inner ring cables

(b) Diagonal cables

(c) Back cables

(d) Load-bearing cables

(e) Anit-Wind cables

Fig. 11 Changes in the cable force at the measurement point under Case I

4.2.2. Changes in displacement

The variation in displacement at the measurement points under Case II is shown in Fig. 12. As the load increased, the displacements at each measurement point decreased approximately linearly. The overall pattern of vertical displacement at the nodes is generally consistent with that observed in Case I, with the maximum vertical displacement still occurring at cable-net measurement point S6, reaching 129.6 mm. The displacement at ring cable measurement point H5 gradually increases, while the displacements at the remaining measurement points decrease. At the rigid boundary, the vertical displacement at measurement point HL1 exhibits a noticeable increasing trend, whereas the displacement variations at other rigid boundary points are relatively minor. At the flexible boundary, the displacement at measurement point B increases by approximately 22.23 mm, while the variation in displacement at the top of the mast (measurement point D) remains relatively small.

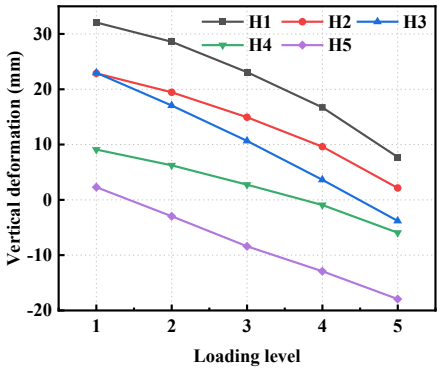

(a) Measurement points H

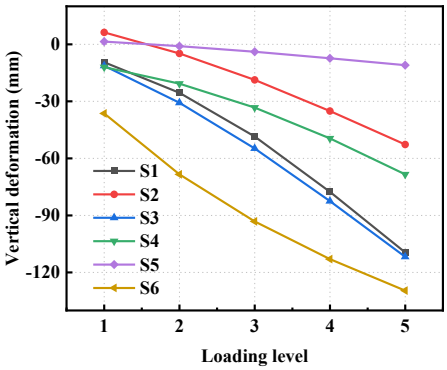

(b) Measurement points S

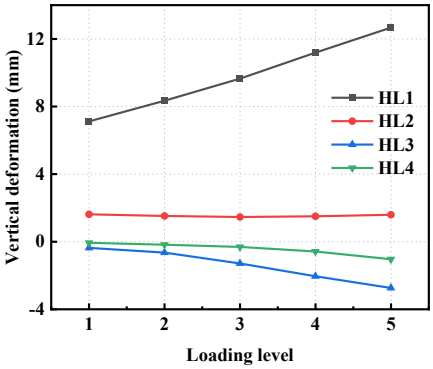

(c) Measurement points HL

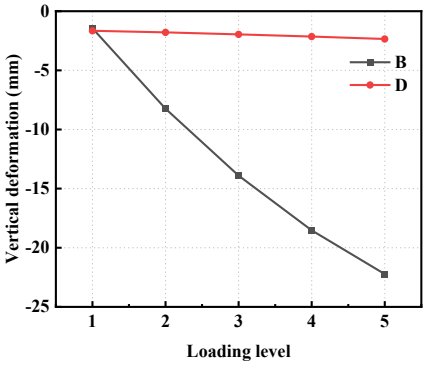

(d) Measurement points B and D

Fig. 12 Changes in the displacement of the measuring point under Case II

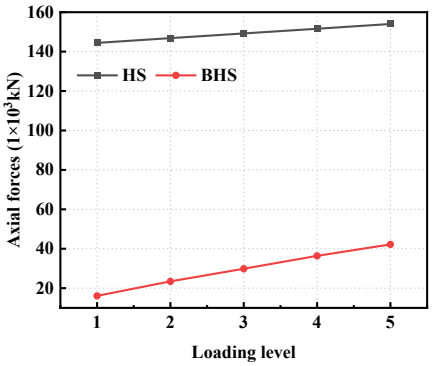

(a) Inner ring cables

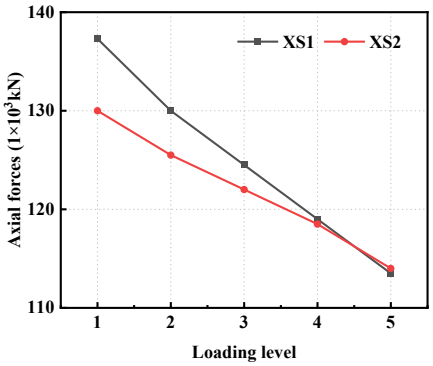

(b) Diagonal cables

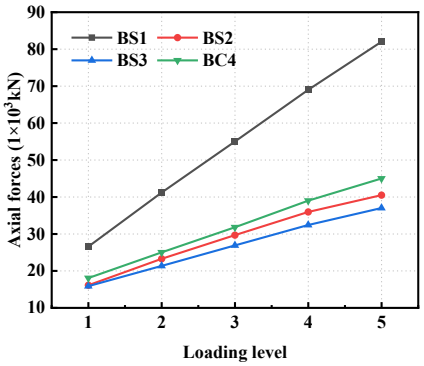

(c) Back cables

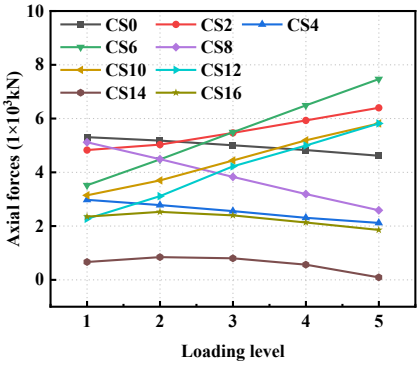

(d) Load-bearing cables

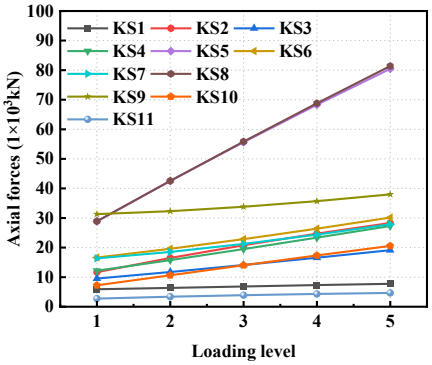

(e) Anit-wind cables

Fig. 13 Changes in the cable force at the measurement point under Case I

4.3 Case III

4.3.1. Changes in cable force

The variation in displacement at the measurement points under Case III is shown in Fig. 13. Unlike Cases I and II, Case III incorporates both dead load and wind suction load, representing a fundamentally different loading scenario. In addition to HS, the internal forces in the BHS components also exhibit a noticeable upward trend, with HS remaining the component subjected to the highest tensile force. In contrast to the previous two cases, the internal forces in the XS components decrease linearly, and by loading level 5, the tensile force in XS2 exceeds that in XS1. The tensile forces in all four BS components increase significantly, with BS1 showing the most pronounced growth. Among the CS components, the tensile forces in CS2, CS6, CS10, and CS12 increase with the load, while those in the remaining CS elements decrease to varying degrees. All KS components exhibit an increasing trend in tensile force, with KS5 and KS8 showing the most distinct patterns. Notably, the tensile forces in KS5 and KS8 are nearly identical throughout the loading process.

4.3.2. Changes in displacement

The displacement variation curves of the measurement points under Case III are presented in Fig. 14. As the load increases linearly, the vertical displacement at measurement point H on the ring cable also increases to varying degrees. The closer the point is to the mast, the smaller the magnitude of vertical displacement observed. The maximum displacement still occurs at mesh measurement point S6, reaching 194.8 mm. Displacements at the other S points also increase approximately linearly with the applied load. For the rigid ring beam, the displacement at measurement point HL1 decreases, while the displacements at the other HL points show a linear increase with loading. Similar to Cases I and II, the displacement at the mast top remains nearly unchanged. At the flexible boundary, measurement point B exhibits a clear linear displacement trend in the opposite direction.

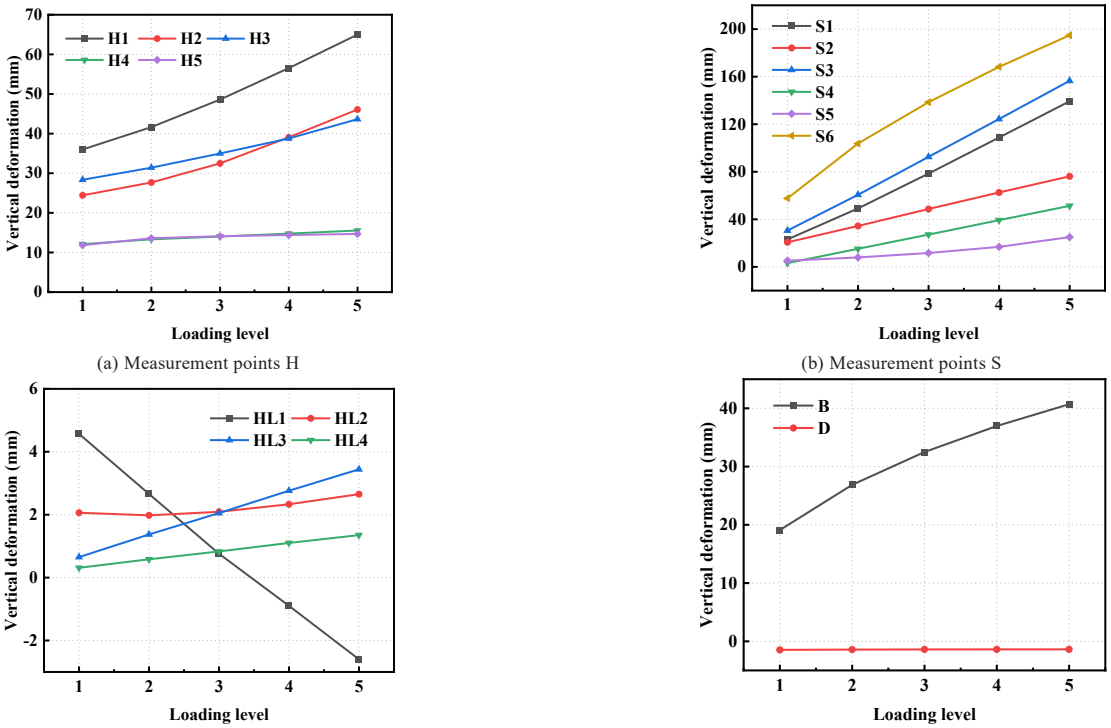

Fig. 14 Changes in the displacement of the measuring point under Case III

5. Finite element analysis

5.1.Model details

For the experimental model of the single-layer cable net structure, a numerical model is established using the general-purpose finite element software ANSYS. This model includes the single-layer saddle-shaped cable net and the supporting steel structure. All cables are modeled using the LINK180 element, which can be configured via the KEYOPT switch to allow only tensile behavior. The cable mesh structure is prestressed by adding cell initial strains in order to apply prestress. The supporting steel structure, including steel masts, ring beams, and struts, is modeled using BEAM188 elements. The cable clamps are simulated using MASS21 elements[23]. The finite element model is shown in Fig. 15, with the material properties of the components listed in the Table 5.

Table 5
Material mechanics parameters in finite element model

Members	Elastic modulus E (MPa)	Thermal expansion coefficient α (1/℃)	Density ρ
Cables	1.9×10^5	1.2×10^{-5}	7.85×10^3
Steel members	2.06×10^5	1.2×10^{-5}	7.85×10^3

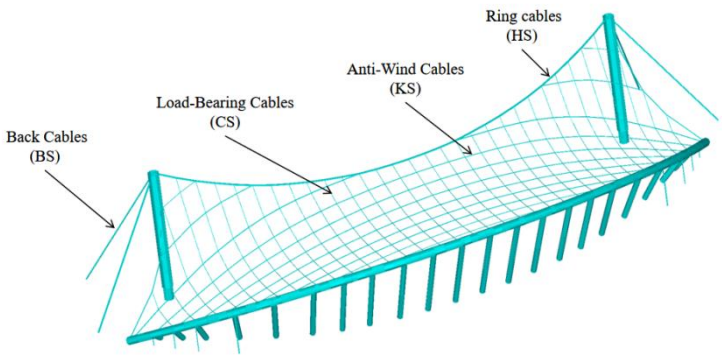

Fig. 15 Finite element model

5.2.FEM verification

5.2.1.Comparison of cable forces

The three types of load cases used in the experiment were successfully simulated, with both the loading method and loading points consistent with the experimental setup. Due to the large volume of data, Fig. 16 presents the comparison of cable forces between the experimental and finite element results for each cable under Load Case I. The measured displacements closely match the numerically calculated values, and the overall trends are in good agreement.

Fig. 17 shows the comparison of cable forces at each measurement point under Load Case I. The results indicate that the cable forces under different loading conditions exhibit similar trends in both the test and simulation, with only minor discrepancies. However, across Load Cases I, II, and III, the largest average deviation in cable force occurs at measurement point XS1, with average errors of 10.6%, 11.1%, and 10.5%, respectively. A detailed comparison of the internal cable forces at XS1 under the three loading conditions is provided in Table 6.

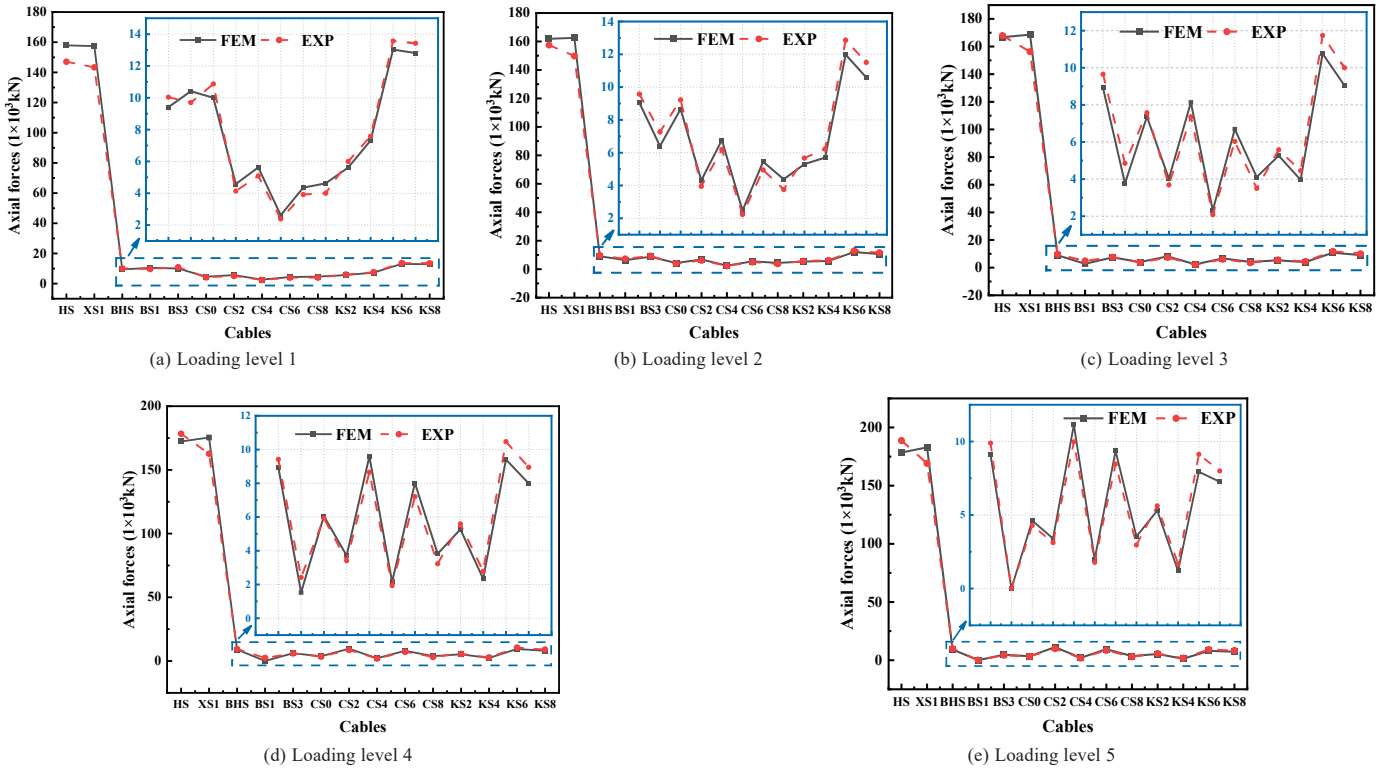

(a) Loading level 1 (b) Loading level 2 (c) Loading level 3

(d) Loading level 4 (e) Loading level 5

Fig. 16 Comparison of cable force

Table 6
Comparison of cable forces at measuring point XS 1

Loading cases	Loading levels	Cable force (kN) FEM	Cable force (kN) EXP	Deviation(%)
I	1	157.65	143.34	9.98
	2	165.37	149.80	10.40
	3	172.89	156.26	10.65
	4	180.42	162.71	10.88
	5	187.95	169.17	11.10
II	1	166.42	150.12	10.86
	2	173.96	155.73	11.71
	3	181.49	166.44	9.04
	4	189.03	169.55	11.49
	5	196.57	174.86	12.42
III	1	137.30	124.44	10.33
	2	130.11	118.56	9.74
	3	124.51	113.68	9.53
	4	119.22	106.81	11.62
	5	113.49	101.92	11.35

5.2.2. Comparison of displacement

Due to the large volume of data, Fig. 17 displays only the displacement comparison charts between the experimental and finite element results for each measurement point under Load Case I. The measured displacements exhibit good agreement with the simulation results, and the overall trend is consistent. However, under Load Cases I, II, and III, the largest average vertical displacement error occurs at measurement point S3, with deviations of 10.79%, 11.68%, and 11.29%, respectively. Table 6 presents a comparison of the internal forces of cable S3 across the three loading cases.

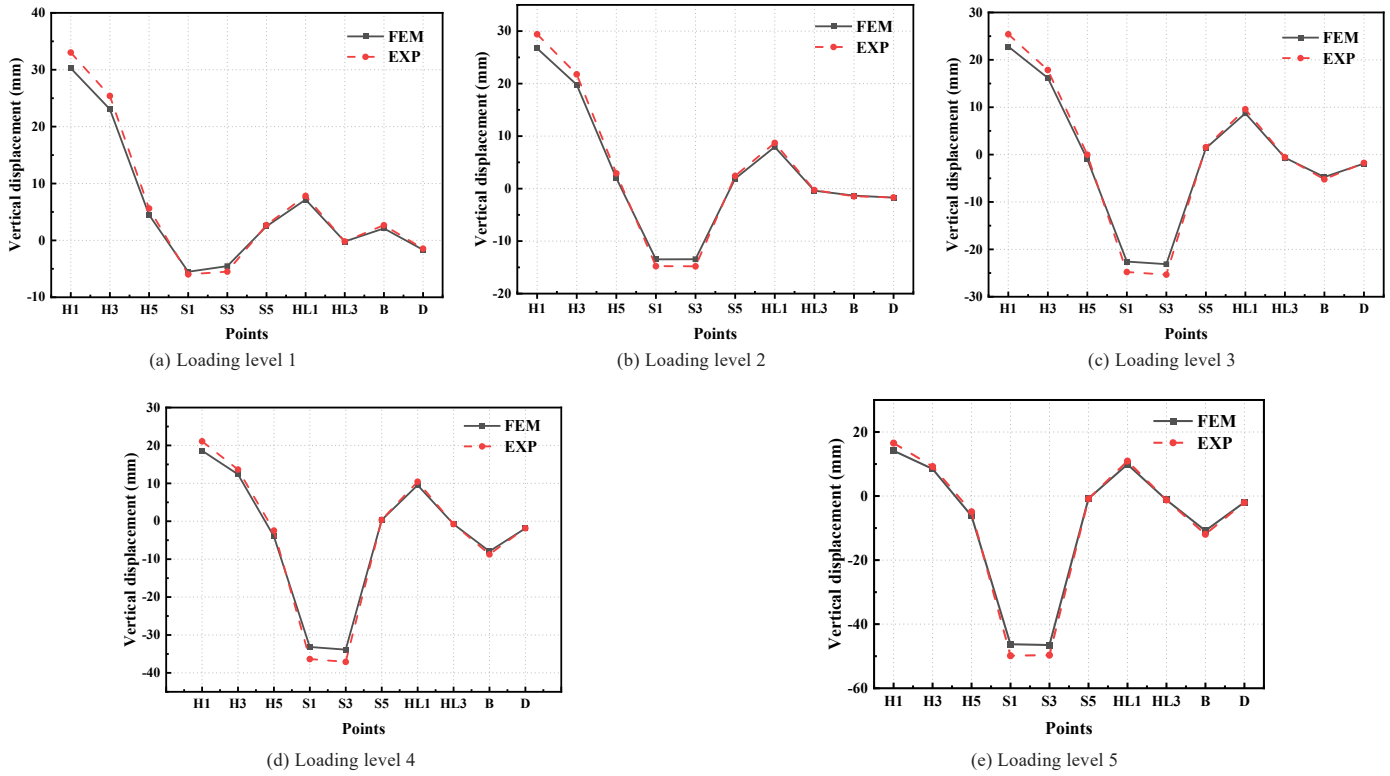

(a) Loading level 1 (b) Loading level 2 (c) Loading level 3

(d) Loading level 4 (e) Loading level 5

Fig. 17 displacement comparison chart

Table 7
Displacement comparison of measuring point S3

Loading cases	Loading levels	displacement (mm) EXP	displacement (mm) FEM	Deviation (%)
	1	-4.44	-4.93	11.04%
	2	-13.26	-14.8	11.61%
I	3	-23.04	-25.35	10.03%
	4	-33.88	-37.11	9.52%
	5	-44.45	-49.68	11.77%
	1	-12.89	-11.3	-12.32%
	2	-33.35	-30.75	-10.48%
II	3	-61.40	-54.8	-10.75%
	4	-93.35	-82.5	-11.62%
	5	-128.83	-111.8	-13.22%
	1	31.32	34.91	11.46%
	2	62.29	69.07	10.00%
III	3	95.38	105.94	11.05%
	4	125.25	141.08	12.64%
	5	159.49	177.54	11.32%

6. Conclusions

In this study, the roof structure of the Xiatian Cultural Park Stadium was selected as the research subject. A static load test was conducted on a 1:10 scaled physical model to investigate the performance of a novel single-layer saddle-shaped cable network system. The structural behavior under various loading conditions was analyzed through both experimental testing and finite element simulation. The main conclusions are as follows:

(1) In the static loading tests of flexible cable-net structures, the electro-servo loading control system effectively regulates both the load application rate and load ratios. This ensures that the test results accurately capture the response characteristics of the prototype structure under static loading, thereby meeting the required accuracy standards. Moreover, this approach provides valuable reference data for subsequent model tests of similar structural systems.

(2) During the progressive application of static loads, the forces in each cable group and the nodal displacements exhibit linear variations corresponding to the load increments. The finite element analysis results demonstrate a high degree of correlation with the experimental data in terms of overall trends, with discrepancies maintained within acceptable limits. This strong agreement validates the accuracy of the numerical simulation approach and confirms the reliability of the experimental procedures, thereby providing a robust reference for structural engineering applications.

(3) The reduction in forces observed in some load-bearing cables is attributed to the arrangement of the load attachment points. Due to spatial constraints imposed by the loading equipment beneath the cable net, the uniformly distributed load attachment points were limited to 22. This limitation caused localized high tension within the cable net and corresponding reductions in tension in adjacent areas, resulting in force loss in certain load-bearing cables. Therefore, future experiments of this nature should focus on further optimizing the layout of load attachment points to improve their distribution and rationality.

Acknowledgments

This research was funded by Hebei Natural Science Foundation, grant

number E2024508238 and Hebei Key Laboratory of Civil Engineering Catastrophe Control and Disaster Emergency Response, grant number HBHK2024-1.

References

[1] Vaezzadeh A, Ahmadizadeh M, Dolatshahi KM. Three-dimensional nonlinear dynamic analysis of slack cable structures using node Relaxation method[J]. Structures, 2021, 29: 586-599.
[2] Cinquini C, Contro R. Prestressing design method for cable net structures[J]. Engineering Structures, 1985, 7: 183-189.
[3] Yan P F, Liu C L, Liu B D, et al. Static Load Test of Cable Net Structure of Xi'an International Football Center with Scaled Model[J]. Progress in Steel Building Structures, 2024, 26(10), 74-87.
[4] Zhang D, Liu TQ, Li S, et al. Three-dimensional laser scanning for large-scale as-built surveying of 2022 Beijing Winter Olympic Speed Skating Stadium: A case study[J]. Journal of Building Engineering, 2022, 59: 105075.
[5] Schek H-J. The force density method for form finding and computation of general networks[J]. Comput Methods Applied Mechanics and Engineering, 1974, 3: 115-134.
[6] Li X, Liu C, Xue S, Li X, Zhang C, Huang L, et al. The modified force density method for form-finding of cable net structure[J]. Thin-Walled Structures, 2024, 195: 111363.
[7] Li X, Xue S, Liu Y. A novel form finding method for minimum surface of cable net[J]. Journal of Building Engineering, 2022, 48: 103939.
[8] Lv H, Jiaming Z, Zhongyi Z, et al. Study on prestress distribution and structural performance of heptagonal six-five-strut alternated cable dome with inner hole[J]. Structures, 2024, 65: 106724.
[9] Huiyun W. Construction Methods for the Calgary Saddleback Stadium - Indoor Stadium for the 1988 Winter Olympics[J]. Building Construction, 1984, 05: 75-76.
[10] Ma S, Chen M H, Dong Y C, et al. Statics and dynamics of pulley-driven tensegrity structures with sliding cable modeling[J]. Applied Mathematical Modelling, 2024, 130, 378-400.
[11] Shichang Z, Xiaoming X, Feng G. Structural design of the steel roof of the swimming pool of Suzhou Olympic Sports Center[J]. Building Structure, 2019, 49, (23).
[12] Shudong G, Jingxun Z, Cunzhi Z, et al. Research on the overall installation program of the large-span saddle-shaped cable network structure of the National Speed Skating Pavilion[J]. Building Technology, 2020, 50(03): 333-336.
[13] Ningyuan Z, Bin L, Lei Z, et al. Research on the forming technology of a novel type structure of double-layer orthogonal cable net with a large opening[J]. Structures, 2024, 63: 106371.
[14] Mingliang Z, Jin W, Jiaming G. Physics-informed radial basis networks for force finding of cable domes[J]. Thin-Walled Structures, 2025, 206: 112675.
[15] Yaqiong T, Qing Lv, Tuanjie L, et al. Self-equilibrium, stability, and accuracy degradation of imperfect prismatic tensegrities with additional cable nets[J]. Engineering Structures, 2023, 284, 115981.
[16] F Benedettini, Rega G. Planar non-linear oscillations of elastic cables under superharmonic resonance conditions[J]. Journal of Sound and Vibration, 1989, 132(3): 353-366.
[17] Lu Yang, Shi Ga ng, Yin Hao, et al. Full-scale experimental study on the influence of damages on the static behavior of the single-layer cable net structure[J]. Structures, 2015, 3153-162.
[18] Fabio Rizzo, Caracoglia Luca. Examination of artificial neural networks to predict windinduced displacements of cable net roofs[J]. Engineering Structures, 2021, 245112956.
[19] Sun F, Y-Q W, Y-J S, et al. The inflection performance analysis of the complex single layer cable net under horizontal load[J]. Oxford: Elsevier Science Ltd, 2005: 395-399.
[20] Guojun S, Shuo X, Jinzhi W. Study on mechanical properties of truss cable structure under low cyclic loading[J]. Journal of Building Engineering, 2022 , 58: 105051
[21] Guojun S, Shuo X, Jinzhi W, et al. Shaking table test and simulation on seismic performance of aluminum alloy reticulated shell structures under elastic and elastic-plastic stage[J]. Journal of Building Engineering, 2024, 110878.
[22] Load Code for Building Structures[S], Beijing, China Construction Industry Press,2012.
[23] Amin V, Kiarash M D. Progressive collapse resistance of cable net structures[J]. Journal of Constructional Steel Research, 2022, 195:107347.

Advanced Steel Construction – Vol. 22 No. 1 (2026) 48–63
DOI:10.18057/IJASC.2026.22.1.5

ANALYTICAL AND NUMERICAL INVESTIGATION OF ULTRA-HIGH-PERFORMANCE CIRCULAR CONCRETE-FILLED DOUBLE-TUBES UNDER FIRE CONDITIONS

Mohamed Ghannam [1], Sameh Lotfy [2], A.H.A. Abdelrahman [1, *], Mohammad AlHamaydeh [3] and Md Kamrul Hassan [4]

[1] *Structural Engineering Department, Faculty of Engineering, Mansoura University, Egypt*
[2] *Civil Engineering Department, MISR Higher Institute for Engineering and Technology, Mansoura, Egypt*
[3] *Department of Civil Engineering, American University of Sharjah, PO Box 26666, Sharjah, United Arab Emirates,*
[4] *Lecturer in Fire Safety Engineering, School of Engineering, Design and Built Environment, Western Sydney University, Penrith, NSW 2751, Australia*
** (Corresponding author: E-mail: a_hussain@mans.edu.eg)*

ABSTRACT

This study presents an analytical and numerical investigation of ultra-high-performance concrete-filled double-skin tubular (UHPC-CFDST) columns with circular cross-sections under fire conditions. An automated algorithm was employed to develop and verify a finite element (FE) model capable of accurately simulating CFDST columns incorporating different concrete types (normal concrete, ultra-high-performance concrete (UHPC), and lightweight concrete) in both core and ring regions. The validated model was used to examine the influence of key parameters, offering deeper insight into the behavior of such columns under fire. Three temperature-dependent material models were developed to represent UHPC, lightweight concrete, and high-strength steel at elevated temperatures. Additionally, a finite difference-based thermal model was proposed to simulate the temperature distribution across the column cross-section and to predict fire resistance (FR) time. To the best of the authors' knowledge, existing fire design standards do not provide specific models for CFDST columns under fire, and available research in this area is limited. This study addresses this gap by evaluating the applicability of Eurocode 4 (EC4) and proposing a simplified modification that improves the prediction accuracy of fire resistance for UHPC-CFDST columns.

ARTICLE HISTORY

Received: 18 July 2025
Revised: 29 September 2025
Accepted: 5 October 2025

KEYWORDS

Concrete-filled double- tubes;
Ultra-high-performance concrete;
Analytical model;
Numerical model;
Fire standards;
Axial load capacity;
Fire resistance

1. Introduction

Concrete-filled double-skin tubular (CFDST) columns were first introduced in 1989 [1], and since then, they have gained significant attention from researchers and increasing popularity in the construction industry due to their advantages over conventional concrete-filled steel tube (CFST) columns. These advantages include higher strength, lighter structural weight with improved ductility, better fire performance, and enhanced cyclic behavior [1-8].

A CFDST column consists of two concentric steel tubes, with the annular gap between them filled with concrete, while the core remains hollow. When the hollow core is also filled with concrete, the system is referred to as a concrete-filled double tube (CFDT) column. Various parameters influencing the behavior of CFDST and CFDT columns have been studied, including the nominal steel ratio (α_n), the hollow ratio (χ) defined for CFDST columns as $\chi = D_i/(D_O\text{-}2t_O)$, the concrete compressive strength (f_c'), the yield strength of the outer and inner steel tubes ($f_{syo,}$ and f_{syi} respectively), and the diameter-to-thickness ratio (D/t) for both tubes [3, 9-11].

The interaction between steel tubes and the concrete ring in CFDST columns has been investigated by Tao *et al.* [3] and Huang *et al.* [11]. At the initial loading stage, no interaction occurs between the outer tube and the concrete ring due to the difference in Poisson's ratio between steel and concrete. However, as axial loading increases, the resulting lateral strain leads to contact and interaction between the two materials. A different behavior is observed between the inner tube and the concrete ring: interaction occurs early in the loading process due to the higher lateral strain of the steel tube compared to the concrete. As the concrete enters the elastic-plastic stage, this interaction gradually diminishes.

When the peak load is reached, contact is formed again between concrete ring and inner tube as a result of larger lateral strain of concrete compared to steel due to cracks formation of in concrete ring [3, 11]. Huang *et al.* [11] found numerically that load axial capacity decreased by 15% and 26 % for square and circular columns, respectively as the hollow ratio increased from zero to 0.75. It was found that the effect of hollow ratio on concrete stress is more significant in circular columns compared to square ones. However, column ductility is not affected [3, 11].

From the FE model analysis that was proposed by Huang *et al.* [11] it was found that, the axial Load capacity of stub CFDST columns increases by about 71% due to an increase in concrete strength from 30 MPa to 90 MPa. When the steel yield strength of the outer tube increased by approximately 79 %, the axial load capacity increased by about 30%. When the nominal steel ratio increased by 3 times, the axial capacity increased by 62 and 72 % for square and circular columns, respectively. From the research done previously [3, 10, 11], it was found that, inner tube yield strength, and width-to-thickness ratio have no significant effect on the axial capacity of stub CFDST columns because of the small steel area on the inner tube compared to the outer tube, the main role of inner tube is confining the concrete ring. The inner tube width-to-thickness ratio affects the failure mode of the inner tube.

CFDT columns have many advantages that overcome the conventional CFST and CFDST columns. Compared to CFDST columns, filling the central void with concrete (CFDT columns) improves load capacity and reduces inner tube buckling [12]. A key advantage of CFDT columns that overcome both CFST and CFDT columns is their high fire resistance [2, 13, 14], as the outer concret ring protect the inner steel tube from temperature development during fire, Besides, CFDT columns provide more load capacity compred to CFST and CFDST columns as a result of the pressence of inner concrete core which is not available in CFDST columns and inner steel tube which is not availale in CFST columns.

Lu *et al.* [15] provide some design guidelines for CFDST columns in fire. Increasing yield strength and/or thickness of the inner tube and decreasing the yield strength and/or thickness of the outer tube help in improving the fire resistance. A similar finding was obtained by Romero *et al.* [2]; drain holes in the outer tube are beneficial as they help to release the water vapor pressure. The minimum thickness of the concrete ring is 50 mm, using steel fiber in concrete help in increasing the fire resistance. Xiong [16] could not decide which has better fire performance CFST columns or CFDST columns

Some researchers provide design models for CFDST columns in fire [17-21]. Yao *et al.* [22] presented a design model based on the Rankine approach for columns subjected to uniform temperature, while Yao *et al.* [23] used the Rankine approach for non-uniform heating. [15] present fire design tables. Some researchers tried to improve the fire performance of CFDST columns. Jia-qi *et al.* [13] found that using stainless steel in the outer tube increases the fire resistance compared with using carbon steel. Shekastehband *et al.* [24] used found that using stiffeners with the inner tube and outer tube can increase the fire resistance of the CFDST column significantly as the stiffener in the outer tube absorbs more heat, allowing the outer tube to withstand applied load for a longer time beside stiffeners increase the contact between steel tube and concrete core and reduce buckling of steel tubes this was also concluded at ambient temperature [9]. Zhu *et al.* [19], Zhu *et al.* [20]and Zhu *et al.* [21]

presented a design model for circular CFDT columns under axial and eccentric load based on Eurocode 4 [25] design procedures.

Using HSC and UHPC is considered a modern method to improve the fire performance of CFDST and CFDT columns. Ultra-high performance concrete (UHPC) has been increasingly used nowadays due to its advantages, such as high strength, high fracture capacity, and high durability. Using ultra-high performance concrete (UHPC) in CFDST and CFDT columns has a dual benefit; from one side, UHPC will lead to increased CFDT column capacity; from another side, steel tubes will help in overcoming one of the main disadvantages of UHPC which is brittleness by providing more ductility to the column. Also steel tube will help in increasing column capacity by the confinement that will be provided to the concrete [26].

Many researches have been conducted to investigate the fire behaviour of UHPC as it has been considered as a relatively new construction material [27-34]. Banerji and Kodur [31] and Xiong and Liew [35] found that compressive strength and elastic modulus of UHPC are reduced in a higher rate compared to reduction occurred in normal strength concrete (NSC) at elevated temperatures. However, Banerji and Kodur [31] found that the presence of steel fibers helps in reducing the degradation in tensile strength and ductility in UHPC compared to conventional concrete. Many researchers find the addition of polypropylene fibers to UHPC reduces significantly concrete spalling [34, 36, 37], which is explained as a result of the melting of polypropylene at high temperatures which maintains internal vapor pressure and prevents explosive spalling.

Xiong and Liew [38] found that using NSC and UHPC give similar fire performance for CFST columns, however using Ultra High Strength Concrete (UHSC) gives higher fire resistance compared with using NSC and HSC. A similar finding was obtained by Xiong and Liew [39]. Xiong and Liew [39] found that using buckling curve “d” in Eurocode simplified model and M-N interaction diagram give a good prediction for the fire resistance of CFST column. However, the M-N interaction diagram gives better predictions in cases of high load lever (especially > 0.65). Wang *et al.* [40] found that increasing the steel fiber and course aggregates can significantly increase the fire resistance of the CFST column filled with UHPC. Wang *et al.* [40] proposed a design model for CFST column filled with UHPC.

Romero *et al.* [2] found that using UHPC in the core of CFDT columns may give lower fire resistance compared to NSC. This is because the load level was kept constant and, so the load value applied on the UHPC column was bigger than the NSC columns. In slender columns, the concrete core do not have a significant effect on column capacities. However, its main role is participating in the column stiffness and preventing inner tube buckling and reducing the temperature in the inner tube, also, in the same study, it was found that Eurocode 4 gives unsafe prediction for the fire resistance of CFDT columns.

Camargo *et al.* [41] and Lopes and Rodrigues [14] presented studies on restrained CFDT columns with HPC for circular and square columns, respectively. The results show that HSC do not have a significant effect in increasing the critical time but can increase the failure time for restrained square columns. Besides, the study shows that the available design codes are insufficient for designing these types of columns.

Although extensive research has been conducted on the fire behavior of concrete-filled steel tube (CFST) columns, studies on the fire performance of CFDST and CFDT columns filled with high-strength concrete (HSC) or ultra-high-performance concrete (UHPC) remain limited [2, 14, 41]. To the best of the authors’ knowledge, current fire design standards do not provide a design model for CFDST columns incorporating UHPC. This study aims to address this research gap through analytical and numerical investigations of ultra-high-performance concrete-filled double-skin tubular (CFDST) columns under fire.

Three material models were developed using existing experimental data for UHPC, lightweight concrete (LWC), and high-strength steel at elevated temperatures. An automated algorithm was employed to develop a verified finite element (FE) model that accurately simulates circular CFDST columns with different concrete types—normal concrete, LWC, and UHPC—in the core and ring regions. The validated FE model was then used to perform a parametric study to better understand the behavior of these columns under fire conditions.

In addition, a finite difference (FD) model was developed in MATLAB to simulate the temperature distribution across the cross-section and predict fire resistance based on Eurocode 4, Part 1.2. A simplified analytical model based on EC4 Part 1.2 is also proposed to estimate the axial load capacity and fire resistance of CFDST columns under various fire exposure scenarios.

2. Material properties at elevated temperature

This section is divided into two subsections. The first subsection compiles available experimental data on the mechanical properties of ultra-high-performance concrete (UHPC) at elevated temperatures. The second subsection reviews the thermal and mechanical properties of high-strength steel under elevated temperature conditions.

2.1. Mechanical properties of UHPC under fire

In the literature, three types of material fire tests are commonly reported: stressed, unstressed, and residual conditions. In residual conditions, specimens are heated to a target temperature, maintained until a uniform temperature is achieved throughout the section, then cooled before being loaded to failure. In unstressed conditions, specimens are similarly heated and held at a constant temperature, but are loaded to failure without cooling. Stressed conditions are similar to unstressed ones, except that a predetermined load is applied during the heating process [31]. Residual testing is simpler to conduct and is suitable for evaluating material properties in the post-fire stage, whereas unstressed testing is more appropriate for assessing properties during fire exposure, which is the focus of this paper. Accordingly, the collected data for HSC and UHPC under fire are limited to unstressed conditions, as listed in Table 1. Previous studies have shown that concrete strength does not significantly influence thermal expansion [42]. The data set in this section will be used to propose the material model for UHPC at elevated temperature in section 4.2.

Table 1
Details of recent fire test on HSC and UHPC at elevated temperature

Ref.	Specimens shape (mm)	Specimens size (mm)	Temperature limit (^{O}C)	*fc*’ (MPa)
Xiong [16] and Xiong and Liew [35]	Cylinder	100X200	800	166.6
Banerji and Kodur [31]	Cylinder	75X150	750	171 and 177
Choe *et al.* [43]	Cylinder	100X200	700	100,150 and 200
Lee *et al.* [42]	Cylinder	100X200	700	83, 134.8 and 184.5
Khaliq [44]	Cylinder	100X200	800	64 and 72
Cheng *et al.* [45]	Cylinder	100X200	800	79, 78.3, 81.4 and 85.5
Phan and Carino [46]	Cylinder	100X200	450	98.2, 81.2, and 72.3

2.2. Mechanical properties of high strength steel at elevated temperatures

Two main types of experiments are used to assess the mechanical behavior of steel coupons at elevated temperatures: steady-state tests and transient-state tests. In the transient test, a tensile load is applied while the temperature is gradually increased until failure occurs. In contrast, the steady-state test involves heating the coupons to a target temperature, maintaining it for a period to ensure uniform distribution, and then applying the tensile load until failure. Due to its relative simplicity, the steady-state method is more commonly adopted in experimental research. In this study, the most recent steady-state test data available for high-strength steel are compiled, as shown in Table 2. The data set in this section will be used to propose the material model for high strength steel at elevated temperature in section 4.2.

3. Previous experimental fire tests on CFDST Columns

This section summarizes available fire resistance tests conducted on CFST columns filled with UHPC, as well as CFDT and CFDST columns filled with either UHPC or NSC. Table 3 presents the collected data, where D_o and D_i are the outer and inner tube diameters, t_o and t_i are the corresponding wall thicknesses, f_{yo} and f_{yi} represent the yield strengths of the outer and inner tubes, and f'_{co} *and* f'_{ci} are the cylinder compressive strengths of the concrete ring and core, respectively. L denotes the column length, n is the load ratio, and FR is the fire resistance duration in minutes. This experimental database will be used in the parametric study and to validate the finite element (FE) model. The data set in table 3 shows the limitation of available test result on CFDT column under elevated temperature.

Table 2
Collected fire test on high strength steel at elevated temperature

Ref.	Temperature limit (^{O}C)	*Fy* (MPa)
Chen *et al.* [47]	940	789
Lange and Wohlfeil [48]	900	431.5, 445.6
Qiang *et al.* [49]	700	690
Qiang *et al.* [50]	700	460
Choi *et al.* [51]	900	701
Heidarpour *et al.* [52]	600	1283, 1331
Wang *et al.* [53]	900	965
Li and Song [54]	800	780

Table 3
Summary of test data of CFDST and CFST (with UHPC) members under fire

Shape	Ref.	No. of specimens	D_o/D_i (mm)	t_o/t_i (mm)	L (mm)	f'_{co}/f'_{ci} MPa	f_{yo}/f_{yi} MPa	n	FR min
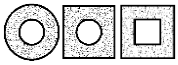	[55]	6	280-300 / 140-225	5/5	3810	38 cu	320/320	0.32-0.65	40-240
	[2]	6	200/114	3-6/8-3	3180	30/150	232-407/329-512	0.2	33-104
	[56]	12	101-127/50-76	3-4	600	38-41 fcu	597-430/762-449	Residual strength	60-90
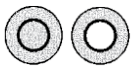	[17]	6	325/219-159	6/6	3800	46.8 fcu	295-255/285-260	0.4-0.6	68-17
	[16]	6	219-200/114-100	16-12/6.3-8	3810	172-163	432-785/468-825	0.33-0.95	15-25
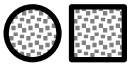	[16]	16	200-273	16-10	3810	161-181	418-785	0.34-0.88	18-192

4. Finite element modelling

4.1. General

A Finite element (FE) program, ABAQUS [57] was used to develop the FE model for CFDST columns. The inner and the outer steel tubes were modelled using an S4R shell element with 4 nodes having six degrees of freedom for each node. The inner and outer concrete core was modelled using 8 node C3D8R solid element with 3 degrees of freedom for each node.

A sequential-coupled thermal stress analysis was performed to simulate the fire behavior of CFDST columns. First, a thermal analysis was performed to simulate the temperature development within the column cross-section during the fire, and then the temperature development through the cross-section during the fire was imported into the stress analysis through a predefined field in the stress analysis. The meshing size in the thermal and the stress analysis was identical. Thermal analysis was performed as previously established by the authors [58]. The Finite element (FE) model is presented in Fig. 1.

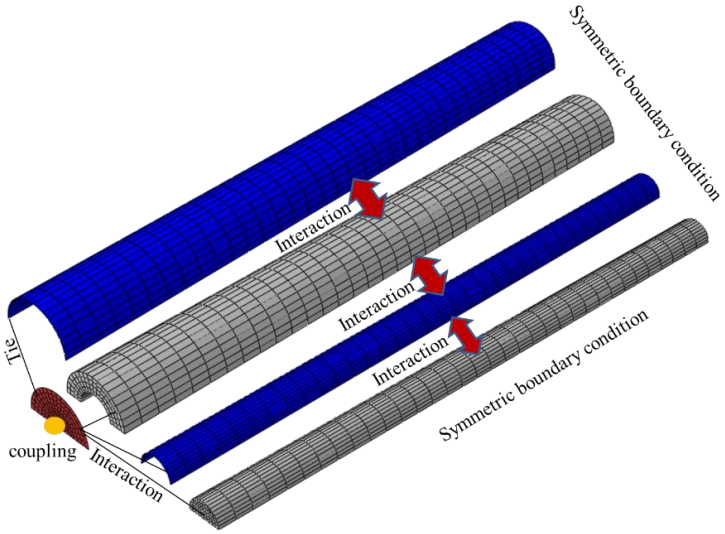

Fig. 1 Finite element model

4.2. Material properties

Eurocode 3 [59] was adopted for modeling the mechanical behavior of both the inner and outer steel tubes. For concrete material modeling, the Concrete Damage Plasticity (CDP) model was employed, with plasticity parameters and fracture energy defined according to the recommendations by Liu *et al.* [60]. The behavior of normal-strength concrete (NSC) in both the outer ring and inner core was modeled using Eurocode 2 [61] , with the tensile stress behavior defined by the CEB-FIB model [62].

For ultra-high-performance concrete (UHPC), a new temperature-dependent strength reduction model was developed based on experimental data reported in previous studies [25, 42, 57, 63]. The adopted stress–strain relationship followed the model proposed by Lie and Irwin [64]. Additionally, a new thermal expansion model for UHPC was proposed, derived from experimental results reported by Lee *et al.* [42]. The proposed strength reduction factor, thermal expansion, and modulus of elasticity reduction factor are illustrated in Fig. 2 (a, b, and c), and are defined by Eqs. (1–3).

The reduction factor for compressive strength is shown in the next equation

$$\begin{cases} 1.0 & T = 20 \\ -3.21x10^{-3}T + 1.0642 & 20 < T \le 100 \\ 1.1679x10^{-3}T + 0.6263 & 100 < T \le 200 \\ 4.157x10^{-9}\,T^3 - 6.584x10^{-6}\,T^2 + 2.075x10^{-3}\,T + 0.675 & 200 < T < 1000 \end{cases} \quad (1)$$

Thermal expansion is shown in the next equation

$$\begin{cases} \left[\frac{1}{342.233-0.5044T+45423.8860/T} - 0.0004\right] / (T-20) & 20 < T \le 625 \\ 0.0097/(T-20) & T > 625 \end{cases} \quad (2)$$

The reduction factor for the modulus of elasticity is shown in the next equation

$$\begin{cases} 1 & T = 20 \\ 1.267x10^{-6}\,T^2 - 2.279x10^{-3}\,T + 1.04 & 20 < T < 1000 \end{cases} \quad (3)$$

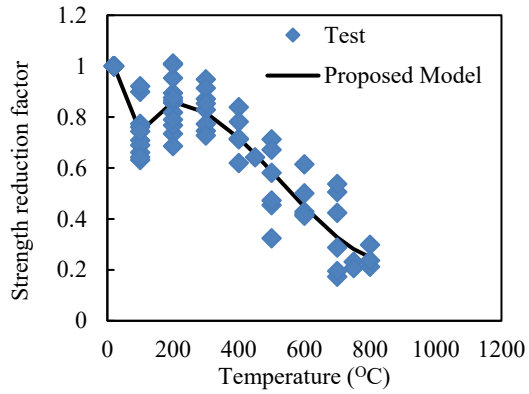

(a) Strength reduction factor

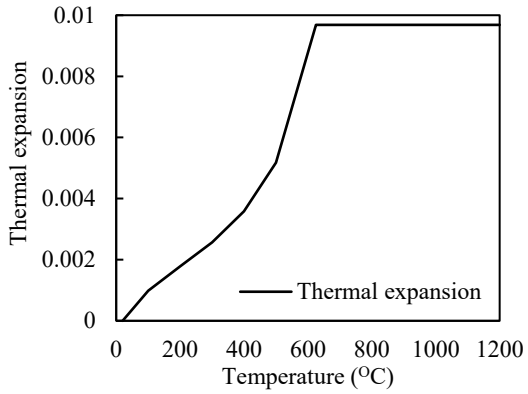

(b) Thermal expansion

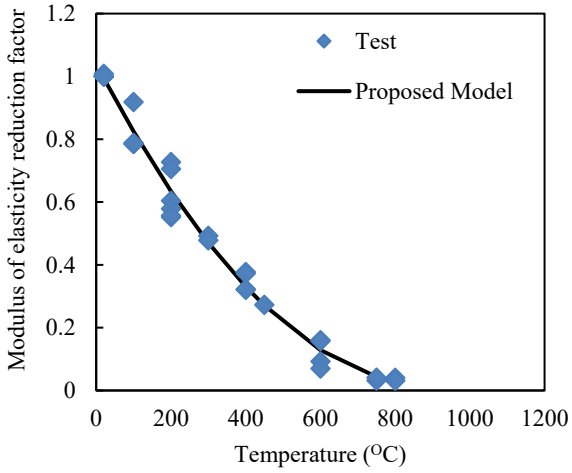

(c) Modulus of elasticity reduction factor

Fig. 2 proposed model for UHPC

A temperature-dependent material model was also developed for lightweight concrete (LWC), based on previously published experimental data [58, 59, 61, 65] and the compressive stress–strain relationship specified in [66].

The proposed model is illustrated in Fig. 3, and its mathematical formulation is defined by Eqs. (4–8).

The reduction factor for compressive strength is shown in the next equation

$$\begin{cases} 1.0 & T = 20 \\ \dfrac{0.5672}{1.0 + 0.0197 * \mathrm{EXP}(0.0089 * \mathrm{T})} + 0.434 & 20 < T \leq 800 \end{cases} \quad (4)$$

The peak strain value is shown in the next equation

$$\begin{cases} 0.0025 & T = 20 \\ 0.0025 \times (0.9915 + 2.653 \times 10^{-5} \times T^2 - 1.598 \times 10^{-6} \times T^{2.5} + 2.7389 \times 10^{-8} \times T^3) & 20 < T \leq 800 \end{cases} \quad (5)$$

The reduction factor for the modulus of elasticity is shown in the next equation

$$\begin{cases} 1.0 & T = 20 \\ 0.6518 + 0.0014 \times T - 0.123T^{0.5} + 0.2907 \ln(T) & 20 < T \leq 800 \end{cases} \quad (6)$$

The reduction factor for tensile strength is shown in the next equation

$$\begin{cases} 1.0 & T = 20 \\ 0.8897 - 0.0019T - 2.0174 \times 10^{-10} \times T^3 + 0.0333T^{0.5} & 20 < T \leq 800 \end{cases} \quad (7)$$

Thermal expansion is shown in the next equation

$$\begin{cases} 9.1 \times 10^{-6} & T = 20 \\ 9.2676 \times 10^{-6} - \dfrac{6.1894 \times 10^{-4}}{T} + \dfrac{0.0896}{T^2} - \dfrac{2.06981927}{T^3} & 20 < T \leq 800 \end{cases} \quad (8)$$

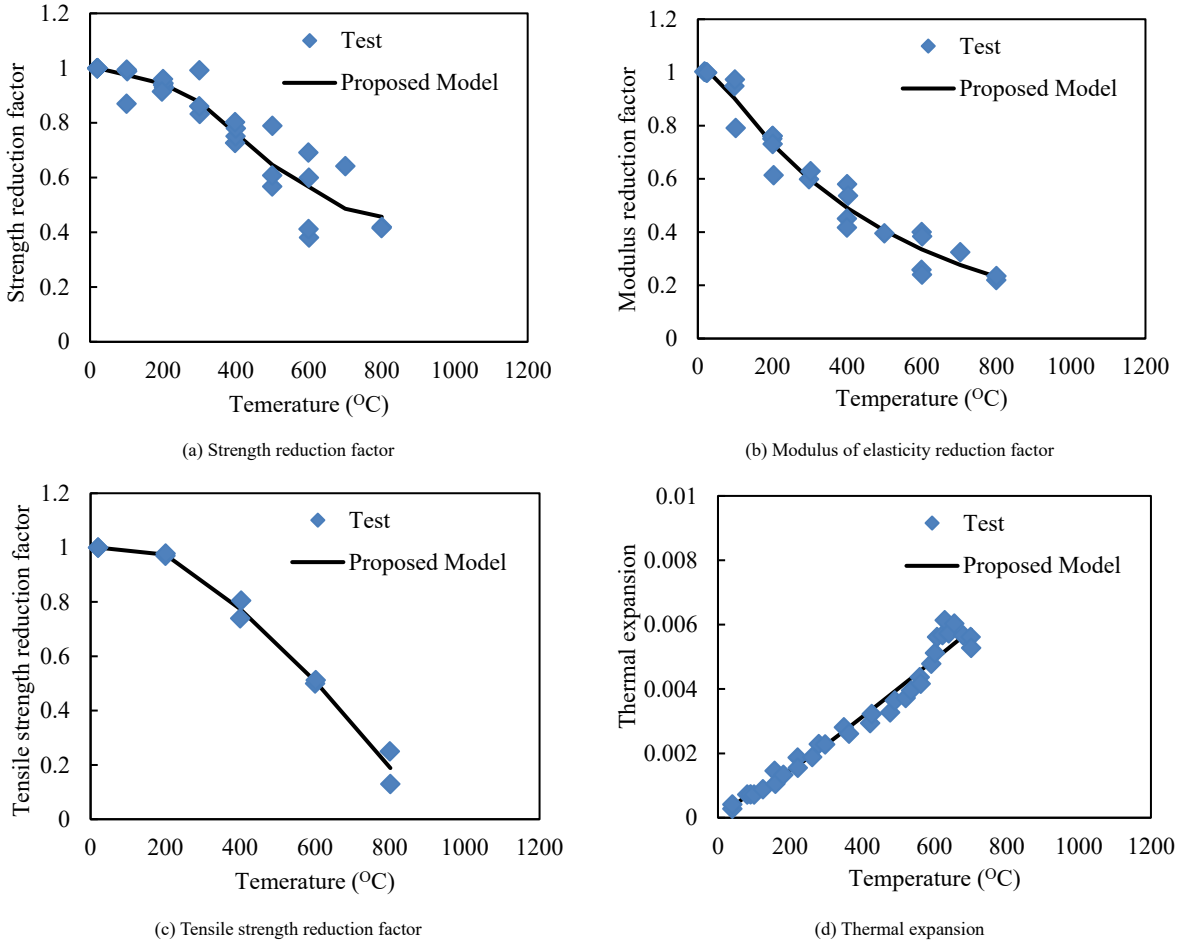

(a) Strength reduction factor

(b) Modulus of elasticity reduction factor

(c) Tensile strength reduction factor

(d) Thermal expansion

Fig. 3 Proposed model for LWC

Tables 4 and 5 present a comparison between the results obtained from the proposed model and those from existing standards, evaluated against experimental data for UHPC and LWC, respectively. The standards included in the comparison are: Eurocode 2 (EC2) [61], Eurocode 4 (EC4) [25], he Koudr model for ultra-high-performance concrete [31], ACI [67], AISC [68], Australian standards [69] and ASCE [70].

According to EC2, concrete is categorized into four classes: NSC, Class 1, Class 2, and Class 3. NSC is further divided based on the type of coarse aggregate, either carbonate (calcareous) or siliceous, which are referred to in Table 4 as Euro_Car and Euro_Sili, respectively. Both Euro_Car and Euro_Sili correspond to concrete with a maximum cylinder compressive strength of 50 MPa. High-strength concrete in EC2 is divided into three categories: Class 1 (up to 60 MPa), Class 2 (up to 80 MPa), and Class 3 (up to 90 MPa), which are referred to in Table 4 as Euro_Class1, Euro_Class2, and Euro_Class3, respectively.

The results indicate that the proposed model provides the most accurate predictions when compared to the existing standards and codes.

Table 4
Evaluation for the proposed mode of UHPC

	Test/ Euro_car	Test/ Euro_sili	Test/ Euro _class1	Test/ Euro _class2	Test/ Euro _class3	Test/ Kodur [31]	Test/ AISC	Test/ AS/NZ 2327	Test/ ASCE	Test/ Proposed model
Compressive strength										
Mean	0.853	0.979	1.000	1.071	1.357	1.051	0.984	0.869	0.841	1.000
COV	0.197	0.264	0.248	0.225	0.319	0.215	0.233	0.222	0.256	0.182
Modulus of elasticity										
Mean	1.375	1.302	-	-	-	0.993	0.843	0.761	1.302	1.004
COV	0.264	0.282	-	-	-	0.161	0.178	0.223	0.282	0.164

Table 5
Evaluation of the proposed model of LWC

	Test/EC4	Test/AISC	Test/AS/NZ2327	Test/ASCE	Test/ACI216R-89	Test/Proposed model
Compressive strength						
Mean	1.100	1.100	1.172	1.100	1.134	1.016
COV	0.172	0.158	0.225	0.254	0.183	0.128
Modulus of elasticity						
Mean	-	0.819	0.944	-	0.971	1.014
COV	-	0.346	0.370	-	0.158	0.127
Thermal expansion						
Mean	-	-	-	-	0.983	1.010
COV	-	-	-	-	0.118	0.101

A third model was proposed to describe the material behavior of high-strength steel (HSS) at elevated temperatures. This model was developed using previous test results ([47-54]) and aims to provide reduction factors for strength and elastic modulus, following the stress–strain formulation introduced by Wang *et al.* [53]. Verification of the proposed model against experimental data is presented in Fig. 4, while comparisons with existing codes and standards are provided in Table 6. The proposed model for lightweight concrete (LWC) is detailed in Eqs. (9-10).

The reduction factor for yielding proof strength is shown in the next equation

$$\begin{cases} 1.0 & 20 \le T \le 200 \\ 0.030 + 0.9522 \times EXP(-9.4163 \times 10^{-13} \times T^{4.2949}) & 200 < T \le 1000 \end{cases} \quad (9)$$

$$\begin{cases} 1.0 & 20 \le T \le 200 \\ \dfrac{1.0126 + 3.3205 \times 10^{-13} \times T}{1.0 - 2.8338 \times 10^{-4} \times T^{4.4408}} & 200 < T \le 1000 \end{cases} \quad (10)$$

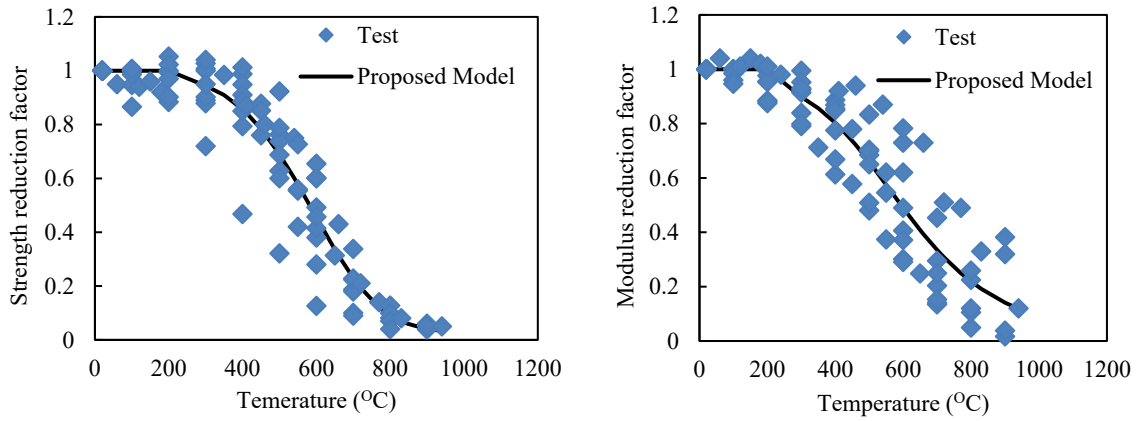

(a) Strength reduction factor (b) Modulus of elasticity reduction factor

Fig. 4 proposed model for HSS

Table 6
Evaluation of the proposed model for HSS

	Test/EC3	Test/ASCE	Test/AISC	Test/AS/NZ	Test/Proposed model
Yield strength					
Mean	0.920	1.398	0.906	1.197	1.003
COV	0.221	0.325	0.222	0.378	0.223
Modulus of elasticity					
Mean	1.485	1.698	1.428	2.191	1.012
COV	0.834	0.684	0.758	1.048	0.384

Based on the previous figures and tables, the proposed material models for UHPC, LWC, and high-strength steel demonstrate better agreement with test results compared to existing codes and models.

4.3. Interaction between steel tubes and concrete

Contact interaction was defined between the inner surface of the inner steel tube and the outer surface of the inner concrete core and between the outer surface of the inner steel tube and inner surface of the outer concrete core and between the inner surface of the outer steel tube and the outer surface of the outer concrete core. The contact interaction has a tangential behavior with a friction coefficient of 0.25 and a hard contact as normal behavior, which allow separation after contact.

4.4. Initial imperfections

Initial imperfection was introduced to the stress analysis through a separate pre-buckling analysis and using the 1st mode of buckling as an initial condition stress analysis with a maximum amplitude of L/1000 [71, 72].

4.5. Verification of finite element model

Limited experimental studies have investigated the fire behavior of concrete-filled double-skin tubular (CFDST) columns incorporating ultra-high-performance concrete (UHPC) or ultra-high-strength concrete (UHSC). In this study, finite element (FE) model verification was conducted using test results reported by Romero *et al.* [2]. Their experimental program involved testing twelve circular CFDST columns: six specimens under ambient conditions and six under elevated temperatures. The fire tests followed the ISO 834 standard fire curve [73]. All specimens were hinged, with a total column length of 3315 mm and an effective heated length of 3036 mm.

The specimen dimensions and material properties used in the experimental program are summarized in Table 7. The table also presents the fire resistance (FR) times obtained experimentally (FR_test) and those predicted by the proposed FE model (FR_FE). The average ratio of test-to-predicted fire resistance is 0.97, indicating good agreement between the experimental and numerical results.

Fig. 5 compares the displacement–time response from the test with that of the FE simulation, showing close correlation. Minor discrepancies can be attributed to initial geometric imperfections observed in the test specimens and the actual furnace temperature variations, which were not explicitly reported—only that the ISO 834 curve was followed. The verified FE model and the proposed temperature-dependent material models will be employed in the subsequent parametric study.

Table 7
Specimens details [2]

Spec. Name	D_{outer}	t_{outer}	D_{inner}	t_{inner}	Fy_{outer}	fc'_{outer}	Fy_{inner}	fc'_{inner}	N-applied	FR_test	FR_FE	FR Test / FE
C200-3-30-C114-8-00	200	3	114.3	8	300	46	377	0	283	76	77.68	1.02
C200-3-30-C114-8-30	200	3	114.3	8	332	46	403	45	325	104	105.4	1.01
C200-3-30-C114-8-150	200	3	114.3	8	272	44	414	136	355	98	84.75	0.86
C200-6-30-C114-3-00	200	6	114.3	3	407	43	343	0	329	48	41.08	0.86
C200-6-30-C114-3-30	200	6	114.3	3	377	44	329	42	392	45	40.81	0.91
C200-6-30-C114-3-150	200	6	114.3	3	386	43	343	126	415	33	38.7	1.17

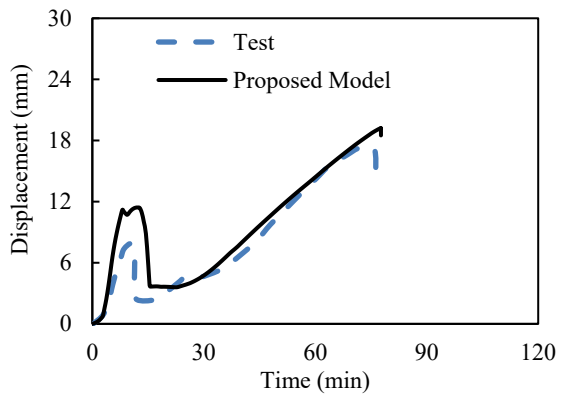

(a) C200-3-30-C114-8-00

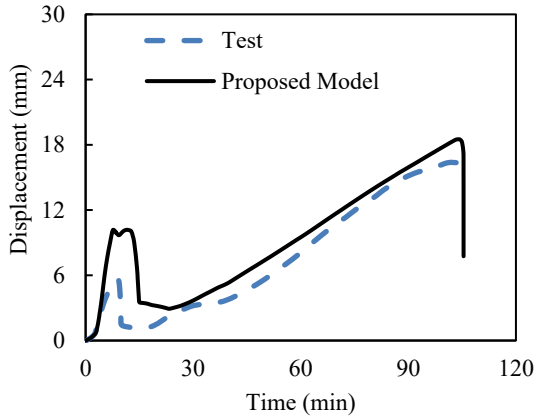

(b) C200-3-30-C114-8-30

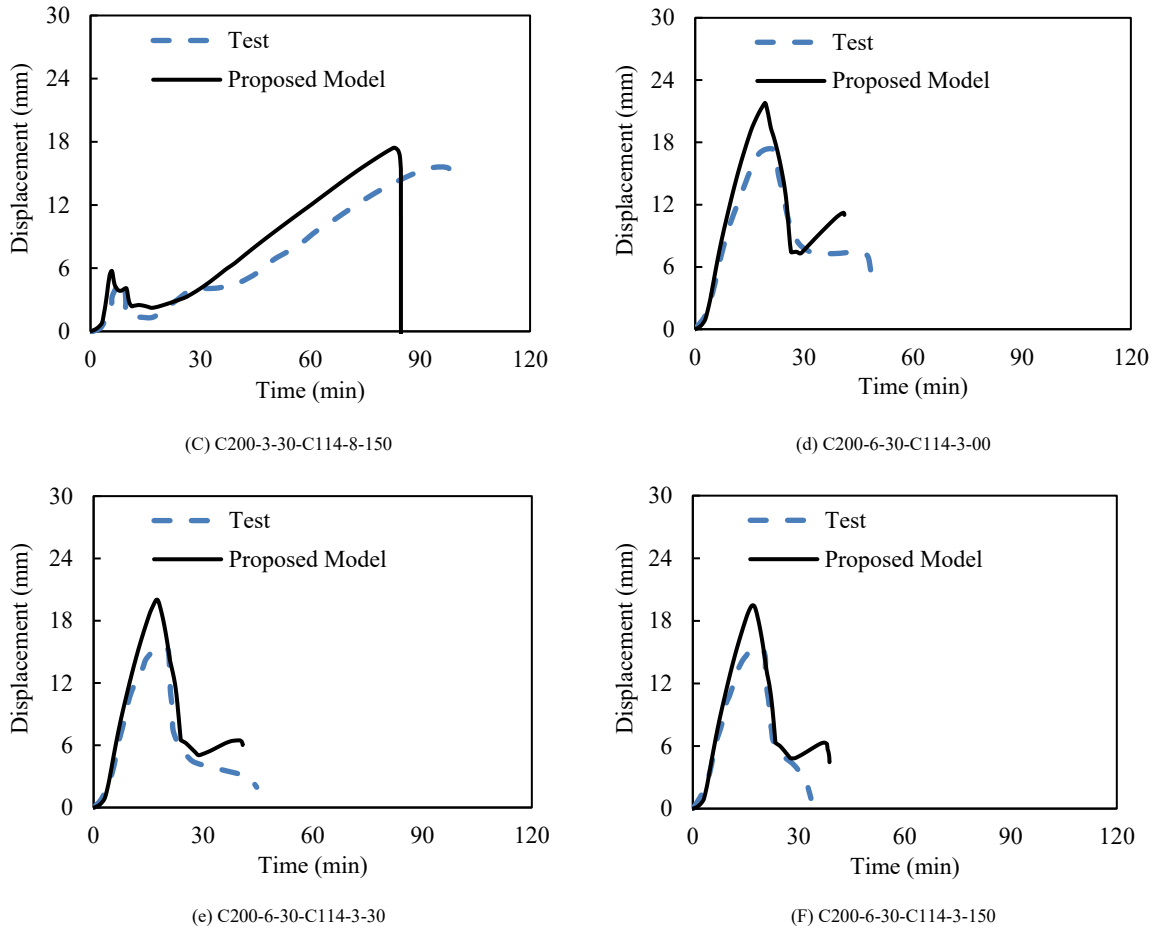

(C) C200-3-30-C114-8-150

(d) C200-6-30-C114-3-00

(e) C200-6-30-C114-3-30

(F) C200-6-30-C114-3-150

Fig. 5 Verification of the FE model

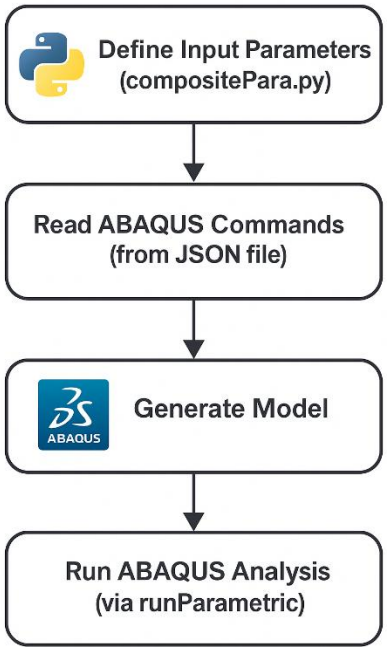

Fig. 6 Automated Finite Element Modeling Workflow for CFDT Columns Using Python and ABAQUS

4.6. Automated FE model

An automated finite element (FE) modeling framework was developed using the Python programming language. This framework allows users to define all column input parameters directly within the Python environment. The model is then automatically generated, executed in ABAQUS, and the simulation results are extracted without the need for manual intervention.

This automated approach offers significant benefits for both engineers who are not familiar with ABAQUS and researchers conducting extensive parametric studies. It streamlines the modeling process, reduces human error, and significantly saves time by automating model creation, execution, and post-processing.

Fig. 6 illustrates the workflow of the Python script. The user provides the input parameters through the compositePara file. ABAQUS-specific commands are parsed from a structured JSON file, and the model is then executed using the runParametric module.

5. Parametric studies

This section presents the results and discussion of the parametric study. The control column has an outer diameter of 500 mm with a 5 mm wall thickness, and an inner tube diameter of 300 mm with a thickness of 3 mm. The column is filled with ultra-high-performance concrete (UHPC) with a compressive strength of 120 MPa, and the steel has a yield strength of 360 MPa.

Fig. 7 illustrates the load distribution among the different components of the column during fire exposure. Fig. 7a presents the load distribution ratio of each component relative to the total applied load, while Fig. 7b shows the ratio relative to the initial applied load at the onset of fire exposure. The column undergoes several distinct stages before failure. Initially, the outer steel tube expands and carries the majority of the load. As its temperature increases, material degradation occurs, leading to a reduction in its load-carrying capacity. It eventually contracts until the loading plate contacts the outer concrete ring. Due to the high temperature, the outer concrete expands and begins to carry a significant portion of the load, more so than the inner steel tube and concrete core. As the outer concrete degrades, the inner steel tube and concrete core take on a greater share of the load. The inner steel tube, owing to its higher thermal expansion, carries more load than the concrete core until it also deteriorates. Ultimately, the inner concrete core becomes the sole load-bearing component until it too fails due to material degradation and excessive load.

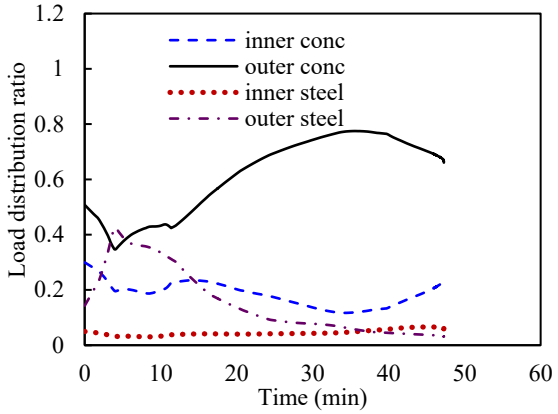

a) Ratio with total applied load

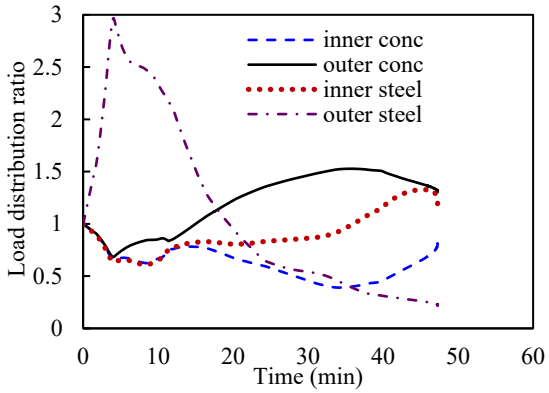

b) Ratio with applied load on each element at the beginning of fire condition

Fig. 7 load participation from different element

5.1. Effect of load level

The load level was changed by range from 0.1 to 0.7, as expected, increasing the load level decreases the fire resistance (FR) time and decreases the expansion of the column at the 1st phase. This is clearly indicated in Fig. 8.

5.2. Effect of inner width to thickness ratio

Fig. 9 shows the effect of the inner tube width to thickness (Di/ti) ratio, and it can be seen that increasing the Di/ti ratio leads to a decrease in FR time. Increasing the Di/ti ratio decreases the tube thickness, which makes to more vulnerable to local buckling. Besides, less thickness leads to high-temperature development in the inner steel tube.

5.3. Effect of outer width to thickness ratio

In contrary to the previous section, increasing the outer tube width-to-thickness (Do/to) ratio will lead to an increase in FR time. This is indicated in Fig. 10. Decreasing the Do/to ratio will increase the outer tube expansion of outer tube at the 1st phase. The load level was kept constant, so decreasing the Do/to ratio will decrease the load value. As the external tube fail in an earlier stage of the fire exposure, decreasing the Do/to ratio will lead to an increase in the FR time as a result of reducing load value.

5.4. Effect of steel tube strength

Fig. 11 shows the effect of steel tube strength (f_Y). Increasing steel tube strength decreases the FR time of CFDT columns. As mentioned before, in all columns, the load level was kept constant to a value of 0.4, so increasing f_Y will lead to an increase in the loading value on the column and as steel tubes (especially outer steel tubes) fail in an early stage of fire resistance this will increase the load on the inner and outer concrete and inner steel tube which will be responsible in carrying the whole applied load.

5.5. Effect of steel types

Four combinations were used to study the effect of steel tube types: inner and outer steel tube are stainless steel, inner and outer steel tubes are carbon steel, inner steel tube is stainless and outer is carbon and finally, inner steel tube is carbon and outer is stainless. In order to understand the difference in behavior been stainless steel and carbon steel under elevated temperatures, it's important to study their thermal and mechanical material properties, as illustrated in Figs. 12 and 13, respectively. As can be seen that stainless steel has less thermal conductivity and specific heat compared to carbon steel. However, carbon steel has a lower reduction strength factor compared to stainless steel up to nearly 600^{O}C. After that, the reduction factor of carbon steel began to be more than that of stainless steel. Fig. 14 shows that using stainless steel for the outer tube and carbon steel for the inner tube results in better behaviour. This is because steel at the outer tube provides slower temperature development through the column due to its material properties. While using carbon steel at the inner tube gains the benefit of carbon steel material properties, which has a lower reduction factor compared to stainless as, generally, the column fails when the inner tube temperature does not exceed 600 ^{O}C.

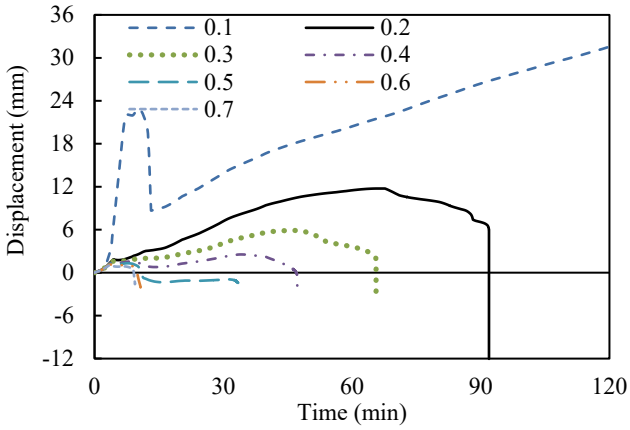

Fig. 8 Load level

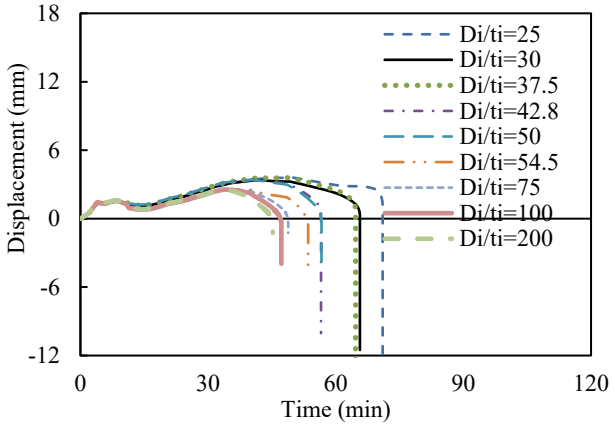

Fig. 9 Effect of inner width to thickness ratio

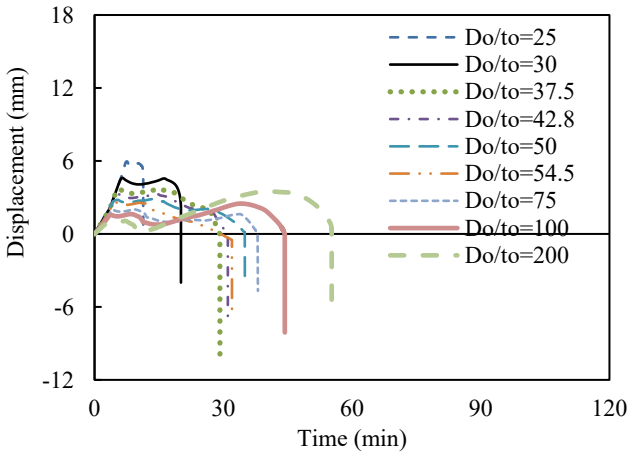

Fig. 10 Effect of outer width to thickness ratio

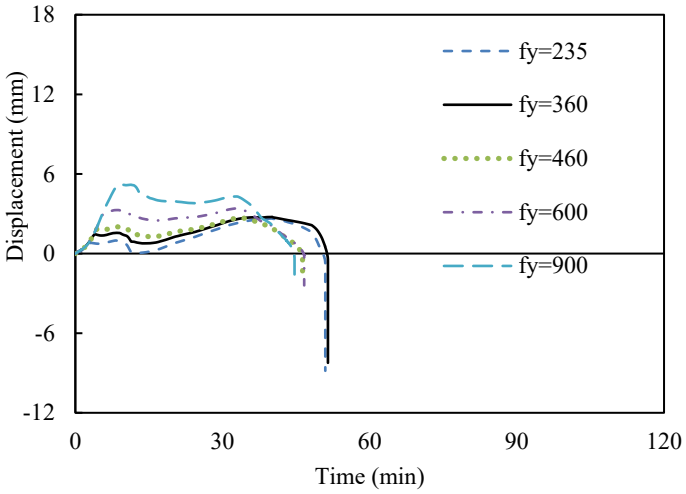

Fig. 11 Effect steel tube strength

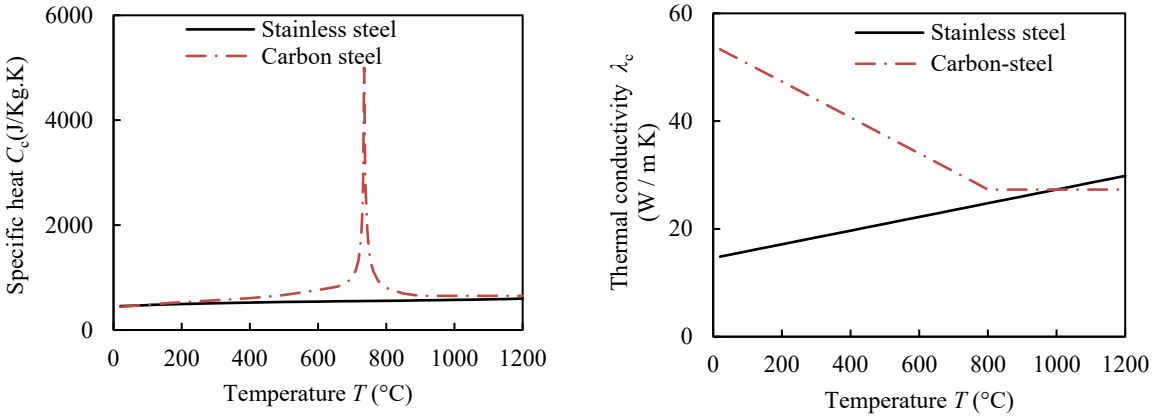

a) Specific heat

b) Thermal conductivity

Fig. 12 Thermal material properties of steel

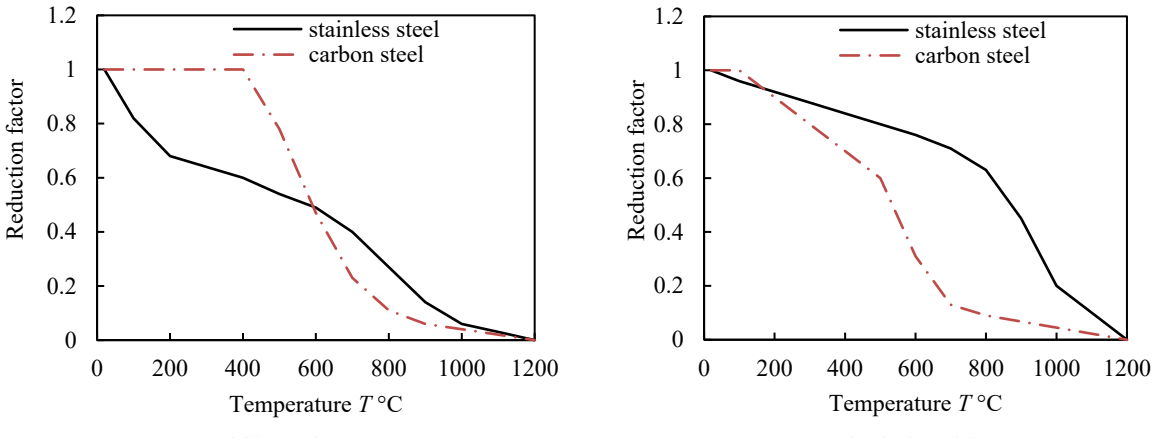

a) Yield strength

b) Elastic modulus

Fig. 13 mechanical material properties of steel

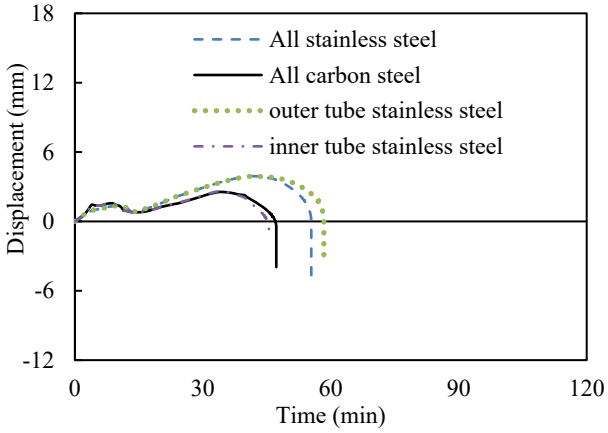

Fig. 14 Effect steel tube strength

5.6. Effect of inner-to-outer tube diameter ratio

The effect of inner to outer tube diameter (χ=Di/(Do-2to)) is shown in Fig. 15. Generally, it can be seen that increasing the ratio of inner to outer tube diameter will lead to an increase in the FR time. As mentioned before, the outer steel tube and outer concrete ring will carry most of the applied load at an early loading stage leaving the inner steel tube and inner concrete core to carry the load at a later stage. Increasing the inner tube diameter will increase the capacity of the inner steel tube and inner concrete core as a result of increasing its cross-sectional area, which in turn will increase the fire resistance time, especially at later stages of fire exposure.

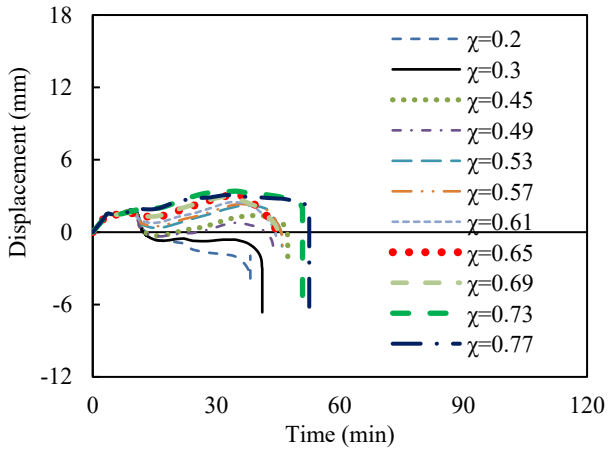

Fig. 15 Effect of inner to outer tube Diameter

5.7. Effect of slenderness ratio

The effect of column slenderness is shown in Fig. 16. It can be seen that the figure can generally be divided into three groups: 1st group from slenderness 24 to 80; in this stage, increasing column slenderness leads to an increase in FR time as a result of increasing flexural buckling. However, the 2nd group for slenderness, from 92 to 116, had a higher FR time than the slenderness group of 80. In the 2nd group, due to the larger column length, two actions opposite to each other take place. The first is flexural buckling, which tends to decrease the column flexural stiffens and thus the FR time. The second action is as a column length increases its expansion increases more, which takes a longer time to contract and therefore increases FR time. In the 2nd group, the second action overcomes the decrease in column flexural stiffness and, thus, the FR time increases.

The last and 3rd groups for the slenderness of 124, 136 and 144, the column length become larger and thus, the decrease in column flexural stiffness becomes more pronounced and therefore, the FR time decreases again.

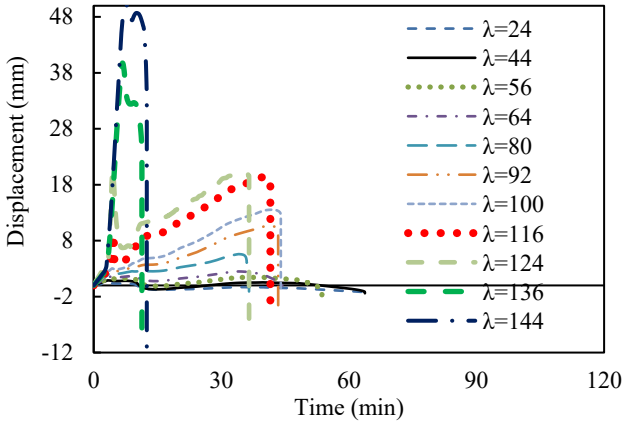

Fig. 16 Effect of column slenderness

5.8. Effect of concrete grade

As expected, increasing concrete compressive strength increases FR time, as indicated in Fig. 17 as the concrete ring and concrete core will be responsible for carrying the applied load after the outer and inner steel tube fails respectively as mentioned before.

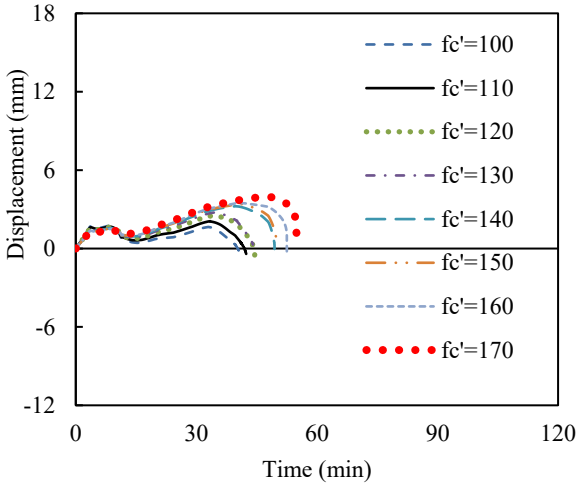

Fig. 17 Effect of concrete compressive strength

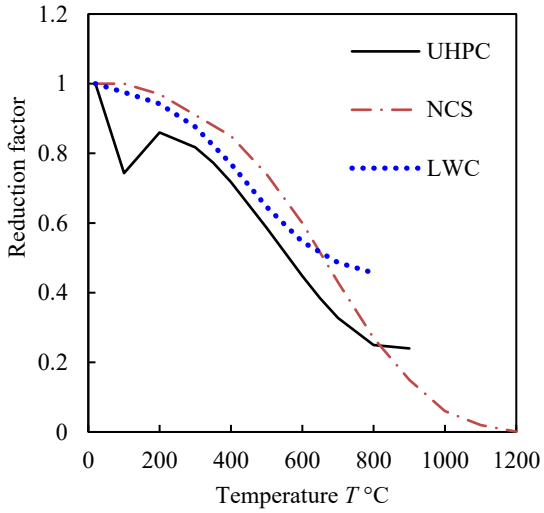

a) Compressive strength reduction factor

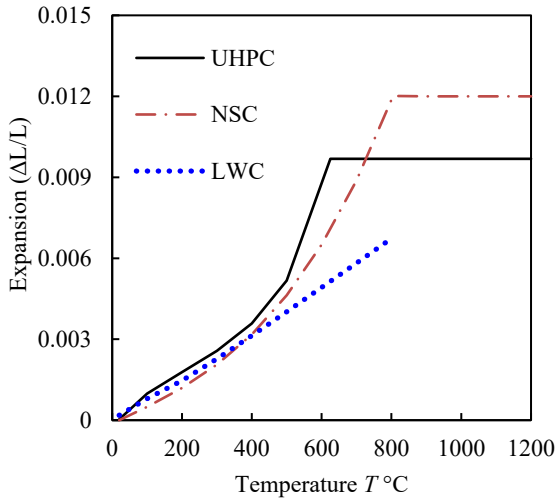

b) Expansion

Fig. 18 Mechanical material properties of concrete

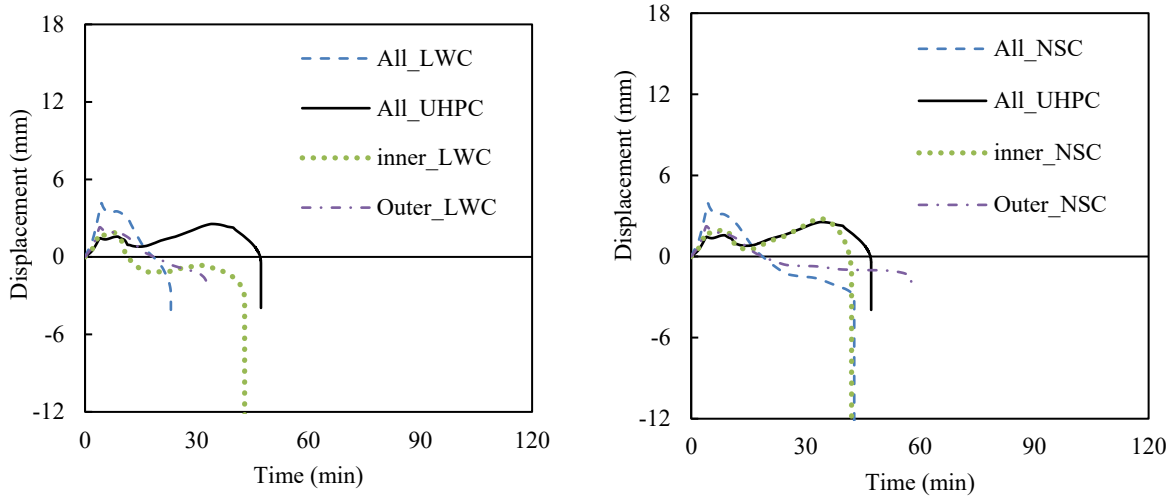

(a) LWC (b) NSC

Fig. 19 Effect of concrete type

5.9. Effect of concrete type

In this section, the effect of using different types of concrete, including Ultra high performance concrete (UHPC) normal strength concrete (NSC) and lightweight concrete (LWC) is investigated. Fig. 18 shows the effect in material properties between different types of concrete.

In Fig. 19a, four combinations were investigated: 1st LWC was used in the outer ring and in the inner core, 2nd combination UHPC was used in the outer ring and in the inner core, 3rd combination LWC was used in the inner concrete core and UHPC was used in the outer ring, while LWC was used in the outer ring and UHPC was used in inner core in the 4th combination.

It can be found that using UHPC in the outer ring and inner core gives higher FR time compared to other combinations. This is explained due to the closer reduction of the compressive strength factor between LWC and UHPC as indicated in Fig. 18a. However, UHPC has higher expansion compared to LWC, which gives UHPC more time to resist the applied force before material degradation and column failure.

In Fig. 19b, another four combinations were investigated using NSC: 1st NSC was used in the outer ring and in the inner core, 2nd combination UHPC was used in the outer ring and in the inner core, 3rd combination NSC was used in the inner concrete core and UHPC was used in the outer ring, while NSC was used in the outer ring and UHPC was used in inner core in the 4th combination. From Fig. 19b, it can be observed that using NSC at the outer ring and UHPC at the inner core give higher FR time. This is due to the lower reduction factor of NSC compared to UHPC as indicated in Fig. 18 (Unlike LWC's reduction factor is close to UHPC reduction factor), which results in decreasing the material degradation of the outer ring as it is exposed to higher temperature compared to inner core.

5.10. Effect of eccentricity

As illustrated in Fig. 20, eccentricity has a pronounced negative influence on the fire resistance of CFDST columns. The fire resistance decreased sharply from 47 minutes under concentric loading to 10 minutes when the eccentricity reached 0.1 of the column diameter. This reduction is primarily attributed to the combined effects of increased flexural demand induced by eccentric loading and the degradation of material properties at elevated temperatures, which accelerate the loss of column strength.

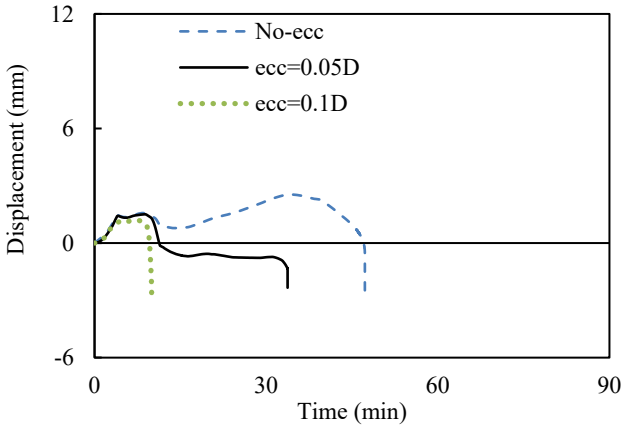

Fig. 20 Effect of Eccentricity

6. Evaluation of Eurocode 4

Eurocode 4 part 1.2 [25] is required the most widely accepted method in designing fire resistance of CFST columns under fire. In this section, an evaluation for Eurocode 4 part 1.2 [25] is performed using the results obtained from the parametric study. The evaluation is done through the comparison of the fire resistance (FR) time obtained from FE and from Eurocode; details are presented in the following sections.

6.1. Existing EC4 design approach

Eurocode 4 Part 1.2 provides a design model for evaluating the fire resistance of CFST columns. In this section, modifications to the Eurocode 4 model are proposed to extend its applicability to CFDT columns. The original EC4 Part 1.2 model is presented in Eq. 11.

$$N_{Rd,T} = \chi * N_{pl,Rd,T}$$

$N_{pl,Rd,T}$ is the cross-section capacity at elevated temperatures

$$N_{pl,Rd,T} = A_{\text{out,st,T}} \times f_{\text{out,st,y,T}} + A_{\text{out,c,T}} \times f_{\text{out,c,T}} + A_{\text{in,st,T}} \times f_{\text{in,st,y,T}} + A_{\text{in,c,T}} \times f_{\text{in,c,T}}$$

$$\chi = \frac{1}{\phi + \sqrt{\phi^2 - {\lambda_T}^2}} \qquad (11)$$

$$\phi = 0.5\,(1 + \alpha\,(\lambda_T - 0.2) + \lambda_T^2) \qquad \alpha = 0.49 \text{ related to buckling curve "c"}$$

where.

$$\lambda_T = \sqrt{N_{pl,R,T}\,/N_{cr,T}}$$

$$N_{cr,T} = \pi^2\,(E\,I)_{eff,T}\,/L^2$$

$$(E\,I)_{eff,T} = \varphi_{s,T}\,E_{s,T}\,I_s + \varphi_{c,T}\,E_{c,T}\,I_c + \varphi_{r,T}\,E_{r,T}\,I_r$$

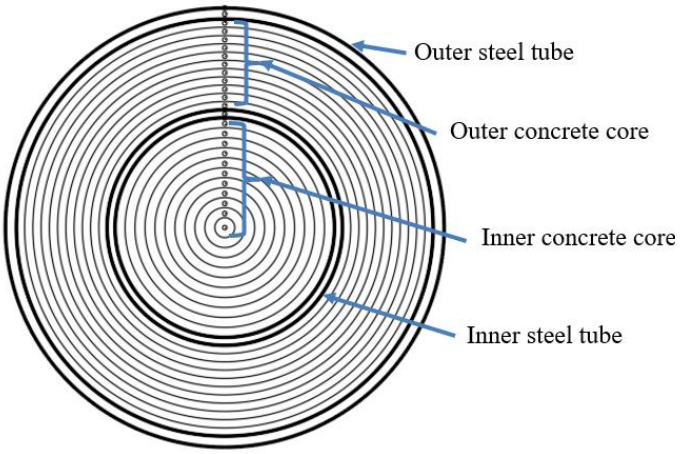

Fig. 21 Cross-section layers and divisions

6.2. Temperature development in CFDT columns

A finite difference (FD) model was developed using MATLAB to simulate the temperature distribution within CFDT columns. The formulation of this model is based on previous research by the authors for CFST and CFDST columns [58, 62]. The developed model predicts the temperature evolution at various locations across the cross-section, which is subsequently used to evaluate the temperature-dependent mechanical properties of the outer and inner steel tubes, as well as the outer and inner concrete regions.

The finite difference (FD) method was adopted in this study due to its simplicity, reduced computational cost, and shorter model-building time compared with the finite element (FE) approach [58, 62, 74]. To the authors' knowledge, no previous FD-based model has been developed for predicting the temperature distribution in CFDST columns; most available studies focus on CFST columns [62-64, 75], The authors have previously proposed a model for CFDST columns[58], and the present study extends this work by introducing an FD model to simulate temperature development through CFDST columns, thereby addressing this research gap.

In the proposed model, the cross-section was discretized into 11 layers for both the outer and inner concrete regions. The first and last layers in these regions were assigned half the thickness of the intermediate layers. For the inner and outer steel tubes, three layers were used, with the middle layer having twice the thickness of the first and last layers. The discretization scheme is illustrated in Fig. 21. To minimize accumulated numerical errors, the time step was selected as shown in the accompanying table.

Table 8
Time intervals (Δt) calculation

Time interval (Δ*t*) (sec)	Tube thickness (*t*) (mm)
0.03	$t \leq 3$
0.1	$3 < t \geq 5$
0.25	$5 < t \geq 7$
0.5	$7 < t \geq 12$
1	$t > 12$

The governing heat transfer equations, formulated based on [58, 62, 74], are presented in Equations [12-23].

For the outer surface of the steel tube:

$$T_{s1\_out}^{n+1} = T_{s1\_out}^{n} + \frac{\Delta t \times h_{total}}{\rho_{s1\_out}^{n} C_{s1\_out}^{n} \times \Delta x_{s1\_out}} - \frac{\Delta t}{\rho_{s1\_out}^{n} C_{s1\_out}^{n} \times \Delta x_{s1\_out} \times \left(\Delta x_{s1\_out} + \frac{\Delta x_{s2\_out}}{2}\right)} \times \left(\frac{K_{s1\_out}^{n} + K_{s2\_out}^{n}}{2}\right) \times \left(T_{s1\_out}^{n} - T_{s2\_out}^{n}\right) \quad (12)$$

where h_{total} (W/m^2) is the total heat energy from convection and radiation.

For the intermediate steel layer:

$$T_{s2\_out}^{n+1} = T_{s2\_out}^{n} + \frac{\Delta t}{\rho_{s2\_out}^{n} C_{s2\_out}^{n} \times \Delta x_{s2\_out} \times \left(\Delta x_{s1\_out} + \Delta x_{s2\_out}/2\right)} \times \left(\frac{K_{s1\_out}^{n} + K_{s2\_out}^{n}}{2}\right) \times \left(T_{s1\_out}^{n} - T_{s2\_out}^{n}\right) - \frac{\Delta t}{\rho_{s2\_out}^{n} C_{s2\_out}^{n} \times \Delta x_{s2\_out} \times \left(\Delta x_{s3\_out} + \Delta x_{s2\_out}/2\right)} \times \left(\frac{K_{s2\_out}^{n} + K_{s3\_out}^{n}}{2}\right) \times \left(T_{s2\_out}^{n} - T_{s3\_out}^{n}\right) \quad (13)$$

For the inner surface of the steel tube:

$$T_{s3\_out}^{n+1} = T_{s3\_out}^{n} + \frac{\Delta t}{\rho_{s3\_out}^{n} C_{s3\_out}^{n} \times \Delta x_{s3\_out} \times \left(\Delta x_{s3\_out} + \Delta x_{s2\_out}/2\right)} \times \left(\frac{K_{s2\_out}^{n} + K_{s3\_out}^{n}}{2}\right) \times \left(T_{s2\_out}^{n} - T_{s3\_out}^{n}\right) - \frac{\Delta t \times h_j}{\rho_{s3\_out}^{n} C_{s3\_out}^{n} \times \Delta x_{s3\_out}} \times \left(T_{s3\_out}^{n} - T_{c1\_out}^{n}\right) \quad (14)$$

For the outer concrete layer:

$$T_{c1\_out}^{n+1} = T_{c1\_out}^{n} \frac{\Delta t \times h_j}{\rho_{c1\_out}^{n} C_{c\_out}^{n} \times \Delta x_{c1\_out}} \times \left(T_{s3\_out}^{n} - T_{c1\_out}^{n}\right) - \frac{\Delta t}{\rho_{c1\_out}^{n} C_{c1\_out}^{n} \times \Delta x_{c1\_out} \times \left(\Delta x_{c1\_out} + \Delta x_{c2\_out}/2\right)} \times \left(\frac{K_{c1\_out}^{n} + K_{c2\_out}^{n}}{2}\right) \times \left(T_{c1\_out}^{n} - T_{c2\_out}^{n}\right) \quad (15)$$

For the intermediate concrete layer:

$$T_{cm\_out}^{n+1} = T_{cm\_out}^{n} + \frac{\Delta t}{\rho_{cm\_out}^{n} C_{cm\_out}^{n} \times \Delta x_{cm\_out} \times (\Delta x_{c(m-1)\_\mathrm{out}}/2 + \Delta x_{cm\_out}/2)} \times \left(\frac{K_{c(m-1)\_\mathrm{out}}^{n} + K_{cm\_out}^{n}}{2}\right) \times \left(T_{c(m-1)\_\mathrm{out}}^{n} - T_{cm\_out}^{n}\right) - \frac{\Delta t}{\rho_{cm\_out}^{n} C_{cm\_out}^{n} \times \Delta x_{cm\_out} \times (\Delta x_{cm\_out}/2 + \Delta x_{c(m+1)\_\mathrm{out}}/2)} \times \left(\frac{K_{cm\_out}^{n} + K_{c(m+1)\_\mathrm{out}}^{n}}{2}\right) \times \left(T_{cm\_out}^{n} - T_{c(m+1)\_\mathrm{out}}^{n}\right) \quad (16)$$

For the last concrete layer in the ring:

$$T_{cm\_out}^{n+1} = T_{cm\_out}^{n} + \frac{\Delta t}{\rho_{cm\_out}^{n} C_{cm\_out}^{n} \times \Delta x_{cm\_out} \times (\Delta x_{cm\_out} + \Delta x_{c(m-1)\_\mathrm{out})/2)} \times \left(\frac{K_{cm\_out}^{n} + K_{c(m-1)\_\mathrm{out}}^{n}}{2}\right) \times \left(T_{c(m-1)\_\mathrm{out}}^{n} - T_{cm\_out}^{n}\right) - \frac{\Delta t \times h_j}{\rho_{cm\_out}^{n} C_{cm\_out}^{n} \times \Delta x_{cm\_out}} \times \left(T_{cm\_out}^{n} - T_{s1\_\mathrm{in}}^{n}\right) \quad (17)$$

For the outer steel layer of the inner tube:

$$T_{s1\_\mathrm{in}}^{n+1} = T_{s1\_\mathrm{in}}^{n} + \frac{\Delta t \times h_{j\_in}}{\rho_{s1\_\mathrm{in}}^{n} C_{s1\_\mathrm{in}}^{n} \times \Delta x_{s1\_\mathrm{in}}} \times \left(T_{cm\_out}^{n} - T_{s1\_\mathrm{in}}^{n}\right) - \frac{\Delta t}{\rho_{s1\_in}^{n} C_{s1\_in}^{n} \times \Delta x_{s1\_in} \times \left(\Delta x_{s1\_in} + \frac{\Delta x_{s2\_in}}{2}\right)} \times \left(\frac{K_{s1\_in}^{n} + K_{s2\_in}^{n}}{2}\right) \times \left(T_{s1\_in}^{n} - T_{s2\_in}^{n}\right) \quad (18)$$

For the intermediate steel layer:

$$T_{s2\_\mathrm{in}}^{n+1} = T_{s2\_\mathrm{in}}^{n} + \frac{\Delta t}{\rho_{s2\_\mathrm{in}}^{n} C_{s2\_\mathrm{in}}^{n} \times \Delta x_{s2\_\mathrm{in}} \times (\Delta x_{s1\_\mathrm{in}} + \Delta x_{s2\_\mathrm{in}}/2)} \times \left(\frac{K_{s1\_\mathrm{in}}^{n} + K_{s2\_\mathrm{in}}^{n}}{2}\right) \times \left(T_{s1\_\mathrm{in}}^{n} - T_{s2\_\mathrm{in}}^{n}\right) - \frac{\Delta t}{\rho_{s2\_\mathrm{in}}^{n} C_{s2\_\mathrm{in}}^{n} \times \Delta x_{s2\_\mathrm{in}} \times (\Delta x_{s3\_\mathrm{in}} + \Delta x_{s2\_\mathrm{in}}/2)} \times \left(\frac{K_{s2\_\mathrm{in}}^{n} + K_{s3\_\mathrm{in}}^{n}}{2}\right) \times \left(T_{s2\_\mathrm{in}}^{n} - T_{s3\_\mathrm{in}}^{n}\right) \quad (19)$$

For the inner surface of the steel tube:

$$T_{s3\_\mathrm{in}}^{n+1} = T_{s3\_\mathrm{in}}^{n} + \frac{\Delta t}{\rho_{s3\_\mathrm{in}}^{n} C_{s3\_\mathrm{in}}^{n} \times \Delta x_{s3\_\mathrm{in}} \times (\Delta x_{s3\_\mathrm{in}} + \Delta x_{s2\_\mathrm{in}}/2)} \times \left(\frac{K_{s2\_\mathrm{in}}^{n} + K_{s3\_\mathrm{in}}^{n}}{2}\right) \times \left(T_{s2\_\mathrm{in}}^{n} - T_{s3\_\mathrm{in}}^{n}\right) - \frac{\Delta t \times h_{j\_in}}{\rho_{s3\_\mathrm{in}}^{n} C_{s3\_\mathrm{in}}^{n} \times \Delta x_{s3\_\mathrm{in}}} \times \left(T_{s3\_\mathrm{in}}^{n} - T_{c1\_\mathrm{in}}^{n}\right) \quad (20)$$

For the outer concrete layer:

$$T_{c1\_\mathrm{in}}^{n+1} = T_{c1\_\mathrm{in}}^{n} \frac{\Delta t \times h_{j\_in}}{\rho_{c1\_\mathrm{in}}^{n} C_{c1\_\mathrm{in}}^{n} \times \Delta x_{c1\_\mathrm{in}}} \times \left(T_{s3\_\mathrm{in}}^{n} - T_{c1\_\mathrm{in}}^{n}\right) - \frac{\Delta t}{\rho_{c1\_\mathrm{in}}^{n} C_{c1\_\mathrm{in}}^{n} \times \Delta x_{c1\_\mathrm{in}} \times (\Delta x_{c1\_\mathrm{in}} + \Delta x_{c2\_\mathrm{in}}/2)} \times \left(\frac{K_{c1\_\mathrm{in}}^{n} + K_{c2\_\mathrm{in}}^{n}}{2}\right) \times \left(T_{c1\_\mathrm{in}}^{n} - T_{c2\_\mathrm{in}}^{n}\right) \quad (21)$$

For the intermediate concrete layer:

$$T_{cm\_in}^{n+1} = T_{cm\_in}^{n} + \frac{\Delta t}{\rho_{cm\_in}^{n} C_{cm\_in}^{n} \times \Delta x_{cm\_in} \times (\Delta x_{c(m-1)\_\mathrm{in}}/2 + \Delta x_{cm\_in}/2)} \times \left(\frac{K_{c(m-1)\_\mathrm{in}}^{n} + K_{cm\_in}^{n}}{2}\right) \times \left(T_{c(m-1)\_\mathrm{in}}^{n} - T_{cm\_in}^{n}\right) - \frac{\Delta t}{\rho_{cm\_in}^{n} C_{cm\_in}^{n} \times \Delta x_{cm\_in} \times (\Delta x_{cm\_in}/2 + \Delta x_{c(m+1)\_\mathrm{in}}/2)} \times \left(\frac{K_{cm\_in}^{n} + K_{c(m+1)\_\mathrm{in}}^{n}}{2}\right) \times \left(T_{cm\_in}^{n} - T_{c(m+1)}^{n}\right) \quad (22)$$

For the last concrete layer in the ring:

$$T_{\mathrm{cm\_in}}^{n+1} = T_{\mathrm{cm\_in}}^{n} + \frac{\Delta t \times 2}{\rho_{\mathrm{cm\_in}}^{n} c_{\mathrm{cm\_in}}^{n} \times \Delta x_{\mathrm{cm\_in}} \times (\Delta x_{\mathrm{c(m-1)\_in}}/2 + \Delta x_{\mathrm{cm\_in}})} \times \left(\frac{K_{\mathrm{c(m-1)\_in}}^{j} + K_{\mathrm{cm\_in}}^{j}}{2}\right) \times \left(T_{\mathrm{c(m-1)\_in}}^{j} - T_{\mathrm{cm\_in}}^{j}\right) \quad (23)$$

where the superscript *n* denotes the time step in seconds; cm refers to the layer number *m* in the concrete core; the subscript sm rrefers to the layer number *m* in the steel tube; the subscript _out denotes the outer tube or outer core, while the subscript _in denotes the inner tube or inner core. *T* represents the temperature (°C); *d* is the distance from the outer surface of the considered layer to the column center (m); Δx is the layer thickness (m); Δt is the time interval (s); *C* is the specific heat capacity ($J/kg \cdot K$); ρ is the material density (kg/m^3); *K* is the thermal conductivity (W/m·K); α_c is the convective heat transfer coefficient; and h_j is the thermal conductance between the steel tube and the concrete (W/m^2K).

Fig. 22 shows the validation of the proposed analytical model (AM) against the finite element (FE) results at multiple points across the CFDST cross-section. A good agreement was achieved between the two models in terms of temperature prediction. The verification was performed on a column with an outer steel tube of 500 mm diameter and 5 mm thickness, and an inner steel tube of 300 mm diameter and 3 mm thickness. The concrete infill consisted of ultra-high-performance concrete (UHPC) with a compressive strength of 120 MPa, while both steel tubes had a yield strength of 360 MPa.

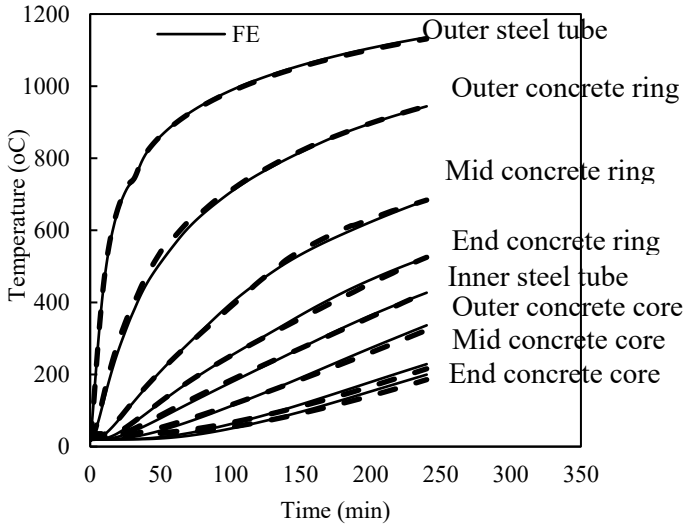

Fig. 22 Verification of FD model

6.3. Proposed buckling curve modification

This section presents a comparative analysis of fire resistance (FR) times predicted by Eurocode 4 (EC4), implemented through a MATLAB-based analytical model, against those obtained from a validated finite element (FE) model. In the corresponding figure, the X-axis represents the FR time predicted by the FE model, while the Y-axis shows the FR time estimated using both the original and the modified EC4 formulations.

The results indicate that the standard EC4 substantially underestimates the fire resistance of CFDT columns incorporating ultra-high-performance concrete (UHPC). To improve prediction accuracy, a modification to the EC4 buckling curve was proposed. Based on regression analysis, the buckling curve factor (α) was adjusted to 0.85.

The applicability of the proposed buckling curve is limited to the following parameter ranges: load level from 0.1 to 0.7; inner tube diameter-to-thickness ratio between 25 and 200; outer tube diameter-to-thickness ratio between 25 and 200; inner-to-outer tube diameter ratio from 0.2 to 0.77; steel yield strength between 235 and 900 MPa; concrete cylinder strength between 100 and 170 MPa; and slenderness ratio from 25 to 144.

As shown in Fig. 23, the modified EC4 model yields predictions that align more closely with the FE results. Table 9 summarizes the comparative performance: the average test-to-prediction ratio improved from 1.464 (original EC4) to 0.992 (modified EC4), while the coefficient of variation (COV) was reduced from 0.311 to 0.298.

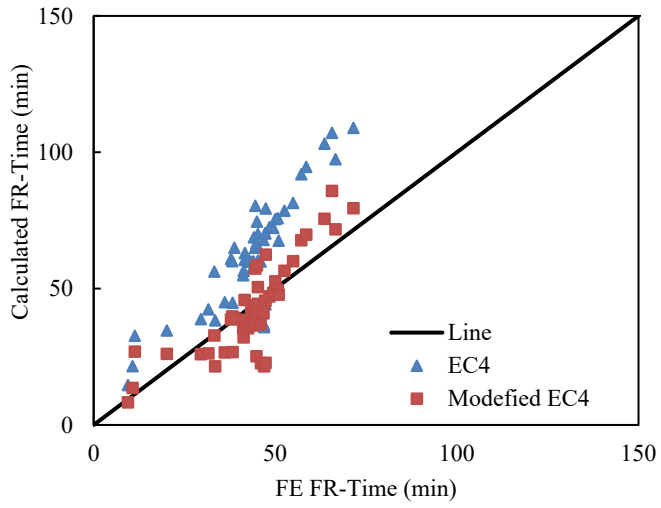

Fig. 23 Evaluation f EC4 1.2

Table 9
Comparison between EC4 and modified model

	EC4	Modified EC4
Mean	1.464	0.992
COV	0.311	0.298

7. Conclusions

This paper presents an analytical and numerical investigation aimed at enhancing the understanding of ultra-high-performance concrete-filled double-skin tubular (UHPC-CFDT) columns under fire conditions and addressing the existing research gap in this field. Based on available experimental data, three temperature-dependent material models were developed to simulate the behavior of UHPC, lightweight concrete, and high-strength steel at elevated temperatures.

A validated finite element (FE) model was developed, showing strong agreement with existing test results. Additionally, an automated Python-based FE modeling framework was established, enabling efficient model generation, analysis execution, and data extraction. This tool is particularly valuable for engineers with limited experience in Abaqus and for expediting extensive parametric studies.

Based on the parametric investigations conducted and the proposed models, the following conclusions and recommendations can be drawn:

- Fire resistance increases with the outer tube diameter-to-thickness ratio (Do/to), the inner-to-outer tube diameter ratio, and the concrete compressive strength. For example, fire resistance increased from 11 to 55 minutes as the Do/to ratio rose from 25 to 200.
- In contrast, fire resistance decreases with higher load levels, inner tube diameter-to-thickness ratio, and steel yield strength. Among these, load level had the most pronounced effect, with fire resistance increasing nearly tenfold as the load level decreased from 0.7 to 0.2.
- The optimal material configuration under fire conditions was identified as stainless steel for the outer tube, carbon steel for the inner tube, normal-strength concrete in the outer ring, and UHPC in the inner core.
- A finite difference model was developed to accurately simulate temperature distribution across the cross-section of UHPC-filled CFDT columns during fire exposure.
- The Eurocode 4 (EC4) design approach was evaluated against the FE results. It was found that EC4 provides unconservative predictions for the fire resistance of UHPC-filled CFDT columns. A simplified modification is proposed by adjusting the buckling curve factor (α) to 0.85, thereby improving the accuracy of the nominal resistance prediction under fire.

In conclusion, this study focused on circular CFDT columns exposed to fire. Further research is recommended to investigate the fire behavior of UHPC-filled CFDT columns with square, octagonal, or hexagonal cross-sections and various geometric and material configurations.

References

[1] Le TT, Patel VI, Liang QQ, Huynh P. Numerical modeling of rectangular concrete-filled double-skin steel tubular columns with outer stainless-steel skin. Journal of Constructional Steel Research. 2021;179:106504.

[2] Romero ML, Espinos A, Portolés JM, Hospitaler A, Ibañez C. Slender double-tube ultra-high strength concrete-filled tubular columns under ambient temperature and fire. Engineering Structures. 2015;99:536-45.

[3] Tao Z, Han L-H, Zhao X-L. Behaviour of concrete-filled double skin (CHS inner and CHS outer) steel tubular stub columns and beam-columns. Journal of Constructional Steel Research. 2004;60:1129-58.

[4] Tao Z, Han L-H. Behaviour of concrete-filled double skin rectangular steel tubular beam–columns. Journal of Constructional Steel Research. 2006;62:631-46.

[5] Han L-H, Huang H, Tao Z, Zhao X-L. Concrete-filled double skin steel tubular (CFDST) beam–columns subjected to cyclic bending. Engineering Structures. 2006;28:1698-714.

[6] Mohan AP, S A. Non-Linear Analysis of Concrete Filled Double Skin Circular Steel Column. International Journal of Engineering Research & Technology (IJERT). 2016;5:204-6.

[7] Elchalakani M, Hassanein MF, Karrech A, Yang B. Experimental investigation of rubberised concrete-filled double skin square tubular columns under axial compression. Engineering Structures. 2018;171:730-46.

[8] Hassanein MF, Elchalakani M, Karrech A, Patel VI, Daher E. Finite element modelling of concrete-filled double-skin short compression members with CHS outer and SHS inner tubes. Marine Structures. 2018;61:85-99.

[9] Ghannam M, Metwally IM. Numerical investigation for the behaviour of stiffened circular concrete filled double tube columns. Structures. 2020;25:901-19.

[10] Karthika S, Ranjitham M. Study of Strength and Behaviour of Concrete Filled Double Skin Tubular Square Columns under Axial Compressive Loads. International Journal of Engineering Research & Technology (IJERT). 2016;5:746-51.

[11] Huang H, Han L-H, Tao Z, Zhao X-L. Analytical behaviour of concrete-filled double skin steel tubular (CFDST) stub columns. Journal of Constructional Steel Research. 2010;66:542-55.

[12] Ekmekyapar T, Al-Eliwi BJM. Concrete filled double circular steel tube (CFDCST) stub columns. Engineering Structures. 2017;135:68-80.

[13] Jia-qi -L, Rui -W, Hui -Z, Hui-wen -W. - STUDY ON THE FIRE PERFORMANCE OF CONCRETE-FILLED DOUBLE-SKIN TUBULAR COLUMNS WITH EXTERNAL STAINLESS STEEL TUBES. - Engineering Mechanics. 2020;- 37:- 125.

[14] Lopes RFR, Rodrigues JPC. Behaviour of restrained concrete filled square double-skin and double-tube hollow columns in case of fire. Engineering Structures. 2020;216:110736.

[15] Lu H, Zhao X-L, Han L-H. FE modelling and fire resistance design of concrete filled double skin tubular columns. Journal of Constructional Steel Research - J CONSTR STEEL RES. 2011;67:1733-48.

[16] Xiong M. Fire resistance of ultra-high strength concrete filled steel tubular columns: PhD Dissertation, National University of Singapore, Singapore; 2013.

[17] Wan C-Y, Zha X-X, Dassekpo J-BM. Analysis of axially loaded concrete filled circular hollow double steel tubular columns exposed to fire. Fire Safety Journal. 2017;88:1-12.

[18] Imani R, Bruneau M, Mosqueda G. Simplified analytical solution for axial load capacity of concrete-filled double-skin tube (CFDST) columns subjected to fire. Engineering Structures. 2015;102:156-75.

[19] Zhu H, Ahmed M, Li C, Kong X, Chen S, Yang Q et al. Fire resistance of square double-skin concrete-filled steel tubular columns and concrete-filled double steel tubular columns. Engineering Structures. 2024;319:118882.

[20] Zhu H, Chen S, Ahmed M, Liang QQ. Experimental and numerical investigations of circular concrete filled steel double-skin and double-tube columns exposed to fire. Thin-Walled Structures. 2024;198:111766.

[21] Zhu H, Chen S, Ahmed M, Li C, Kong X, Ghazali H et al. Behavior and design of eccentrically loaded circular concrete-filled double steel tubular beam-columns under fire exposure. Thin-Walled Structures. 2025;208:112806.

[22] Yao Y, Li H, Tan K-H. Theoretical and numerical analysis to concrete filled double skin steel tubular columns under fire conditions. Thin-Walled Structures. 2016;98:547-57.

[23] Yao Y, Liu M, Guo H. Concrete filled double skin steel tubular columns subjected to non-uniform heating. Journal of Constructional Steel Research. 2019;158:263-78.

[24] Shekastehband B, Taromi A, Abedi K. Fire performance of stiffened concrete filled double skin steel tubular columns. Fire Safety Journal. 2017;88:13-25.

[25] Eurocode-4. Design of composite steel and concrete structures, part 1.2 General rules, Structural fire design. London: BS EN 1994-1-2:2005. British Standards Institution; 2005.

[26] Shen P, Lu J-X, Zheng H, Lu L, Wang F, He Y et al. Expansive ultra-high performance concrete for concrete-filled steel tube applications. Cement and Concrete Composites. 2020;114:103813.

[27] Liu K, Wu C, Li X, Liu J, Tao M, Fang J et al. The influences of cooling regimes on fire resistance of ultra-high performance concrete under static-dynamic coupled loads. Journal of Building Engineering. 2021:103336.

[28] Zhang D, Liu Y, Tan KH. Spalling resistance and mechanical properties of strain-hardening ultra-high performance concrete at elevated temperature. Construction and Building Materials. 2021;266:120961.

[29] Li Y, Du P, Tan KH. Fire resistance of ultra-high performance concrete columns subjected to axial and eccentric loading. Engineering Structures. 2021;248:113158.

[30] Lyzwa J, Zehfuss J. Experimental Investigations of ultra-high performance concrete exposed to natural fires. Fire Safety Journal. 2021:103399.

[31] Banerji S, Kodur V. Effect of temperature on mechanical properties of ultra-high performance concrete. Fire and Materials. 2021.

[32] Li Y. Effect of post-fire curing and silica fume on permeability of ultra-high performance concrete. Construction and Building Materials. 2021;290:123175.

[33] Mai V-C, Nguyen T-C, Dao C-B. Numerical simulation of ultra-high-performance fiber-reinforced concrete frame structure under fire action. Asian Journal of Civil Engineering. 2020:1-8.

[34] Du Y, Qi H-H, Huang S-S, Liew JR. Experimental study on the spalling behaviour of ultra-high strength concrete in fire. Construction and Building Materials. 2020;258:120334.

[35] Xiong M-X, Liew JR. Mechanical behaviour of ultra-high strength concrete at elevated temperatures and fire resistance of ultra-high strength concrete filled steel tubes. Materials & Design. 2016;104:414-27.

[36] Banerji S, Kodur V, Solhmirzaei R. Experimental behavior of ultra high performance fiber reinforced concrete beams under fire conditions. Engineering Structures. 2020;208:110316.

[37] Chen H-J, Yu Y-L, Tang C-W. Mechanical properties of ultra-high performance concrete before and after exposure to high temperatures. Materials. 2020;13:770.

[38] Xiong M-X, Liew JR. Buckling behavior of circular steel tubes infilled with C170/185 ultra-high-strength concrete under fire. Engineering Structures. 2020;212:110523.

[39] Xiong M-X, Liew JR. Fire resistance of high-strength steel tubes infilled with ultra-high-strength concrete under compression. Journal of Constructional Steel Research. 2021;176:106410.

[40] Wang T, Yu M, Zhang X, Xu L, Huang L. Experimental study and proposal of a design model of ultra-high performance concrete filled steel tube columns subjected to fire. Engineering Structures. 2023;280:115697.

[41] Camargo AL, Rodrigues JPC, Fakury RH, Laim L. Fire Resistance of Axially and Rotationally Restrained Concrete-Filled Double-Skin and Double-Tube Hollow Steel Columns. Journal of Structural Engineering. 2019;145:04019128.

[42] Lee YW, Kim GY, Gucunski N, Choe GC, Yoon MH. Thermal strain behavior and strength degradation of ultra-high-strength-concrete. Materials and structures. 2016;49:3411-21.

[43] Choe G, Kim G, Gucunski N, Lee S. Evaluation of the mechanical properties of 200 MPa ultra-high-strength concrete at elevated temperatures and residual strength of column. Construction and Building Materials. 2015;86:159-68.

[44] Khaliq W. Mechanical and physical response of recycled aggregates high-strength concrete at elevated temperatures. Fire safety journal. 2018;96:203-14.

[45] Cheng F-P, Kodur V, Wang T-C. Stress-strain curves for high strength concrete at elevated temperatures. Journal of Materials in Civil Engineering. 2004;16:84-90.

[46] Phan LT, Carino NJ. Effects of test conditions and mixture proportions on behavior of high-strength concrete exposed to high temperatures. ACI Materials Journal. 2002;99:54-66.

[47] Chen J, Young B, Uy B. Behavior of high strength structural steel at elevated temperatures. Journal of structural engineering. 2006;132:1948-54.

[48] Lange J, Wohlfeil N. Examination of the mechanical properties of steel S460 for fire. Journal of Structural Fire Engineering. 2010.

[49] Qiang X, Bijlaard F, Kolstein H. Dependence of mechanical properties of high strength steel S690 on elevated temperatures. Construction and Building Materials. 2012;30:73-9.

[50] Qiang X, Bijlaard FS, Kolstein H. Deterioration of mechanical properties of high strength structural steel S460N under steady state fire condition. Materials & Design (1980-2015). 2012;36:438-42.

[51] Choi I-R, Chung K-S, Kim D-H. Thermal and mechanical properties of high-strength structural steel HSA800 at elevated temperatures. Materials & Design. 2014;63:544-51.

[52] Heidarpour A, Tofts NS, Korayem AH, Zhao X-L, Hutchinson CR. Mechanical properties of very high strength steel at elevated temperatures. Fire safety journal. 2014;64:27-35.

[53] Wang W, Zhang Y, Xu L, Li X. Mechanical properties of high-strength Q960 steel at elevated temperature. Fire Safety Journal. 2020;114:103010.

[54] Li G-Q, Song L-X. Mechanical properties of TMCP Q690 high strength structural steel at elevated temperatures. Fire Safety Journal. 2020;116:103190.

[55] Lu H, Han L-H, Zhao X-L. Fire performance of self-consolidating concrete filled double skin steel tubular columns: Experiments. Fire Safety Journal. 2010;45:106-15.

[56] Mohd Zuki SS, Shahidan S, Choong K, Jayaprakash J, Ali N. Concrete-Filled Double Skin Steel Tubular Columns Exposed to ASTM E-119 Fire Curve for 60 and 90 Minutes of Fire. MATEC Web of Conferences. 2017;103:02009.

[57] ABAQUS. ABAQUS standard user's manual, Version 6.14. USA: Dassault Systèmes Corp., Providence, RI; 2014.

[58] Abdelrahman AHA, Ghannam M, Lotfy S, AlHamaydeh M. Heat Transfer in Ultra-High-Performance Concrete-Filled Double-Skin Tubes Under Fire Conditions. Fire Technology. 2023;59:1519-54.

[59] Eurocode-3. Part 1-2 Design of steel structures, Part 1-2, General rules, structural fire design. BS EN 1993-1-2:2005. British Standards Institution, London; 2005.

[60] Liu X, Liu Z, Hui Y, Wang J. Research on the Concrete-Filled Double Skin steel Tubular (CFDST) columns subjected to axial force after fire. Structures. 2023;57:105213.

[61] Eurocode-2. Design of concrete structures, Part 1-2, General rules, structural fire design. London: BS EN 1992-1-2:2004, British Standards Institution; 2005.

[62] Ghannam M, Song TY. Fire Resistance Design of Concrete-Filled Steel Tube Stub Columns. Fire Technology. 2021;57:911-42.

[63] Xiong M-X, Liew JYR. Buckling behavior of circular steel tubes infilled with C170/185 ultra-high-strength concrete under fire. Engineering Structures. 2020;212:110523.

[64] Lie T, Irwin R. Fire resistance of rectangular steel columns filled with bar-reinforced concrete. Journal of Structural Engineering. 1995;121:797-805.

[65] Baloch WL, Khushnood RA, Memon SA, Ahmed W, Ahmad S. Effect of Elevated Temperatures on Mechanical Performance of Normal and Lightweight Concretes Reinforced with Carbon Nanotubes. Fire Technology. 2018;54:1331-67.

[66] Albozagre H, Naghipour M. Experimental study of the behaviour of the concrete-filled double-skin columns with stainless-steel outer tubes subjected to post-earthquake fire. Structures. 2025;75:108541.

[67] ACI216R-89. Guide for Determining the Fire Endurance of Concrete Elements. American Concrete Institute. 1994.

[68] AISC. Specification for Structural Steel Buildings. Standard ANSI/AISC 360-16. United States of America: American Institute of Steel Construction, Inc; 2016.

[69] AS/NZS_2327. composite structures composite steel-concrete construction in building. Sydney, Australia: Australian Standard/New Zealand Standard, Standards Australia; 2017.

[70] ASCE. Structural fire protection. Manual No. 78. ASCE Committee on Fire Protection, Structural Division, American Society of Civil Engineers, New York, USA. 1992.

[71] Ci J, Ahmed M, Liang QQ, Chen S, Chen W, Sennah K et al. Experimental and numerical investigations into the behavior of circular concrete-filled double steel tubular slender columns. Engineering Structures. 2022;267:114644.

[72] Xiong M-X, Xiong D-X, Liew JYR. Behaviour of steel tubular members infilled with ultra high strength concrete. Journal of Constructional Steel Research. 2017;138:168-83.

[73] ISO-834-1. Fire-resistance tests-Elements of building construction-Part 1: General requirements. Geneva: International Organization for Standardization; 1999.

[74] Harmathy T. Fire safety design and concrete. United Kingdom,: Longman Scientific and technical; 1993.

[75] Lie TT, Chabot M. A method to predict the fire resistance of circular concrete filled hollow steel columns. Journal of Fire Protection Engineering. 1990;2:111-24.

Advanced Steel Construction – Vol. 22 No. 1 (2026) 64–77
DOI:10.18057/IJASC.2026.22.1.6

APPLICATION OF IMPROVED DUAL-POPULATION OPTIMIZATION FRAMEWORK IN DESIGN OF GRID STRUCTURE

Xu-Chen Xu [2, *], Hong-Bo Liu [1, 3], Zhi-Hua Chen [1, 2] and Ting Zhou [4]

[1] *State Key Laboratory of Hydraulic Engineering Simulation and Safety, Tianjin University, Tianjin 300072, China*
[2] *Department of Civil Engineering, Tianjin University, Tianjin 300072, China*
[3] *Department of Civil Engineering, Hebei University of Engineering, Handan 056000, China*
[4] *School of Architecture, Tianjin University, Tianjin 300072, China*
** (Corresponding author: E-mail: xcxu_2015@163.com)*

ABSTRACT

With the advantages of simple form, beautiful appearance, uniform force and strong span ability, grid structure has been widely used in long-span space structure. The traditional design often relies on the experience of engineers with low efficiency and using heuristic algorithms to drive design is a very good way. Simple genetic algorithm is a typical heuristic algorithm, the concept is clear, but easy to "precocious" or even not convergence. Based on the idea of "dual-population evolution", this paper introduces a series of strategies, and constructs an improved dual-population genetic algorithm (IDPGA). Two subpopulations evolve independently and exchange some individuals to prevent falling into local optima and expand searching capabilities. Then, combined with ABAQUS script, two acceleration strategies are adopted to form an intelligent optimization framework for solving the grid structure design problems, including static and dynamic optimization problems. The results show that the algorithm is effective, reliable, robust and accurate. In addition, in practical application, a satisfactory engineering solution can be found without fully exerting the optimization ability of the algorithm.

ARTICLE HISTORY

Received: 21 February 2025
Revised: 3 June 2025
Accepted: 4 June 2025

KEYWORDS

Grid structure;
Dual-population;
Genetic algorithm;
Optimization;
Design

1. Introduction

Grid structure generally including trusses, reticulated shells and other structural forms has been widely used in railway stations, exhibition centers, auditoriums, stadiums, terminals and other large public facilities. The traditional structural design often relies on the experience of engineers, who initially draw up the structural design parameters for trial calculation, and adjust them repeatedly according to the results until a satisfactory design scheme is obtained. The whole design process is tedious, the workload is large, the labor cost is high, and the obtained design scheme is not necessarily the optimal scheme in theory. Therefore, how to reduce labor costs and effectively improve design efficiency is of great significance. The working principle of heuristic algorithms is that people simulate biological phenomena in nature to solve practical problems. The requirements of the algorithms for problems are relatively "mild", and many cases prove that the algorithms are effective and reliable. Using heuristic algorithms to design grid structure can undoubtedly significantly improve efficiency.

With the improvement of computer's computing power, heuristic algorithms have gradually been applied to various fields. Doğan et al.[1] used hunting search algorithm to carry out the effect of beam-to-column connections on the minimum weight design of steel plane frames. Talaslioglu [2, 3] utilized pareto archived genetic algorithm to optimize the design of tubular lattice girders in a way of minimizing its entire weight and joint displacement and maximizing its load-carrying capacity and utilized a multi-objective design optimization approach – ImpNSGAII to concern with the design optimization of geometrically nonlinear lattice girders. Kunz et al.[4] implemented the TLBO method for weight-based optimization of space trusses.

Genetic algorithm is a typical heuristic algorithm, whose structure is clear and easy to understand, but it is easy to "precocious" and the solution is not accurate or even convergent. In order to improve the search performance, scholars have made many attempts in the past to solve their own problems. At the level of algorithm, Srinivasa et al.[5] proposed an adaptive migration model, Li et al.[6] proposed a multi-population agent genetic algorithm (MPAGAFS), Park et al.[7] proposed a dual-population genetic algorithm, Umbarkar et al.[8] proposed a multi-threaded parallel dual-population genetic algorithm, and Pourvaziri et al.[9] proposed a mixed multi-population genetic algorithm. These algorithms have achieved good results in solving individual mathematical optimization problems, but a considerable part of the algorithms are limited to solving individual unconstrained optimization problems, while the vast majority of practical engineering problems are multi-constrained optimization problems. Obviously, it is difficult to apply these algorithms to the grid structure in dealing with constrained optimization problems.

Regarding the optimization of grid structure, Mu et al. [10, 11] directly used genetic algorithm to solve an optimal design problem of a 3-bar planar truss. Then the "niche" technology was introduced into the genetic algorithm, the fuzzy control idea was used to dynamically adjust the recombination and mutation probability, and the finite element software ANSYS was used to design the roof of a parrot pavilion with three different initial decision variables. Li et al.[12] considered symmetry and directly used genetic algorithm to carry out topology optimization design for a 72-bar grid, by judging whether the cross-sectional area of the bar is a small number to determine whether the bar is available. Some solutions have been obtained basically of own. However, they are all individual optimization cases, and there is a lack of systematic research on the optimization design of grid structures. The application of genetic algorithms in grid structures is even less. From careful observation of these few cases, it can be discovered that in some problems, the algorithm still oscillates in the late stage of evolution, does not fully converge, and even develops in a worse direction. There is still a large optimization space and the algorithm is not complete.

For the detailed design stage of the grid structure, this paper improves the genetic algorithm to overcome its shortcomings, uses it to solve the problem of determining the cross-section of the members, and conducts a systematic study on its performance.

2. Optimization framework

2.1. Construction of IDPGA

Dual population evolution means that two populations evolve separately and interfere with each other, which not only ensures population diversity but also prevents population from falling into local optimal. Based on this idea, a series of strategies are introduced to improve the simple genetic algorithm to form an improved dual-population genetic algorithm (IDPGA), in which one subpopulation is responsible for detecting, the other for developing. The detailed structure of the algorithm has been explained in reference[13]. Here are some main strategies.

Elite remaining strategy: For detecting subpopulation and developing subpopulation, the best individuals of the parent are taken out, the remaining individuals evolve into offspring, the worst individuals in the offspring are removed, and the best individuals in the parent are added to form a new generation of population. It can ensure that the best individuals in the evolution process will not be lost due to recombination and mutation, and improve the accuracy of the algorithm.

Dynamic migration operator: After each generation, a certain number of individuals are exchanged between the detecting subpopulation and developing subpopulation. Considering that the number is too small to interfere with, and

too large number may completely break the evolution rhythm, resulting in difficult convergence. When the algorithm was used to solve complex mathematical problems in reference[13], considering that the population size of most problems is 100, the size of the dynamic migration operator is set to a random integer between 5 and 1/10 of the population size. This parameter value is adopted in this paper.

Separation of objective and constraints: The selection operator adopts the tournament selection, thus avoids the combination of constraints and the objective function and the introduction of penalty function. When evaluating individuals, there is no longer to calculate the fitness, but to directly determine the superiority or inferiority based on the objective value and constraint violation of the individual.

Normalization of constraints: The influence of constraints on individuals is considered as evenly as possible to eliminate the difference of magnitudes among different constraints and avoid premature evolution of individuals in one direction.

The complete process of IDPGA is shown in Fig. 1.

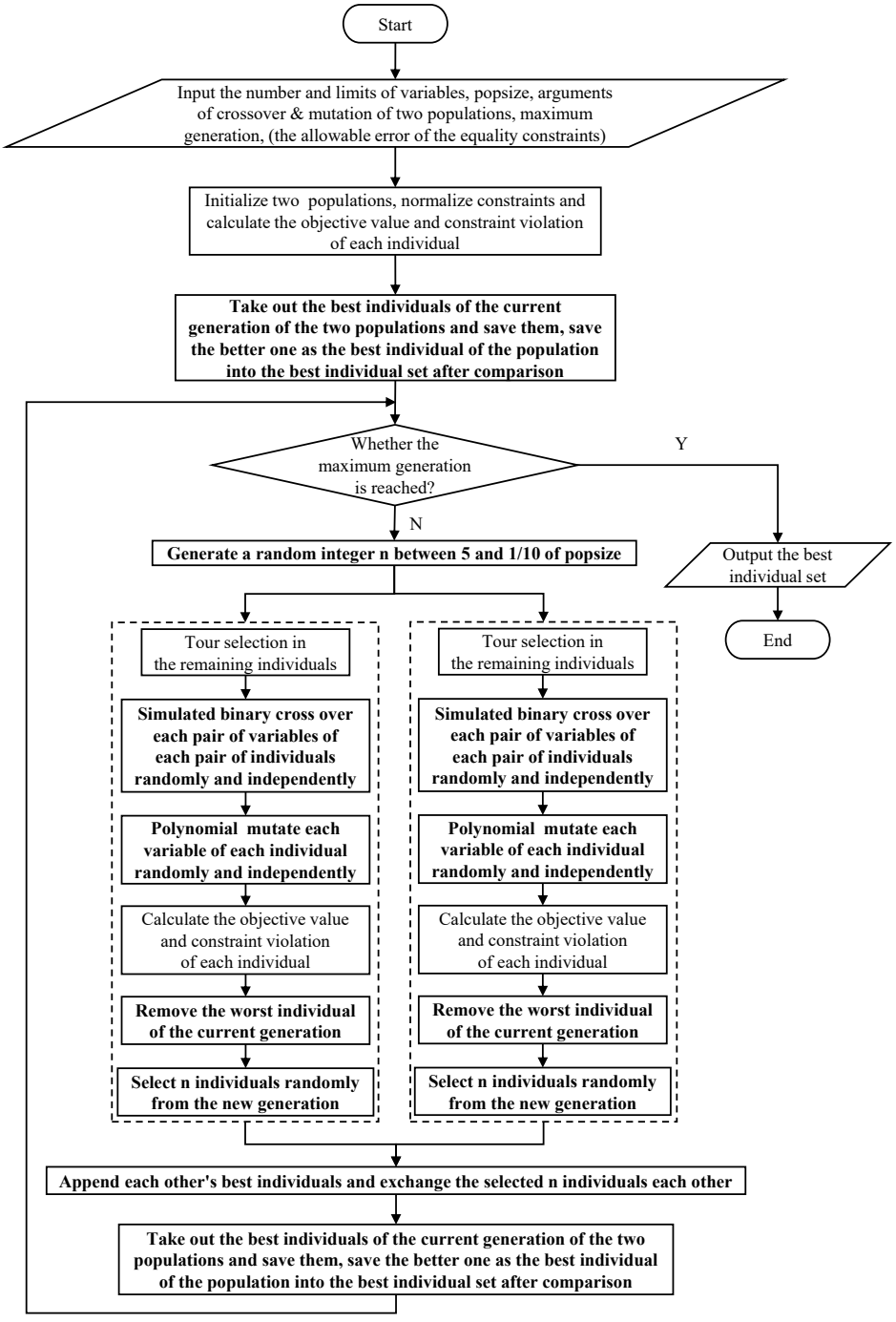

Fig. 1 The flowchart of IDPGA

2.2. Benchmarks and results

In reference[13], 14 benchmarks has been selected to test the performance of IDPGA. It is found that the algorithm is reliable with good robustness and high accuracy. Here is a brief explanation of the results of f6. The mathematical description and optimum are shown as Eq. (1).

The contour lines of objective and feasible region of decision variables are plotted in Fig. 2. The optimum is marked with a red point. The feasible region is small and the contour lines are dispersive, which means it is difficult to find the optimum.

$$\begin{aligned} &\min f(\mathbf{x}) = -\frac{\sin^3(2\pi x_1)\sin(2\pi x_2)}{x_1^3(x_1+x_2)} \\ &s.t.\begin{cases} g_1(\mathbf{x}) = x_1^2 - x_2 + 1 \le 0 \\ g_2(\mathbf{x}) = -x_1 + (x_2-4)^2 + 1 \le 0 \\ 0 \le x_i \le 10 \quad (i=1,2) \end{cases} \\ &f_{opt}(1.2280, 4.2454) = -0.0958 \end{aligned} \tag{1}$$

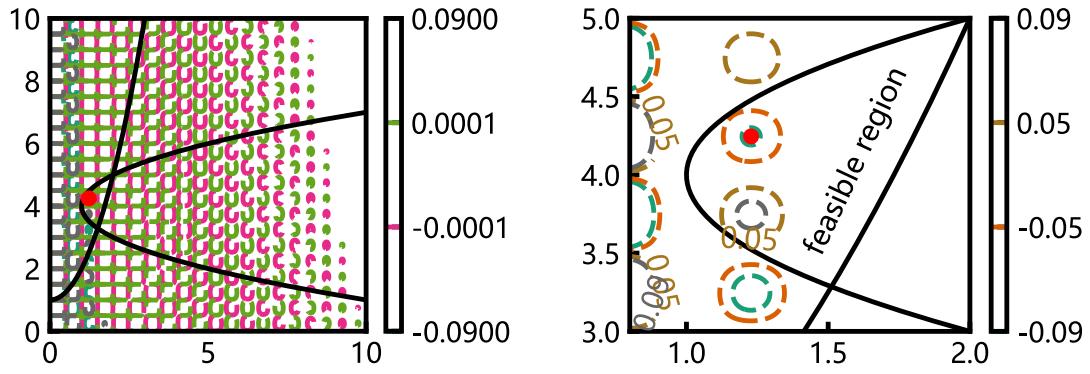

(a) f6 (b) f6_local

Fig. 2 The contour lines and feasible region

IDPGA was run 30 times to solve f6 and the results are shown in Table 1. The constraint violation here is the sum of constraints after normalization. Then the decision variables corresponding to the best and worst results of 30 runs are presented as shown in Table 2.

In general, the final solution found is a feasible solution with constraint violation of 0.000000, which illustrates IDPGA is effective. Meanwhile, the best solution obtained by IDPGA is equal to the theoretical optimum, and the decision variables obtained are very close to the theoretical point, which illustrates IDPGA is accurate. The standard deviation of objective is 0.0000, which illustrates IDPGA performs relatively good robustness. So IDPGA is reliable.

The whole evolution processes of the best and worst results of 30 runs are plotted in Fig. 3. Thereinto, IDPGA-B means the best result and IDPGA-W means the worst result.

Table 1
The objective and constraint violation of 30 runs

Objective				Constraint violation		
Best	Worst	Mean	SD	Min.	Max.	Mean
-0.0958	-0.0958	-0.0958	0.0000	0.000000	0.000000	0.000000

Table 2
Decision variables corresponding to the best and worst results

Theoretical	Best	Worst
(1.2280, 4.2454)	(1.2280, 4.2454)	(1.2280, 4.2454)

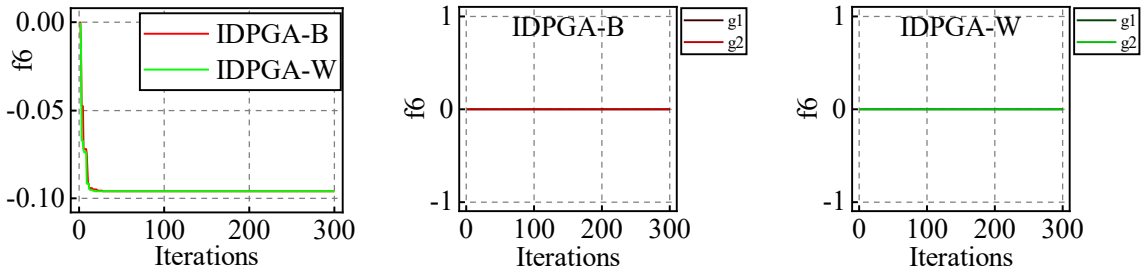

(a) objective (b) constraint violation

Fig. 3 The evolution figures

Constraint violation approaches zero at the beginning of evolution, similarly, the objective decreases very quickly at the beginning, which means IDPGA has searched for a feasible solution very quickly. Moreover, it is obviously discovered that IDPGA has converged to an acceptable solution before the stop criterion.

The errors of the simulated value relative to the theoretical value are calculated and shown in Fig. 4. The red columns mean feasible solutions and the green columns mean infeasible solutions.

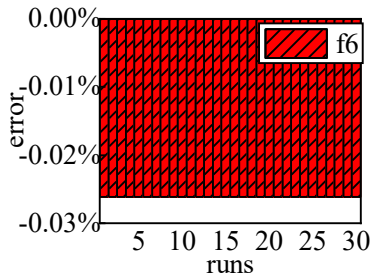

Fig. 4 The errors

Combined with the conclusions above, it can be seen IDPGA is able to obtain acceptable solutions in the face of complex mathematical problems, even better solutions in some cases.

For the benchmarks mentioned in reference[13], this paper supplemented the calculation of the Euclidean distance between the solutions obtained of 30 times and the theoretical optimal point, and plotted these distances as Nightingale rose diagrams, as shown in Fig. 5. Each sector in each diagram represents the decision variable of the solution once, and the radius of the sector represents the distance between the solution and the theoretical optimal point. Nightingale Rose diagram is a bar chart in polar coordinate system, all the data are distributed in a sector, and the sector radius represents the size of the data. Since the area of the sector is squared with the radius, the diagram scales the data proportionally and can intuitively show the difference among similar data.

From Fig. 5, the sector distribution in each diagram is relatively uniform, and the radius of most sectors is close to each other, which indicates that the distance between the solution and the theoretical optimum is close, and IDPGA is relatively stable. Except for problems f3 and f12, the distance between the results of other problems and the theoretical optimum is small, which shows that IDPGA solves most problems more accurately. By observing the decision variables of problems f3 and f12, it is found that there are differences of orders of magnitude between each component. Meanwhile, the algorithm adopts constraint normalization processing to avoid the influence of such differences as much as possible, and considers the influence of each component evenly as much as possible in the search process. Such results show that this constraint normalization processing is not universal.

Considering that the actual engineering optimization problems are simpler than these mathematical optimization problems, IDPGA is still reliable.

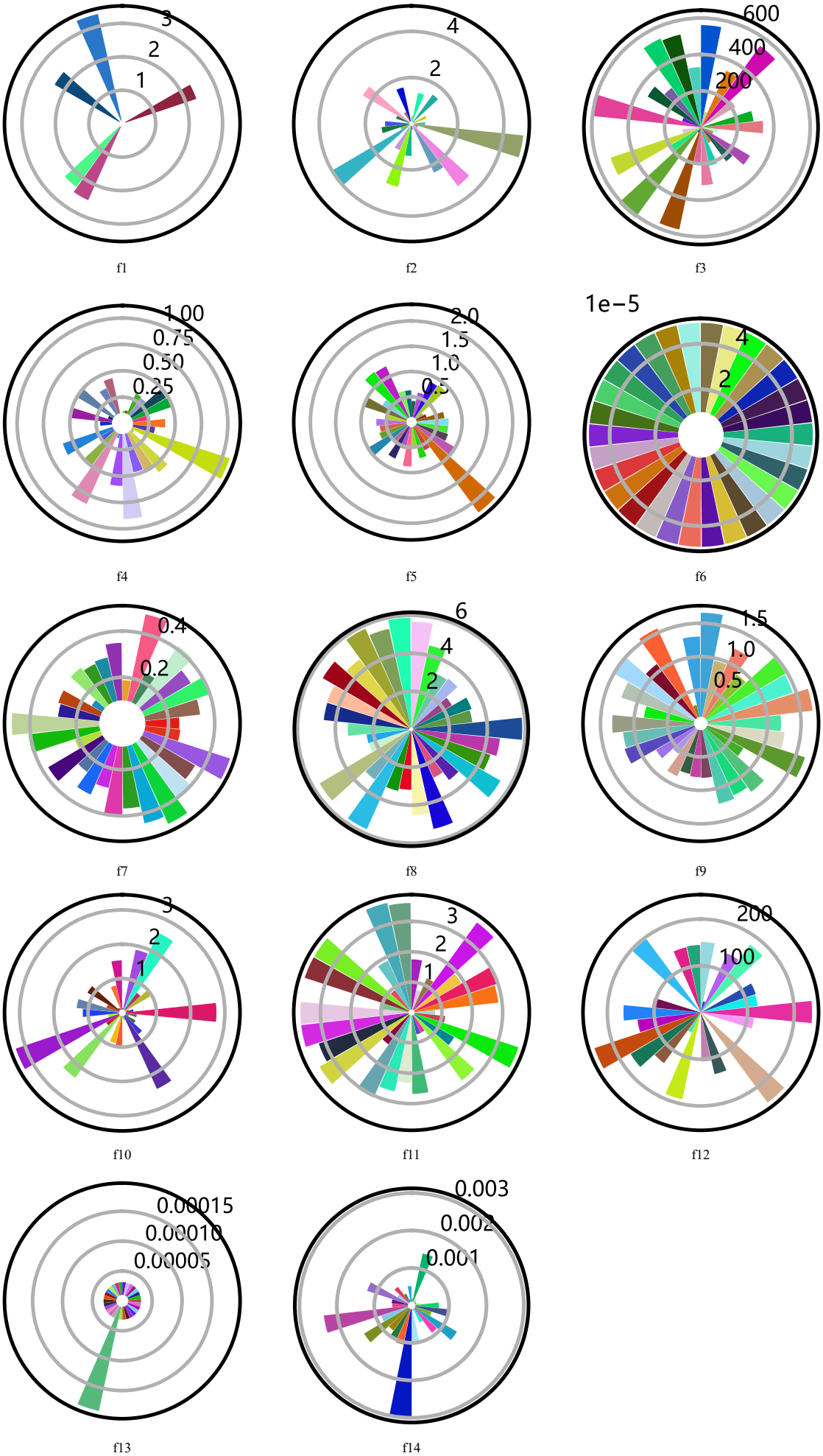

Fig. 5 The distance between the solution and the theoretical optimum

2.3. Interaction between IDPGA and ABAQUS

There is no universal algorithm, and the application of any algorithm has certain restrictions. In other words, if an algorithm is suitable for solving a certain problem or a certain class of problems, there must be other problems that are "powerless", which is the famous "No Free Lunch" theory[14]. Therefore, this paper will not look for the so-called "universal" algorithm, nor will it look for complex algorithms, but as far as possible to apply IDPGA to grid structure optimization problems. Considering that the algorithm in this paper is completed in the current popular Python language, while the secondary development script of the general finite element analysis software ABAQUS supports Python language, and considering that there are few scripts for the co-simulation optimization of Python and ABAQUS in the existing literature, this paper uses ABAQUS as a solver for simulation. So only one programming language, Python is required to achieve all optimization functions, which facilitates the subsequent development of specialized ABAQUS plugins.

In fact, corresponding to the various functional modules in the GUI of ABAQUS, there are special program blocks in the model script. The GUI model corresponds to the object of the Python language, each function module of the GUI corresponds to each class of Python, and the parameters under a function module of the GUI correspond to various functions under a class of Python. In this paper, the interactive optimization script for the mechanical performance of the grid structure is compiled by referring to 'Python 3.10.9 Help Documentation'[15], 'Scripting User's Guide', 'Scripting Reference Guide' and 'Getting Started With Abaqus: Interactive Edition' in the ABAQUS help document[16].

In the optimization framework, IDPGA generates the initial model parameters and creates the initial analysis script, ABAQUS runs the parameterized script for analysis and writes the result data to the txt file, IDPGA reads the data from the txt file, updates the model and continues to drive the iteration, repeating these processes until the iteration is completed, as shown in Fig. 6.

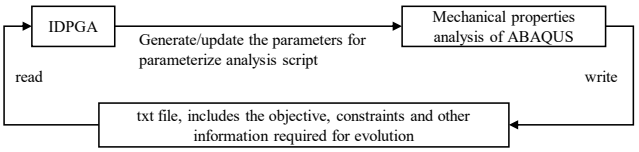

Fig. 6 The diagram of interaction between IDPGA and ABAQUS

When the IDPGA solves mathematical problems, it first initializes the population, then calculates the corresponding objective and constraint violation and other information of different individuals. Since the objective and constraint function are both explicit, the solving speed is very fast, so the information of individuals is solved one by one. When solving the grid structure optimization problem, ABAQUS needs to be repeatedly called for multiple analyses. ABAQUS takes a certain amount of time to create the model and perform the analysis. For each generation, the optimization framework needs to calculate the information such as the objective and constraint violation of each individual. In other words, ABAQUS is repeatedly called for analysis and writing many times (population size). If the model is still analyzed one by one, obviously, the time cost will be quite large. The optimization framework adopts two acceleration strategies for analysis, which gives full play to the computer hardware, saves solving time and improves solving efficiency.

Specific operations of grouping and parallel computing strategy: Firstly, the maximum number of models that can be simultaneously solved by ABAQUS is set according to the computer hardware. Then, all models that need to be submitted for analysis are grouped, that is, the population size is divided by this number, and the number of groups is obtained by adding one after the round down. Finally, according to these groups, ABAQUS is called at the same time to analyze all models in a certain group. Until the models of all groups have been analyzed.

When running the optimization framework in practice, the Python subprocess module 'subprocess' is used to call ABAQUS through the shell layer. In addition, multiple processes are created through the class 'Popen' to run multiple ABAQUS models "simultaneously", and the function 'wait' is set to block to realize the writing after completing. It is worth noting that the creation of multiple processes through the 'Popen' is sequential, so multiple ABAQUS models are not strictly running at the same time, but the time difference caused by the creation of processes is very small, almost instantaneous, and can be considered at the same time.

Comparison strategy between parent and offspring: Careful observation of the structure of IDPGA shows that each iteration needs to calculate the objective and constraint violation of all individuals. For mathematical problems, this time is very short, but for grid structure optimization problems, the time of calling ABAQUS is very large. In IDPGA, the developing subpopulation has a small recombination probability and mutation probability, and the individuals are not easy to lose in the evolution, while the detecting subpopulation has a large recombination probability and mutation probability, and the individuals are easy to lose in the evolution. In other words, when the parent individuals of a certain generation evolve into a new generation of offspring individuals, some individuals may not participate in recombination and mutation, but are directly retained, so the algorithm does not need to calculate the objective and constraint violation of these individuals again, thereby further saving the solving time.

3. Static performance optimization problem of grid structure

3.1. Description of problems

The optimization design problem of static performance of grid structure with constraints of stress and displacement can be described as follows: the objective is the mass of grid structure, the constraints are the allowable stress of each member and the allowable displacement of each node, and the decision variable is the cross-sectional area of each member, and the problem is to find the minimum mass of grid structure. Correspondingly, the mathematical expression of the problem is shown as Eq. (2), where $f(\mathbf{x})$ is the mass of grid structure, ρ is the density of material, A_i and L_i are the cross-sectional area and length of each member, n is the number of members, $\sigma_j(\mathbf{x})$ and $[\sigma]$ are stress and allowable stress of each member, the allowable stresses of the tension member and compression member are often different in practice, $\delta_k(\mathbf{x})$ and $[\delta]$ are displacement and allowable displacement of each node, the allowable displacements of nodes in each direction are often different in practice, $A_{\max}$ and $A_{\min}$ are the upper and lower bounds of the cross-sectional area of each member respectively.

$$\begin{aligned} &\min f(\mathbf{x}) = \sum_{i=1}^{n} \rho A_i L_i \\ &s.t. \begin{cases} \sigma_j(\mathbf{x}) \le [\sigma] & (j = 1,2,...,p) \\ \delta_k(\mathbf{x}) \le [\delta] & (k = p+1, p+2,...,q) \\ A_{\min} \le A_i \le A_{\max} & (i = 1,2,...,n) \end{cases} \end{aligned} \tag{2}$$

The normalization of stress and displacement constraints adopts the form as Eq. (3).

$$\begin{cases} \dfrac{\sigma_j(\mathbf{x}) - [\sigma]}{[\sigma]} \le 0, & j = 1,2,...,p \\ \dfrac{\delta_k(\mathbf{x}) - [\delta]}{[\delta]} \le 0, & k = p+1, p+2,...,q \end{cases} \tag{3}$$

3.2. Simulation settings

The optimization framework was utilized to solve design problems of 10-bar plane truss, 52-bar plane truss, 200-bar plane truss and 120-bar single-layer lattice shell successively. Considering the scale of the problem, computers with different hardware were used for different problems, as shown in Table 3. Hardware 1: Intel Core i7-7700 3.60GHz, 16 GB RAM, 8CPUs, single thread, Win10 platform. Hardware 2: AMD EPYC 7H12 2.60GHz, 32 GB RAM, 32CPUs, single thread, Win10 platform.

Table 3
Computer properties of different problems

Grid structure	Hardware	Whether to adopt the two acceleration strategies
10-bar plane truss	1	No
52-bar plane truss	1	Yes
200-bar plane truss	2	Yes
120-bar single-layer lattice shell	2	Yes

Parameters of IDPGA: The population size was taken as 100. The probabilities of recombination and mutation of developing subpopulation were set as 0.3 and 0.001, the probabilities of recombination and mutation of detecting subpopulation were set as 0.9 and 0.05. The arguments η_c and η_m of

developing subpopulation were set as 1 and 5, the arguments η_c and η_m of detecting subpopulation were set as 1 and 100. The maximum number of generations was different for different problems. The stop criterion was that the maximum number of generations had been reached.

All results were automatically written to Excel files after the optimization framework finished running.

3.3. Problems solving

3.3.1. Optimization design of 10-bar plane truss

The grid structure in this problem is a plane truss composed of 10 elements. As shown in Fig. 7, vertical and downward concentrated force are applied to nodes 2 and 4 respectively. The objective is the mass of the structure, and the 18 constraints include stress constraints of 10 elements and horizontal and vertical displacement constraints of nodes 1, 2, 3 and 4. The decision variable is the cross-sectional area of each element, and 10 in total.

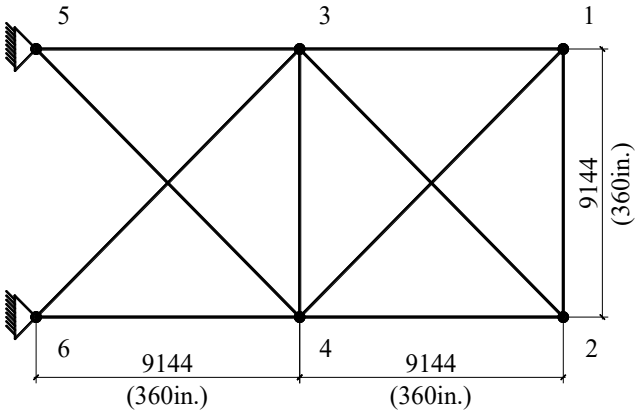

Fig. 7 Diagram of the 10-bar plane truss

The optimization framework was applied to solve this problem for 13 times consecutively, and the results were statistically analyzed, including the objective, constraint violation and time consumption, as shown in Table 4.

Table 4
Optimization results of 13 runs

Run	Objective (t)	Constraint violation	Time (h)
1	2.36287	0	18.0740
2	2.37119	0	17.8861
3	2.37320	0	17.6013
4	2.38420	0	17.5708
5	2.36838	0	17.4421
6	2.36346	0	17.7583
7	2.36565	0	17.6355
8	2.35837	0	17.6093
9	2.37954	0	17.5962
10	2.37536	0	17.6283
11	2.35842	0	17.8011
12	2.36553	0	17.7377
13	2.36240	0	17.7004
Best	2.35837	0	17.4421
Worst	2.38420	0	18.0740
Mean	2.36835	0	17.6955
SD	0.00765	-	-

From the constraint violation, the constraint violation of any solution is 0, that is, all constraints are satisfied, indicating that all solutions are feasible solutions, and IDPGA is reliable. From the objective, 13 solutions are close, the best result is 2.35837t, and the worst result is 2.38420t, both of which are close, indicating that IDPGA is robust. From the time consumption, IDPGA takes less than 18h to solve this problem on average. Then, the evolution process diagram of the objective of the 13 results was uniformly drawn, as shown in Fig. 8.

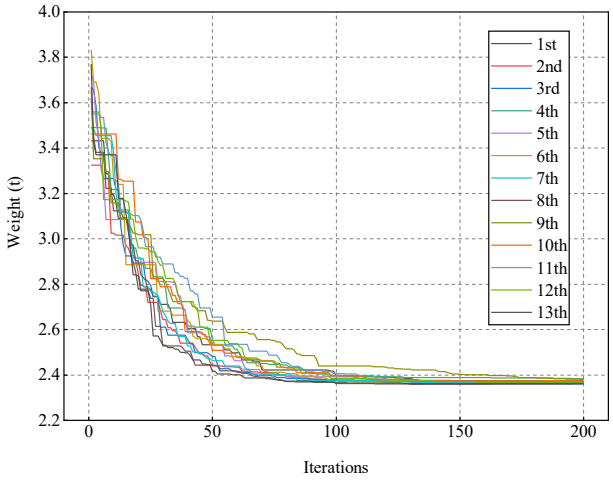

Fig. 8 The evolution process of the objective of 13 results

It can be seen that the objective decreases rapidly before 100 iterations, and then slowly decreases and gradually converges. In most cases, after about 150 iterations, the algorithm has obtained a satisfactory solution. Next, the objectives of the 30 results were plotted in a bar chart, as shown in Fig. 9.

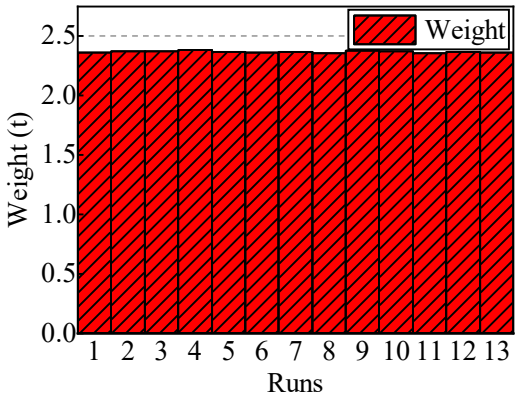

Fig. 9 The bar chart of the objectives of 13 runs

It can be intuitively seen that the height of each bar is very close to others, which shows that the algorithm has good robustness again. Finally, some of the best results reported by other existing algorithms were selected and compared with the results of this algorithm. All the results were listed in Table 5.

Table 5
The best results reported by other algorithms

Algorithm	PSO[17]	PSOPC[17]	HPSO[17]
Objective (t)	2.53184	2.53714	2.50926
Algorithm	GA[18]	FEAPGEN[19]	GSS[20]
Objective (t)	2.48566	2.52057	2.51003

It can be seen that the best value of 2.35837t obtained by IDPGA is better than the results reported above, indicating that the algorithm has good accuracy. Accordingly, the optimized model is shown in Fig. 10, where the maximum stress of the tension element is 144.21MPa, the maximum stress of the compression element is -58.13MPa, the maximum horizontal displacement of the node is -14.57mm, and the maximum vertical displacement is -50.80mm.

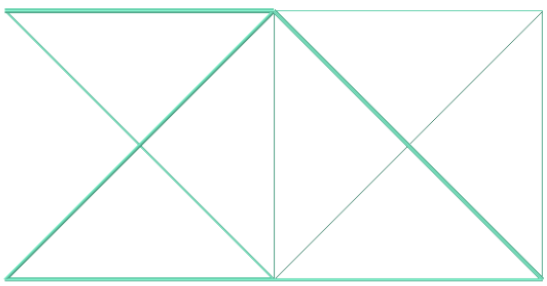

Fig. 10 The diagram of optimized model

3.3.2. Optimization design of 52-bar plane truss

The grid structure in this problem is a plane truss composed of 52 elements. As shown in Fig. 11, the elements are divided into 12 groups according to the cross-sectional area, the group number is identified by the number without brackets, and the horizontal right and the vertical upward concentrated force are applied to the nodes (1), (2), (3) and (4), respectively. The objective is the mass of the structure, because of asymmetrical force, and the 52 constraints include stress constraints of 52 elements and no displacement constraints of nodes. The decision variable is the cross-sectional area of each element, and 12 in total.

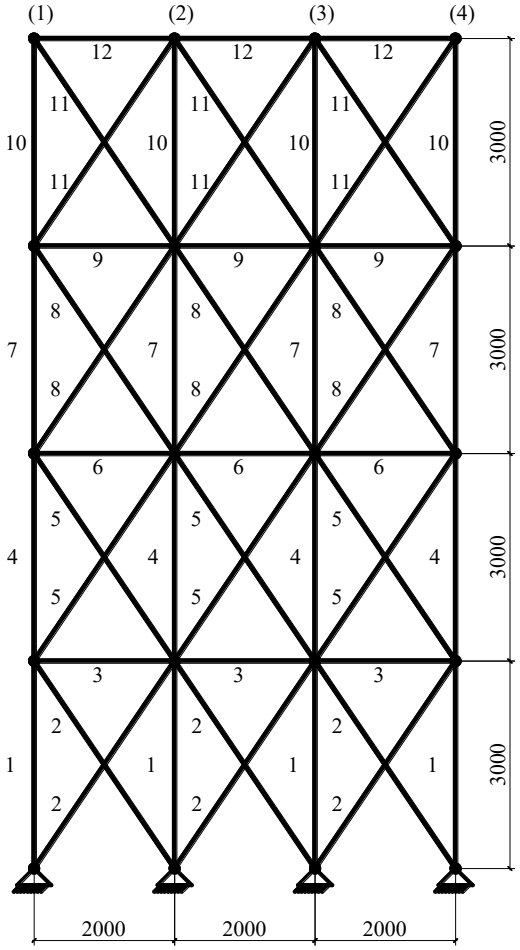

Fig. 11 Diagram of the 52-bar plane truss

From the results of 10-bar plane truss, it can be seen that IDPGA is very robust. Therefore, the optimization framework was only run once to solve the next problems. Similarly, the results were statistically analyzed as shown in Table 6.

Table 6
Optimization results

Objective (t)	Constraint violation	Time (h)
1.89667	0	46.9925

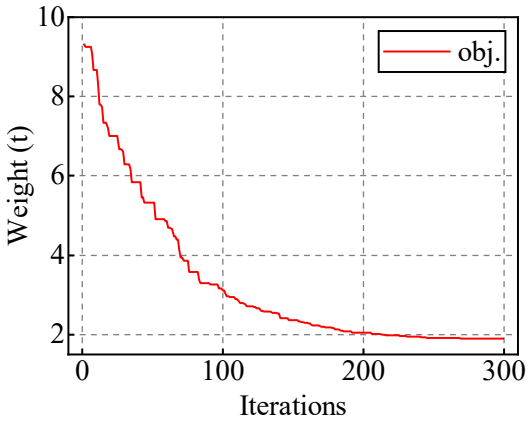

Fig. 12 The evolution process of the objective

Similarly, the constraint violation of the solution is 0, indicating that the solution is a feasible solution. IDPGA takes about 47h to solve this problem. The evolution process diagram of the objective was drawn, as shown in Fig. 12.

It can be seen that the objective decreases rapidly before 200 iterations, and then slowly decreases and gradually converges. After about 250 iterations, the algorithm has obtained a satisfactory solution. Finally, some of the best results reported by other existing algorithms were selected and compared with the results of this algorithm. All the results were listed in Table 7.

Table 7
The best results reported by other algorithms

Algorithm	WCA[21]	IMBA[21]	DE[22]
Objective (t)	1.90261	1.90261	1.90261
Algorithm	AEDE[22]	FWA[23]	IFWA[24]
Objective (t)	1.90261	1.90261	1.90261

It can be seen that the best value of 1.89667t obtained by IDPGA is better than the results reported above, indicating that the algorithm has good accuracy. Accordingly, the optimized model is shown in Fig. 13, where the maximum stress of the tension element is 179.99MPa, the maximum stress of the compression element is -144.00MPa.

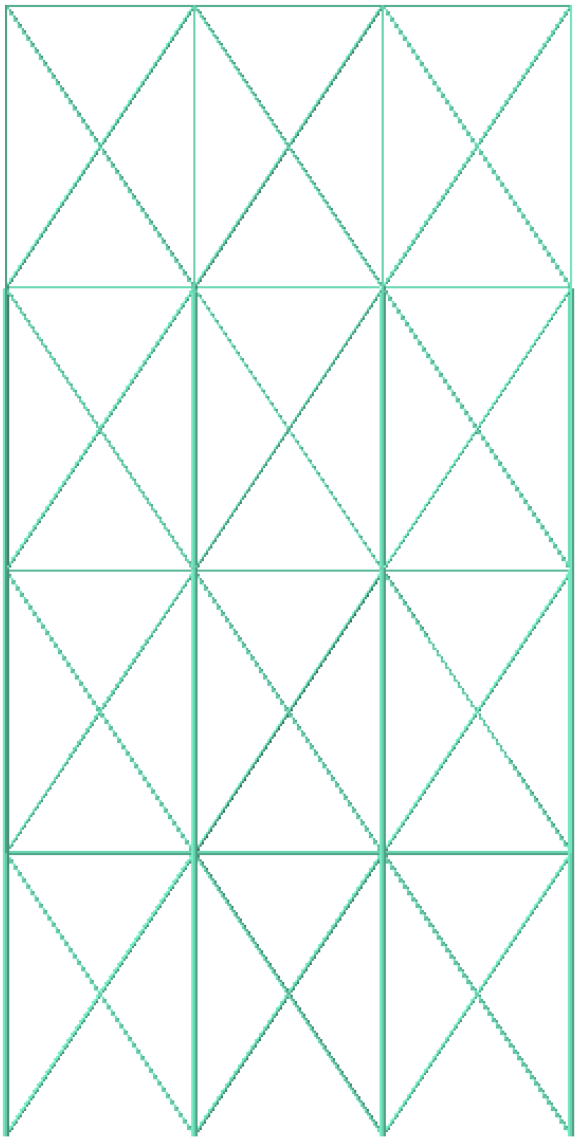

Fig. 13 The diagram of optimized model

3.3.3. Optimization design of 200-bar plane truss

The grid structure in this problem is a plane truss composed of 200 elements. As shown in Fig. 14, the elements are divided into 29 groups according to the cross-sectional area, the group number is only identified by the number without brackets in the semi-structure because of symmetry, the horizontal right concentrated force is applied to the nodes (1), (6), (11), (16), (21), (26), (31),

(36), (41), (46) and (51), and the vertical downward concentrated force is applied to the nodes (1) to (55). The objective is the mass of the structure, and the 200 constraints include stress constraints of 200 elements and no displacement constraints of nodes. The decision variable is the cross-sectional area of each element, and 29 in total.

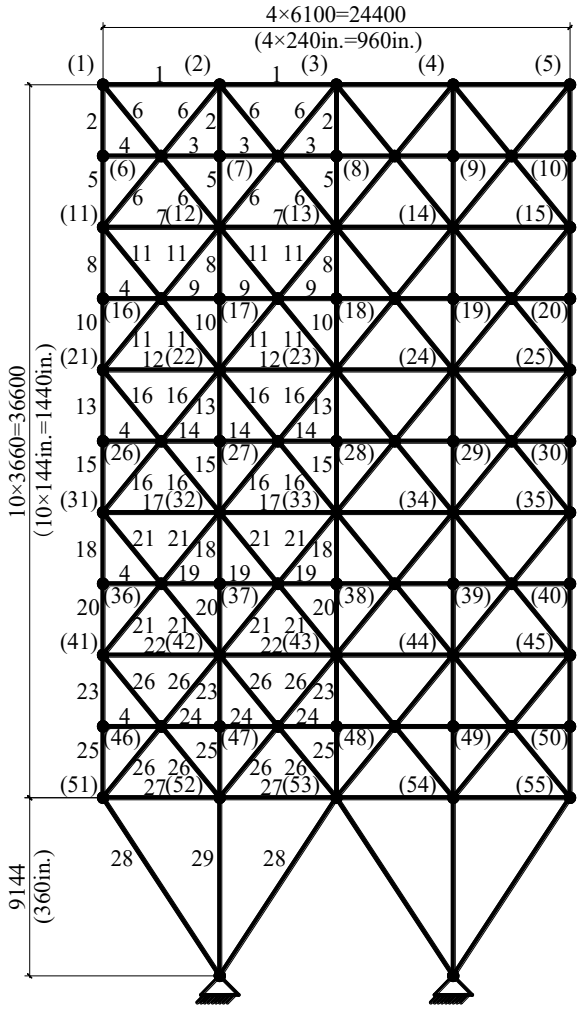

Fig. 14 Diagram of the 200-bar plane truss

The optimization framework was run once to solve the next problems. Similarly, the results were statistically analyzed as shown in Table 8.

Table 8
Optimization results

Objective (t)	Constraint violation	Time (h)
12.32858	0	28.3835

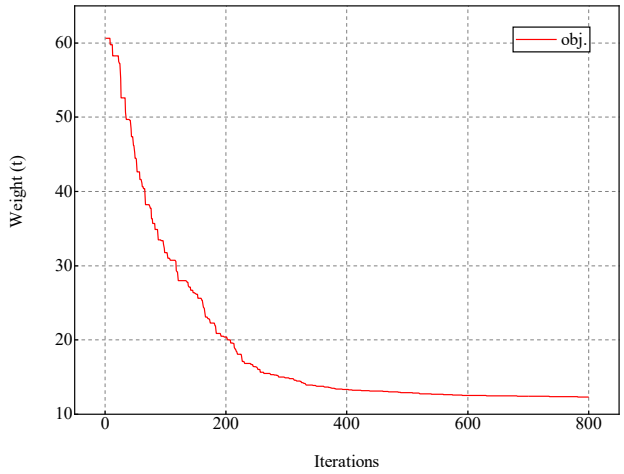

Fig. 15 The evolution process of the objective

Similarly, the constraint violation of the solution is 0, indicating that the solution is a feasible solution. IDPGA takes about 28h to solve this problem. The evolution process diagram of the objective was drawn, as shown in Fig. 15.

It can be seen that the objective decreases rapidly before 400 iterations, and then slowly decreases and gradually converges. After about 600 iterations, the algorithm has obtained a satisfactory solution. Finally, some of the best results reported by other existing algorithms were selected and compared with the results of this algorithm. All the results were listed in Table 9.

Table 9
The best results reported by other algorithms

Algorithm	ESASS[25]	DE[22]	AEDE[22]
Objective (t)	12.73483	12.65594	12.63640
Algorithm	FWA[23]	IFWA[24]	
Objective (t)	12.59987	12.45077	

It can be seen that the best value of 12.32858t obtained by IDPGA is better than the results reported above, indicating that the algorithm has good accuracy. Accordingly, the optimized model is shown in Fig. 16, where the maximum stress of the tension element is 68.88MPa, the maximum stress of the compression element is -68.90MPa.

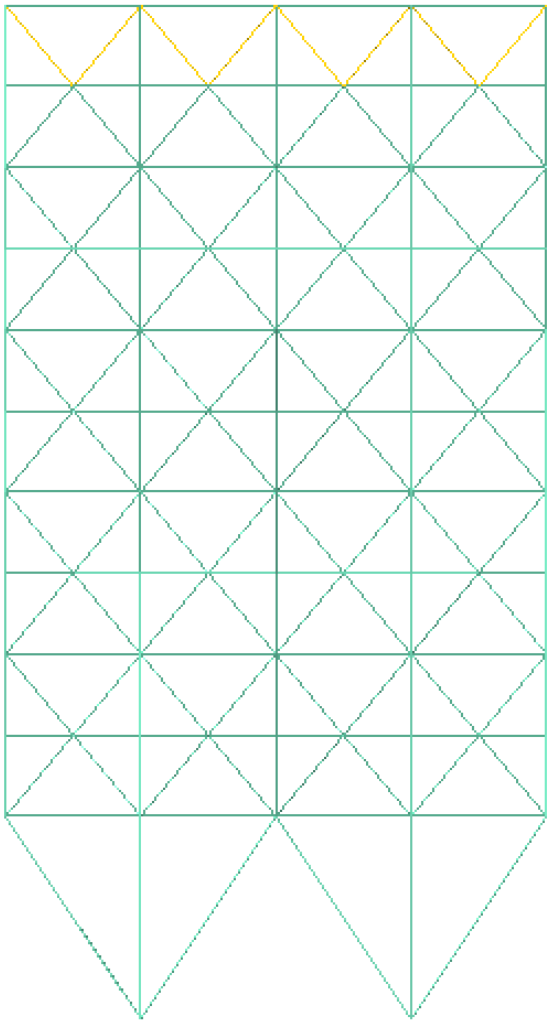

Fig. 16 The diagram of optimized model

3.3.4. Optimization design of 120-bar single-layer lattice shell

The grid structure in this problem is a single-layer lattice shell composed of 120 elements. As shown in Fig. 17, the elements are divided into 7 groups according to the cross-sectional area, the group number is only identified by the number without brackets in a single block because of symmetry, and the vertical downward concentrated force is applied to the nodes (1), (2), (3), and other symmetric nodes respectively.

The material is steel, and the allowable stresses of the tension and

compression elements are different. According to the definition of the American code for the design of steel structures, AIC-ASD[26], the allowable stress of the tension element adopts the form as Eq. (4), where $[\sigma]_{\text{tension}}$ is the allowable stress, f_y is the yield strength of steel.

$$[\sigma]_{\text{tension}} = 0.6 f_y \tag{4}$$

The allowable stress of the compression element is calculated according to two failure modes of elastic buckling and plastic buckling respectively as Eq. (5). E is the elastic modulus of steel, C_c is the critical slenderness ratio parameter, $C_c = \sqrt{\frac{2\pi^2 E}{f_y}}$, λ_i is the slenderness ratio of the ith element, $\lambda_i = \frac{k_i L_i}{r_i}$, k_i is the calculated length coefficient of the ith element, and is 1 for all the elements in this problem, r_i is the section rotation radius of the ith element, and the relationship between it and the cross-sectional area can be defined as $r_i = aA_i^b$ [27], a and b are two constants related to the type of section, and are 0.4993 and 0.6777 for pipes respectively.

$$[\sigma]_{\text{compression}i} = \begin{cases} \dfrac{\left(1 - \dfrac{\lambda_i^2}{2C_c^2}\right) f_y}{\dfrac{5}{3} + \dfrac{3\lambda_i^2}{8C_c} - \dfrac{\lambda_i^3}{8C_c^3}} & \lambda_i < C_c \ (\textit{plastic buckling}) \\ \dfrac{12\pi^2 E}{23\lambda_i^2} & \lambda_i \geq C_c \ (\textit{elastic buckling}) \end{cases} \tag{5}$$

The objective is the mass of the structure. The constraints include the stress constraints of 120 elements and the displacement constraints of all free nodes in three directions. Due to the symmetry, only the constraints of a single block are taken, and there are 19 constraints in total. The decision variable is the cross-sectional area of each element, and 7 in total.

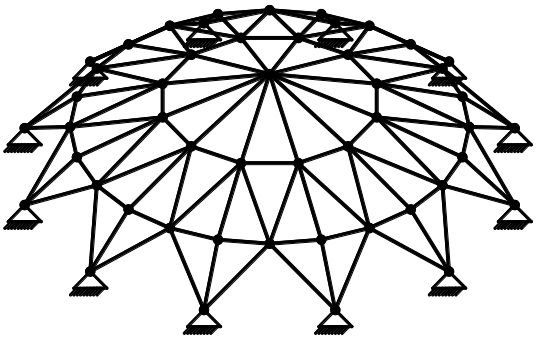

(a) 3D view

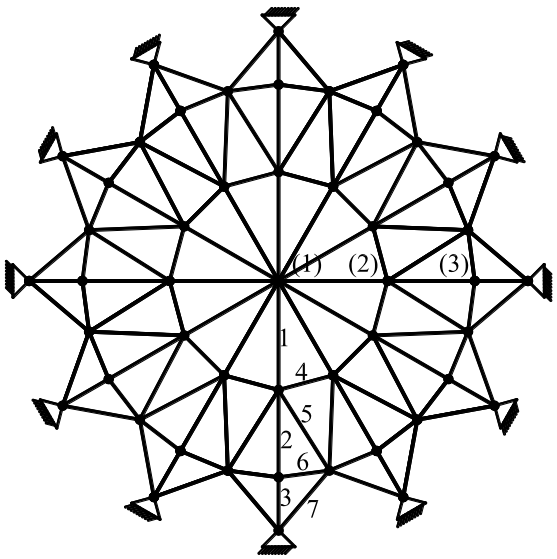

(b) Top view

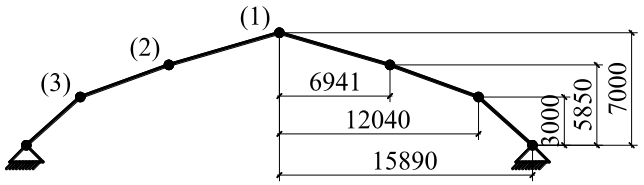

(c) Side view

Fig. 17 Diagram of the 120-bar single-layer lattice shell

The optimization framework was run once to solve the next problems. Similarly, the results were statistically analyzed as shown in Table 10.

Table 10
Optimization results

Objective (t)	Constraint violation	Time (h)
14.44850	0	32.9462

Similarly, the constraint violation of the solution is 0, indicating that the solution is a feasible solution. IDPGA takes about 33h to solve this problem. The evolution process diagram of the objective was drawn, as shown in Fig. 18.

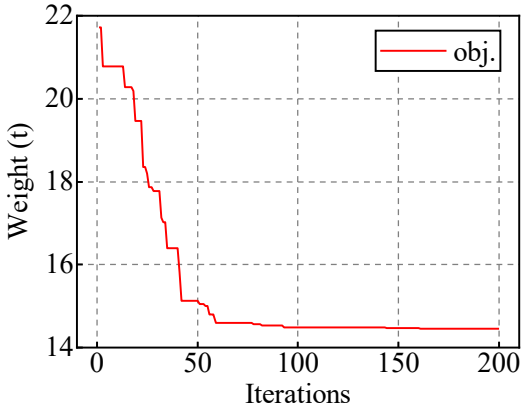

Fig. 18 The evolution process of the objective

It can be seen that the objective decreases rapidly before 60 iterations, and then slowly decreases and gradually converges. After about 100 iterations, the algorithm has obtained a satisfactory solution. Finally, some of the best results reported by other existing algorithms were selected and compared with the results of this algorithm. All the results were listed in Table 11.

Table 11
The best results reported by other algorithms

Algorithm	PSO[28]	MSPSO[28]	HPSSO[29]
Objective (t)	15.08283	15.08250	15.08197
Algorithm	CA[30]	EHO[31]	EHOC[32]
Objective (t)	15.08441	15.34355	15.34355

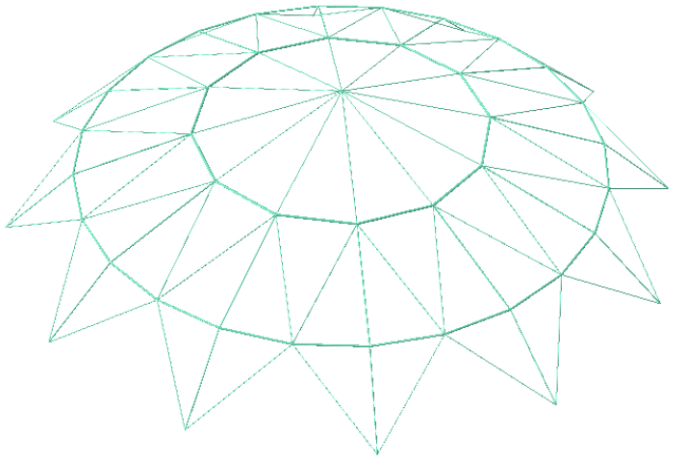

Fig. 19 The diagram of optimized model

It can be seen that the best value of 14.44850t obtained by IDPGA is better than the results reported above, indicating that the algorithm has good accuracy. Accordingly, the optimized model is shown in Fig. 19, where the maximum stress of the tension element is 11.95MPa, the maximum stress of the compression element is -20.10MPa, the maximum displacements of the node are 0.93mm in x direction and y direction, and -5.00mm in z direction.

4. Dynamic performance optimization problem of grid structure

4.1. Description of problems

The optimization design problem of dynamic performance of grid structure with constraints of frequency can be described as follows: the objective is the mass of grid structure, the constraints are several order frequency constraints of grid structure, and the decision variable is the cross-sectional area of each member, and the problem is to find the minimum mass of grid structure. Correspondingly, the mathematical expression of the problem is shown as Eq. (6), where $\omega_j(\mathbf{x})$ and $[\omega]_j$ are the natural frequency and allowable frequency of the *j*th order.

$$\begin{aligned} &\min f(\mathbf{x}) = \sum_{i=1}^{n} \rho A_i L_i \\ &s.t. \begin{cases} \omega_j(\mathbf{x}) \geq [\omega]_j & (j = 1,2,...,q) \\ A_{\min} \leq A_i \leq A_{\max} & (i = 1,2,...,n) \end{cases} \end{aligned} \tag{6}$$

The normalization of frequency constraints adopts the form as Eq. (7).

$$\frac{-\omega_j(\mathbf{x}) + [\omega]_j}{[\omega]_j} \leq 0, \qquad j = 1,2,...,q \tag{7}$$

4.2. Simulation settings

The optimization framework was utilized to solve design problems of 10-bar plane truss, 37-bar plane truss, 200-bar plane truss and 1410-bar double-layer lattice shell successively. Similarly, computers with different hardware were used for different problems, as shown in Table 12. Hardware 1 and Hardware 2 are the same as above.

Table 12
Computer properties of different problems

Grid structure	Hardware	Whether to adopt the two acceleration strategies
10-bar plane truss	1	No
37-bar plane truss	2	Yes
200-bar plane truss	2	Yes
1410-bar double-layer lattice shell	2	Yes

Parameters of IDPGA: The maximum number of generations was different for different problems. Other parameters are the same as above.

All results were automatically written to Excel files after the optimization framework finished running.

4.3. Problems solving

4.3.1. Optimization design of 10-bar plane truss

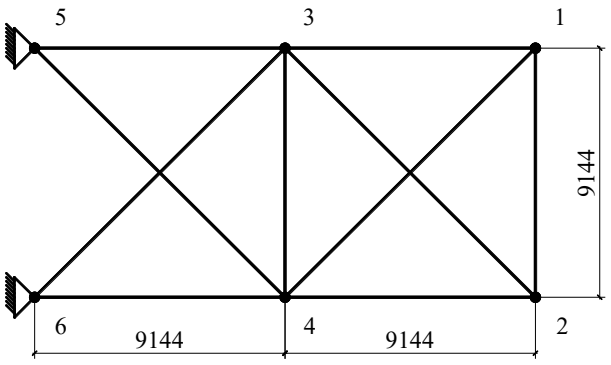

Fig. 20 Diagram of the 10-bar plane truss

The grid structure in this problem is a plane truss composed of 10 elements. As shown in Fig. 20, the concentrated mass is applied to nodes 1, 2, 3 and 4 respectively. The objective is the mass of the structure, and the constraints include natural frequencies of the first 3 orders of structure. The decision variable is the cross-sectional area of each element, and 10 in total.

The optimization framework was run once to solve the next problems. Similarly, the results were statistically analyzed as shown in Table 13.

Table 13
Optimization results

Objective (t)	Constraint violation	Time (h)
0.54183	0	22.5678

Similarly, the constraint violation of the solution is 0, indicating that the solution is a feasible solution. IDPGA takes about 23h to solve this problem. The evolution process diagram of the objective was drawn, as shown in Fig. 21.

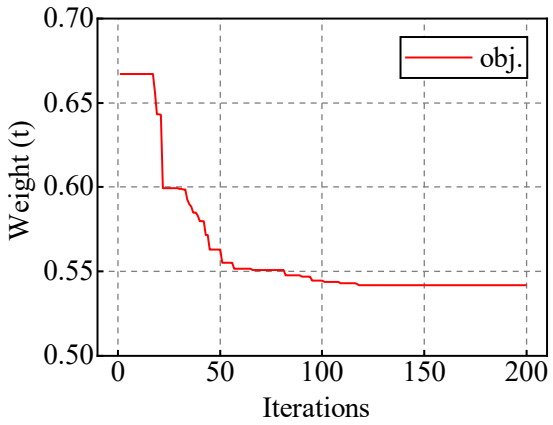

Fig. 21 The evolution process of the objective

It can be seen that the objective decreases rapidly before 50 iterations, and then slowly decreases and gradually converges. After about 100 iterations, the algorithm has obtained a satisfactory solution. Finally, some of the best results reported by other existing algorithms were selected and compared with the results of this algorithm. All the results were listed in Table 14.

Table 14
The best results reported by other algorithms

Algorithm	GA[33]	PSO[34]	CSS[35]
Objective (t)	0.54275	0.53798	0.53195
Algorithm	ECSS[35]	CSS-BBBC[36]	
Objective (t)	0.52925	0.52909	

It can be seen that the best value of 0.54183t obtained by IDPGA is better than the results reported by GA, worse than that reported by the other four algorithms. This phenomenon does not indicate that the solution obtained by IDPGA is poor, because the algorithm was randomly run once, while the solutions of other algorithms in the table are their own best solutions of many runs. In fact, the solution obtained by IDPGA is close to the best of other algorithms, and the first 3 natural frequencies of the structure obtained are 7.0014Hz, 15.691Hz and 20.004Hz respectively. Such results are acceptable in engineering, and IDPGA still has good accuracy. Accordingly, the optimized model is shown in Fig. 22.

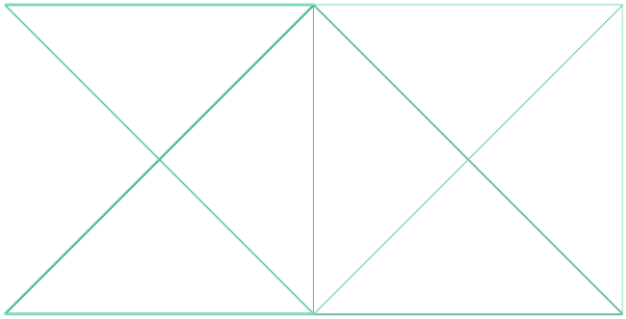

Fig. 22 The diagram of optimized model

4.3.2. Optimization design of 37-bar plane truss

The grid structure in this problem is a plane truss composed of 37 elements. As shown in Fig. 23, the positions of the nodes in the lower chords are fixed, the concentrated mass is applied to nodes in the lower chords respectively. The objective is the mass of the structure, and the constraints include natural frequencies of the first 3 orders of structure. The decision variables are the cross-sectional areas of the upper chords and the web members and the vertical ordinates of the nodes in the upper chords, considering symmetry, 19 in total.

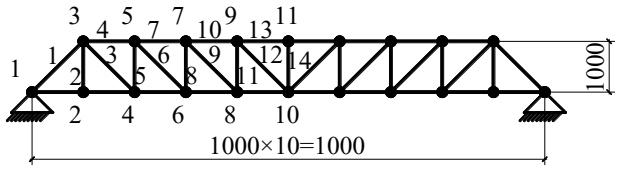

Fig. 23 Diagram of the 37-bar plane truss

The optimization framework was run once to solve the next problems. Similarly, the results were statistically analyzed as shown in Table 15.

Table 15
Optimization results

Objective (t)	Constraint violation	Time (h)
0.36777	0	25.7763

Similarly, the constraint violation of the solution is 0, indicating that the solution is a feasible solution. IDPGA takes about 26h to solve this problem. The evolution process diagram of the objective was drawn, as shown in Fig. 24.

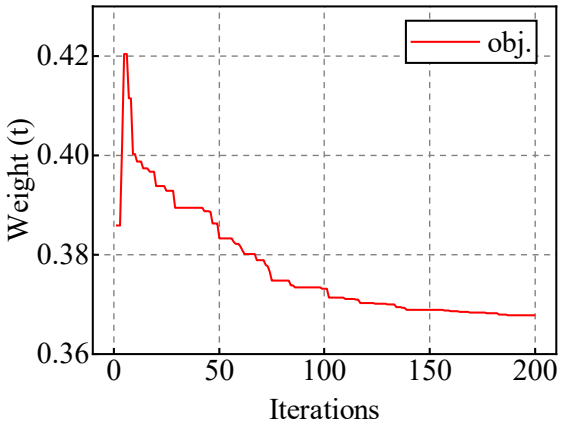

Fig. 24 The evolution process of the objective

It can be seen that the objective decreases rapidly before 100 iterations, and then slowly decreases and gradually converges. After about 180 iterations, the algorithm has obtained a satisfactory solution. Finally, some of the best results reported by other existing algorithms were selected and compared with the results of this algorithm. All the results were listed in Table 16.

Table 16
The best results reported by other algorithms

Algorithm	GA[33]	PSO[37]	NHPGA[38]
Objective (t)	0.36884	0.37720	0.36303
Algorithm	CSS[35]	ECSS[35]	HRPSO[39]
Objective (t)	0.36284	0.36238	0.36472

It can be seen that the best value of 0.36777t obtained by IDPGA is better than the results reported by GA and PSO, worse than that reported by the other four algorithms. Similarly, this phenomenon does not indicate that the solution obtained by IDPGA is poor, the solution obtained by IDPGA is close to the best of other algorithms, and the first 3 natural frequencies of the structure obtained are 20.009Hz, 40.063Hz and 60.004Hz respectively. Such results are acceptable in engineering, and IDPGA still has good accuracy. Accordingly, the optimized model is shown in Fig. 25.

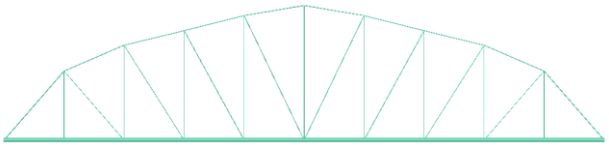

Fig. 25 The diagram of optimized model

4.3.3. Optimization design of 200-bar plane truss

The grid structure in this problem is a plane truss composed of 200 elements. As shown in Fig. 26, the concentrated mass is applied to nodes (1), (2), (3), (4) and (5) respectively. The objective is the mass of the structure, and the constraints include natural frequencies of the first 3 orders of structure. The decision variables are the cross-sectional areas of each member, considering symmetry, 29 in total.

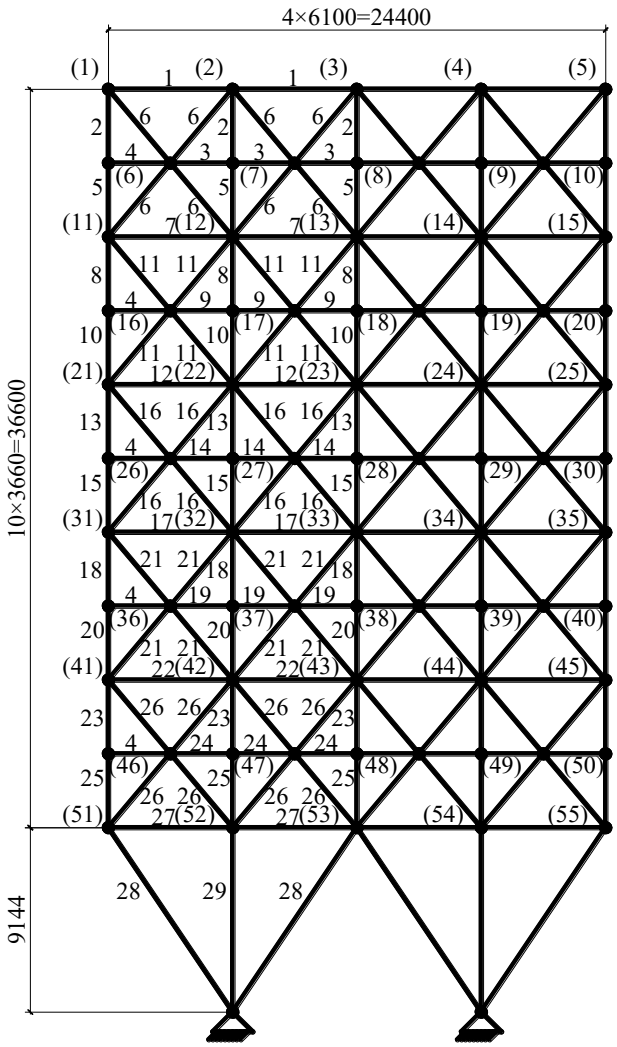

Fig. 26 Diagram of the 200-bar plane truss

The optimization framework was run once to solve the next problems. Similarly, the results were statistically analyzed as shown in Table 17.

Table 17
Optimization results

Objective (t)	Constraint violation	Time (h)
2.20373	0	29.2922

Similarly, the constraint violation of the solution is 0, indicating that the solution is a feasible solution. IDPGA takes about 29h to solve this problem. The evolution process diagram of the objective was drawn, as shown in Fig. 27.

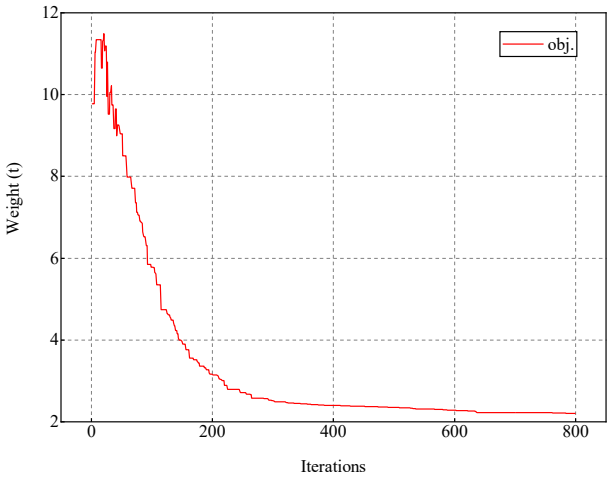

Fig. 27 The evolution process of the objective

It can be seen that the objective decreases rapidly before 300 iterations, and then slowly decreases and gradually converges. After about 600 iterations, the algorithm has obtained a satisfactory solution. Finally, some of the best results reported by other existing algorithms were selected and compared with the results of this algorithm. All the results were listed in Table 18.

Table 18
The best results reported by other algorithms

Algorithm	CSS[35]	ECSS[35]	CBO[40]
Objective (t)	2.25986	2.29861	2.16115
Algorithm	ECBO[40]	SOS-ABF[41]	CSS-BBBC[36]
Objective (t)	2.15808	2.16488	2.29861

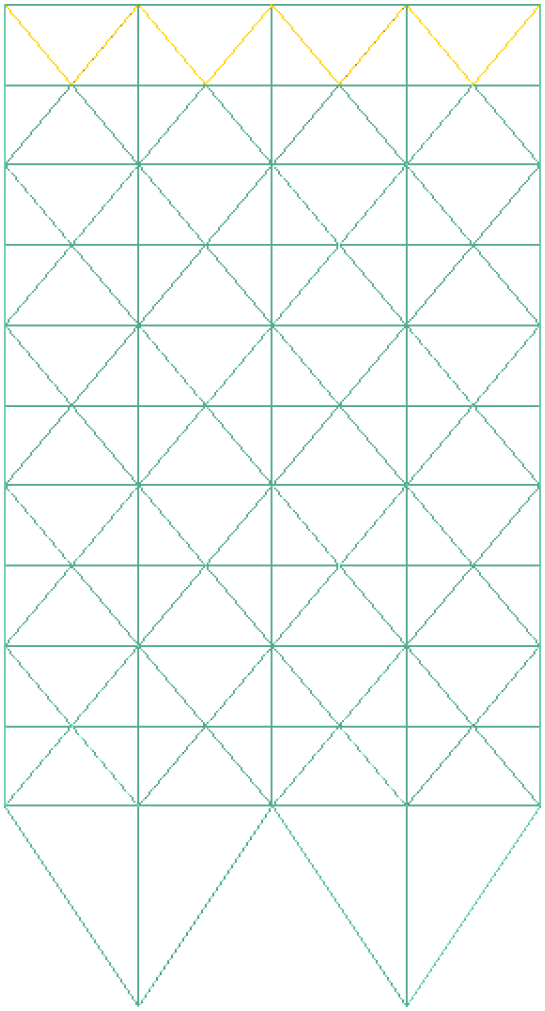

Fig. 28 The diagram of optimized model

It can be seen that the best value of 2.20373t obtained by IDPGA is better than the results reported by CSS, ECSS and CSS-BBBC, worse than that reported by the other three algorithms. Similarly, this phenomenon does not indicate that the solution obtained by IDPGA is poor, the solution obtained by IDPGA is close to the best of other algorithms, and the first 3 natural frequencies of the structure obtained are 5.0057Hz, 12.708Hz and 15.128Hz respectively. Such results are acceptable in engineering, and IDPGA still has good accuracy. Accordingly, the optimized model is shown in Fig. 28.

4.3.4. Optimization design of 1410-bar double-layer lattice shell

The grid structure in this problem is a double-layer lattice shell composed of 1410 elements. As shown in Fig. 29, the concentrated mass is applied to all free nodes respectively. The objective is the mass of the structure, and the constraints include natural frequencies of the first and third orders of structure. The decision variables are the cross-sectional areas of each member, considering symmetry, 47 in total in a single block.

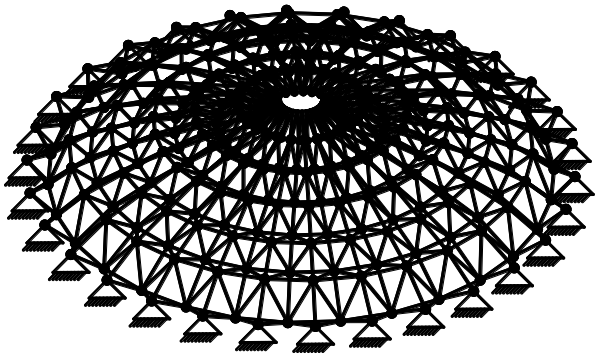

(a) 3D view

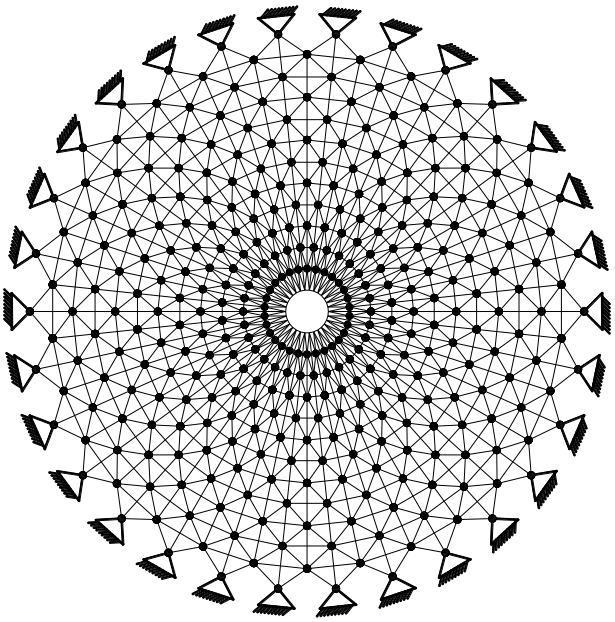

(b) Top view (line width not shown)

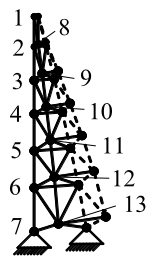

(c) Diagram of a single block

Fig. 29 Diagram of the1410-bar double-layer lattice shell

The optimization framework was run once to solve the next problems. Similarly, the results were statistically analyzed as shown in Table 19.

Table 19
Optimization results

Objective (t)	Constraint violation	Time (h)
10.69489	0	89.7813

Similarly, the constraint violation of the solution is 0, indicating that the solution is a feasible solution. IDPGA takes about 90h to solve this problem. The evolution process diagram of the objective was drawn, as shown in Fig. 30.

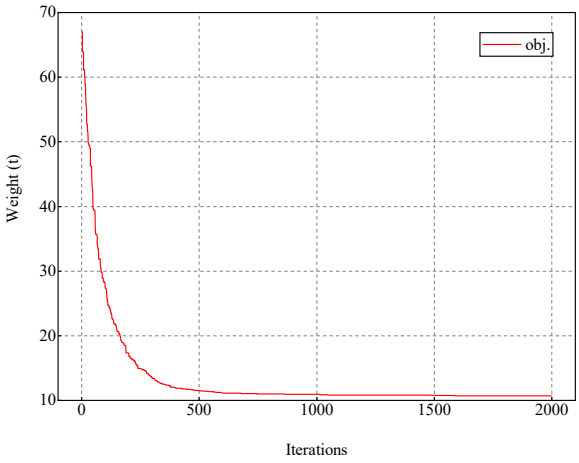

Fig. 30 The evolution process of the objective

It can be seen that the objective decreases rapidly before 500 iterations, and then slowly decreases and gradually converges. After about 700 iterations, the algorithm has obtained a satisfactory solution. Finally, some of the best results reported by other existing algorithms were selected and compared with the results of this algorithm. All the results were listed in Table 20.

Table 20
The best results reported by other algorithms

Algorithm	ECBO[42]	ECBO-Cascade[42]	DPSO[43]
Objective (t)	10.73919	10.50420	10.45384
Algorithm	VPS[44]	BB-BC[45]	HS[45]
Objective (t)	10.49183	10.77211	10.92270

It can be seen that the best value of 10.69489t obtained by IDPGA is better than the results reported by ECBO, BB-BC and HS, worse than that reported by the other three algorithms. Similarly, this phenomenon does not indicate that the solution obtained by IDPGA is poor, the solution obtained by IDPGA is close to the best of other algorithms, and the first 3 natural frequencies of the structure obtained are 7.0001Hz, 7.0001Hz and 9.0008Hz respectively. Such results are acceptable in engineering, and IDPGA still has good accuracy. Accordingly, the optimized model is shown in Fig. 31.

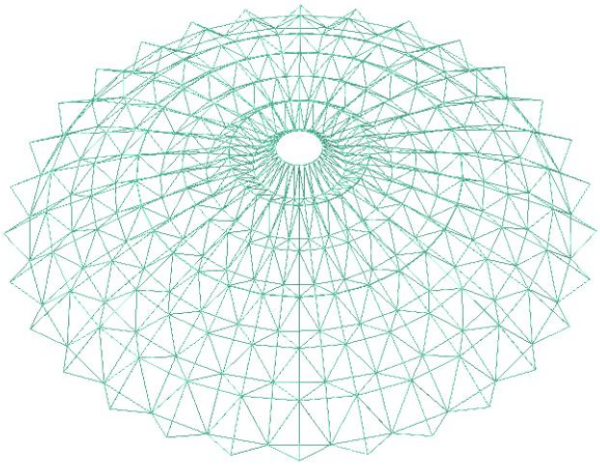

Fig. 31 The diagram of optimized model

5. Conclusions

Based on IDPGA proposed before, combined with ABAQUS, a simulation optimization framework is developed to optimize the static and dynamic performance of grid structures. In order to improve the solving efficiency, two strategies are introduced in the optimization framework, including grouping and parallel computing strategy and comparison strategy between parent and offspring. The feasibility and effectiveness of IDPGA for grid structure optimization design are verified by solving 8 engineering problems, and it proves that the algorithm has great accuracy and robustness once again.

The results show that the algorithm can converge when the iteration reaches a certain number for different problems. At the beginning of the iteration, the objective decreases rapidly and then decreases slowly and converges gradually. Before reaching the maximum number of iterations, the algorithm has found a satisfactory solution, a completely acceptable solution in the engineering field. "No free lunch theory" points out that there is no universal algorithm. In other words, no algorithm can be effective for all problems. In this paper, when solving the grid structure optimization problem, in most cases, it is randomly run once, and the obtained results are close to or better than the best values of other algorithms, which is sufficient to show that the algorithm in this paper is suitable for solving the grid structure optimization problem.

This research further expands the application of genetic algorithm and promotes the intelligent design of grid structure. Meanwhile, this research enriches the structure optimization script completed by Python language, and provides some inspiration for the application of IDPGA in the optimization design of other structures.

It is worth noting that the optimization framework takes a long time to solve the grid structure optimization problem. Some reasons are analyzed. Firstly, the idea of "dual population evolution" determines that two populations participate in the evolution at the same time, which takes longer than a single population. Secondly, due to the limitation of computer hardware, the solving efficiency will be greatly improved if the computing platform suitable for large-scale simulation is selected. Thirdly, limited by the expertise of researchers, there is still room for improvement of the interactive script between IDPGA and ABAQUS. Therefore, further improving the efficiency of the optimization framework is a research direction. For example, among the best results of adjacent 10 generations, if the difference between the best and the worst results is within 5%, it is considered that the algorithm has converged and the iteration is terminated.

In addition, parameter tuning is a current hot issue in the field of algorithms. The optimal parameter combination of an algorithm needs to be determined by other methods, which is also a future research direction of this paper. The algorithm parameters in this paper cannot be guaranteed to be optimal, but the searching results show that the combination of these parameters is reliable and effective.

Author Contributions

Formal analysis, Xuchen Xu; Investigation, Hongbo Liu; Methodology, Zhihua Chen; Software, Xuchen Xu; Supervision, Zhihua Chen; Validation, Hongbo Liu; Visualization, Zhihua Chen; Writing – original draft, Xuchen Xu; Writing – review & editing, Hongbo Liu & Ting Zhou.

Declarations

Conflict of Interest On behalf of all authors, the corresponding author states that there is no conflict of interest.

Replication of Results All scripts of algorithms are completed in Python and all contours are plotted with Matplotlib. Some or all data, models, or code that support the findings of this study are available from the corresponding author upon reasonable request.

References

[1] DOGAN E;SEKER S;SAKA M P, et al. Investigating the Effect of Joint Behavior on the Optimum Design of Steel Frames via Hunting Search Algorithm. Adv Steel Constr, v. 14, n. 2, p. 166-83, 2018.
[2] TALASLIOGLU T. Design Optimization of Tubular Lattice Girders. Adv Steel Constr, v. 15, n. 3, p. 274-87, 2019.
[3] TALASLIOGLU T. Design Optimization of Lattice Girders According to Member and Joint-Related Design Constraints. Adv Steel Constr, v. 17, n. 2, p. 181-98, 2021.
[4] KUNZ F F;SANTOS P D E;CARDOSO E U, et al. Teaching-Learning Based Optimization Method Considering Buckling and Slenderness Restriction for Space Trusses. Adv Steel Constr, v. 18, n. 1, p. 446-52, 2022.
[5] SRINIVASA K G;SRIDHARAN K;SHENOY P D, et al. A Dynamic Migration Model for self-adaptive Genetic Algorithms. Springer-Verlag Berlin, Berlin, 2005.
[6] LI Y M;ZHANG S J, ZENG X P. Research of multi-population agent genetic algorithm for feature selection. Expert Systems with Applications, v. 36, n. 9, p. 11570-81, 2009.
[7] PARK T, RYU K R. A Dual-Population Genetic Algorithm for Adaptive Diversity Control. Ieee Transactions on Evolutionary Computation, v. 14, n. 6, p. 865-84, 2010.

[8] UMBARKAR A J;JOSHI M S, HONG W C. Multithreaded Parallel Dual Population Genetic Algorithm (MPDPGA) for unconstrained function optimizations on multi-core system. Appl Math Comput, v. 243, p. 936-49, 2014.
[9] POURVAZIRI H, NADERI B. A hybrid multi-population genetic algorithm for the dynamic facility layout problem. Applied Soft Computing, v. 24, n. p. 457-69, 2014.
[10] MU Z G; CHEN Y Z; XIU L. Application of Genetic Algorithm in Optimum Design of Space Grid Structures. Spatial Structures, v. 52, p. 4, 2003, (in Chinese)
[11] MU Z G; LIANG J; SUI J, et al. Study of Optimum Design of Single Layer Dome Structures Based on Niche Genetic Algorithm. Journal of Building Structures, v. 115, p. 9, 2006. (in Chinese)
[12] LI Y M; LU X Y. Topological optimization of reticulated structures based on Genetic Algorithms. Journal of Shandong University of Architecture and Engineering, v. 8, p. 11+90, 2004. (in Chinese)
[13] CHEN Z;XU X, LIU H. Improved Dual-Population Genetic Algorithm: A Straightforward Optimizer Applied to Engineering Optimization. Sustainability, v. 15, n. 20, p. 14821, 2023.
[14] WOLPERT D H, MACREADY W G. Coevolutionary free lunches. IEEE Transactions on Evolutionary Computation, v. 9, n. 6, p. 721-35, 2005.
[15] Python 3.10.9 documentation. Python Software Foundation, BeOpen.com, Corporation for National Research Initiatives, Stichting Mathematisch Centrum. 2022.
[16] SIMULIA User Assistance 2022. Dassault Systèmes Simulia Corp, Providence, RI, USA, 2022.
[17] LI L J;HUANG Z B, LIU F. A heuristic particle swarm optimization method for truss structures with discrete variables. Computers & Structures, v. 87, n. 7, p. 435-43, 2009.
[18] TOĞAN V, DALOĞLU A T. An improved genetic algorithm with initial population strategy and self-adaptive member grouping. Computers & Structures, v. 86, n. 11, p. 1204-18, 2008.
[19] CAMP C;PEZESHK S, CAO G. Optimized Design of Two-Dimensional Structures Using a Genetic Algorithm. Journal of Structural Engineering, v. 124, n. 5, p. 551-9, 1998.
[20] KAZEMZADEH AZAD S;HASANÇEBI O, SAKA M P. Guided stochastic search technique for discrete sizing optimization of steel trusses: A design-driven heuristic approach. Computers & Structures, v. 134, n. p. 62-74, 2014.
[21] SADOLLAH A;ESKANDAR H;BAHREININEJAD A, et al. Water cycle, mine blast and improved mine blast algorithms for discrete sizing optimization of truss structures. Computers & Structures, v. 149, n. p. 1-16, 2015.
[22] HO-HUU V;NGUYEN-THOI T;VO-DUY T, et al. An adaptive elitist differential evolution for optimization of truss structures with discrete design variables. Computers & Structures, v. 165, n. p. 59-75, 2016.
[23] TAN Y, ZHU Y. Fireworks Algorithm for Optimization; Advances in Swarm Intelligence. Springer Berlin Heidelberg, Berlin, Heidelberg, 2010.
[24] GHOLIZADEH S, MILANY A. An improved fireworks algorithm for discrete sizing optimization of steel skeletal structures. Engineering Optimization, v. 50, n. 11, p. 1829-49, 2018.
[25] AZAD S K, HASANÇEBI O. An elitist self-adaptive step-size search for structural design optimization. Applied Soft Computing, v. 19, n. p. 226-35, 2014.
[26] AISC. Manual of Steel Construction, Allowable Stress Design, 9th edition. American Institutes of Steel Construction, Inc, Chicago, Illinois, USA, 1989.
[27] SAKA M P. Optimum Design of Pin-Jointed Steel Structures With Practical Applications. Journal of Structural Engineering, v. 116, n. 10, p. 2599-620, 1990.
[28] TALATAHARI S;KHEIROLLAHI M;FARAHMANDPOUR C, et al. A multi-stage particle swarm for optimum design of truss structures. Neural Computing and Applications, v. 23, n. 5, p. 1297-309, 2013.
[29] KAVEH A;BAKHSHPOORI T, AFSHARI E. An efficient hybrid Particle Swarm and Swallow Swarm Optimization algorithm. Computers & Structures, v. 143, n. p. 40-59, 2014.
[30] REYNOLDS R G. An Introduction to Cultural Algorithms. Proceedings of the third annual conference on evolutionary programming. World Scientific, San Diego, California, USA, 1994.
[31] WANG G G;DEB S, COELHO L D S. Elephant Herding Optimization; 2015 3rd International Symposium on Computational and Business Intelligence (ISCBI). IEEE Computer Society, NW Washington, DC, US, 2015.
[32] JAFARI M;SALAJEGHEH E, SALAJEGHEH J. An efficient hybrid of elephant herding optimization and cultural algorithm for optimal design of trusses. Engineering with Computers, v. 35, n. 3, p. 781-801, 2019.
[33] LINGYUN W;MEI Z;GUANGMING W, et al. Truss optimization on shape and sizing with frequency constraints based on genetic algorithm. Computational Mechanics, v. 35, n. 5, p. 361-8, 2005.
[34] GOMES H M. Truss optimization with dynamic constraints using a particle swarm algorithm. Expert Systems with Applications, v. 38, n. 1, p. 957-68, 2011.
[35] KAVEH A, ZOLGHADR A. Shape and size optimization of truss structures with frequency constraints using enhanced charged system search algorithm. Asian Journal of Civil Engineering, v. 12, n. p. 2011.
[36] KAVEH A, ZOLGHADR A. Truss optimization with natural frequency constraints using a hybridized CSS-BBBC algorithm with trap recognition capability. Computers & Structures, v. 102-103, n. p. 14-27, 2012.
[37] MIGUEL L F F, FADEL MIGUEL L F. Shape and size optimization of truss structures considering dynamic constraints through modern metaheuristic algorithms. Expert Systems with Applications, v. 39, n. 10, p. 9458-67, 2012.
[38] WEI L;TANG T;XIE X, et al. Truss optimization on shape and sizing with frequency constraints based on parallel genetic algorithm. Structural and Multidisciplinary Optimization, v. 43, n. 5, p. 665-82, 2011.
[39] KAVEH A, JAVADI S M. Shape and size optimization of trusses with multiple frequency constraints using harmony search and ray optimizer for enhancing the particle swarm optimization algorithm. Acta Mechanica, v. 225, n. 6, p. 1595-605, 2014.
[40] KAVEH A, GHAZAAN M I. Enhanced Colliding Bodies Algorithm for Truss Optimization with Frequency Constraints. J Comput Civil Eng, v. 29, n. 6, p. 04014104, 2015.
[41] TEJANI G G;SAVSANI V J, PATEL V K. Adaptive symbiotic organisms search (SOS) algorithm for structural design optimization. Journal of Computational Design and Engineering, v. 3, n. 3, p. 226-49, 2016.
[42] KAVEH A, GHAZAAN M I. Optimal design of dome truss structures with dynamic frequency constraints. Structural and Multidisciplinary Optimization, v. 53, n. 3, p. 605–21, 2016.
[43] KAVEH A. Optimal analysis and design of large-scale domes with frequency constraints. Smart Structures and Systems, v. 18, n. p. 733-54, 2016.
[44] KAVEH A, ILCHI GHAZAAN M. A new hybrid meta-heuristic algorithm for optimal design of large-scale dome structures. Engineering Optimization, v. 50, n. 2, p. 235-52, 2018.
[45] KAVEH A, ZOLGHADR A. Optimal design of cyclically symmetric trusses with frequency constraints using cyclical parthenogenesis algorithm. Advances in Structural Engineering, v. 21, n. 5, p. 739-55, 2018.

Advanced Steel Construction – Vol. 22 No. 1 (2026) 78–95
DOI:10.18057/IJASC.2026.22.1.7

STUDY ON DYNAMIC PERFORMANCE OF STEEL-WOOD COMPOSITE BEAM-COLUMN JOINTS UNDER IMPACT LOAD

Chang Wu [1, 2], Ying-Ni Fan [1, *], Yue-Han Zhang [1] and Yu-Tong Tian [1]

[1] *School of Civil Engineering, Lanzhou University of Technology, Lanzhou 730050, China*
[2] *Western Center of Disaster Mitigation in Civil Engineering of Ministry of Education, Lanzhou University of Technology, Lanzhou 730050, China*
** (Corresponding author: E-mail: 3121825025@qq.com)*

ABSTRACT

This paper proposes a novel steel-timber hybrid beam-column joint suitable for the "timber above and steel below" low-rise hybrid structural system. Sleeves and L-shaped connectors are set up at the joints. Sleeves are set up to prevent the wood from cracking, while L-shaped connectors prevent the steel column from twisting when connecting the upper wood column to the lower I-beam. In order to investigate the impact resistance, the deformation characteristics, damage mechanism and energy dissipation capacity were investigated through tests and numerical simulations. The effects of key parameters such as impact mass, velocity, position, impactor shape, and beam end constraints on the impact resistance of the joints were also analyzed. The results show that the joint's performance overall was excellent, in which the L-shaped connector served as the primary deformation zone. The joint's deformation and displacement under the same impact conditions were reduced significantly by reinforcing the connector's thickness. Furthermore, the spring support replaced the crossbeam's restraint function effectively during the tests. The parametric analysis revealed that an increase in the hammer's velocity at impact leads directly to a significant increase in the impact's peak force and a prolonged impact platform. In contrast, an increase in the hammer's mass had a limited effect on the impact's peak force, and merely extended its decay process. Based upon the experimental results and parametric analysis, the vulnerabilities of the steel-timber hybrid joint in the "timber above and steel below" structural system were identified, and corresponding improvement measures are proposed.

ARTICLE HISTORY

Received: 18 January 2025
Revised: 14 June 2025
Accepted: 15 June 2025

KEYWORDS

Steel-timber hybrid structure;
Beam-column node;
Impact test;
Dynamic properties;
Damage mechanism

1. Introduction

With the growing demand for green, low-carbon and sustainable building structures, assembled structures are gradually becoming a hot research topic in the engineering field. However, impact events occur in people's daily lives in a wide range, from a simple cup of water falling from a high shelf to a space shuttle colliding with a meteor [1]. This paper synthesizes the characteristics of residential houses in Northwest China, and proposes an "timber above and steel below" structure. Due to the large difference in material properties between steel and wood, the joint connections have complex stresses, so it is innovative to design a steel-wood combined connection joint, and focus on its dynamic response under the action of impact loading. Many scholars have conducted relevant research on hybrid structures. While the research on hybrid structures mainly focuses on the combination of steel with concrete, aluminum alloy and other materials, and mainly discusses their seismic performance [2-5], A lot of research has also been done on the mechanical properties of structures under impact loading, Zhang et al. [6] conducted numerical evaluations using LS-DYNA to assess the nonlinear dynamic response and failure behavior of supported reinforced concrete (RC) beams subjected to impact and blast loads. Damian et al. [7-8] developed detailed nonlinear three-dimensional finite element models (FEMs) using ABAQUS and conducted rigorous validations to ensure consistency between the model and published experimental tests with respect to force and displacement time histories. Ja'e et al. [9] investigated the structural impact resistance of lightweight fiber reinforced concrete. Zeng et al. [10-11] investigated the dynamic response of reinforced concrete (SRC) composite members under transverse impact through experiments and numerical simulations. Zhu et al. [12] researched cruciform steel-reinforced concrete-filled steel tubes' impact performance under lateral impact loads. Kang et al. [13] investigated the dynamic response of steel-tube concrete beams in the peak phase under lateral impact, Huang et al. [14-19] investigated the mechanical properties, dynamic response and computational methods of steel, concrete and composite beams under impact by means of experiments and numerical simulations.

Furthermore, Yang et al. [20-21] investigated the mechanical properties of steel-wood composite beams and composite joints through tests and finite element analysis. Kia et al.[22] conducted an experimental study on the bearing capacity, failure mechanisms, stiffness, and ductility of 48 hybrid members with wrapped steel bars adhered within wooden sleeves under concentric axial compression, and compared them with bare wooden columns. Chen et al. [23-27] proposed a variety of new types of beam-column steel-timber connection joints and investigated the damage modes and mechanical properties of the new types of joints under cyclic loading through tests and finite elements. Dourado et al. [28] investigated steel-timber joints' fracture behavior under quasi-static loading, and Zheng et al. [29] discussed the importance of connections between concrete-filled steel tubular columns and composite beams for structural resistance to floor-by-floor collapse. Moreover, through experimental and numerical studies, they compared three different types of connections and two types of shear connectors, and explored their failure modes, vertical resistance-deformation mechanisms, and strain-deformation relations.

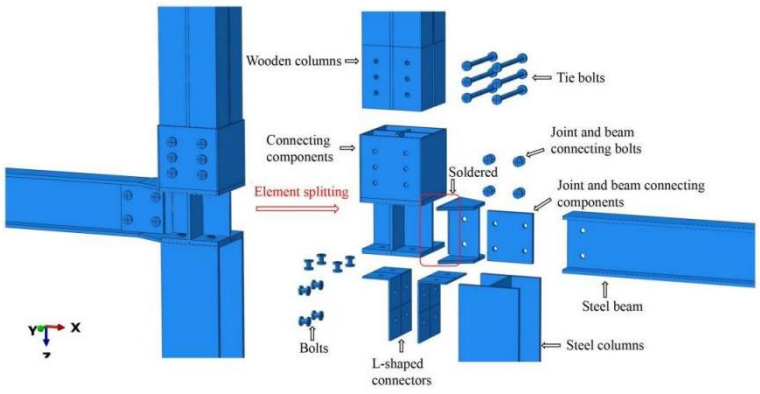

Fig. 1 Schematic diagram of joint construction

In summary, the existing research on composite structures mainly focuses on steel-mixed and steel-aluminum structures, and the research on structural performance under dynamic loading mainly focuses on reinforced concrete structures, while the research on steel-wood composite structures is limited to static research, especially in the research on the dynamic response of steel-wood structures under impact loading is still lacking, especially in the failure mechanism of steel-wood composite members under dynamic loading, which is yet to be studied in depth and detail. In particular, the failure mechanism of steel-wood composite members under dynamic loading is still in need of in-depth and detailed research.

This paper proposes a novel hybrid steel-timber beam-column joint, cut cross groove in the middle of the wooden post, and fix and connect the cross connecting key with the wooden post through tie bolts; at the same time, set a circle of sleeve on the periphery of the cross connecting key to prevent the wood from cracking. A connecting plate is set at the bottom of the cross connecting key, and the connection between the lower I-beam and the cross connecting key is realized through L-shaped connectors and bolts; a trapezoidal connecting key is welded to the side of the cross connecting key, and the steel beam is connected to the cross connecting key through bolts and connecting plate, as shown in Fig. 1. Through experimental research and numerical simulation, the deformation mode, damage mechanism and energy consumption capacity of steel-wood hybrid beam-column nodes are investigated, and the key parameters are analyzed to investigate the effects of different impact conditions on the impact resistance of steel-wood hybrid beam-column joint.

2. Douglas fir lumber material property tests

The moisture content of the Douglas fir timber used was measured according to the “Method for the Determination of the Moisture Content of Wood” (GB/T 1931-2009) [30]. Through measurement and calculation analysis, it was found that the Douglas fir timber’s average moisture content was 10.79%, which complies with the value (9% to 12%) in relevant specifications.

The load-displacement curve of wood along the grain was measured according to the “Test Method for Compression Strength Parallel to Grain of Wood” (GB/T 1935-2009) [31], as shown in Fig. 2.

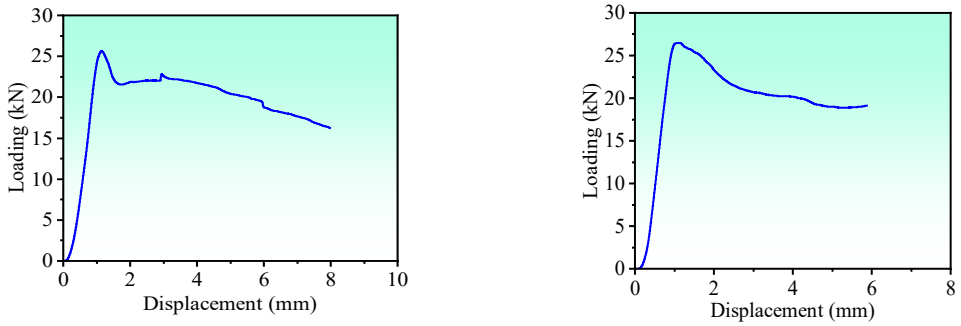

(a) Specimen I (b) Specimen II

Fig. 2 Compression resistance curve of wood with parallel grain

According to the data in the figure, the minimum compressive load-bearing capacity of Douglas fir wood along the grain is 21.04 kN, the maximum is 27.54 kN, and the average is 24.51 kN. The minimum compressive strength is 52.10 MPa, the maximum is 67.69 MPa, and the mean is 60.95 MPa. The mean compressive strength along the grain when the specimen’s moisture content is 12% is 56.97 MPa.

The specimen’s tensile strength was measured by the relevant provisions of the “Test Method for Tensile Strength Parallel to Grain of Wood” (GB/T 1938-2009) [32], and the test process is shown in Fig. 3.

Fig. 3 Tensile strength test of wood along the grain

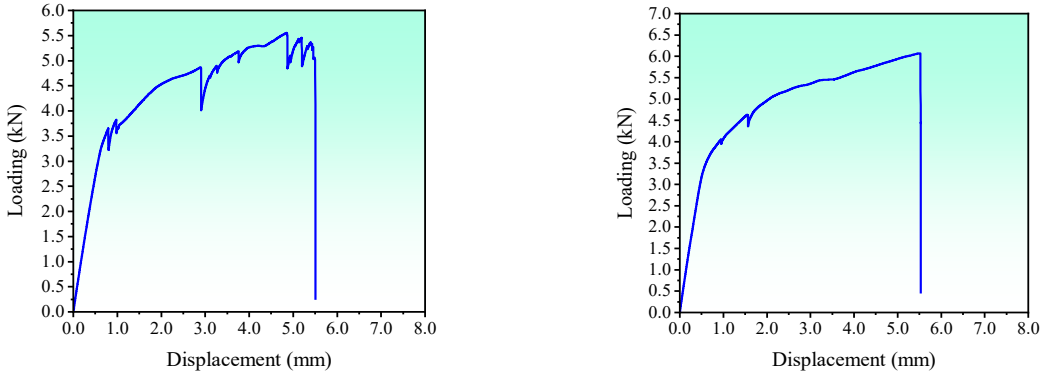

(a) Specimen I (b) Specimen II

Fig. 4 Tensile curve diagram of wood along the grain

According to the data in Fig. 4, Douglas fir wood's minimum tensile load-bearing capacity is 4.96 kN, the maximum is 5.85 kN, and the mean is 4.96 kN. The minimum tensile strength is 79.52 MPa, the maximum is 95.88 MPa, and the mean is 86.67 MPa. When the specimen's moisture content is 12%, the mean tensile strength along the grain is 84.93 MPa.

The mean value of the reduction coefficients of the wood's grain-longitudinal tensile strength, flexural strength, and compressive strength, which is (0.80+0.446+0.567)/3=0.6, was used to reduce the wood properties. The reduction coefficients for different influencing factors are shown in Table 1, and the material property test results on the reduced wood are detailed in Table 2.

Table 1
Discount factors for different impact factors

Stress state of wood	Parallel grain tensile strength	Compressive strength of smooth grain	Bending strength
Effects of natural wood defects K_{Q1}	0.80	0.66	0.75
Effects of wood drying defects K_{Q2}	——	0.90	0.85
Long-term load strength effects K_{Q3}	1.0	1.0	1.0
Wood size effects K_{Q4}	——	0.75	0.89
Discount factor K_Q	0.80	0.446	0.567

Note: Since the wood used in this test was new and not subjected to long-term loading, the factor K_{Q3} for this item is 1.0;

Table 2
Adjustment results of wood material performance tests

Norm	Moisture content%	Flexural modulus of elasticity （MPa）	Bending strength （MPa）	Compressive strength of smooth grain （MPa）	Parallel grain tensile strength （MPa）
Average value	10.79	10290	36.08	34.18	50.96

3. Steel-wood hybrid beam-column node drop hammer impact test

3.1. Joint location selection

This experiment used Q235 steel with an elastic modulus of $E = 2.06 \times 10^5$ MPa, in which Douglas fir's measured elastic modulus is $E = 10290$MPa. The construction form of the middle-layer, middle-column joint was taken as the research object (as illustrated in Fig. 5). Because the upper column in the "upper wood and lower steel" system is a wooden column, the difference in material properties leads to different lateral stiffness. Therefore, under the condition of constant boundary constraints, it is necessary to calculate the column length for the simplified model of the joint.

The moment of inertia is calculated according to eq. (1):

$$I = \frac{bh^3}{12} = \frac{200^4}{12} = 133333333mm^4 \quad (1)$$

The steel columns are H-beam columns and their moment of inertia is calculated according to eq. (2):

$$I = \frac{BH^3 - bh^3}{12} = 46104900mm^4 \quad (2)$$

Where: B-bottom width;
H -- the height of the I-beam;
h -- the internal height of the I-beam;
b -- the 1/2 bottom width;

The length ratio of steel columns to wood columns is calculated according to eq. (3) while ensuring that the columns' bending stiffness overall was the same.

$$\frac{L_{steel}}{L_{numb}} = \frac{E_{steel}I_{steel}}{E_{numb}I_{numb}} = \frac{2.06\times10^5\times46104900}{10290\times133333333} = 1.41 \quad (3)$$

Here, an approximate value of 1.5 was taken, such that the steel column was 1.5m and the wooden column was 1m.

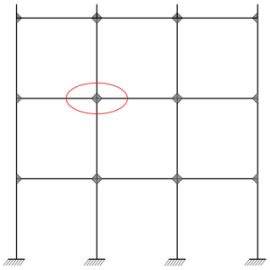

Fig. 5 Simplified model of node structure

3.2. Specimen design

In order to investigate the effects of impact location, sleeve thickness and L-shaped connector thickness on the impact resistance of steel-wood composite beam-column joints. In this paper, this experiment conducted drop hammer impact tests on six steel-wood hybrid columns, with three impacts on the steel column's mid-span, two on the joint location, and one on the wooden column's mid-span. Among them, the design specimens, M-SWMC-S-1-3 and M-SWMC-J-1-2, are intended to investigate the effect of the thickness of the sleeve and L-shaped connector on the impact resistance of the joint, while M-SWMC-S-1, M-SWMC-J-2, and M-SWMC-W are used to investigate the most unfavorable position of the structure under the same impact conditions. Considering that during lateral impact, the beam in the direction of the impact provides support to the joint, and in the actual frame, this beam is semi-rigid, the remote end of the joint does not restrict the entire beam's lateral displacement. Therefore, to determine the column member's dynamic response when subjected to impact load alone, this experiment used semi-rigid spring supports to replace the beams to provide reaction force, This support combines the characteristics of a rigid and flexible support by means of elastic deformation of the spring element and a damping mechanism that provides limited rotational or translational restraint while also absorbing and transferring loads, as shown in Fig. 6. The maximum constant load it can withstand is 500kN, with a maximum allowable vertical displacement of 200mm. The main parameters considered in the experiment were the hammer's mass (M), its velocity (V), and the impact location. In this design, the specimen size is selected according to the principle of simplified modeling in section 2.1 of the text to select the length of the member, and its cross-section dimensions refer to the "Code for the Design of Steel Structures" and the "Manual for the Design of Wooden Structures" [33] [34] design the joint. At the joint, the steel column designed is an H-shaped steel 200mm×200mm×8mm×12mm and a length of 1500mm. The wooden column has a cross-sectional dimension of 200mm×200mm and a length of 1000mm. The sleeves at the joints and L-shaped connectors are all constructed by welding, including three 5mm sleeves and three 10mm sleeves, eight 6mm L-shaped connectors, and four 10mm L-shaped connectors. The specimens' geometric parameters are detailed in Table 3, and the physical diagrams of each part of the components are shown in Fig. 7.

Naming Explanation: In "M-SWMC-S", "M" stands for "Middle", referring to the middle joint of the column; "SWMC" is the abbreviation for "Steel-wood Mixed Columns"; "S" represents that the impact location is at the mid-span of the steel column, "J" indicates that the impact location is at the joint, and "W" signifies that the impact location is at the mid-span of the wooden column.

Fig. 6 Physical drawing of spring support

Table 3
Geometric parameters of test pieces

Serial number	Specimen number	Impact position	Section size（mm）	Joint's sleeve thickness（mm）	Thickness of L-shaped connector（mm）
1	M-SWMC-S-1	Steel column span center	200×200	5	6
2	M-SWMC-S-2	Steel column span center	200×200	10	6
3	M-SWMC-S-3	Steel column span center	200×200	5	10
4	M-SWMC-J-1	Nodal	200×200	10	10
5	M-SWMC-J-2	Nodal	200×200	10	6
6	M-SWMC-W	center of Wooden pole spanning	200×200	5	6

(a) Overall diagram of unassembled components (b) Groove and hole cutting diagram of wooden column (c) Sleeve for joint without cross-piece

Fig. 7 Detailed drawing of test component elements

3.3. Measurement program

The core measurements in this experimental test included the specimen's vertical displacement (at the joint, the steel column's mid-span, and the wooden column's mid-span), acceleration (at the joint, the steel column's mid-span, and the wooden column's mid-span), as well as the L-shaped connectors' strain and the strain on the opposite side of the impact location on the steel and wooden columns. The joint's vertical displacement and the column's deflection at the mid-span were measured directly using dynamic displacement meters, while the strain was measured through strain gauges. Detailed measurement point layouts are shown in Figs. 8, 9, and 10.

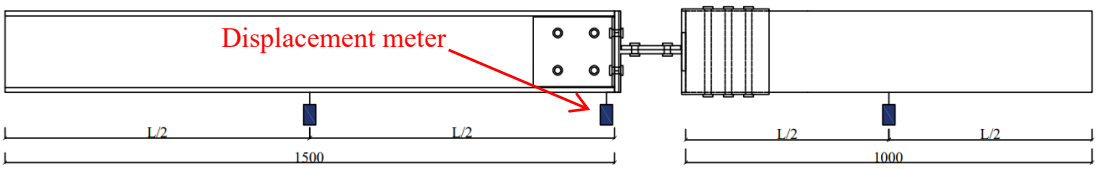

Fig. 8 Displacement meter layout

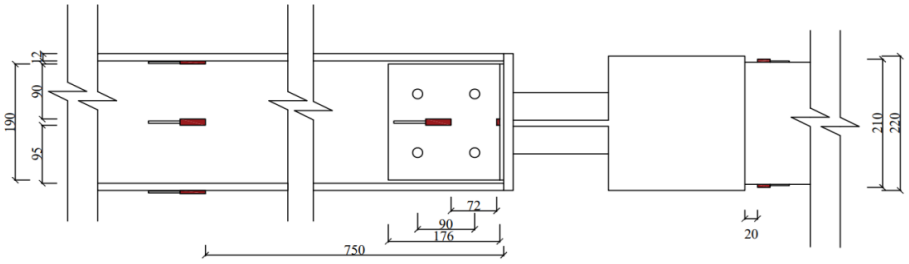

Fig. 9 Specimen strain gauge layout

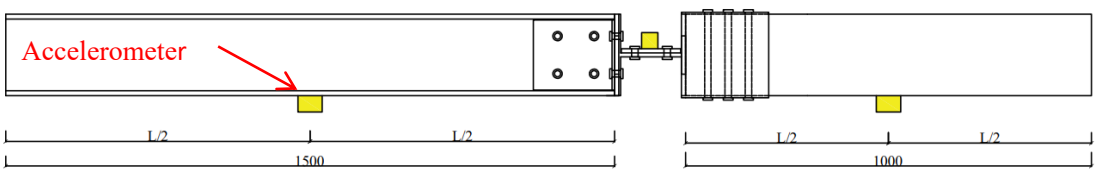

Fig. 10 Accelerometer arrangement

3.4. Impact test device set-up

The drop hammer impact test for the joints in this study was conducted on a large platform with a maximum lifting height of 18 meters and a maximum impact energy of 330,000 joules. Equipped with a high-precision dynamic data testing system, a high-speed camera (to record the joints' failure and deformation process), and a safety control system, this platform meets the experimental requirements fully. Figs. 11 and 12 show the experimental apparatus's schematic diagrams.

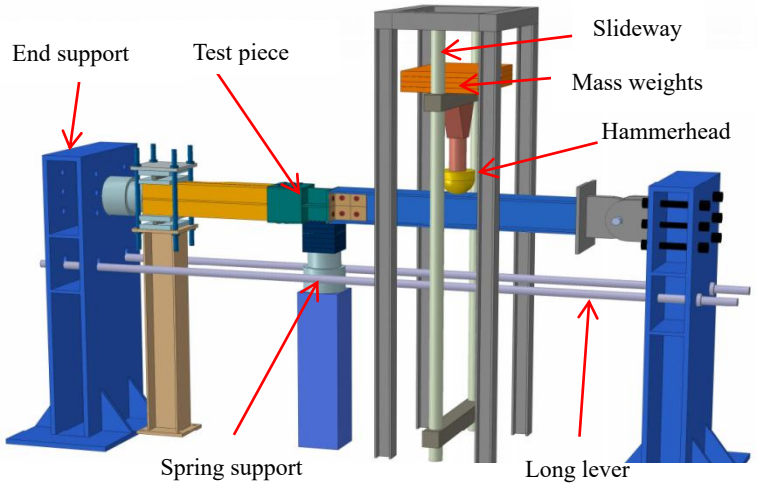

Fig. 11 Sketch of the test setup

Fig.12 Front of test loading device

This test takes falling stone impact as the research background, and the impact location is the middle of the steel column span, at the joint, and the middle of the wooden column span, respectively. Considering that the size of falling stone impact energy is mainly determined by the impact velocity and falling stone mass, therefore, referring to the research of Gao et. al [35] and combining with the impact height of the impact test platform of the falling hammer impact test platform and the mass of the falling hammer, the impact test parameters in Table 4 are designed. To simulate different experimental parameters' influence on the steel-wood mixed column joints' dynamic performance under drop hammer impact, controlled experiments were designed with varying drop hammer speeds, impact times, and impact locations, with a total of six specimens for steel-wood hybrid columns.

Table 4
Table of impact test parameters for steel-wood hybrid column nodes

Specimen number	Impact mass M	Impact velocity V	Impact energy EK(kJ)	Impact Height H（m）	Number of impacts
		3.16	1.60	0.5	
M-SWMC-S-1	320	4.47	3.20	1	3
		6.32	6.39	2	
		3.16	1.60	0.5	
M-SWMC-S-2	320	4.47	3.20	1	3
		6.32	6.39	2	
	320		6.39		
M-SWMC-S-3	420	6.32	8.39	2	3
	500		9.99		
		3.16	1.60	0.5	
M-SWMC-J-1	320	4.47	3.20	1	3
		5.48	4.80	1.5	
		3.16	1.60	0.5	
M-SWMC-J-2	320	4.47	3.20	1	3
		5.48	4.80	1.5	
		3.16	1.60	0.5	
M-SWMC-W	320	4.47	3.20	1	3
		5.48	4.80	1.5	

During the experiment, the drop hammer system's force sensor and dynamic displacement sensor, respectively, recorded the time history curves of the impact's force and vertical displacement of the impact point precisely. The impact process for the M-SWMC-S-2 specimen can be divided into three main stages through the time history curve: peak, stability, and attenuation. Specifically, this process is subdivided into eight stages: non-contact; initial contact; common downward movement; maximum displacement; rebound upward; imminent separation; rebound separation; and oscillation and stillness. Part of the process is shown in Fig. 13.

(a) The head is not in contact with the specimen

(b) Initial contact between the hammer head and the specimen

(c) The oscillation of the specimen tends to be static

Fig. 13 Diagram of partial impact process

3.5. Test loading process

Figs. 14-15, respectively, show the deformation mode and local deformation of specimens M-SWMC-S-1 and M-SWMC-S-2 in this impact test overall, which analyzed multiple impacts' influence on the deformation of different components of the specimens under the same impact energy. Comparing the two specimens, the structural deformation is mainly concentrated in the bending at the joints and the tensile deformation of the L-shaped connector; the plastic hinge is first formed in the tensile region of the L-shaped connectors, and gradually extends to the beam section in the core area of the joint, and to the connection between the wooden columns and the steel sleeve. These deformations increased as the height of each impact gradually increased. Especially after the third impact, the deformation of the L-connector reached a serious level, which led to a change in the relative position between the H-shaped beam column and the bottom plate of the joint's sleeve, and eventually led to the separation of the two. Although the specimen M-SWMC-S-2 was strengthened in the thickness of the sleeve, it did not have a significant effect on the overall deformation of the member, and the displacement difference between the L-shaped connector and the bottom plate of the sleeve still increased with the increase in the number of impacts, indicating that the strengthening of the sleeve thickness has a limited effect on the improvement of the fatigue performance of the connector.

As there was no change in the first two specimens' hammer mass, Therefore, the test was carried out on specimen M-SWMC-S-3 with the thickness of the reinforced L- shaped connector. As can be seen in Fig. 16, compared to specimen M-SWMC-S-1, specimen M-SWMC-S-3's deformation overall was smaller than that of the first two specimens. After the third impact, M-SWMC-S-3 showed significant changes, the column tilted as a whole, the bolts connecting

the L-shaped connector to the joint base plate tilted, and plastic hinges were first formed at the connection between the L-shaped connector and the bolts and expanded to the periphery with the increase of the number of impacts; the L-shaped connector appeared to be slightly bent on the opposite side of the impacts, and plastic hinges were formed in the bending place, which led to the concentration of the stresses. Wood post cracks extend radially in the direction of the wood fibers; two vertical cracks appeared along the joint cross-member at the slotted end of the wood column, and the cracks extended from the slotted edge to the center of the column. Despite the multiple damage to M-SWMC-S-3, with the strengthened L- shaped connector, its impact resistance is still significantly higher than that of M-SWMC-S-1, highlighting the critical role of the strength of the L-shaped connector on the impact resistance of the joint.

Next, the location where the joint sustained impact was changed to investigate its influence on the components' overall and dynamic performance. By comparing the deformation of joints M-SWMC-J-1 and M-SWMC-J-2 with L-shaped connectors of different thicknesses under the same hammer mass and velocity, From Fig. 17 and Fig. 18, it can be seen that under the impact of the two joints, the impact side of the L-shaped connector is deformed in tension and bending, and the plastic hinge is formed and expanded firstly here, and at the same time, the joint base plate and the H-beam column are displaced vertically relative to each other. Due to the different thicknesses of the L-shaped connectors, the overall deformation of M-SWMC-J-1 is obviously smaller than that of M-SWMC-J-2, and the displacement between the node base plate and the H-shaped steel column is also smaller. Comparing specimens M-SWMC-J-1 and M-SWMC-J-2, because of the L-shaped connectors' reinforcement, specimen M-SWMC-J-1's deformation was significantly less than that of specimen M-SWMC-J-2. Further, there was a notable difference in the displacement between the joint baseplate and the H-shaped steel attributable primarily to the L-shaped connectors' thickness. When joint M-SWMC-J-2 was compared with joint M-SWMC-S-2, it was found that when the impact was at the joint, cracks appeared on the wooden column's upper part and sides. However, when the impact was at the steel column's mid-span, there was almost no significant deformation in the wooden column, indicating that the impact's location has a significant effect on the wooden column's deformation.

For the joint M-SWMC-W, the impact's location was changed again. As can be seen in Fig. 19, when the impact was on the wooden column, depression in the span of a wooden post, plastic hinges form rapidly in depressions and extend along the length of the wood post, and cracks appeared in the direction of the length of the extended wood columns, deformation of the L-shaped connector appeared, and displacement of the bottom plate of the node and the upper end of the H-beam columns appeared. After the third impact, the deformation of the L-shaped connector increased dramatically, the plastic hinge region was further extended, and the depth of the depression and the extent of the damage at the impact of the wooden column were significantly enlarged. When the impact location in the wood column, it not only had a significant effect on the joint's L-shaped connectors, but also caused significant damage to the wooden column itself. Similarly, because the L-shaped connectors were weak, significant deformation occurred at the connection between the steel column and the joint.

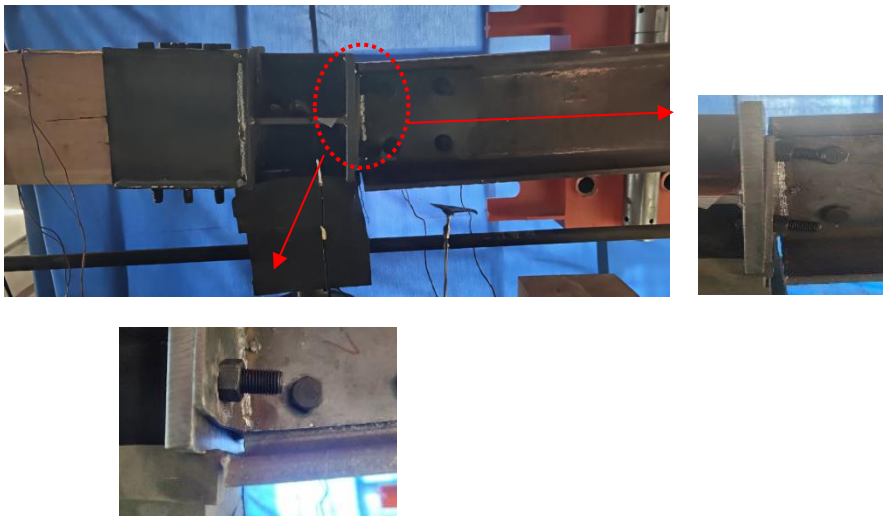

Fig. 14 Deformation mode of specimen M-SWMC-S-1 after impact

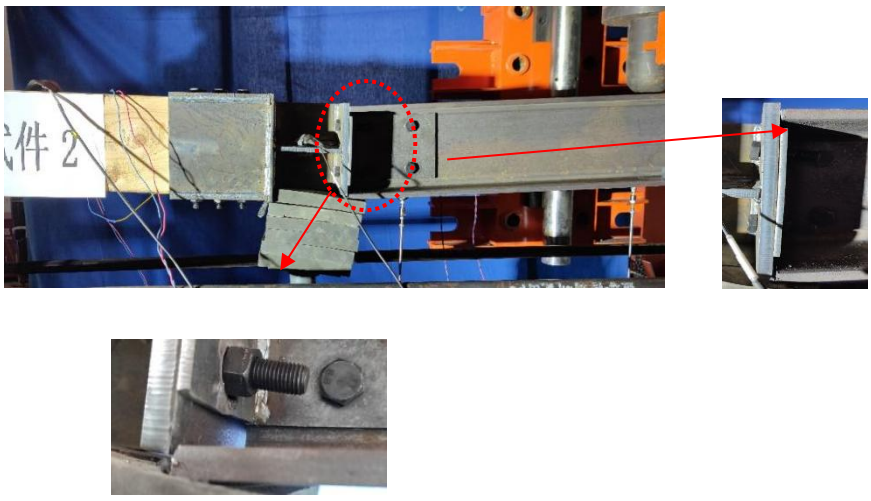

Fig. 15 Deformation mode of specimen M-SWMC-S-2 after impact

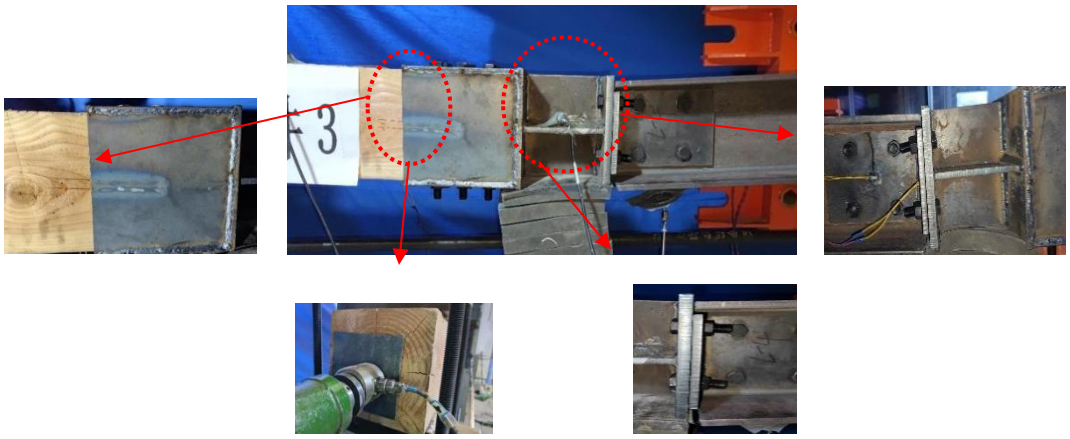

Fig. 16 Deformation mode of specimen M-SWMC-S-3 after impact

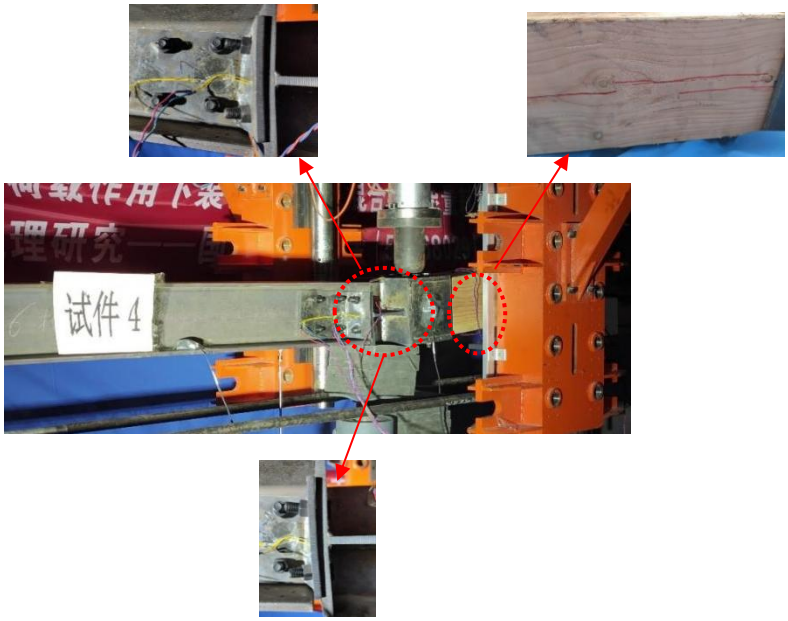

Fig. 17 Deformation mode of specimen M-SWMC-J-1 after impact

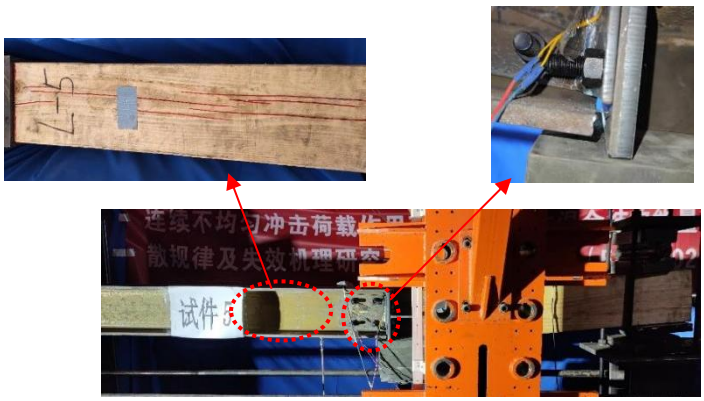

Fig.18 Deformation mode of specimen M-SWMC-J-2 after impact

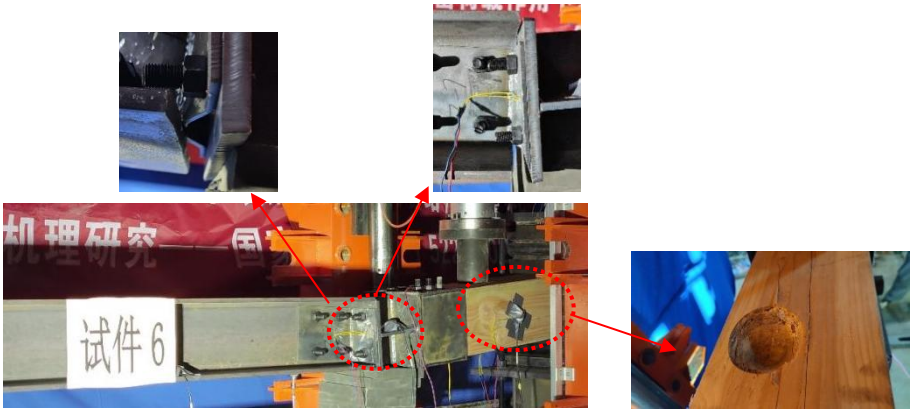

Fig. 19 Deformation mode of specimen M-SWMC-W after impact

4. Test results

4.1. Time history curves of impact force

Fig. 20(a)-(c) illustrates the M-SWMC-S-1-3 specimen's impact force-time course curves under three consecutive impacts. A detailed analysis of these impacts' effects on the M-SWMC-S-1 specimen revealed that, because of the hammer's lower height, the first impact placed the specimen in the elastic stage, which resulted in an impact force-time history curve that differed from the subsequent two impacts. The latter two exhibited similar trends, with peak impact forces of 91.8 kN, 433.3 kN, and 475.5 kN, respectively. The smaller peak impact forces of 190 kN and 215 kN during the second and third impacts indicated that consecutive impacts do not alter the impact forces' development pattern. The duration of the three consecutive impacts increased progressively (from 0.0233s to 0.0318s), which suggests that the impact energy intensifies with increasing velocity, and thereby prolongs the time for the impact's force to decay to zero. The accumulation of residual deformation under multiple impacts did not affect the dynamic changes in the single-impact force significantly. For M-SWMC-S-2, the results showed that the development trend of impact forces under three consecutive impacts also conformed to the pattern aforementioned. In the case of M-SWMC-S-3 under three impacts, the peak values were 276.9 kN, 468.7 kN, and 522.2 kN, respectively. Notably, the difference between the second and third peak values was significantly smaller than that between the first and second, which can be attributed to the cumulative damage from the first two impacts, which caused the weak points in the component to yield, and thereby limited the further surge in impact force and stabilized the peak values. The maximum impact force is shown in Fig. 21.

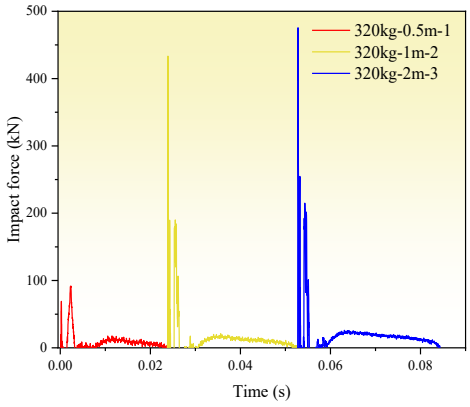

(a) M-SWMC-S-1

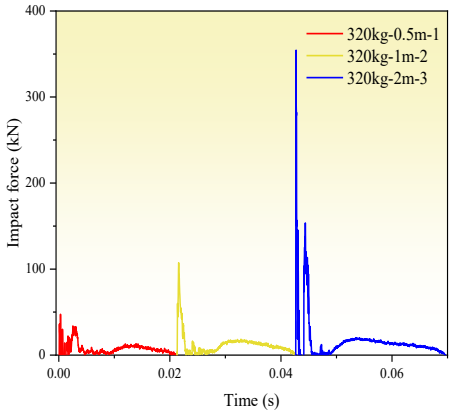

(b) M-SWMC-S-2

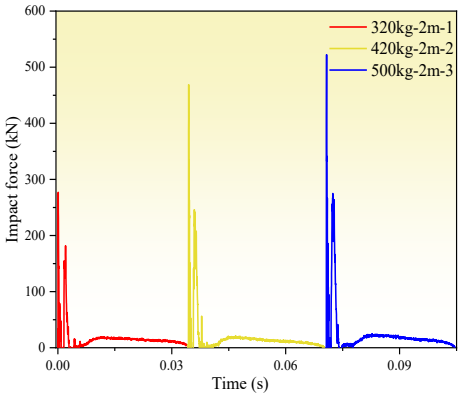

(c) M-SWMC-S-3

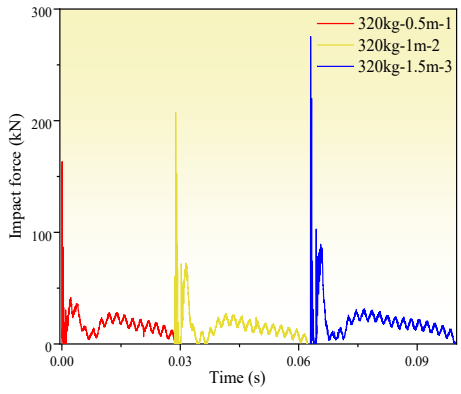

(d) M-SWMC-J-1

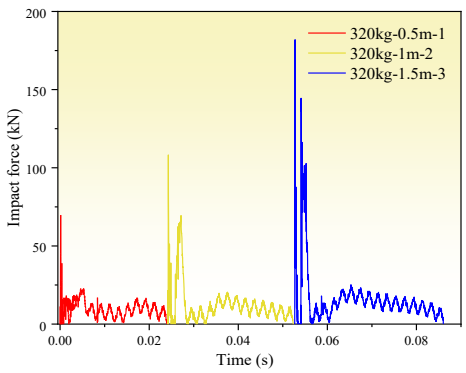

(e) M-SWMC-J-2

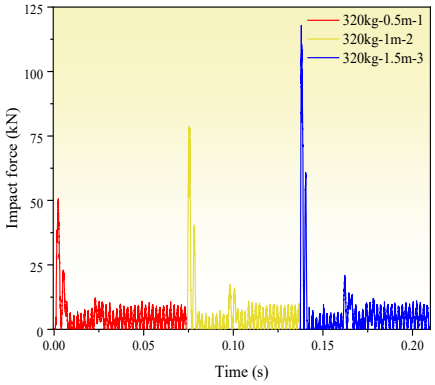

(f) M-SWMC-W

Fig. 20 Impact force-time course curve of specimen 1-6

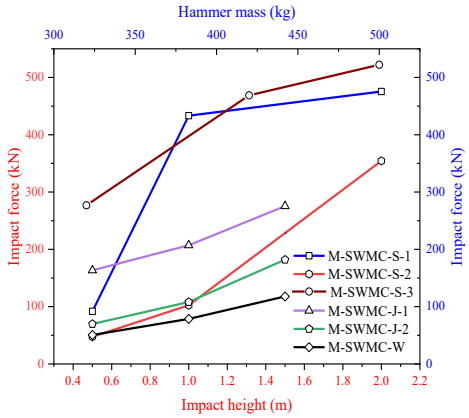

Fig. 21 Maximum impact force of specimen 1-6

Fig. 20(d)-(f) shows the time-history curves of the impact force for specimens M-SWMC-J-1-2 and M-SWMC-W. A detailed analysis of the results of three consecutive impacts on specimens M-SWMC-J-1 and M-SWMC-J-2 revealed that the two specimens' impact force trends were similar. However, because the L-shaped connectors were thicker, M-SWMC-J-1's peak force was higher than that of M-SWMC-J-2, and provided the joint with greater strength. The abnormally high peak impact force in M-SWMC-J-2's second impact is attributable to the larger vertical displacement caused by its L-shaped connectors' weakness, which enhanced the spring support's reaction force and affected the peak impact force subsequently. In contrast, M-SWMC-J-1 had lower secondary peak values because of its high-strength connectors, small displacement, and weak spring reaction force.

Analysis of specimen M-SWMC-W's impact force time-history curve revealed that, because wood (specifically, soft Douglas fir) was used as the impact target, the hammer's peak impact force was significantly lower than that of the other five specimens, and reflected the wood's low strength characteristic. In addition, the impact's duration was notably prolonged. This is because the soft wood converts kinetic energy into strain energy gradually through slow deformation during the hammer and the specimen's joint movement, rather than absorbing it rapidly. Table 5 summarizes the peak impact forces and durations for all six specimens.

Table 5
Table of impact force parameters

Test piece	First impact force peak(kN)	Second Impact Peak(kN)	Third Impact Peak(kN)	Duration of first impact(s)	Second Impact Duration(s)	Duration of third impact(s)
M-SWMC-S-1	91.8	433.3	475.5	0.0233	0.0294	0.0318
M-SWMC-S-2	47.4	107.3	354.4	0.0213	0.0211	0.0269
M-SWMC-S-3	276.9	468.7	522.2	0.0343	0.0356	0.0346
M-SWMC-J-1	163.3	207.1	275.4	0.0209	0.0413	0.0367
M-SWMC-J-2	68.6	108.2	181.9	0.0241	0.0285	0.0334
M-SWMC-W	50.6	78.0	117.9	0.0740	0.0636	0.0720

4.2. Time history curves of displacement

Fig. 22 displays the six specimens' vertical displacement time-history curves under three impacts, and shows that they exhibited similar trends: after the initial impact, the displacement increased and then decreased. This phase involved the hammer and the specimen's joint downward movement, followed by a rebound. The specimen continued to move upwards because of the spring support's reaction force, and exceeded its initial position eventually, which manifested as a negative valley value in the displacement curve. Subsequently, the peak displacement results from the superposition of the hammer's secondary fall and the specimen's downward movement. The final stable displacement is attributable to residual deformation. This indicates that the impact's energy has a significant influence on the specimens' residual deformation. Taking specimen M-SWMC-S-1 as an example, after three consecutive impacts with a 320kg hammer at a height of 0.5m, its deformation remained within the elastoplastic range. The residual deformation after a single impact was not significant, with a cumulative residual deformation of 27.5mm after three impacts, which increased to 6.6mm, 9.1mm, and 11.8mm, respectively, after each impact. In contrast, specimen M-SWMC-S-2 exhibited different deformation characteristics under the same conditions: the residual deformation after the first impact was 6.4mm,

with almost no increase after the second impact, indicating that the spring support mitigated deformation effectively. However, the third impact increased the deformation significantly to 10.2mm, and resulted in a cumulative deformation of 23.1mm. Notably, during the second fall of the hammer, the displacement surges, reflecting that the increased velocity prompted the specimen to dissipate more energy through plastic deformation. Because of the combined increase in the hammer's velocity and mass, specimen M-SWMC-S-3 had a significantly enhanced impact force and support reaction force, which led to the specimen's increased negative displacement. The final residual deformation reached 21.0mm, further confirming that the impact's energy had a pronounced effect on the specimen's residual deformation. The maximum displacement is shown in Fig. 23.

For specimen M-SWMC-J-1, the impact tests at the joint revealed that as the hammer's height increased, the impact's peak force rose gradually (25.2mm, 34.8mm, 44.4mm). The residual deformation also accumulated progressively, with 4.8mm after the first impact, increasing to 7.4mm after the second, and reaching 15.7mm after the third, resulting in a total residual deformation of 27.9mm. Although M-SWMC-J-2 exhibited a similar displacement trend, compared to M-SWMC-J-1, the residual deformation was reversed. After the first impact, the residual deformation was significant (15.2mm), and then decreased to 11.1mm and 7.4mm, with a cumulative total of 33.7mm. This phenomenon is attributable to its thinner L-shaped connectors, which formed plastic hinges under joint impacts quickly, absorbed energy effectively, and strengthened as the number of impacts increased, thereby limiting subsequent displacements. Specimen M-SWMC-W's residual deformation behavior was similar to that of M-SWMC-J-2, with values of 19.9mm, 12.3mm, and 5.4mm in sequence, and a cumulative total of 37.6mm. Similar to M-SWMC-J-2, the significant formation of plastic hinges in the L-shaped connectors after the first impact inhibited the displacement response to subsequent impacts significantly.

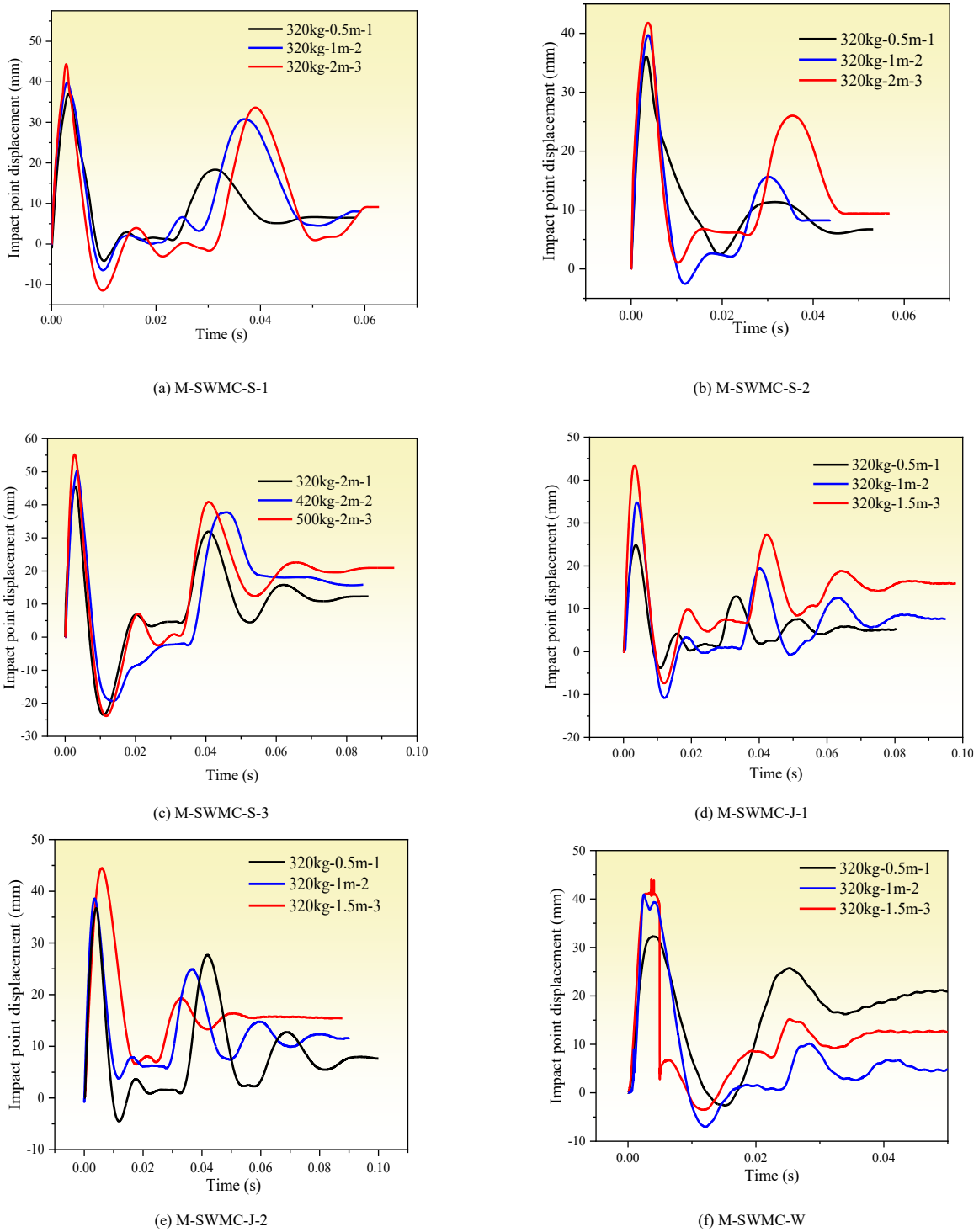

(a) M-SWMC-S-1

(b) M-SWMC-S-2

(c) M-SWMC-S-3

(d) M-SWMC-J-1

(e) M-SWMC-J-2

(f) M-SWMC-W

Fig. 22 Displacement time curve of specimens 1-6

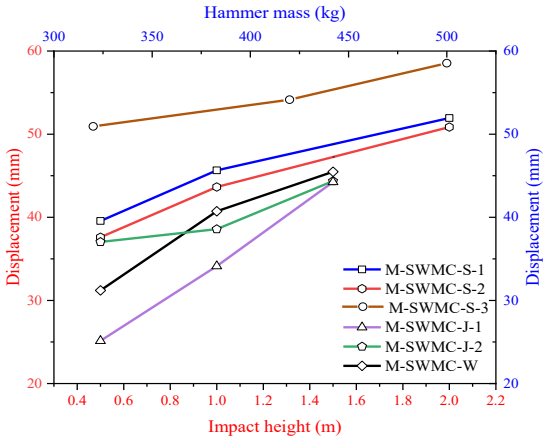

Fig. 23 Specimens 1-6 of maximum displacement

4.3. Time history curves of acceleration

In this experiment, accelerometers were installed at three locations on specimen 1, and we analyzed the acceleration changes by taking M-SWMC-S-1 as an example. Fig. 24(a)-(d) shows that during the second impact, the peak acceleration reached 7861m/s² at the impact's location and 5240m/s² at the joint. During the third impact, these values increased to 8294m/s² and 7840m/s², respectively.

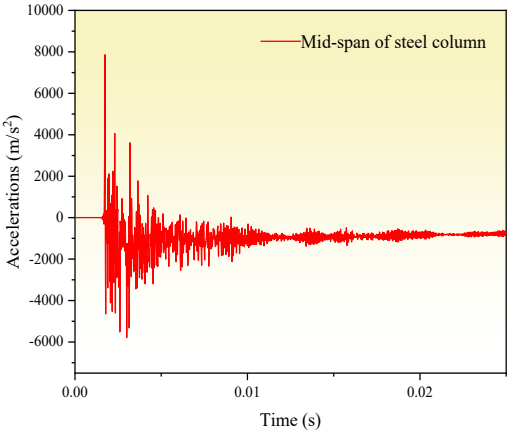

(a) M-SWMC-S-1 second impact mid-span of steel column acceleration

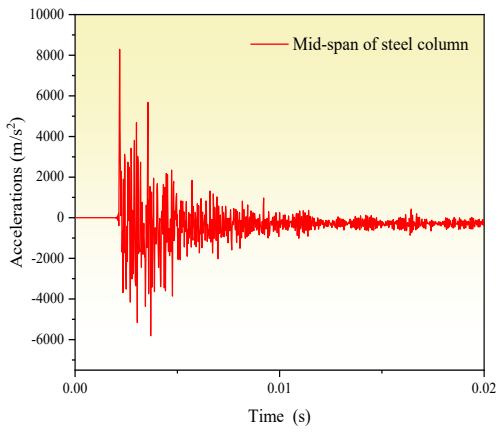

(b) M-SWMC-S-1 third impact mid-span of steel column acceleration

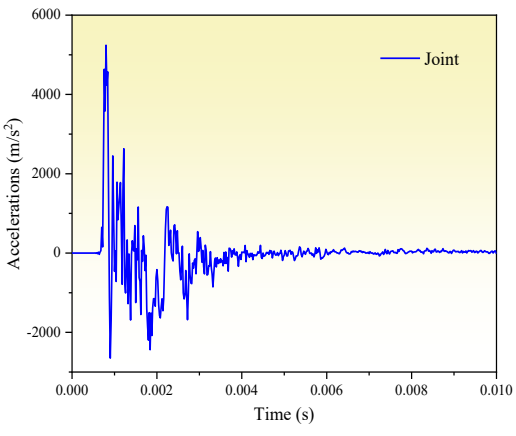

(c) M-SWMC-S-1 acceleration at second impact joint

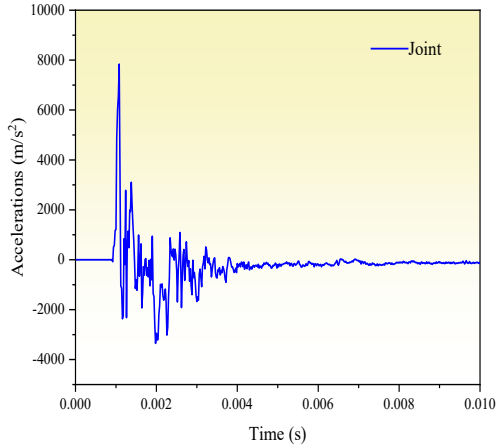

(d) M-SWMC-S-1 acceleration at third impact joint

Fig. 24 Acceleration time-course curve of specimen 1

5. Numerical simulation

5.1. Constitutive relation

5.1.1. Constitutive model of steel

During the establishment of the new joint in this paper, Q235 steel was used for the joint sleeve, L-shaped connectors, steel columns, steel beams, and joint-to-beam connectors, and grade 8.8 M16 bolts were used for bolts. Under the action of impact load, the joint was in a large deformation stage in the later stage, and significant deformation or even fracture may occur at the steel beam flange, web, L-shaped connector, and other locations in the joint area. Therefore, this paper adopted a metal ductile damage model and the comprehensive fracture criterion based upon stress triaxiality that Wierzbicki et al. proposed [36]. Its expression is as eq. (4).

$$\bar{\varepsilon}_d \begin{cases} \frac{\varepsilon_{d1}}{1+3\eta} & -\frac{1}{3} < \eta \le 0 \\ \varepsilon_{d1} + (\varepsilon_{d2} - \varepsilon_{d1})(3\eta)^2 & 0 < \eta \le 0 \\ \frac{\varepsilon_{d2}}{3\eta} & \frac{1}{3} < \eta \end{cases} \tag{4}$$

Where: ε_{d1} is the initial fracture strain under pure shear (η=0), and the Q235b grade steel in this paper was 0.133; ε_{d2} is the initial fracture strain under

the uniaxial tensile condition (η=1/3), and the Q235b grade steel in this paper was 0.273 [37].

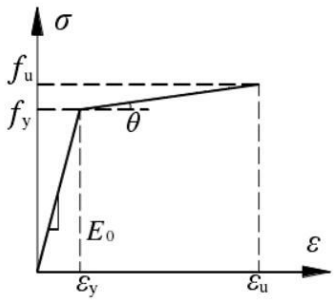

Fig. 25 Constitutive relation of steel

Table 6
Material performance parameters for strain rate effect

Density of steel (kg/m³)	Elastic modulus (GPa)	Poisson's ratio	Yield strength (MPa)	Failure strain	Ultimate strength (MPa)
7800	210	0.3	354.70	0.18	467.36

5.1.2. Constitutive model of wood

The constitutive model of wood adopts the ideal elastoplastic model that Chen proposed [38]. As shown in Fig. 26, f_{ce} represents the equivalent maximum compressive stress, and f_c represents the compressive strength, where $f_{ce} = 0.93f_c$. denotes the maximum elastic compressive strain, ε_{ce} represents the ultimate compressive strain, ε_{tu} represents the ultimate tensile strain, and E denotes the elastic modulus of wood. The mathematical expression is given in Eq. (5).

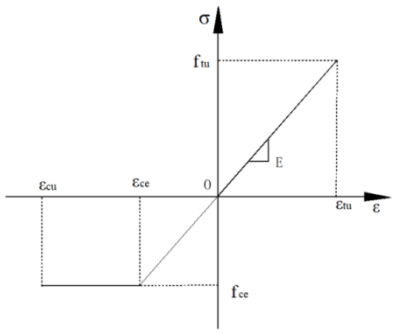

Fig. 26 Constitutive relation curve of wood

$$\sigma_w = \begin{cases} E & \varepsilon_{ce} \le \varepsilon \le \varepsilon_{tu} \\ f_{ce} & \varepsilon_{ce} \le 0 \\ f_{tu} & 0 \le \varepsilon_{tu} \end{cases} \quad (5)$$

The orthotropic materials' elastic phase analysis was conducted using the engineering constant method in Abaqus. Douglas fir wood's material properties in the model are shown in Table 7.

Table 7
Mechanical parameters of Douglas fir

E1	E2	E3	υ12	υ13	υ23	G12	G13	G23
11890	780	409	0.45	0.47	0.32	713	890	215

Note: The units of E and G are MPa; subscripts 1, 2, and 3 represent the longitudinal, radial, and tangential directions of the wood, respectively.

5.2. Model establishment

In this paper, the "surface-to-surface" contact method is utilized to construct a solid contact pair by clearly defining the master and slave surfaces of the contact according to Table 8. The "Penalty" friction formula is applied tangentially to simulate the friction force, and the coulomb coefficient of friction of the contact surfaces in the nodal model is set to 0.4 by the simple friction test of each member and the range of friction coefficients of the contact surfaces of the reference materials [39], and the coulomb coefficient of friction of the contact surfaces of the impactor and the member is set to 0.3 [40]. For the normal direction, "Hard" contact was selected, which allowed separation after contact. ABAQUS/Explicit was employed for the FEA, which is suitable for dynamic loading. Steel columns, wooden columns, steel beams, joint sleeves, L-shaped connectors, etc., were all simulated using three-dimensional solid elements with an eight-node linear hexahedral reduced integration format (C3D8R).

Table 8
Definition of contact master and slave surfaces

Different category	Surface stiffness	Mesh compactness	Area size
Contact surface	High stiffness	Thinly spread	Large area
Contact surface	Small stiffness	Compressed	Small area

5.3. Validation of finite element analysis methods

Figs. 27 and 28 compare the experimental and finite element simulation deformation modes under specimen M-SWMC-J-2's third impact load. It can be seen that both deformation modes exhibited bending deformation at the joint, separation between the H-shaped steel column and the bottom plate of the joint sleeve, and bending deformation of the L-shaped connector.

(a) Deformation pattern of specimen M-SWMC-J-2 test

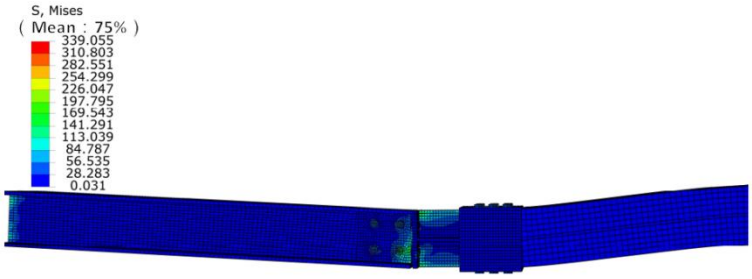

(b) Specimen M-SWMC-J-2 finite element simulation deformation mode

Fig. 27 Comparison of deformation patterns after impact for specimen M-SWMC-J-2

(a) Test L-connector deformation modes

(b) Finite element simulation of L-connector deformation modes

Fig. 28 Comparison of local deformation modes of specimen M-SWMC-J-2

Fig. 29 compares the impact force between the mid-span impact test and the finite element simulation of specimen M-SWMC-J-2 under a hammer velocity of V_0=5.477m/s and hammer mass of M=320kg. The results indicated that the impact's first peak force was 264.5kN in the simulation and 275.4kN in the experiment, with an error of only 4.1%, demonstrating high consistency before and after the peak. However, there were significant differences in the second peak and the plateau section. This is attributable to the reaction force that the spring support generated in the experiment when the specimen and the hammerhead moved upwards, which is not accounted for in the simulation. Consequently, the impact's subsequent simulated force was lower.

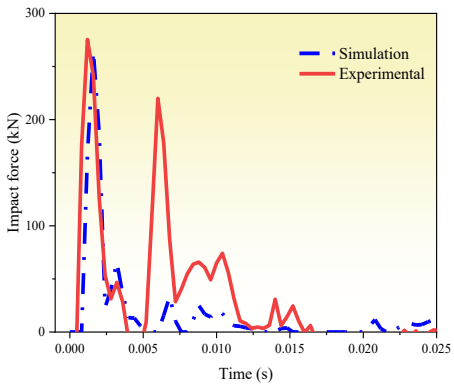

Fig. 29 Comparison of time-range curves of impact force for specimen M-SWMC-J-2

5.4. Destruction mechanisms

5.4.1. Nodal deformation patterns

Summarizing the joint's deformation characteristics at three impact locations, it was found that the steel column and the wooden column exhibited different deformation modes because their material properties differed. Steel columns, due to high modulus of elasticity and ductility, are mainly subject to local buckling or bending deformation under impact, and plastic deformation is concentrated in the joint connections, which maintains better overall integrity; wood columns, as anisotropic materials, are prone to brittle cracking or out-of-plane instability near the point of impact under impact, accompanied by fiber tearing or cross-grain cracking. At lower impact energies, changes in the impact's location had a limited effect on the joint overall, which manifested primarily as local deformation at the point of impact. This is because of the instantaneous nature of the impact process, where the energy fails to diffuse rapidly throughout the entire specimen, and the stress wave does not propagate to the other end of the impact's location, which causes significant deformation to occur locally (particularly in weak areas), and triggers out-of-plane instability. However, this local deformation dissipates most of the impact's energy effectively, which limits the propagation of stress to other parts, and keeps most specimen areas in an elastic state, while plastic deformation is concentrated at the joints and connections. Specifically, the displacement between the H-shaped steel and the bottom of the joint sleeve is caused by the L-shaped connector's tension and bending. Fig. 30 shows the structural plastic strain and stress programs under different impact locations. The quantitative comparison shows that steel absorbs energy through localized plastic deformation due to its ductility, while wood components dissipate energy through localized cracking due to their brittle characteristics. Quantitative comparisons show that steel absorbs energy through localized plastic deformation by virtue of material ductility, while wood components dissipate energy through localized cracking due to their brittle characteristics, and that the energy absorption mechanisms of the two are significantly different due to differences in material properties.

5.4.2. Damage evolution

Under an impact energy of V_0=7m/s and M=500kg, specimen M-SWMC-S-2's damage evolution (taking the steel's mid-span impact as an example) can be explained through the equivalent plastic strain. Fig. 31 shows that at the impact's peak force, stress waves propagated from the impact location to the joint, which caused minor plastic damage initially at the connection between the joint and the beam. As the impact process progressed, the stress waves were transmitted toward the beam ends and the ends of the wooden column, and the damage also extended along the specimen's joint toward both ends of the steel beam and the connections between the wooden column and the joint. During the plateau phase of the impact's force, the damage concentrated in the steel column's mid-span impact zone, the connections between the steel beam and the joint, as well as the connections between the wooden column and the joint, with significant aggravation of bending deformation at the joint. By the end of the plateau phase, the specimen's deformation reached its limit, and the damage accumulated to its maximum value and no longer increased. The L-shaped connector bent under tension, displacement occurred at the connection between the joint and the steel column, and the steel beam and joint connector were compressed and deformed. In the attenuation stage of the impact's force, although there was some rebound in the bending of the joint overall, the equivalent plastic strain remained relatively stable until the end of the impact.

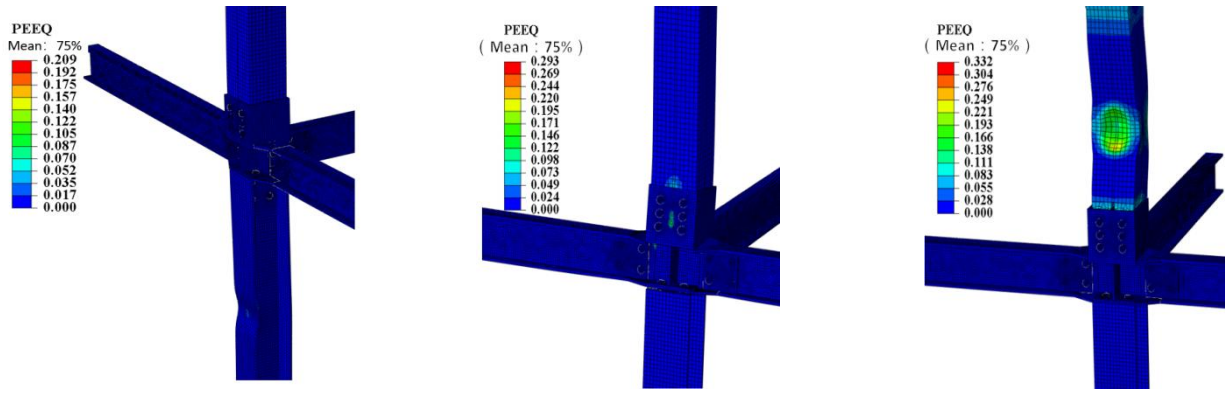

(a) Plastic strain in the span of impact steel

(b) Plastic strain at impact joint

(c) Plastic strain at impact on a wooden column

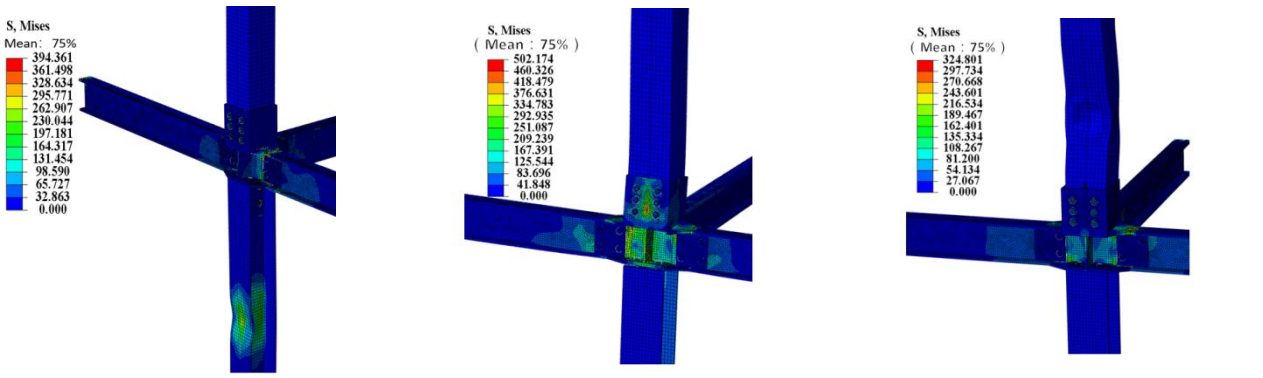

(e) Impact steel span-time stress cloud (f) Stress cloud at impact joint (g) Stress cloud at the time of impact on a wooden post

Fig. 30 Joint deformation pattern under impact loading

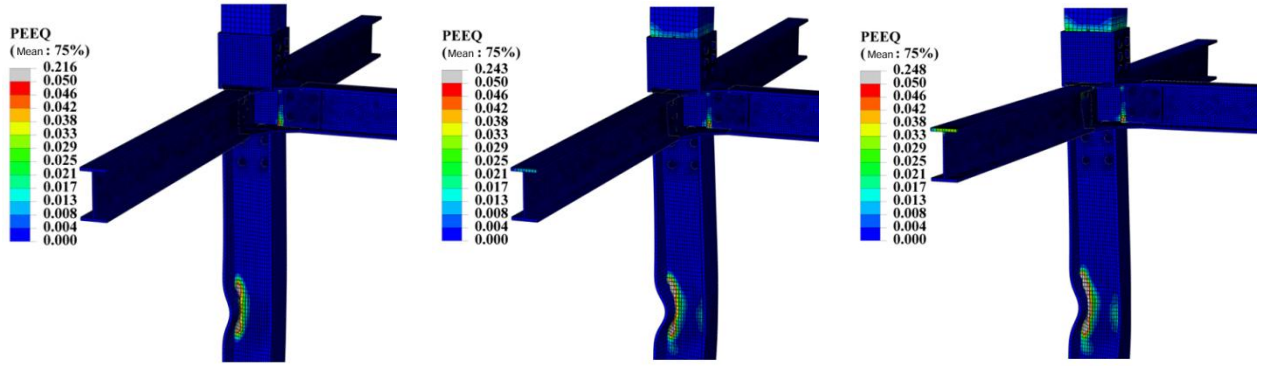

(a) At peak impact force (b) At the impact platform stage (c) When deformation reaches its maximum

Fig. 31 Joint's equivalent plastic strain development when the impact location is in the steel span

6. Parametric study

6.1. Different hammer masses

The dynamic response of joint M-SWMC-S-2 increases with increasing impact mass when the impact velocity V_0=7m/s (Fig. 32). The maximum displacements and maximum impact forces at the joints for different hammer masses are shown in Fig. 33. When the hammer mass increases from 320 kg to 700 kg, According to the conservation of momentum, the initial momentum of the impactor interacts with the specimen to produce an increased impulse, the joint displacement increased with the hammer's mass and reached a maximum of 240mm at 700kg without convergence in the displacement curve, indicating the column's failure overall. The increase in the impact force plateau value, displacement, and impact duration is consistent with the impulse theory, i.e., the increase in mass prolongs the time of action between the impactor and the specimen, which allows for a more adequate transfer of energy and leads to an expansion of the deformation region.

Deformation patterns of H-beam columns demonstrate the relationship between energy absorption and material plasticity development. At a hammer mass of 320 kg, the small impact momentum causes only a slight local deformation. The energy is mainly absorbed by the elasticity of the steel column; with the increase of mass, the impulse increases to promote the transfer of stress waves to the joints, and the plastic deformation gradually extends from the impact point to the joints and beam ends. When the mass reaches 700kg, the L-connector is damaged in tension and bending due to the excessive impulse, leading to the failure of the structure as a whole. It is worth noting that the increase in the peak impact force is not significant. This is because the development of impact force in the early stage is mainly limited by the impact velocity, while the effect of mass increase is more concentrated in the later stage of stabilization and decay, reflecting the stage-by-stage mechanism of the impulse-momentum relationship in the process of dynamic response.

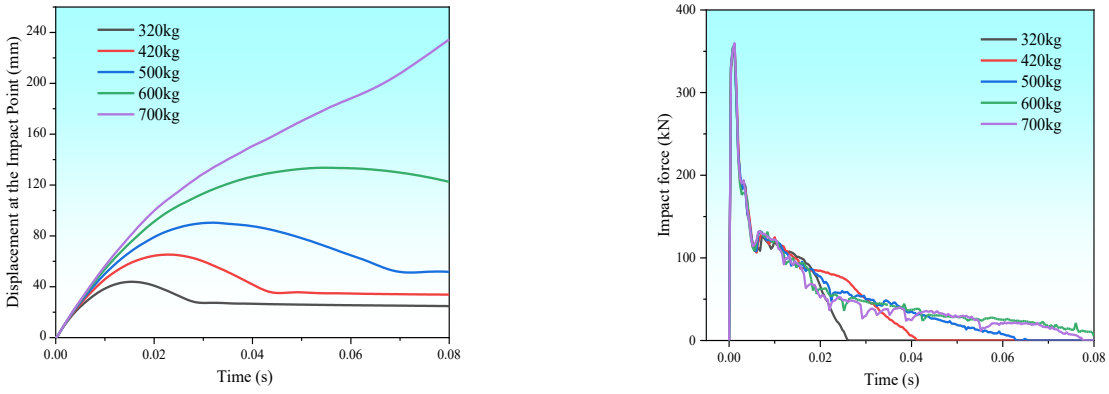

(a) Vertical displacement time course Curve (b) Impact force time course Curve

Fig. 32 Dynamic response of the joint under different hammer masses

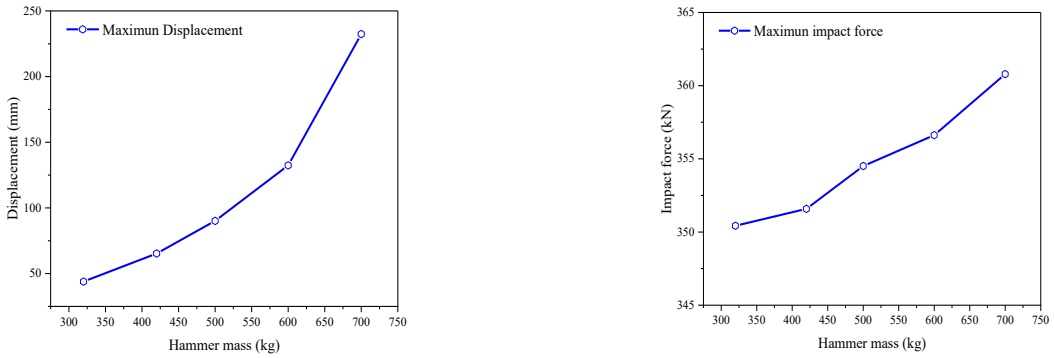

(a) Maximum displacement (b) Maximum impact force

Fig. 33 The maximum displacements and maximum impact forces at the joints for different hammer masses

6.2. Different hammer velocities

The dynamic response of the joint M-SWMC-S-2 shows a regular variation with the increase of the impact velocity V_0 at the falling hammer mass M = 320 kg (Fig. 34). The maximum displacements and maximum impact forces at the joints for different hammer velocities are shown in Fig. 35. The increase in impact velocity increases the initial momentum of the impactor, and according to the momentum theorem, the impulse generated when interacting with the specimen also increases, resulting in a significant increase in the peak impact force, plateau value and displacement of the impact point. When V_0 was less than or equal to 7m/s, because of the small initial momentum and the short duration of the shock action, the impact force plateau was not evident. However, at V_0=10m/s, a significant increase in the momentum of the impactor and prolongation of the interaction time with the specimen, a significant impact force plateau, and the impact's duration was extended greatly. When V_0 was greater than or equal to 7m/s, the displacement at the impact point increased steadily with increasing velocity. The member is in the elastic phase because the impulse transmitted by the impactor does not exceed the limit of absorption of the elastic deformation energy of the material. At V_0=10m/s, excessive initial momentum that causes the impulse to exceed the elastic limit of the material by a wide margin, causes the member to enter an elastic-plastic phase and the difference between the post-impact displacement and the maximum displacement decreases.

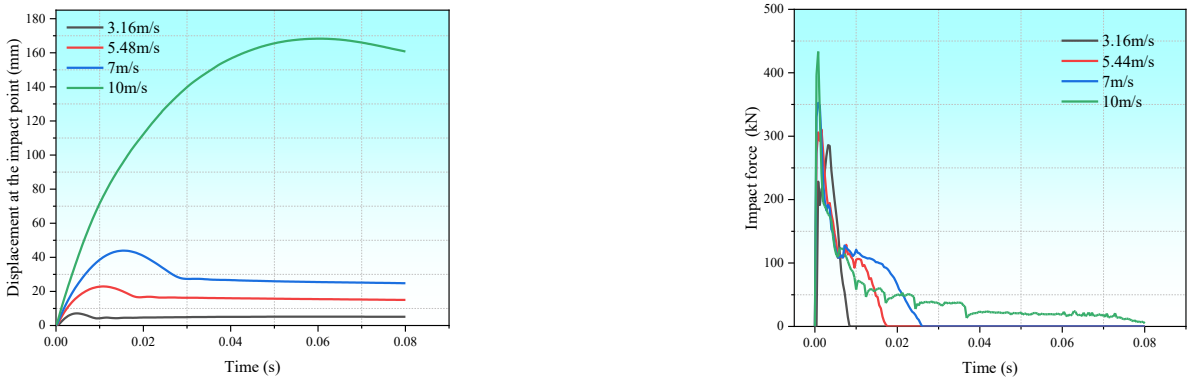

(a) Vertical displacement time history curve (b) Impact force time history curve

Fig. 34 Dynamic response of the joint under different hammer velocities

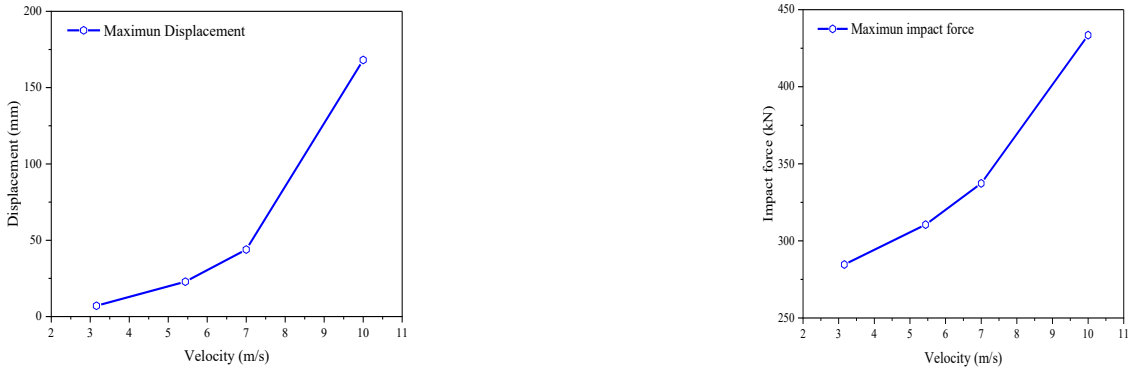

(a) Maximum displacement (b) Maximum impact force

Fig. 35 The maximum displacements and maximum impact forces at the joints for different hammer velocities

From observing the deformation patterns: At V_0=3.16m/s, deformation occurred at the H-shaped steel column's flange at the impact site, with no plastic deformation at the joint. As the velocity increases, the impulse transmitted by the impactor increases, the plastic deformation region gradually expands, and the stress wave is transmitted to the joints, resulting in displacements of the beam ends, the L-shaped connectors, and the base plate. At V_0=10m/s, the significant deformation of the steel column span due to excessive impulse, which formed a plastic hinge between the baseplate and the L-shaped connector. The bolt holes were enlarged, and displacement arose between the connecting plate and the beam. The connection edge between the wood column and the joint sleeve pulled apart, resulting in the joint's severe deformation overall.

6.3. Different impact locations

Under the condition of a falling hammer mass M=320kg, impact velocity V_0=7m/s (i.e., constant initial momentum), taking joint M-SWMC-S-2 as an example, the impacts of different impact positions on the joint are different due to different impulse transmission paths and material properties. When impacting the steel column span and node, because both materials are steel, the stress wave propagation characteristics are similar, so the displacement and impact force curves are similar in shape (Fig. 36); however, the displacement is larger when impacting the joint, this is due to the joint as the core of the structural connection, it is easy to generate displacement with the steel column connection, and it is easier to trigger deformation of the connection during the transfer of the impulse, which results in the accumulation of the displacement. Wooden columns are more susceptible to denting upon impact due to the low modulus of elasticity of the material and weak plastic deformation capacity. The low efficiency of impulse transfer leads to longer impact action time, longer duration of the impact force platform, and because the wood itself absorbs a large amount of energy, it is difficult for the stress wave to be transmitted to the joints and steel columns to keep them in an elastic state. The maximum displacement and maximum impact force of the joints at different impact locations are shown in Fig. 37.

From the deformation mode, when impacting the steel column span and joint, the impulse causes the L-shaped to be tensile and bending, triggering the displacement of the joint base plate and the steel column, and when impacting the joint because it is closer to the connectors, the impulse transfer is more direct, and the displacement response is more significant; When impacting wooden columns, the plastic deformation (depression) and elastic deformation (cracks on the bottom surface of the connection edges and voids in the upper part) of the wood effectively dissipate the impulse, limiting the propagation of the stress wave to the nodes and the steel columns, thus avoiding deformation of the latter two.

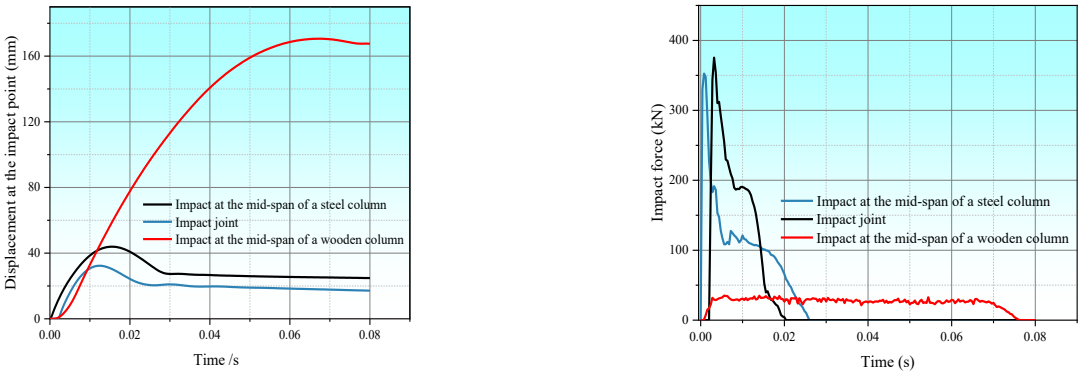

(a) Vertical displacement time history curve

(b) Impact force time history curve

Fig. 36 Dynamic response of the joint at different impact locations

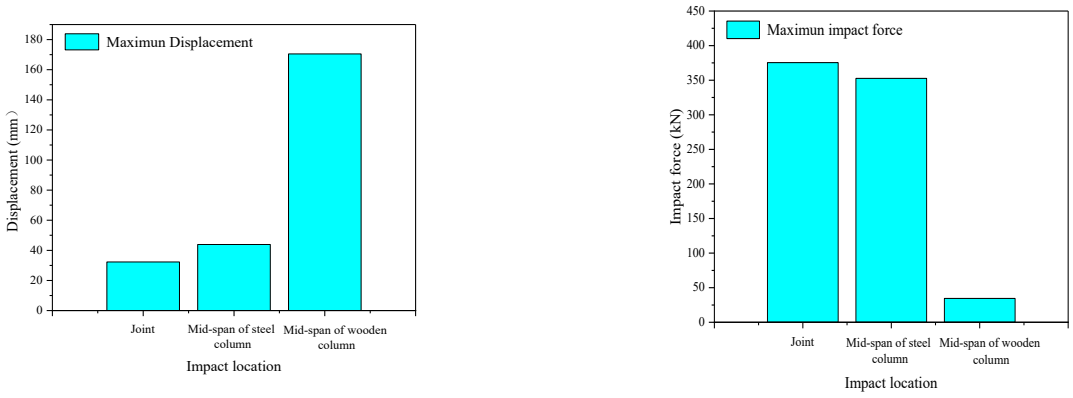

(a) Maximum displacement

(b) Maximum impact force

Fig. 37 The peak displacements and peak impact forces at the joints for different impact locations

7. Conclusion

This paper conducted experiments and finite element simulations that focused on the new prefabricated steel-wood hybrid columns, and investigated their performance in resisting impact. The conclusions drawn from the study are as follows:

(1) The hammer impact test reveals that the key deformation characteristic of the new steel-wood hybrid beam-column joint is the bending deformation at the joint, which in turn triggers the bending of the overall member. By adjusting the impact location, the weakest link in the structure was found to be the connection area between the L-shaped connector and the wooden column at the joint. Further experiments showed that increasing the L-shaped connector's thickness reduced its deformation under the same impact energy and mitigated the column's bending overall effectively. Combining the results of the comparative tests, the optimum parameters were determined to be: sleeve thickness of 5mm and L-shaped connector thickness of 10mm. Therefore, the actual design should focus on strengthening the strength of the L-shaped connector to ensure that the joints will not be damaged before the members, so as to improve the impact resistance of the overall structure.

(2) The drop weight impact test and the joint's finite element simulation showed that, when the component's impact resistance under three impact locations was compared, the dynamic response and deformation mode were similar when the steel column and the joint sustained impact. In contrast, the damage to the wooden column itself was significantly greater than the former

two when the column sustained impact. Therefore, it is recommended that special attention be paid to the wood's force transmission mechanism in the design of steel-wood hybrid structures.

(3) Upon analyzing the experimental and simulation data, it was found that an increase in the hammer's velocity enhanced the impact's peak force and extended the impact plateau significantly, indicating that the hammer's velocity is a crucial influencing factor. On the other hand, an increase in the hammer's mass extended the impact's force decay time primarily, and had a limited influence on the peak value, suggesting that the impact attributable to the hammer's mass is concentrated in the later stages of the impact.

(4) The structure dissipated impact energy primarily through the component's plastic strain energy and the L-shaped connector under impact. As the wooden column's capacity to dissipate energy was much lower than that of other parts of the hybrid column, the situation in which the wooden column fails before the component under impact should be considered fully during design.

Acknowledgments

This work is supported by the National Natural Science Foundation of Chi na (Grant No.52268029)and the Open Fund of Shock and Vibration of Enginee ring Materials and Structures Key Laboratory of Sichuan Province (Grant No .20kfgk03).

Authorship contribution statement

Chang Wu: Conceptualization, Data curation, Methodology, Software, Visualization, Writing - original draft, Writing - review & editing.

Yingni Fan: Investigation, Writing - review & editing, Software, Validation, Supervision.

Yuehan Zhang: Writing - review & editing, Validation.

Yutong Tian: Software, Investigation, Methodology.

Conflict of interest statement

We declare that we have no financial or personal relationships with others or organizations that can inappropriately influence our work.

References

[1] Gou B. L., Wang X. L., Wu C. (2023). Experimental and numerical study on the behavior of single-layer spherical reticulated shells under the combined action of temperature and impact load, Thin-Walled Structures, 182: 110333.

[2] Fábio C., Isabel V., João A., Eduardo A. (2024). Experimental characterization of bond between concrete and HDG steel tubes for mixed steel-concrete structures. Materials and Structures, 57.

[3] Xu F., Yuan Z., Liu N., Li Z. X., Jia L. G., Xu W. (2023). An experimental study on seismic performance of steel composite beam-column regid joint and buckling restrained knee-braced. Advanced steel construction, 19(4): 375-382.

[4] Feng J., Jin J., Xia J., Fang Y. Z. (2021). Experimental study on seismic performance of PEC composite column-steel beam frame with welded T-stub strengthened connections. Advanced steel construction, 44974-981.

[5] Du Y. F., Li F. Y., Li H., Hong N. (2024). Seismic behavior and resilience assessment of prefabricated beam-column joint with replaceable graded-yielding energy-dissipating connectors. Engineering Structures, 319, 118814-118814.

[6] Zhang C. W., Gholipour G., Mousavi A. (2019). Nonlinear dynamic behavior of simply-supported RC beams subjected to combined impact-blast loading. Engineering Structures, 181: 124-142.

[7] Damian K., Aleksander K., Bartosz M., Dominika Z. (2024). Experimental investigation of steel beam-to-column end-plate joints under static and impact loading. Journal of Constructional Steel Research, 212.

[8] Chen K., Zhao Y., Tan K. H. (2021). Behaviour of steel beam-column joints subjected to quasi-static and impact loads. Journal of Constructional Steel Research, 183.

[9] Deng P., Chang D. S., Chen X. L., ;Zhu Z. Y., Raheel A. (2024). Analysis of the dynamic mechanism of square tubular T-joints with chord flanges subjected to impact loading. Advanced steel construction. 19(4): 375-382.

[10] Zeng L., Liu Y. H., Zhang H., Liu C. J. (2022). Experimental study on dynamic response and residual mechanical behavior of SRC columns under repeated lateral impacts. Engineering Failure Analysis, 138.

[11] Wei J. H., Xue J. Y., Hu Z. B., Qi L. J.(2024). Experimental study on dynamic shear-behavior of H-shaped SRC columns under lateral impact loading. Journal of Constructional Steel Research,213: 108396-.

[12] Zhu X., Kang M., Fei Y. F., Zhang Q. (2021). Impact behavior of concrete-filled steel tube with cruciform reinforcing steel under lateral impact load. Engineering Structures,247.

[13] Kang X. J., Liu Y. H., Zhao L., Yu Z. X., Zhao S. C., Tang H. (2019). Dynamic response analysis method for the peak value stage of concrete-filled steel tube beams under lateral impact. Advanced steel construction. 15(4): 329-337.

[14] Huang Z. J., Cek S., Chen W. S., Paing M., Li D. Q., Hao H.(2025). Impact performance of fibre reinforced geopolymer concrete beams with steel-FRP composite bars, Engineering Structures, 329: 119880-119880.

[15] Huang J. Z., Fu C. J., Yu Z. Q., Huang Y. T., Cai H. M., Chen H. Y., Luo C. S. (2024). Impact resistance performance and simplified calculation method of web-opened steel beams under impact loads, Journal of Constructional Steel Research, 218: 108688-.

[16] Zhu B. R., ZhangY. H., Ye H. Z., Wei Y., Pan J. L., Zhang M. Z.(2025). Low-velocity impact performance of biomimetic 3D printed engineered cementitious composites beams, Construction and Building Materials, 470: 140550.

[17] Zou D. L., Teng J.L., Xu L. (2024). Exploring the impact resistance performance of RC beams based on an enhanced interpretable automated machine learning approach, Structures, 70: 107893-107893.

[18] Zhu Y., Liu Q. G., Zhang X. Y., Xing Z. Q., Zhang W. P., Chen Y., Wang L. (2025). Experimental and numerical investigations of UHPFRC beams under impact loading, Structures, 74: 108360.

[19] Wu Q. J., Zhi X. D., Guo M. H. (2019). Finite element analysis for the progressive failure of FRP-reinforced steel component under low-velocity impact. Advanced steel construction, 15(3): 267-273.

[20] Yang R. Y., Wan J., Zhang X. F. (2021). Modelling of steel-timber composite beams: validation of finite element model and parametric study. Wood Research, 66:5.

[21] Xu L., Navid K., Li M. Z. (2021). Design improvement of a composite-to-steel butt-joint based on finite element analysis. Ocean Engineering, 238.

[22] Kia L., Valipour H. R. (2021). Composite timber-steel encased columns subjected to concentric loading. Engineering Structures, 232.

[23] Chen Z. H., Xu J. H., Ting T.(2022). Seismic research on column base joint of L-shaped CFST columns under cyclic loading. Structures, 45: 1212-1224.

[24] Zhou T., Yang Z. X., Chen Z. H. (2022). Seismic behavior of connections between H-beams and L-shaped column composed of concrete-filled steel tube mono-columns connected by double vertical plates. Journal of Constructional Steel Research, 198.

[25] Chen Z. H., Niu X. Y., Liu J. D., Han K. S. (2021). Seismic study on an innovative fully-bolted beam-column joint in prefabricated modular steel buildings. Engineering Structures, 234.

[26] Chen F., He M. J., Li M. H., Liu J. J., Shu Z. (2023). Recovery testing of self-centering steel-timber hybrid beam-column connections. Construction and Building Materials, 365.

[27] Dong H. Y., Liang X., Cao W. L. (2023). Seismic behavior of mortise–tenon joints reinforced with lightweight steel components. Journal of Building Engineering, 65.

[28] Dourado N., Silva F., Moura D. M. (2018). Fracture behavior of wood-steel dowel joints under quasi-static loading. Construction and Building Materials, 176: 14-23.

[29] Zheng L, Wang W D, Xian W. (2022). Experimental and numerical investigation on the anti-progressive collapse performance of fabricated connection with CFST column and composite beam. Engineering structures, 256.

[30] "Method for the Determination of the Moisture Content of Wood" (GB/T 1931-2009). Beijing: China Standard Press, 2009, [in Chinese].

[31] Test Method for Compression Strength Parallel to Grain of Wood" (GB/T 1935-2009). Beijing: China Standard Press, 2009, [in Chinese].

[32] "Test Method for Tensile Strength Parallel to Grain of Wood" (GB/T 1938-2009). Beijing: China Standard Press, 2009, [in Chinese].

[33] "Code for the Design of Steel Structures"(GB50017-2017). Beijing: Beijing Construction Industry Press. 2017, [in Chinese].

[34] "Handbook of Wood Construction Design", edited by the Editorial Board. Manual of wood structure design. Third edition. China Construction Industry Press.

[35] Gao L., Chang Y. D., Zhang J. F. (2023). Experimental study on buffering energy dissipation of rigid-flexible stacked protection structure of bridge abutment under rockfall impact. Journal of Vibration Engineering, 36(04): 1113-1124.

[36] Wierzbicki T., Xue L. (2005). On the effect of the third invariant of the stress deviator on ductile fracture. Cambridge, MA, USA: MIT Impact and Crashworthiness Lab.

[37] Liao F., Wang M., Tu L. (2019). Micromechanical fracture model parameter influencing factor study of structural steels and welding materials. Construction and Building Materials, 215: 898-917.

[38] Chen Y. X. Flexural analysis and design of timber strengthened with high-strength composites, [in Chinese].

[39] Wang H., Chen A. J., Yang L., Li S. L., He G. J., Wang H. L., (2023). Research on mechanical property of glued timber truss connected by steel plates and bolts, Structures, 57: 105264.

[40] Yan W., Zhang D., Zhao S. J., Zhang X., Wang Z. Q. (2025). Numerical study of low velocity impact resistance of gradient foam sandwich structures, Engineering Fracture Mechanics, 323: 111231.

Advanced Steel Construction – Vol. 22 No. 1 (2026) 96–104
DOI:10.18057/IJASC.2026.22.1.8

RECONSTRUCTION METHOD OF HORIZONTAL TWO-DIRECTIONAL DYNAMIC DISPLACEMENT OF TRANSMISSION TOWER BASED ON LIMITED STRAIN DATA

Qing Zhang [1, 2, *] and Wen-Qiang Jiang [1]

[1] *Hebei Key Laboratory of Electric Machinery Health Maintenance & Failure Prevention, North China Electric Power University, Baoding 071003, China*
[2] *State Key Laboratory of Coastal and Offshore Engineering, Dalian University of Technology, Dalian 116023, China*
** (Corresponding author: E-mail: zhangqing@ncepu.edu.cn)*

ABSTRACT

Transmission towers serve as critical carriers for electric energy transmission, making health monitoring research highly significant. Horizontal dynamic displacement is a key indicator in health monitoring; however, estimating the horizontal displacement of transmission towers using conventional equipment or methods remains challenging. Therefore, this paper proposes a reconstruction method for horizontal two-directional dynamic displacement based on measured strain data. Firstly, the simplified mechanical model of the transmission tower and the strain decoupling formula for main members are established. Then, the two-directional modal superposition method is developed by integrating the stochastic subspace identification (SSI) theory to realize the transformation from strain to displacement. Subsequently, the two-directional vibration simulations of the transmission tower show that the reconstruction error at the 27 m high measuring point is only 2.07%, and the method maintains high precision even under high noise conditions. Finally, a scaled model test of the transmission tower confirms that the reconstructed horizontal two-directional dynamic displacement matches the measured values closely in both time and frequency domains.

ARTICLE HISTORY

Received: 13 June 2025
Revised: 15 June 2025
Accepted: 15 June 2025

KEYWORDS

Transmission tower;
Health monitoring;
Measured strain;
Two-directional displacement reconstruction;
Scaled model test

1. Introduction

The transmission tower is a vital component of the power grid, playing a significant role in clean energy utilization and national energy security[1, 2]. Therefore, monitoring its health to obtain dynamic responses is crucial for ensuring grid safety [3-5]. Among various monitoring indices, the dynamic displacement field, especially the horizontal dynamic displacement, accurately characterizes the overall structural performance[6, 7], is necessary to estimate the safety and dependability of the structure [8-10]. Thus, precise measurement of horizontal two-directional dynamic displacement is critical for health monitoring and performance assessment of transmission tower structures[11].

Displacement can be attained using a variety of measuring equipment[12, 13], such as Total Station, Static Level Meter, Global Navigation and Positioning System (GNSS), Vision-based Measurement System, etc. [14-16]. Nevertheless, the above equipment has the following shortcomings: (1) They require fixed reference points on the structure, which may shift under extreme weather (e.g., typhoons, earthquakes) or long-term use; (2) Their high requirements for sight, light, and expensive cost render them unsuitable for long-term health monitoring of transmission towers.

In order to overcome the above problems, displacement reconstruction technology has become a research hotspot [17-21], namely, the structural displacement can be calculated indirectly using easily measured data, such as acceleration and strain. Acceleration-based methods primarily involve time and frequency domain integration [22, 23]. For overcoming the problem that the sensor is difficult to attain the deflection of the bridge directly, Park et al.[24] developed a method to derive the dynamic displacement of the bridge using measured acceleration, a high-pass filter and an initial velocity estimation algorithm were introduced in view of the non-negligible initial conditions in the integration process, and the field measurement shows that the reconstructed displacement accuracy is well, but the acceleration needs to be segmented and integrated for pseudo-static displacement, and the segmentation principle has not yet been determined. Zhu et al.[25] proposed a frequency domain integration algorithm based on low-frequency attenuation method, then compared with the conventional integration method by simulation, and the superiority of the method was proved, a shaking table test was also conducted to study the effect of precision control factor on the performance of the above method simultaneously. The frequency domain integration algorithm utilizes the filter to reduce the effect of low frequency measurement noise on the acceleration integration process to a certain extent, but it also causes the loss of effective low frequency components in displacement, hence, the selection of the cutoff frequency of the filter has strong experience and autonomy. Additionally, it is difficult to estimate the initial position and velocity accurately without GNSS technology, which leads to many challenges in the reconstruction of non-zero mean dynamic displacement and pseudo-static displacement.

Reconstruction methods based on limited strain data include inverse finite element method (iFEM) [26] and modal superposition technique [27]. You et al.[28] proposed an enhanced inverse beam element iEBT2, numerical analysis and experiments suggest that the inverse element can estimate the deformation accurately in the absence of strain data, but the inverse element type for transmission tower structure has not been studied. The modal superposition method only needs the measured strain and mode shapes of the structure to realize the displacement reconstruction. Therefore, this method is widely used in the shape perception and displacement reconstruction of beam-slab structures. Lu et al.[29] developed a continuous dynamic response analysis algorithm based on decoupled vibration differential equation, and the correctness was confirmed by jacket platform simulation and cantilever beam model test. Skafte et al.[30] proposed a method that can predict the displacement mode shape and response only by measured strain data, and reconstructed the displacement response of a civil structure under random load. However, this technology has not been applied to the horizontal two-directional displacement reconstruction of transmission tower. In addition, some scholars have carried out preliminary research on the displacement reconstruction of lattice tower [31, 32], which can provide reference for the two-dimensional displacement reconstruction of transmission tower.

It can be seen from the above review that there is still no method suitable for horizontal two-directional displacement reconstruction of transmission tower structure. Hence, the two- directional modal superposition method based on limited strain data was proposed in Section II, which can calculate the two-directional displacement of the transmission tower directly from the measured strain data. In Section III, the ANSYS model of transmission tower is built, then the effectiveness and noise immunity of the proposed method are validated by two-dimensional random vibration simulation. In Section IV, a scaled model of a transmission tower is fabricated and the dynamic loading test is conducted to further confirm the practicability of the proposed reconstruction method. Finally, the research is summarized in Section V.

2. Horizontal two-directional displacement reconstruction theory

2.1. Strain decoupling technology of main member

The transmission tower is a complex spatial structure composed of main and brace members, and it is very difficult to carry out displacement reconstruction analysis directly. It is assumed that the transmission tower is always in the range of linear elastic deformation. Note that the transmission tower belongs to the large cantilever structure, which can be considered as a variable cross-section cantilever beam, as shown in Fig. 1. The neutral layer refers to the existence of a transition layer that is neither tension nor compression when the beam is bent, usually located in the geometric center, which is the dotted line in Fig. 1 The transmission tower structure is easy to vibrate along two orthogonal horizontal directions, which is called the main

vibration direction. When there is an angle between the load and the main vibration direction, the response of the transmission tower has components along both main vibration directions, which is called two-dimensional response. The existing method should be improved to make it suitable for the vibration of the transmission tower along any horizontal direction.

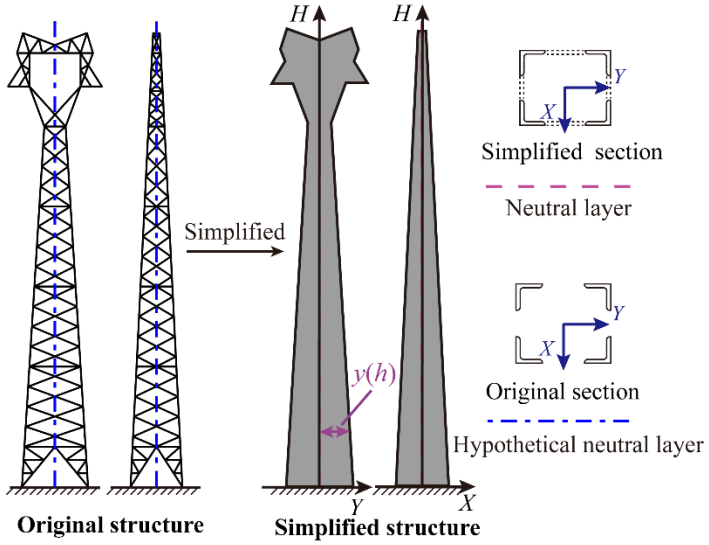

Fig. 1 Transmission tower structure simplification process

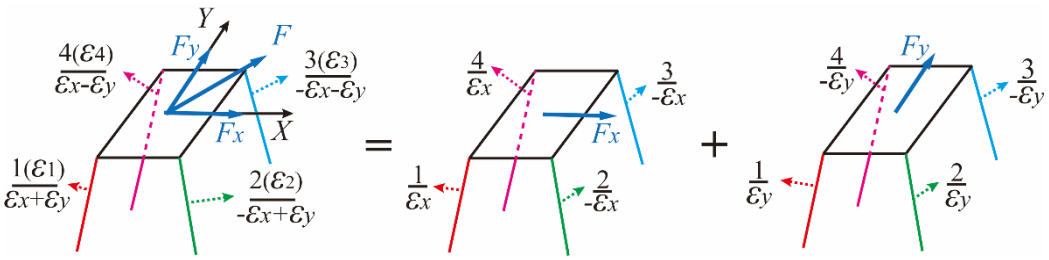

Fig. 2 Strain decoupling process of main member

Fig. 2 suggests the stress state of the main member when the transmission tower generates two-directional displacement. Due to the different synthesis rules of strain and displacement, it is impossible to calculate the strain mode shape along the main vibration direction directly using the main member strain, and the strain decoupling of the main member is needed. The four main members are numbered from 1 to 4, then the effect caused by F is the same as the effect caused by two components Fx and Fy according to the principle of force synthesis.

The strain of the transmission tower under the load of two separate forces can be acquired by the formula:

$$\varepsilon_x = \frac{\varepsilon_1 - \varepsilon_2}{2}, \varepsilon_y = \frac{\varepsilon_1 + \varepsilon_2}{2} \tag{1}$$

where ε_1 and ε_2 are the two-dimensional strains generated by the No.1 main member and the No.2 main member, respectively. The above formula decomposes the synthetic strain generated by the main member under any horizontal load into the strain generated by the component force acting alone along the main vibration direction, which is called the main member strain decoupling formula. Since the strain and displacement mode shapes of the transmission tower in the main vibration direction can be converted to each other, the displacement reconstruction problem in any direction can be solved by decomposing it into the main vibration direction.

2.2. Two-directional modal superposition method

Due to the displacement reconstruction processes in the two main vibration directions are similar, the X direction displacement reconstruction is taken as an example to illustrate the process of the proposed method. It is assumed that the transmission tower is subjected to the action of force F, and a total of $2m$ strain measuring points are arranged on two adjacent main members, the strain $\{\varepsilon_x\}_{m\times 1}$ of the transmission tower under the load of Fx can be calculated by (1) Then the SSI algorithm is used to acquire strain mode shapes $\{\boldsymbol{\Psi}_x\}_{m\times n}$ in the X direction, the flow chart of SSI method is shown in Fig. 3.

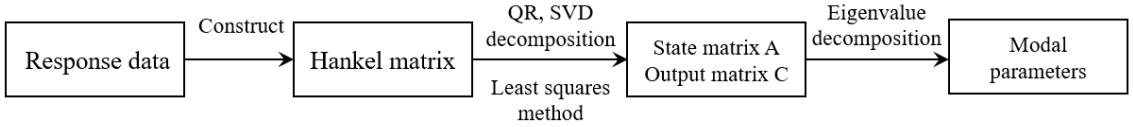

Fig. 3 SSI method process

The modal coordinates are calculated according to the least square method:

$$\{q_x^s\}_{n\times 1} = (\{\boldsymbol{\Psi}_x\}_{m\times n}^T \{\boldsymbol{\Psi}_x\}_{m\times n})^{-1} \{\boldsymbol{\Psi}_x\}_{m\times n}^T \{\varepsilon_x\}_{m\times 1} \tag{2}$$

where n denotes the obtained modal order; the s stands for strain. Then the strain and displacement mode shape function in the X direction $\Psi_x^i(h)$ and $\Phi_x^i(h)$ are acquired by the integral method:

$$\Phi_x^i(h) = \iint \frac{\Psi_x^i(h)}{x(h)} dhdh + Eh + F = \iint f_i(h) dhdh \tag{3}$$

where $x(h)$ is the function between the distance from the response extraction

point to the assumed neutral axis and the height, and the integral constants E and F are both 0. Taking Fig. 1 as an example, this distance is the distance between the point on the main member and the H axis; E and F are integral constants related to boundary conditions. $\Psi_x^i(h)$ is obtained by fitting the strain mode shape value and the corresponding height. Then $f_i(h)$ is expanded by using the Taylor formula to solve the problem of complex integral function:

$$\frac{\Psi_x^i(h)}{x(h)} = f_i(h) = \frac{f_i(h_0)}{0!} + \frac{f_i'(h_0)}{1!}(h-h_0) + \cdots + \frac{f_i^z(h_0)}{z!}(h-h_0)^z + R_z(h) \quad (4)$$

Moreover, the specific mode shape value of the target point can be determined according to its corresponding height coordinates, then the X direction displacement at the corresponding position can be acquired by using the modal superposition principle:

$$\{\mathbf{D}_x^s\} = \{\mathbf{\Phi}_x\}\{q_x^s\}_{n\times 1} \quad (5)$$

where $\{\mathbf{D}_x^s\}$ is the X direction displacement vector of the reconstructed target point; $\{\mathbf{\Phi}_x\}$ represents displacement mode shape matrix. The process of modal superposition is shown in Fig. 4.

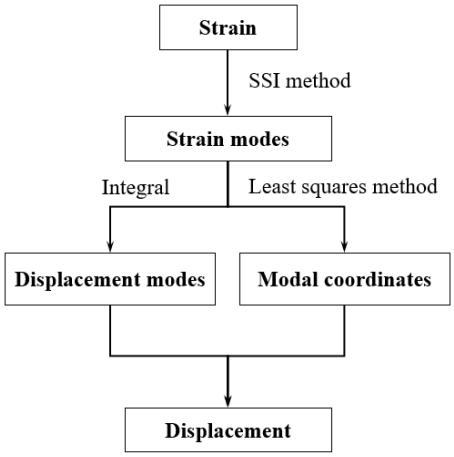

Fig. 4 Modal superposition process

Thus far, the reconstruction of dynamic displacement field in the X direction of transmission tower structure under load F is finished. It is noted that the strain decoupling process is carried out before this, namely, the strain of the transmission tower under load Fy is also known, and the reconstruction procedure of the Y direction dynamic displacement is basically the same as that in X direction, only the strain data used is different. Therefore, the horizontal two-directional displacement reconstruction of the transmission tower can be completed simultaneously. Fig. 5 is the flowchart of the horizontal two-directional displacement reconstruction approach of transmission tower.

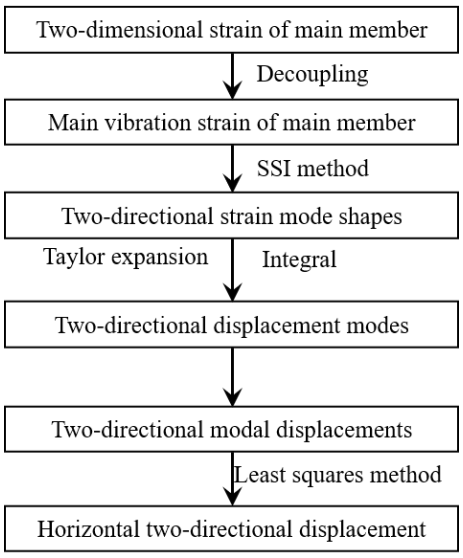

Fig. 5 Horizontal two-directional displacement reconstruction method flowchart

3. Numerical validation via two different beam structures

3.1. Finite element model

Taking a transmission tower of Jiangmen-Gewen line in Guangdong province as the prototype, the finite element model (FEM) is established by using ANSYS software, the beam188 element is used to simulate the members, and the rigid connection is adopted between the members. The material elastic modulus is 206 GPa, the density is 7800 kg/m3, the Poisson's ratio is 0.3, and the damping ratio is 0.04. The tower is a lattice angle steel transmission tower, whose 7 m high head is cat-shaped, the whole height of the tower body and legs is 27 m. The length of cross arm is 1.8 m and the main angle steel specifications including L90 × 8, L80 × 7 and so on. The specific geometric size and built FEM are shown in Fig. 6.

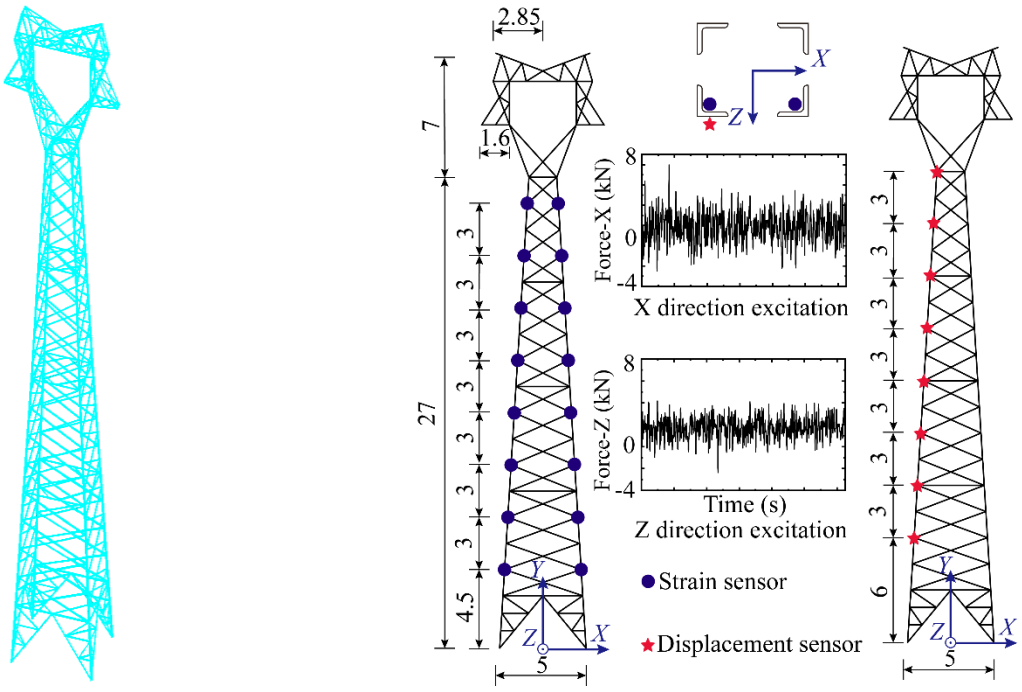

(a) FEM (b) Dynamic response extraction points position (m)

Fig. 6 FEM and extraction point position

Fig. 6(b) shows the specific location of the dynamic response extraction point. 16 dynamic strain extraction points are evenly set along the height direction on the No.1 and No.2 main members of the transmission tower, eight displacement response measuring points are settled to confirm the reconstruction accuracy of proposed method simultaneously, and the dynamic response sampling interval is 0.0025 s. To reflect the ability to reconstruct the displacement field, the placements of the strain and displacement measuring points do not coincide. Random excitations are applied along the horizontal directions (X and Z) in the figure to cause two-dimensional dynamic deformation of the transmission tower. The excitation time history can also be referred to Fig. 6, and the excitation frequency range is 0-20 Hz.

3.2. Reconstruction results analysis

The extracted strain data are processed by strain decoupling formula, and the strain modal parameters are calculated by the SSI algorithm. Fig. 7 shows the obtained stability diagram, the stable point in the diagram represents the stable solution of the modal parameters. The proposed method accurately calculates the first four-order modal parameters in both horizontal directions of the transmission tower without aliasing phenomenon.

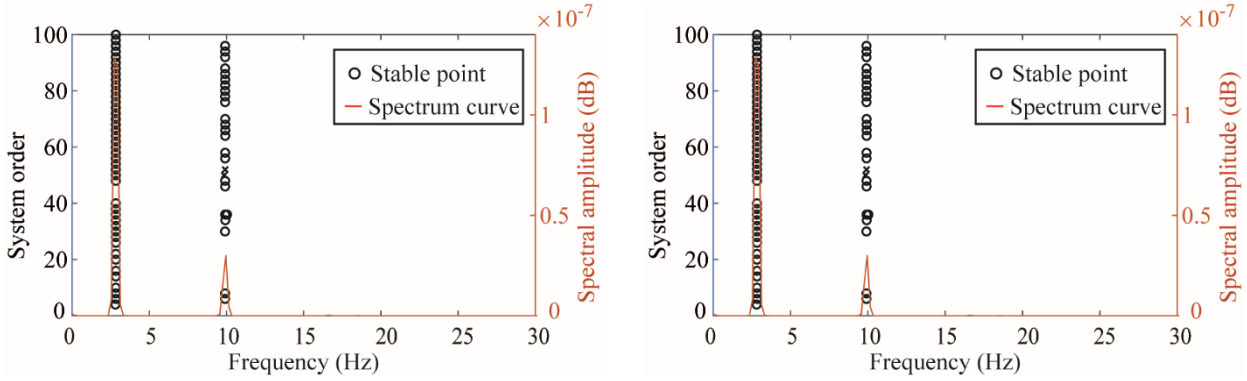

(a) Z direction (b) X direction

Fig. 7 Strain stability diagram

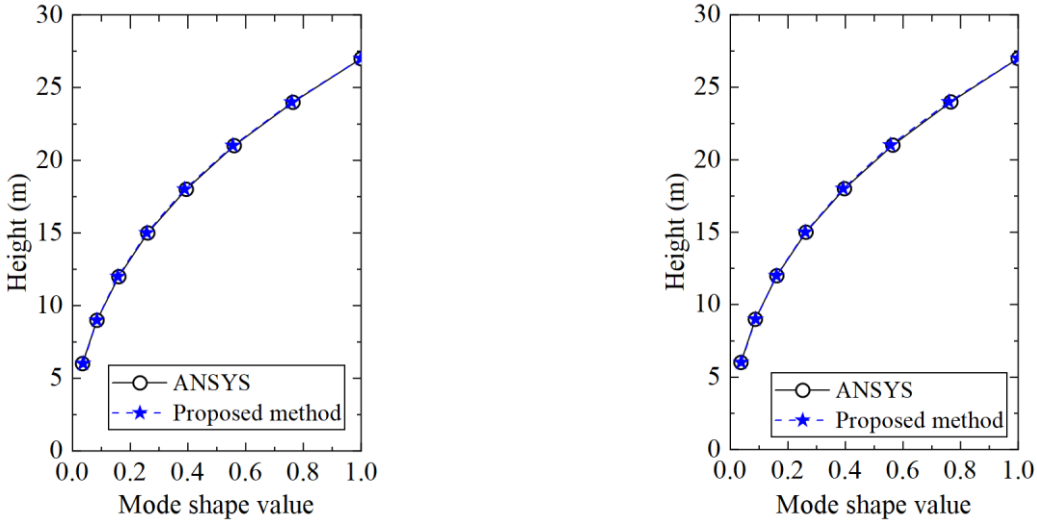

(a) Z direction (b) X direction

Fig. 8 Comparison of different first-order displacement mode shapes

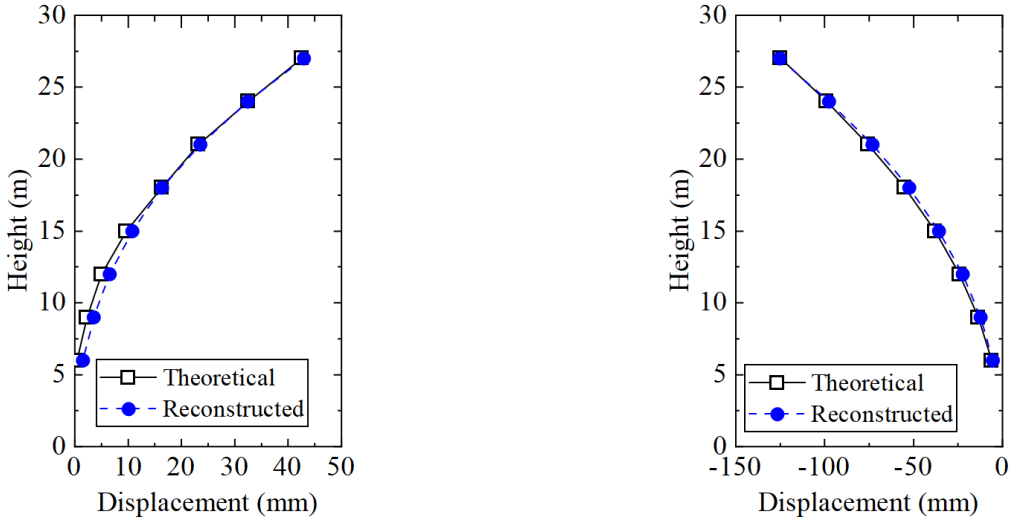

(a) Z direction (b) X direction

Fig. 9 The comparison of the displacement field of the transmission tower at 7 s

We extract the strain mode shapes in the stability diagram to acquire the displacement mode shapes using the developed method, and then contrasted with the ANSYS modal analysis results. The first-order mode is taken as a case, as displayed in Fig. 8. The reconstructed displacement mode shape curve closely coincides with the theoretical curve, indicating that the developed method can calculate the displacement modal parameters of transmission tower accurately based on the limited strain data.

Then we calculate the two-directional displacements of all the target points on the transmission tower structure. Fig. 9 compares the reconstructed two-directional displacement field at 7 s with the theoretical value calculated by ANSYS. It can be seen that the two are very close, indicating that the proposed two-directional modal superposition method can obtain the two-directional displacement field of transmission tower accurately.

For convenience, the following adopts the 27 m high displacement measuring point as an example to compare the reconstructed two-directional displacement and the theoretical value time history calculated by ANSYS. Fig. 10 demonstrates the two-directional dynamic displacement comparison time history diagram, the reconstructed value is very close to the theoretical value at most of the time. which suggests that the proposed method can achieve the accurate reconstruction of two-directional dynamic displacement of the transmission tower only utilizing the strain data.

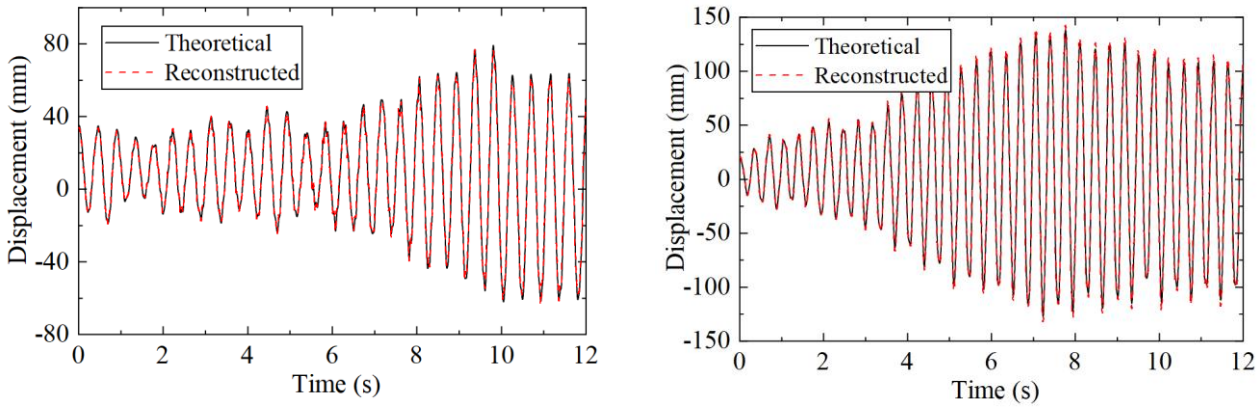

(a) *Z* direction (b) *X* direction

Fig. 10 Dynamic displacement comparison (27 m high)

In order to prove the ability of the proposed method to calculate the displacement of the middle and lower part of the tower, the theoretical displacement and reconstruction displacement of the 12 m and 9 m heights are compared, as shown in Fig. 11. It can be seen that although the reconstruction accuracy is slightly reduced, the reconstruction value and the theoretical value are still in good agreement on the whole.

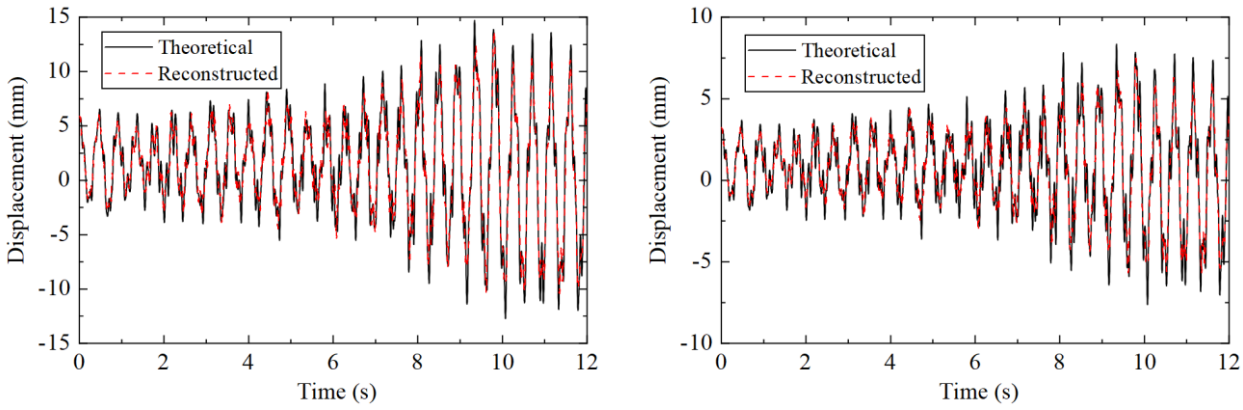

(a) 12 m (b) 9 m

Fig. 11 Dynamic displacement at different heights in the *Z* direction

For investigating the ability of the proposed two-directional displacement reconstruction method to resist noise, different levels for Gaussian white noise were added to dynamic strain collected by ANSYS to simulate measurement noise case. The signal-to-noise ratio (SNR) is commonly used to measure the noise intensity, the calculation formula is:

$$\mathrm{SNR} = 20\log_{10}\left(\frac{f_{\mathrm{signal}}}{f_{\mathrm{noise}}}\right) \tag{6}$$

where f_{signal} is the amplitude of the original signal, and f_{noise} is the amplitude of the noise. It is found that the noise amplitude accounts for less than 10 % through the analysis of the actual strain signal, and the corresponding SNR ratio is 20 dB, so the SNR of noise are set to 20 dB, 40 dB and 60 dB, respectively.

The above has already verified the ability of the developed method to calculate the horizontal two-directional displacement field accurately, so just the reconstruction of the displacement of 27 m high measuring point in the *Z* direction is discussed. Fig. 12 presents the displacement time history at the highest point, with noise at 20 dB, calculated by different methods. The figure suggests that the reconstructed curve is basically consistent with the theoretical displacement curve even in the case of high noise, which demonstrates that the developed reconstruction method has strong robustness. On the other hand, the displacement reconstructed by Park et al.[20] is roughly consistent with the theoretical displacement, but as shown in the enlarged diagram, the reconstruction accuracy is lower than that of the proposed method.

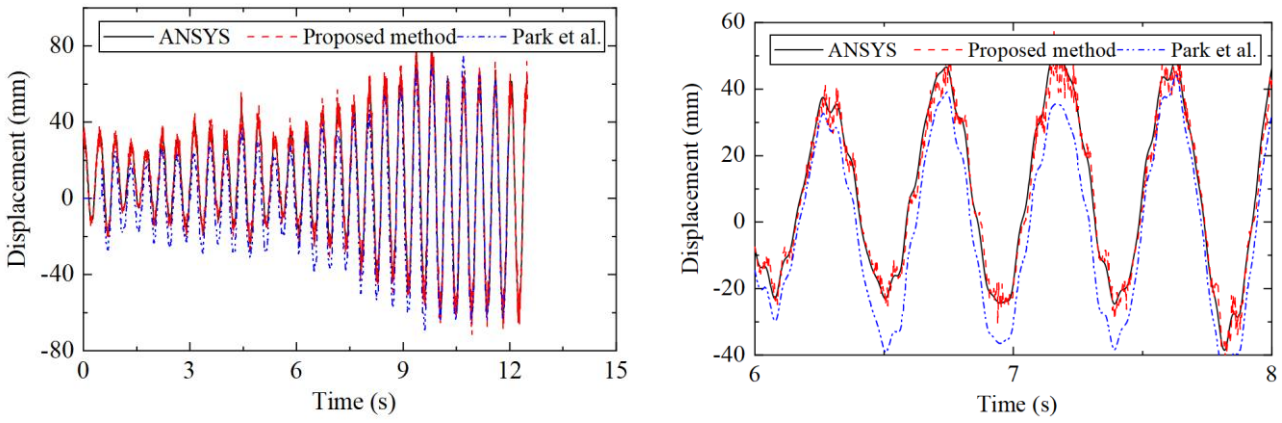

(a) 0-15 s (b) 6-8 s

Fig. 12 The displacement comparison of the 27 m high measuring point (20 dB)

To achieve the quantitative analysis of the reconstruction precision, the error index K is determined to evaluate the reconstruction error degree of each working condition:

$$K = \frac{\sqrt{\frac{1}{N}\sum_{i=1}^{N}(x_t - x_r)^2}}{\max(x_t) - \min(x_r)} \times 100\% \tag{7}$$

where N is the number of extracted data, x_t stands for the theoretical displacement, x_r is the reconstructed displacement. Table 1 shows the error index K under different working conditions. K is only 1.71 % when SNR is 20 dB, showing that the proposed method has a strong ability to resist noise interference for reconstructing two-directional displacement.

Table 1
Error index corresponding to different working conditions

SNR (dB)	K (%)	Standard deviation (%)
20	2.08	3.11
40	1.84	3.07
60	1.71	3.05

4. Test verification

4.1. Scaled model and experimental design

Taking the transmission tower in Section III as the prototype, the scaled model is made according to the similarity theory. The production process can refer to the existing reference [33], the geometric scale ratio of the scale model is 1:15 considering the limitation of laboratory space. On the other hand, the thin aluminum sheet is processed into an equal angle steel section to simulate the structural members to ensure the similarity of the aerodynamic shape, and the scaled model is displayed in Fig. 13.

Fig. 13 Scaled model of transmission tower

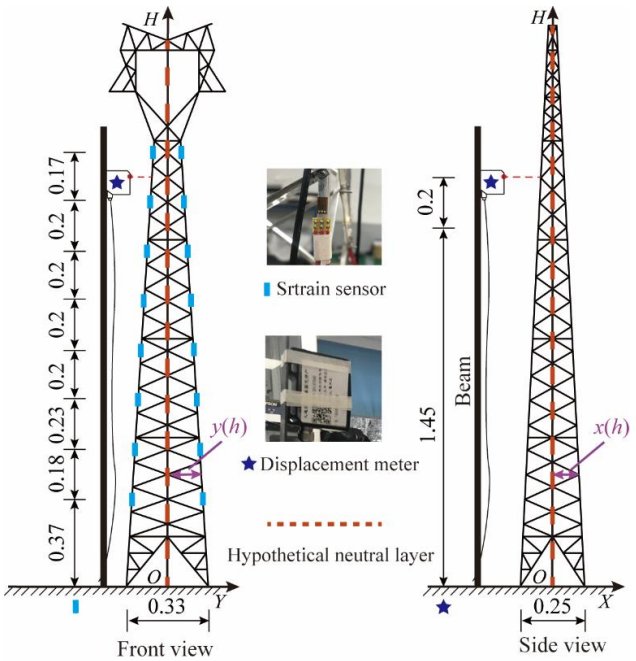

Fig. 14 Sensors photograph and measuring points layout (Unit: m)

Eight pairs (16) of strain gauges were settled along the height on the two main members of the scaled model. In order to facilitate the measurement of displacement response and demonstrate the ability of the developed reconstruction method to calculate the horizontal two-directional displacement field, two displacement sensors were arranged at a height that did not coincide with the strain gauge position, the specific sensor layout is demonstrated in Fig. 14. The sampling rate of the strain response is determined to be 200 Hz, and that of the displacement sensor is determined to 10 kHz, which is then reduced to 600 Hz by re-sampling method. The knocking method is used to make the structure produce a two-directional dynamic displacement with free attenuation. The function $x(h)$ and $y(h)$ of the distance from the sensor on the main member to the assumed neutral layer can be calculated by the geometric size given in the figure.

4.2. Test results and analysis

The proposed main member strain decoupling technique is utilized to handle the collected strain data to calculate that caused by the structure vibration along the main vibration direction. Then the FFT method and SSI method are applied to process the strain time history along the main vibration direction, and the spectrum curves and strain stability diagrams are demonstrated in Fig. 15.

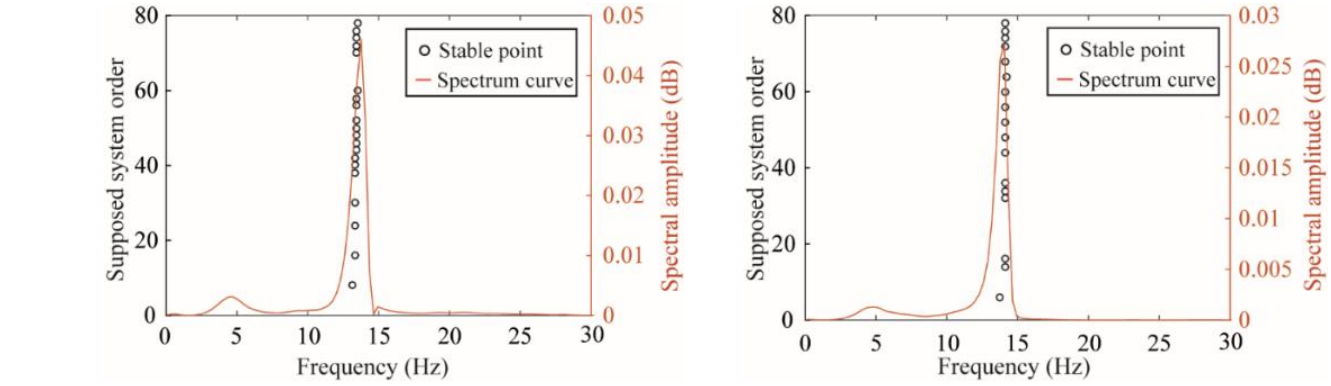

(a) *X* direction (b) *Y* direction

Fig. 15 Strain stability diagrams and spectrum curves in different directions

The dynamic displacement curve of target point is calculated by the proposed method, and the reconstructed results are displayed in Fig. 16. Fig. 16 compares the time history curves measured by two laser displacement meters and the displacement curves calculated by the developed method, the reconstructed two-directional displacement time history is basically the same as the measured displacement time history, and there are only differences at individual times. Considering that the displacement response amplitude is only 0.3 mm, this difference is acceptable, and the larger variation of the initial measured value is caused by the higher measurement accuracy of the strain gauge.

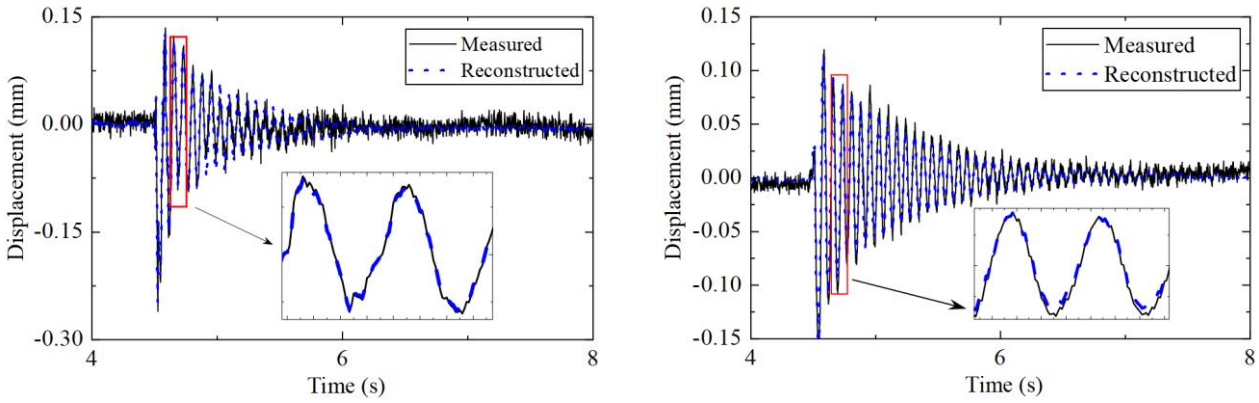

(a) *X* direction (b) *Y* direction

Fig. 16 Two-directional displacement time histories calculated by different methods

The relative error between the reconstructed displacement and the measured displacement in the model test is shown in Table 2, which can be seen that the error is within 10 %, indicating that the proposed method has high accuracy.

Table 2
Model test reconstruction error

Error index	X direction	Y direction
K	7.45%	6.37%

Fig. 17 compares the divergence between the reconstructed two-directional displacement and measured value in the frequency domain. It can be seen from the figure that the spectrum curves of the reconstructed value and the measured value are relatively close, and both of them have peaks at the first-order frequency of the tower, which is consistent with the calculation results of the stability diagram, and the amplitude is basically the same. The two spectrum curves are negligibly different in the frequency bands above and below the first-order frequency, which is related to the different measurement levels of the laser displacement sensor and the strain gauge besides the reconstruction error. Generally, the reconstructed displacement curve can reflect the spectral characteristics of the real displacement of the structure well. The time and frequency domains analysis suggest that reconstructed horizontal two-directional displacement and the measured value are not only very close in the time domain, but also highly consistent in the frequency domain, which proves the precision of the proposed horizontal two-directional displacement reconstruction method.

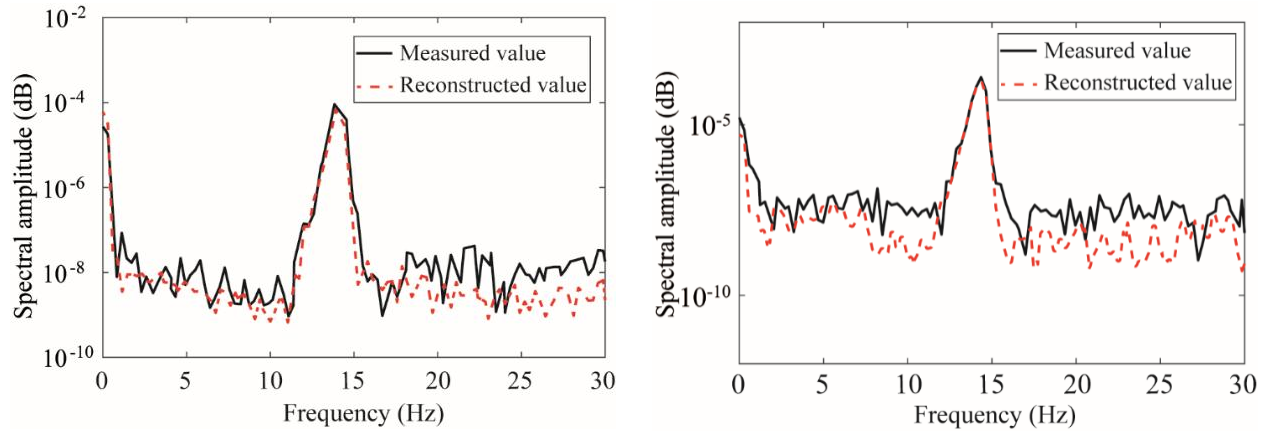

(a) *X* direction (b) *Y* direction

Fig. 17 Comparison of different displacements in frequency domain

5. Summary and conclusion

This paper proposes a horizontal two-directional displacement reconstruction method for transmission towers based on a two-directional modal superposition technique. Firstly, the strain decoupling formula is established to decompose the two-directional displacement reconstruction problem into independent main vibration direction problems. Then, the SSI algorithm is employed to extract strain modes in two orthogonal directions and derive the corresponding displacement mode functions. Finally, the transformation from limited strain measurement data to horizontal two-directional displacements is achieved.

The feasibility of the proposed method is validated through numerical simulations and scaled model tests, with noise immunity analysis showing that the error index remains within 2%. In the model test, even when the displacement amplitude is as low as 0.3 mm, the reconstructed displacements in both orthogonal horizontal directions exhibit high consistency with measured values in both time and frequency domains.

Notably, the proposed reconstruction method enables estimation of horizontal two-directional displacements of transmission tower structures using only limited strain measurements, eliminating the need for initial position information. This feature is of significant importance for operational maintenance and performance evaluation of transmission towers, providing a reliable reference for structural assessment and reducing maintenance costs of power infrastructure. On the other hand, when combined with online modal parameter identification technology, the proposed method can also mitigate the impact of environmental factors on displacement reconstruction.

Acknowledgements

This research was supported by “Three-Three-Three Talents Project” in Hebei Province (Grant No.: C20231056), the Fundamental Research Funds for the Central Universities (Grant No.2024MS132), Natural Science Foundation of Hebei Province of China (Grant No.: E2024502007) and Open Fund of State Key Laboratory of Coastal and Offshore Engineering, Dalian University of Technology (Grant No.: LP2419).

References

[1] An, L.Q., W.Q. Jiang, Y.P. Liu, Q. Shi, Y.D. Wang, and S.X. Liu, EXPERIMENTAL STUDY OF MECHANICAL BEHAVIOUR OF ANGLES IN TRANSMISSION TOWERS UNDER FREEZING TEMPERATURE. Advanced Steel Construction, 2018; 14(3): 461-478.

[2] Wang, W.M., H.N. Li, and L. Tian, PROGRESSIVE COLLAPSE ANALYSIS OF TRANSMISSION TOWER-LINE SYSTEM UNDER EARTHQUAKE. Advanced Steel Construction, 2013; 9(2): 161-172.

[3] Liu, Z.C., X.B. Huang, L. Zhao, G.R. Wen, G.Z. Feng, and Y. Zhang, Research on online monitoring technology for transmission tower bolt looseness. Measurement, 2023; 223: 113703.

[4] Xiong, X.F., S.J. Weng, and J. Wang, An Online Early-Warning Method for Wind Swing Discharge of the Conductor Toward the Tangent Tower and Jumper Toward the Strain Tower. IEEE Transactions on Power Delivery, 2015; 30(1): 114-121.

[5] Zou, Y.F., X. Lei, L. Yan, X.H. He, M. Nie, W.P. Xie, and X.Y. Luo, Full-scale measurements of wind structure and dynamic behaviour of a transmission tower during a typhoon. Structure and Infrastructure Engineering, 2020; 16(5): 820-830.

[6] Chen, D.D., Z.H. Shen, L.S. Huo, and Y. Narazaki, Percussion-based quasi real-time void detection for concrete-filled steel tubular structures using dense learned features. Engineering Structures, 2023; 274: 115197.

[7] Chen, D.D., N.N. Zhang, L.S. Huo, and G.B. Song, Full-range bolt preload monitoring with multi-resolution using the time shifts of the direct wave and coda waves. Structural Health Monitoring-an International Journal, 2023; 22(6): 3871-3890.

[8] Buchoud, E., V. Vrabie, J.I. Mars, G. D'Urso, A. Girard, S. Blairon, and J.M. Hénault, Quantification of Submillimeter Displacements by Distributed Optical Fiber Sensors. IEEE Transactions on Instrumentation and Measurement, 2016; 65(2): 413-422.

[9] Jiao, R.H., Y.Z. Liu, H. He, X.H. Ma, and Z.Y. Li, A Deep Learning Model for Small-size Defective Components Detection in Power Transmission Tower. IEEE Transactions on Power Delivery, 2022; 37(4): 2551-2561.

[10] Pramudita, A.A., D.B. Lin, A.A. Dhiyani, H.H. Ryanu, T. Adiprabowo, and E.A. Yudha, FMCW Radar for Noncontact Bridge Structure Displacement Estimation. IEEE Transactions on Instrumentation and Measurement, 2023; 72: 8504914.

[11] Wang, F.Y., Y.L. Xu, and S. Zhan, CONCURRENT MULTI-SCALE MODELING OF A TRANSMISSION TOWER STRUCTURE AND ITS EXPERIMENTAL VERIFICATION. Advanced Steel Construction, 2017; 13(3): 258-272.

[12] Wang, S.Y., A.Y. Chen, and H.Y. Wan, SEISMIC BEHAVIOUR OF CONCRETE-FILLED STEEL TUBE FRAMES WITH EXTERNAL COMPOSITE WALL PANELS. Advanced Steel Construction, 2021; 17(1): 10-19.

[13] Zhang, J., Y.X. Xu, X.J. Yang, and D.H. Zhang, FIRE-RESISTANCE STUDY OF RESTRAINED STEEL COLUMNS WITH INITIAL LATERAL DISPLACEMENT. Advanced Steel Construction, 2018; 14(1): 22-36.

[14] Cheng, X.X. and Y.J. Ge, An innovative structural health monitoring system for large transmission towers based on GPS. International Journal of Structural Stability and Dynamics, 2019; 19(4): 1971002.

[15] Ge, L.F., K.Y. Koo, M.M. Wang, J. Brownjohn, and D.H. Dan, Bridge damage detection using precise vision-based displacement influence lines and weigh-in-motion devices: Experimental validation. Engineering Structures, 2023; 288: 116185.

[16] Mi, C., Y. Liu, Y.J. Zhang, J.Q. Wang, Y.F. Feng, and Z.W. Zhang, A Vision-Based Displacement Measurement System for Foundation Pit. IEEE Transactions on Instrumentation and Measurement, 2023; 72: 2525715.

[17] Choi, J., J.Y. Chung, K. Kim, and H. Sohn, Seismic-induced permanent displacement estimation combining acceleration and computer vision measurements. Mechanical Systems and Signal Processing, 2023; 200: 110504.

[18] He, Z.Z., L.X. Zhang, H.G. Gao, H.S. Wang, and P. Pan, Estimation of the displacement time history of high-rise building structures using limited measurement data and structural information. Mechanical Systems and Signal Processing, 2023; 202: 110716.

[19] Ma, Z., J. Choi, L. Yang, and H. Sohn, Structural displacement estimation using accelerometer and FMCW millimeter wave radar. Mechanical Systems and Signal Processing, 2023; 182: 109582.

[20] Ma, Z.X., J. Choi, and H. Sohn, Three-dimensional structural displacement estimation by fusing monocular camera and accelerometer using adaptive multi-rate Kalman filter. Engineering Structures, 2023; 292: 116535.

[21] Zhou, Q., Q.S. Li, X.L. Han, K. Xu, and J.W. Wan, Horizontal displacement estimation of high-rise structures by fusing strain and acceleration measurements. Journal of Building Engineering, 2022; 57: 104964.

[22] Lee, H.S., Y.H. Hong, and H.W. Park, Design of an FIR filter for the displacement reconstruction using measured acceleration in low-frequency dominant structures. International Journal for Numerical Methods in Engineering, 2010; 82(4): 403-434.

[23] Liu, F.S., S.J. Gao, and S. Chang, Displacement estimation from measured acceleration for fixed offshore structures. Applied Ocean Research, 2021; 113: 102741.

[24] Park, K.T., S.H. Kim, H.S. Park, and K.W. Lee, The determination of bridge displacement using measured acceleration. Engineering Structures, 2005; 27(3): 371-378.

[25] Zhu, H., Y.J. Zhou, and Y.M. Hu, Displacement reconstruction from measured accelerations and accuracy control of integration based on a low-frequency attenuation algorithm. Soil Dynamics and Earthquake Engineering, 2020; 133: 106122.

[26] Zhu, H.M., Z.F. Du, and Y.G. Tang, Numerical study on the displacement reconstruction of subsea pipelines using the improved inverse finite element method. Ocean Engineering, 2022; 248: 110763.

[27] Li, Z.M., Q.H. Song, Z.Q. Liu, H.F. Ma, B. Wang, and Y.K. Cai, Response prediction of cantilever plates via mode superposition method and combination method of beam functions. Mechanical Systems and Signal Processing, 2023; 200: 110613.

[28] You, R. and L. Ren, An enhanced inverse beam element for shape estimation of beam-like structures. Measurement, 2021; 181: 109575.

[29] Lu, H.C., T.H. Fan, X.C. Li, and C.H. Chen, A rapid time-continuous response analysis algorithm for offshore structures by combination of modal superposition and complex exponential decomposition. Ocean Engineering, 2021; 234: 109272.

[30] Skafte, A., M.L. Aenlle, and R. Brincker, A general procedure for estimating dynamic displacements using strain measurements and operational modal analysis. Smart Materials and Structures, 2016; 25(2): 025020.

[31] Fu, X., Q. Zhang, L. Ren, and H.N. Li, Global Displacement Reconstruction of Lattice Tower Using Limited Acceleration and Strain Sensors. International Journal of Structural Stability

and Dynamics, 2024: 10.1142/S0219455424502420.
[32] Zhang, Q., X. Fu , T. Lai , and L. Ren Wind load identification of lattice towers using multi-source heterogeneous monitoring data. Journal of Wind Engineering and Industrial Aerodynamics, 2023; 236: 105402.
[33] Zhang, Q., X. Fu, L. Ren, and Z.G. Jia, Modal parameters of a transmission tower considering the coupling effects between the tower and lines. Engineering Structures, 2020; 220: 110947.

Advanced Steel Construction – Vol. 22 No. 1 (2026) 105–115
DOI:10.18057/IJASC.2026.22.1.9

EFFICIENT PRESTRESS OPTIMIZATION OF SUSPEN-DOME USING NSGA-III AND MACHINE LEARNING-BASED SURROGATE MODELS

Jin Wang, Ming-Liang Zhu * and Ze-Yun Jin

School of Civil Engineering, Southeast University, Nanjing 210096, China
** (Corresponding author: E-mail: zhumingliang@seu.edu.cn)*

ABSTRACT

Prestress optimization is a critical step in the structural design of suspen-dome, often requiring extensive and time-consuming iterative computations. This study proposes a hybrid framework that integrates the NSGA-III algorithm with machine learning-based surrogate models to address the prestress multi-objective optimization problem of suspen-dome. A comparative analysis of three machine learning algorithms—Deep Belief Network (DBN), Sequence-to-Sequence (Seq2Seq), and Backpropagation Neural Network (BPNN)—is conducted to evaluate surrogate modeling performance. The multi-objective optimization considers four objective functions, and the NSGA-III algorithm is employed to effectively obtain the Pareto front. The optimal solution is selected using multi-criteria decision-making, and a case study is presented to validate the accuracy and efficiency of the proposed method. Results show that the BPNN-based surrogate-assisted optimization achieves the best overall efficiency. The introduction of surrogate models reduces computation time by 95% while maintaining optimization performance comparable to traditional finite element analysis (FEA)-based methods.

ARTICLE HISTORY

Received: 9 December 2024
Revised: 20 June 2025
Accepted: 20 June 2025

KEYWORDS

Suspen-dome;
Prestress optimization;
Multi-objective;
Optimal solution;
Finite element analysis (FEA)

1. Introduction

The suspen-dome, as recommended by Kawaguchi et al.[1], is a hybrid spatial structure consisting of an upper single-layer shell and a lower cable-strut system. The suspen-dome structure is extensively applied in large-span projects, including stadiums and airports, due to its high structural strength and low self-weight[2-4].

After applying prestress, the lower cable-strut system can significantly improve the integral structural performance, enhancing the structure's stability and load-carrying capacity [5]. For the cable-strut system, optimization is usually carried out in terms of minimizing construction costs, reducing self-weight, and optimizing stiffness[6,7]. However, how to design the prestress to achieve these optimization objectives simultaneously remains a challenging question, and this problem is currently addressed mainly through optimization algorithms and finite element iterations. Kitipornchai et al.[8], through the prestress design, systematically considered geometric imperfections, asymmetric loads, span ratios, and connection stiffness to study the buckling problem of the structure. Zhang et al.[9] studied the effect of prestress on the maximum displacement and critical load-carrying capacity of the structure through numerical simulation of the cable in the lattice shell structure but did not optimize the prestress. Kang et al.[10] devised a particular annular suspen-dome structure . The prestress of different loop cables is optimized using a genetic algorithm, enhancing the overall stability of the structure. However, this approach is only suitable for relatively simple structures. Liang et al.[11] recommended a structural prestress optimal model, converting multi-objective optimization into single-objective optimization, thus addressing the collaborative optimization of multiple objectives, but this method is highly subjective. Kaveh[12] used the ECBO algorithm to settle various optimization problems related to the geometry, size, and prestress of suspen-dome, significantly improving structural performance and economy, although the computational efficiency was relatively low. Olofin[13] replaced the steel cables of the suspen-dome structure with carbon fiber-reinforced polymer (CFRP) for prestress design, which proved to be highly effective.

In the past few decades, the handling of multi-objective optimization problems has become increasingly important, especially the issue of balancing different objectives[14,15]. Ishibuchi[16] studied multi-objective optimization algorithms and used evolutionary-based optimization algorithms to solve multi-objective optimization problems, achieving a dynamic balance among multiple objectives. Ma et al.[17] recommended a multi-objective optimization method for the prestress optimization of cable-strut structures, balancing cross-sectional area, stiffness matrix eigenvalues, prestress variance, and prestress error. However, this method requires significant computational power. Chen et al.[18] successfully optimized feasible prestress patterns of cable-strut structures using a multi-objective particle swarm algorithm, greatly improving efficiency, though it mainly applies to simple structures. In multi-objective optimization, the Pareto optimal solution set represents a collection of non-dominated solutions that achieve a balance among multiple objectives. Whereas, in company with the dimensionality of optimization problems increases, frequently used algorithms like NSGA-II[19] and SPEA2[20] encounter multiple challenges[21,22], and most algorithms are difficult to deal with four or more objectives effectively. To tackle these challenges, researchers have recommended upgraded Pareto-based optimization methods and new algorithm designs[23], which help to better explore the Pareto frontier[24]. This guarantees decision-makers to more comprehensively assess solutions multiplicity and scope, permitting them to opt for the optimal solution that best meets their demands [25]. NSGA-III[15] improves the multiplicity and uniformity of solutions by introducing evenly distributed reference points, especially effective in high-dimensional spaces, reinforcing the scope of the Pareto front and maintaining a uniform allocation within solutions.

With the advancement of computer technology applications, machine learning has also profoundly impacted traditional engineering fields[26]. Its powerful predictive capabilities have been widely applied in fault prediction for structural health monitoring[27] and material property prediction[28]. In the design field, machine learning is used for automated generation[29] and optimization of design schemes[30]. Additionally, real-time data learning is employed to adjust control strategies[31]. Furthermore, optimization based on machine learning surrogate models has been widely applied, significantly improving optimization efficiency. Li[32] proposed a surrogate model optimization algorithm that combines the low computational cost of surrogate models with the rapid convergence of Bayesian algorithms, showing strong applicability. Zhou[33] utilized machine learning algorithms to establish a substitute model and perform optimization, greatly enhancing optimization efficiency.

This research proposes a multi-objective prestress optimization framework by integrating NSGA-III with machine learning. The remainder of the paper is organized as follows: Section 2 outlines the multi-objective prestress optimization problem. In *section* 3, a brief description of NSGA-III optimization algorithm and three surrogate models based on machine learning is given. *Section* 4 conducts a case analysis of two different configurations of the suspen-dome, and *Section* 5 provides a summary of the conclusions.

2. Framework

2.1. Objective function

2.1.1. Vertical displacement

The prestress of the suspen-dome structure directly affects the structural stiffness and the selection of cross-sections. Under normal operating conditions, the optimal prestress state should keep the structural stiffness within an appropriate range. Excessive prestress can lead to overly high stiffness, resulting in material waste, while insufficient prestress can increase deflection, affecting the structure's normal performance. Therefore, the maximum vertical

displacement is generally used to measure the structural stiffness, and the objective function is expressed as follows:

$$f_1 = min(|u_z|_{max}) \quad (1)$$

where u_z denotes the maximum nodal vertical displacement.

2.1.2. Horizontal displacement

The lower cable-strut system of the suspen-dome can balance the support reactions of the upper single-layer lattice shell. To reduce construction costs, the radial constraints of the structure are usually released. Under the action of prestress, radial displacement will occur at the structural supports. The radial displacement at the supports of the suspen-dome is set as the optimization objective function, and its expression is as follows:

$$f_2 = min\,(|u_x|_{max}) \quad (2)$$

here, u_x denotes the maximum displacement of the support node.

2.1.3. Steel quantity

For the structural system, minimizing the amount of steel used can reduce the structure's self-weight, thereby enhancing overall performance and economy. By reasonably controlling the amount of steel, it is possible to achieve optimal economic benefits while meeting the comprehensive requirements of structural load, material strength, and design constraints. Therefore, optimizing the steel usage in the lower cable-strut system of the suspen-dome is an effective strategy. The objective function is expressed as follows:

$$f_3 = min(\sum_{i=1}^{n} \rho A_i L_i) \quad (3)$$

where $\boldsymbol{\rho}$ denotes the material density, A_i represents the cross-sectional area, and L_i represents the element length.

2.1.4. Strain energy

The minimum strain energy of the suspen-dome is crucial in design. By minimizing strain energy, the integral energy consumption of the structure can also be significantly reduced, thereby lowering energy loss during actual use and achieving a more sustainable architectural design. The objective function is expressed as follows:

$$f_4 = min\,(E) \quad (4)$$

where E is the total strain energy of the structure.

2.2. Constraint conditions

Based on the above optimization process, there may be solution sets that do not meet the constraints. Therefore, it is necessary to establish constraint conditions, assigning a lower rank to solutions that fail to satisfy these constraints. By setting appropriate constraints, a solution set that meets the specified conditions can be obtained.

2.2.1. Displacement limit

Displacement limit conditions are key restrictions to undertake the safety and normal operation of the structure. By setting the maximum allowable displacement of the structure or its components under extreme conditions, damage can be prevented, and the stability and reliability of the structure can be guaranteed. According to reference [34], the specified limits are as follows:

$$u_{max} \leq H/250 \quad (5)$$

where u_{max} denotes the maximum deflection value.

2.2.2. Stress condition

The struts supporting the upper dome structure are under compression, with the maximum compressive force not exceeding the ultimate load-bearing capacity. Additionally, a partial factor of 0.5 is applied to the cables, meaning the cable force should not exceed 50% of the cable's ultimate load-bearing capacity [34]. Additionally, it must be ensured that the cables do not experience slack, i.e., the cable force must be greater than zero. The expressions are as follows:

$$\begin{cases} 0 < \sigma_t < [\sigma_t] \\ -[\sigma_c] \leq \sigma_c \leq 0 \end{cases} \quad (6)$$

where σ_t and σ_c represent the stresses in the cable-strut structure, and $[\sigma_t]$ and $[\sigma_c]$ represent their ultimate stresses.

2.2.3. Strut stability

As compression members, the struts must ensure their stability under axial pressure. By introducing the coefficient φ, the stability of the struts can be effectively guaranteed, preventing buckling. The expression is as follows:

$$\varphi = \frac{N}{A \times f} \quad (7)$$

where φ is the stability coefficient, N is the axial force, A is the cross-sectional area, and f is the design compressive member's strength.

2.3. Multi-criteria decision analysis

By performing multi-objective optimization on the above four objectives, the Pareto front can be obtained. The Pareto front consists of a set of competing solutions, where each solution outperforms others in certain objectives but may perform worse in others. Since the solutions on the Pareto front cannot be directly compared across multiple dimensions, a method is needed to comprehensively consider the importance of different objectives and select the optimal solution. To this end, this paper adopts the Analytic Hierarchy Process (AHP).

Step1: Decompose the decision-making problem into three levels: the goal level, the criteria level, and the alternatives level. These correspond to the final objective of the decision, the standard influencing the decision, and the alternative options for decision-making, respectively.

Step2: According to the degree of importance, use a scale of 1 to 9, where a higher number indicates greater importance; use this to construct the judgment matrix.

Step3: Based on the judgment matrix, use the eigenvector method to compute the relative weight of each criterion.

Step4: The Consistency Ratio (CR) is used to ensure the logical consistency of the judgment matrix in pairwise comparisons, thereby improving the reliability of weight assignments. The steps for calculating CR are as follows: first, the largest eigenvalue (λ_{max}) of the judgment matrix is determined through eigenvalue decomposition; then, the CR value is calculated using formula. If the CR value is less than 0.1, the consistency of the judgment matrix is considered acceptable, indicating reasonable weight assignments; if the CR value is greater than 0.1, the judgment matrix needs to be adjusted. Calculating CR ensures the scientific rigor and consistency of AHP in multi-criteria decision-making.

$$CR = \frac{\lambda_{max} - n}{(n-1) \times RI} \quad (8)$$

Step5: For each solution, calculate the overall score based on the product of weights for all criteria, as follows:

$$S_j = \sum_{i=1}^{m} \omega_i a_{ij} \quad (9)$$

where w_i is the weight of the i-*th* criterion, and a_{ij} is the score for that criterion.

Step6: Select the solution with the highest score as the final decision.

3. Prestress optimization framework based on surrogate model

The use of external finite element analysis includes both online and offline approaches. In the former, optimization iterations directly call the external finite element program for calculations and return the analysis results to the optimizer. This approach offers high accuracy but incurs significant computational costs, potentially resulting in a lengthy optimization process, especially as each iteration requires considerable time to run the external finite element solver.

In offline analysis, multiple finite element analyses are conducted in advance, with the results stored in a database or neural network surrogate model before optimization begins. During optimization, this database or model is accessed to predict responses under new conditions, eliminating the need for real-time finite element calculations. This method is computationally efficient, though accuracy may be limited by the quantity and scope of prior analyses. To simplify computations, this study has trained a highly accurate neural network surrogate model to streamline analysis. By inputting the structure's prestress, the model outputs internal forces and displacements to predict structural responses. Additionally, a multi-objective algorithm is introduced into the surrogate model to optimize the prestress of the cable-dome structure.

3.1. Machine learning

3.1.1. DBN

Deep Belief Networks (DBN) are a sort of deep learning model composed of numerous layers of Restricted Boltzmann Machines (RBM). They were recommended by Hinton et al.[35] in 2006. DBNs can effectively learn deep feature representations of data through unsupervised, layer-by-layer pre-training. These features can then be utilized for assignments such as classification and regression, allowing DBNs to reveal hidden, hierarchical structural information within the data.

Fig. 1 and Fig. 2 illustrate the core structure of a DBN, which includes a visible layer and multiple hidden layers. Each pair of layers is connected by an RBM. The visible layer is responsible for receiving input datum, whereas each hidden layer processes more abstract representations of data. Multiple RBM layers followed by one or more backpropagation layers are used for fine-tuning. During the training of a DBN, each RBM layer is trained sequentially, utilizing the output from the prior layer as its input to learn higher-level features of the data. After training is complete, the DBN is fine-tuned through added supervised learning layers to enhance performance for specific tasks. In the final layer of the DBN, a BP (Back Propagation) network is set up to accept the output characteristic vectors from the RBMs as its input feature vectors and is trained in a supervised manner to form the neural network.

$$E(E(V,h) = -\sum_i a_i V_i - \sum_j b_j H_j - \sum_{i,j} V_i W_{ij} H_j) \tag{10}$$

In this context, V and H represent the nodes in the visible and hidden layers, respectively, a_i and b_j are the bias terms, and W_{ij} represents the weights between nodes. The training of DBNs involves using this energy function for layer-by-layer pre-training, followed by possible fine-tuning during a subsequent supervised learning phase. Thus, DBNs can capture complex features and patterns in data, possessing powerful predictive and classification capabilities, especially in scenarios involving large volumes of unlabeled data. As technology advances, the potential of DBNs in handling complex data analysis tasks is continually being explored.

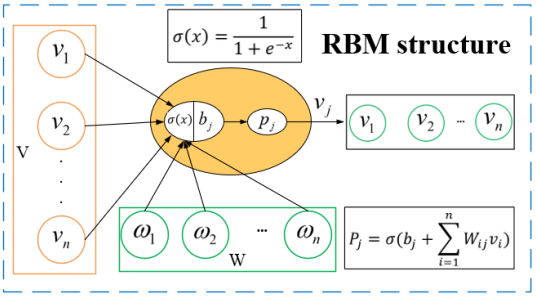

Fig. 1 Proposed architecture of the restricted boltzmann machine (RBM)

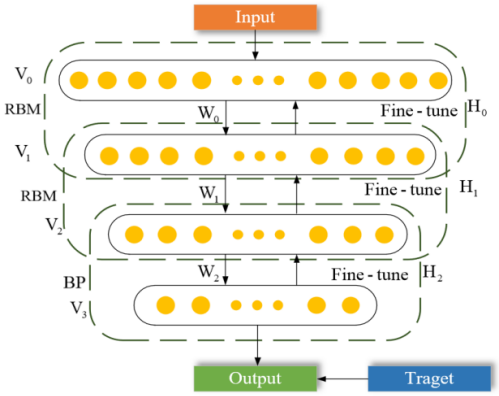

Fig. 2 Hierarchical flowchart of the deep belief network (DBN) training process

3.1.2. Seq2Seq

The Seq2Seq model was introduced in 2015 by Vinyals and Le[36]. The design concept involves two RNN (Recurrent Neural Network) components, an encoder and a decoder, to handle varying input and output sequences. The encoder is accountable for transforming the input sequence into a fixed-length context vector, while the decoder yields the target sequence based on this vector. The core architecture is shown in Fig.3.

Encoder: $h_t = f(x_t, h_{t-1})$, where h_t is the hidden state at time step$t$, and x_t is an element of the input data.

Context Vector: $c = q(\{h_1, h_2, \ldots, h_T\})$, where T is the length of the input data, and the function q is usually taking the last hidden state.

Decoder: Given the context vector c and all previous outputs $y_1, \ldots, y_{t-1}$, it generates the next output y_t. The initial input is set as $s_0 = c$ and the sequence is generated step by step according to the following recurrence:

$$s_t = f(s_{t-1}, y_{t-1}),\ y_t = softmax(W_0 s_t + b_0) \tag{11}$$

Encoder: In the encoder, each input symbol x_t is embedded into a vector $e_t = Embed(x_t) \in R^d$, and passed into a recurrent structure to compute the hidden state recursively:

$$h_t = \Phi(W_x e_t + W_h h_{t-} + b_h),\ \ t = 1,2,\cdots,T \tag{12}$$

where $\phi(\cdot)$is a nonlinear activation function, W_x, W_h are weight matrices, and b_h is a bias term. The final hidden state h_T is regarded as the compressed representation of the entire input sequence, namely the context vector $c = h_T$.

The decoder begins from the initial state $s_0 = c$, and at each step, it takes the output from the previous time step as input to generate the current hidden state and output probability distribution. Specifically, the input symbol at the t-th decoding step is y_{t-1}, which is embedded as $et' = Embed(y_{t-1})$, The hidden state is then updated as:

$$s_t = \Phi\left(W_y e_t^{'} + W_s s_{t-} + b_s\right) \tag{13}$$

Subsequently, the model computes the predicted probability distribution for the current step using a linear transformation followed by a *Softmax* function:

$$\tilde{y}_t = Softmax(W_o s_t + b_o) \tag{14}$$

where $y^t \in R^V$, represents the probability distribution over all words in the target vocabulary, and V is the vocabulary size.

The output sequence is generated in an autoregressive manner. During training, the ground-truth token y_{t-1} (rather than the model's prediction) is fed as input to the next time step (teacher forcing). The model is trained to maximize the conditional probability of the entire target sequence, which corresponds to minimizing the negative log-likelihood loss:

$$L = -\sum_{t=1}^{T'} LogP(y_t | y_1, \cdots, y_{t-1}, x) \tag{15}$$

The conditional probability at each step is determined by the *Softmax* output:

$$P(y_t | y_{<t}, \boldsymbol{x}) = \frac{exp(W_{y_t} s_t)}{\sum_j^V exp(w_j^T s_t)} \tag{16}$$

The Seq2Seq model, through its encoder-decoder structure, models the conditional mapping from variable-length input sequences to variable-length output sequences. It constitutes a sequence of stateful nonlinear transformations and nested probabilistic prediction processes.

The Seq2Seq model is highly flexible and can handle input and output of any length, making it adaptable to various data types. However, it faces challenges such as a heavy burden on the decoder, which must recover all output information from a single fixed-length vector. Additionally, training the model is complex, especially prone to issues like gradient vanishing and explosion in long sequences. Moreover, its high computational demands can limit its use in resource-constrained environments.

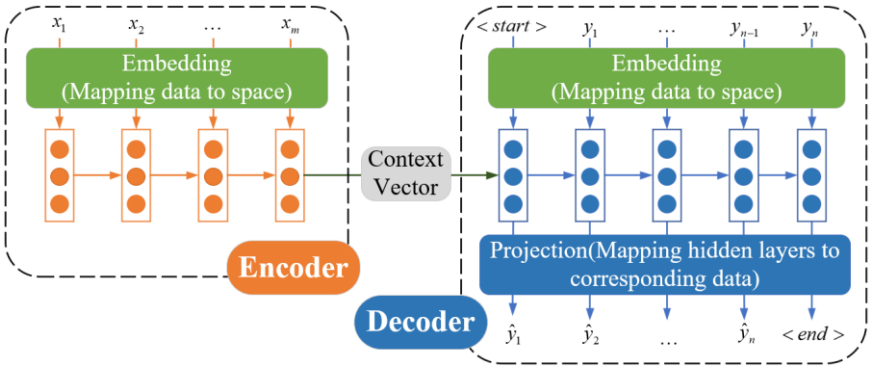

Fig. 3 Illustration of the encoder-decoder architecture in Seq2Seq modeling

3.1.3. BPNN

The Backpropagation Neural Network (BPNN) is a sort of multilayer feed-forward neural network introduced in 1986 by Rumelhart et al.[37]. The training of a BPNN is conducted using the error backpropagation algorithm. This process primarily involves the optimization of a nonlinear objective function. The BP network employs numerical optimization methods to adjust weights, utilizing not only the first-order derivative information of the objective function but frequently also the second-order derivative information.

The structure of the BPNN is shown in Fig.4 and can be uniformly described as:

$$f\left(\boldsymbol{x}^{(k+1)}\right) = \min f\left(\boldsymbol{x}^{(k)} + \omega^{(k)} S(\boldsymbol{x}^{(k)})\right) \tag{17}$$

$$\boldsymbol{x}^{(k+1)} = \boldsymbol{x}^{(k)(\eta)} + \omega^{(k)} S\left(\boldsymbol{x}^{(k)}\right) \tag{18}$$

where $\boldsymbol{x}^{(k+1)}$ represents the vector consisting of all weights and biases of the network; $S(\boldsymbol{x}^{(k)})$ is the search direction in the vector space formed by the components of x; $\eta^{(k)}$ is the step length in the direction of $S(\boldsymbol{x}^{(k)})$ that minimizes $f\left(\boldsymbol{x}^{(k+1)}\right)$.

Thus, the optimization of network weights can be divided into two steps: first, determine the best search direction $S(\boldsymbol{x}^{(k)})$ for the current iteration, and then seek the most optimal iteration step length in this direction.

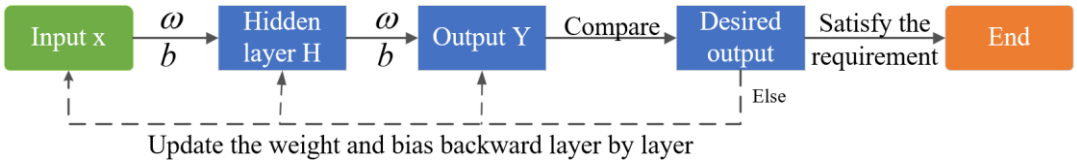

Fig. 4 BPNN Training flowchart

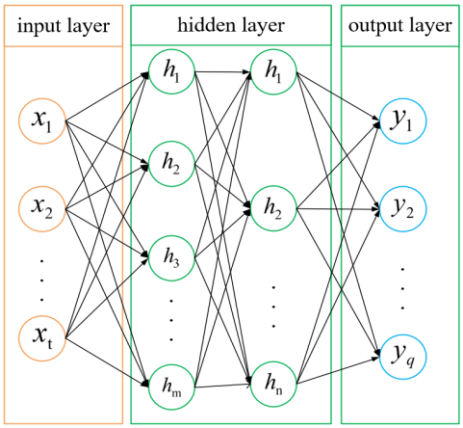

Fig. 5 Architectural diagram of the backpropagation neural network (BPNN)

Fig. 5 introduces the general architecture of BPNN, BPNN is an artificial neural network model used for supervised learning. It calculates output values through forward propagation and adjusts the weights and biases in the network using a backpropagation algorithm, gradually bringing predictions closer to actual values. The structure of BPNN includes an input layer, one or more hidden layers, and an output layer. The input layer receives feature data, the hidden layer transforms features through neurons and activation functions, and the output layer generates the prediction results. In the forward propagation phase, input data flows from the input layer to the output layer, with each neuron computing a weighted sum and generating output signals through an activation function. In the backpropagation phase, the error between the output value and the target value is calculated, and this error is propagated back layer by layer from the output layer to adjust the weights and biases in each layer, gradually reducing the error until the network converges.

$$\alpha_h = \Sigma_{i=1}^{d} v_{ih} x_i + \theta_h \ (i = 1,2,\ldots,d; h = 1,2,\ldots,q) \tag{19}$$

From the hidden layer to the output layer:

$$\beta_j = \Sigma_{h=1}^{q} w_{hj} b_h + \theta_j \ (j = 1,2,\ldots,l; h = 1,2,\ldots,q) \tag{20}$$

Back propagation is to modify the network parameters by computing the error between the output layer and the expected value, so as to the fault gets smaller. The calculation error formula is as follows:

$$E = \frac{1}{2}\Sigma_{k=1}^{l}(y_k - T_k)^2 \tag{21}$$

3.2. Multi-objective optimization algorithm

Although traditional prestress optimization algorithms based on finite element analysis are widely used, they consume considerable time and resources, and they often struggle to balance safety and economic efficiency. As the complexity of prestress optimization design increases, so does the number of objectives that need optimization. In practical engineering, achieving an optimal balance among multiple, often conflicting, objectives is essential. By using multi-objective optimization algorithms, the Pareto frontier and non-dominated solution selection can help identify the best trade-offs among objectives, effectively addressing these challenges. This paper employs three improved multi-objective optimization algorithms to compare their effectiveness in solving the aforementioned multi-objective optimization problems.

NSGA-III (Non-dominated Sorting Genetic Algorithm III) [38,39] is a multi-objective evolutionary algorithm specifically designed to handle complex optimization problems with high-dimensional objective spaces. As illustrated in Fig. 6, NSGA-III builds upon the foundational framework of the NSGA series, with the goal of identifying and maintaining the Pareto front—a set of optimal solutions where no solution is dominated by another across all objectives. The algorithm enhances selection by generating uniformly distributed reference points in the objective space, which helps maintain solution diversity and even distribution. The main steps involve initializing the population, evaluating objective functions, performing non-dominated sorting, and selecting solutions based on reference points. Selected solutions undergo crossover and mutation to create new candidates, updating the population. This process is repeated until the specified number of iterations or convergence conditions are met, resulting in a well-distributed and converged Pareto-optimal set. NSGA-III is widely

applied in fields like engineering and economics, particularly excelling in scenarios requiring the simultaneous optimization of multiple conflicting objectives. Finally, determine if the termination conditions are met. If met, output the final set of non-dominated solutions; otherwise, return to the evaluation step. Through these steps, NSGA-III maintains the diversity and uniformity of solutions while closely approximating the optimal solutions and extensively covering the real Pareto front.

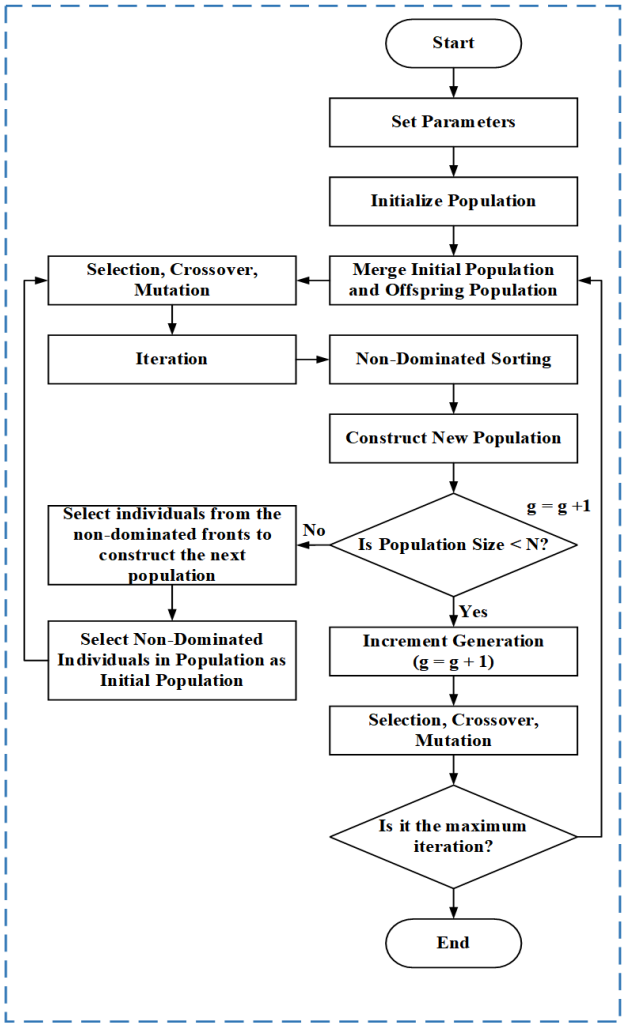

Fig. 6 Process flowchart of the NSGA-III algorithm for multi-objective optimization

3.3. Optimization framework

3.3.1. Step 1: Establish model, group cables and struts, generate initial prestress, and create the dataset

To construct a finite element model of a suspen-dome, the structural symmetry and functional characteristics of the internal cable-struts are utilized to group the rods, reflecting the distribution pattern of internal forces. The prestress range for the cable-struts is determined based on the sectional performance parameters of the cable-strut units. Utilizing the prestress range produced from preliminary design, MATLAB is used to generate initial tension forces uniformly distributed within a specific range. Finite element analysis software then calculates the maximum vertical displacement, lateral support displacement, cable force uniformity coefficient, and maximum cable force value. These calculations form the training dataset for a neural network. This method effectively integrates the structural analysis with machine learning to optimize the design and performance prediction of the suspen-dome.

3.3.2. Step 2: Train the neural network surrogate model

After obtaining the dataset through structural training, the sample dataset is first normalized. Following this, the hyperparameters of the machine learning model are configured to achieve optimal prediction accuracy by setting appropriate model parameters. The dataset is split into training and test sets in a 7:3 ratio. The training set enhances the model's generalization abilities, while the test set evaluates accuracy and stability on new data, establishing a foundation for training the surrogate model. Table 1 shows the parameter settings of the machine learning algorithms applied in this study.

Table 1
Hyperparameters of machine learning algorithms

Algorithms	Hyperparameters
DBN	learning_rate = 0.01, batch_size = 20,number of hidden layers = [30 30],units per layer = 30
Seq2Seq	learning_rate = 0.01, batch_size = 20,number of hidden layers = 20, units per layer = 30
BPNN	learning_rate = 0.01, batch_size = 20,number of hidden layers = 50, units per layer = 30

3.3.3. Step 3: Define the optimization problem and constraints, and carry out the optimization

Define the prestress range for the suspen-dome (Table 2), cross-sectional dimensions, material strengths, and parameters related to the optimization algorithm. Determine the optimization objectives: minimize vertical displacement ($min(f_1)$), minimize horizontal displacement ($min(f_2)$), minimum strain energy ($max(f_3)$), and steel usage of the lower system ($min(f_4)$). Introduce constraints to ensure that the tensile and compressive performance of the components remains within safe limits, and control displacements within the structurally allowable range. Initialize the population, create an initial solution set, and use the surrogate model to represent the initial population or swarm. Select the optimization algorithm, set the optimization parameters, iterate to optimize, and continuously improve the solution set until reaching the maximum iteration count.

3.3.4. Step 4: Select the optimal solution

After obtaining the Pareto frontier, the solution set is normalized. Then, based on the degree of importance, a scale assignment is performed using the AHP. The specific assignment process is as follows:9 for minimum vertical displacement($min(f_1)$),7 for minimum lateral displacement ($min(f_2)$), assigning a weight of 5 to both minimum strain energy ($min(f_3)$) and minimum steel usage ($min(f_4)$) a corresponding judgment matrix is established. Using this matrix, the AHP is performed to compute the final optimal solution on the Pareto front.

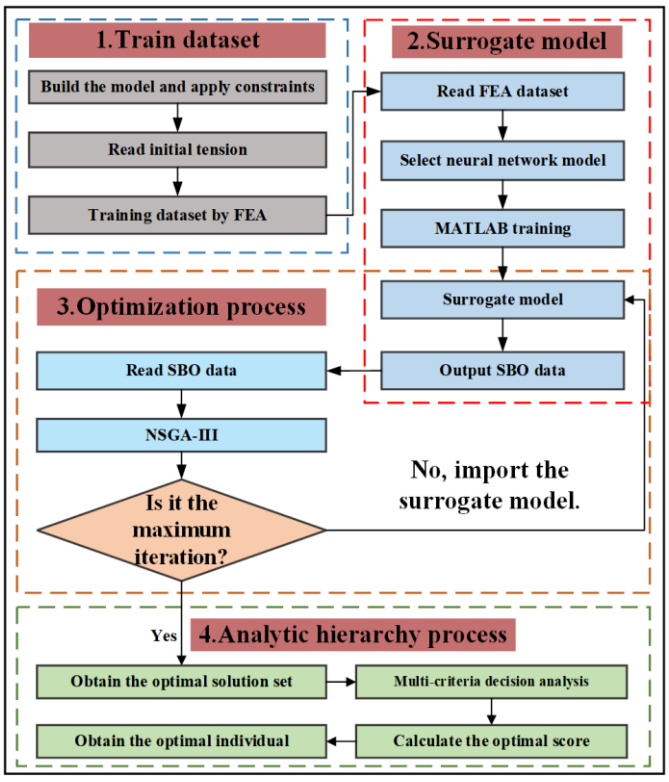

Fig. 7 Flowchart of surrogate-based multi-objective optimization using machine learning algorithms

4. Case study

In the previous content, an optimization algorithm based on neural network surrogate models was established through the introduction of three types of neural networks and optimization algorithms. This approach replaces finite element software-based online analysis with offline analysis based on surrogate models. In this section, two different configurations of suspend-dome models are used to verify the effectiveness and accuracy of this method.

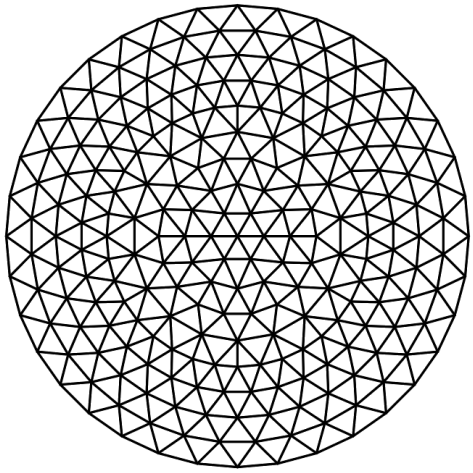

(a) Flat view

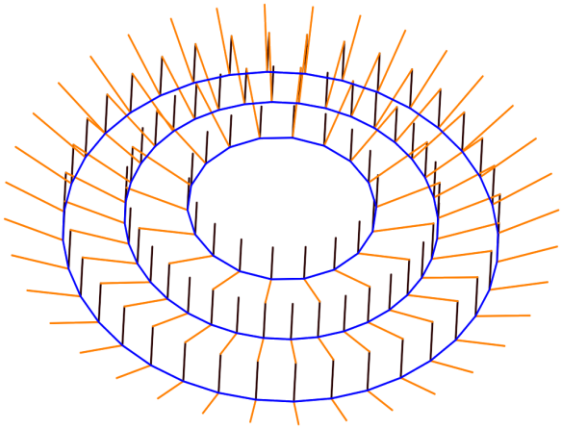

(b) Top view of the lower structure

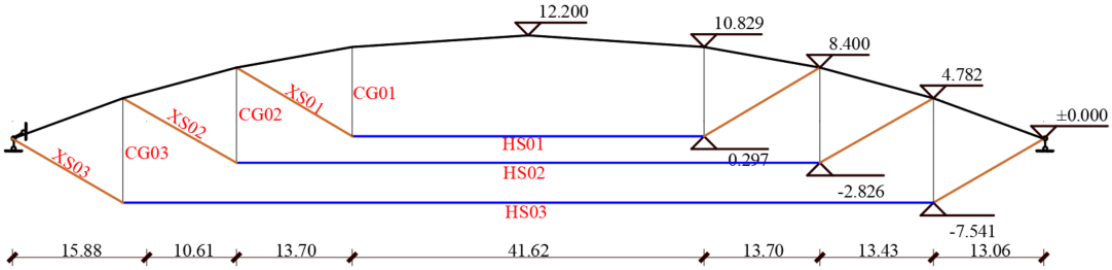

(c) Geometrical size(m)

Fig. 8 Analysis model of suspen-dome No. 1

4.1. Case analysis model

4.1.1. Case1 : Suspen-dome1

Fig. 8 presents the axonometric, top, and elevation views of a suspen-dome structure for a stadium. The upper section is a Geiger-type single-layer shell structure, characterized by a 1:10 aspect ratio. The lower structure features a rib-ring arrangement for the cable-strut support system, which includes three circles of cables. The struts in the lower system are made of standard steel with a Young's modulus of 206 GPa, while the cables use high-strength steel with a Young's modulus of 160 GPa. Around the structure, there are hinge constraints in the y and z directions, with radial constraints released. Table 2 shows the range of initial stress inputs used for training the dataset.

The upper structure of the finite element model is created using the Beam188 element in ANSYS to form a single-layer lattice shell structure. The cable-strut support system in the lower section uses Link180 elements, where the cable elements can only bear tensile forces, and the strut elements can only bear compressive forces. The load conditions are applied according to the requirements of the literature, including a 1.3 times dead load and a 1.5 times live load factor.

4.1.2. Case2 : Levy-type suspen-dome

The structure shown in Fig. 9 is a Levy-type suspen-dome, featuring a single-layer shell as the upper structure and a Levy-type cable-strut system as the lower structure, with constraints consistent with those previously described. Due to the structural symmetry, the cable-strut system is categorized into nine groups: three support groups, three diagonal cable groups, and three circular cable groups. According to Table 2, one thousand sets of initial prestress values are randomly generated for data training.

Table 2
Cross-sectional areas of the structural members

Types	**CG01 ~ 03**			**XS01 ~ 03**			**HS01 ~ 03**		
area/mm^2	8577	5003	4128	6362	2376	1590	9603	3672	1198
min/*k*N	-2000	-1000	-800	600	300	100	800	400	100
max/*k*N	-500	-250	-200	3000	1200	800	4000	2000	500
mean/*k*N	-1250	-625	-500	1800	750	450	2400	1200	300

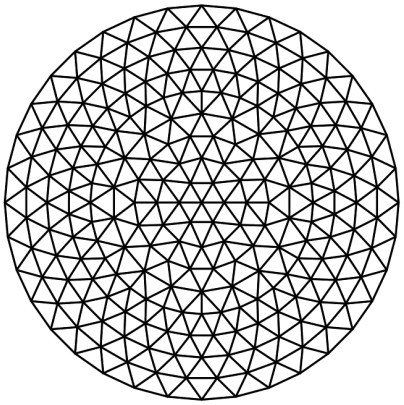

(a) Flat view

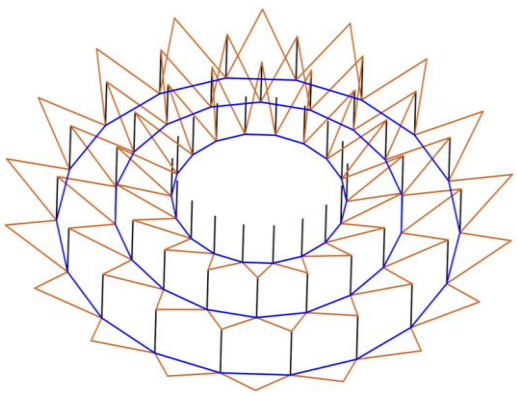

(b) Top view of the lower structure

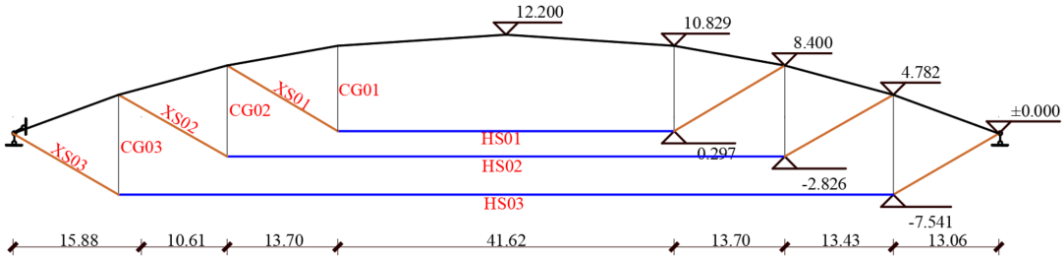

(c) Geometrical size(m)

Fig. 9 Analysis model of suspen-dome No. 2

4.2. Surrogate model

In Section 3, we explore the application of three distinct machine learning algorithms in building surrogate models to accurately capture the complex relationships between input and output data. The model inputs comprise initial tension forces for nine component groups, which are critical parameters influencing structural performance. Outputs include the internal forces within the ring and diagonal cables and the displacements of nodes, covering a total of 11 parameters to fully characterize the structural response under specified tension conditions. To evaluate the performance of each machine learning algorithm, a dataset of 1,000 samples was selected and divided into training and test sets in a 7:3 ratio.

To evaluate the predictive capability of the machine learning model on unseen data, this paper employs the "train-test split" technique. First, the dataset is randomly shuffled to ensure an even distribution of data and to reduce correlation between samples. Then, the dataset is divided into a training set and a test set. The training set is used for model optimization and parameter tuning, enhancing the model's generalization ability, while the test set is reserved for the final evaluation after training is complete, to gauge its real-world performance on new data. This approach allows for a more objective measurement of the model's accuracy and robustness, providing a reliable basis for its applicability in practical scenarios. This approach insures that the model's performance is tested under unbiased conditions, providing a more accurate measure of its generalizability and effectiveness.

Table 3 shows the five metrics used to evaluate model performance: R^2, MSE, RMSE, MAE, and MRE. R^2 assesses the degree of data interpretation by the model; values close to 1 indicate good fit, while values approach 0 indicate poor fit. MSE, RMSE, MAE, and MRE measure prediction errors, with smaller values indicating higher model accuracy. Where y_i and y_i' represent the actual values and forecasted values, separately, $\bar{y}$ represents the average of the actual values in the sample, SS_{res} is the sum of squared residuals, SS_{tot} is the entire sum of squares, and N is the entire number of specimens in the dataset.

Table 3
Evaluation indexes of machine learning regression model

Name	Formulas
R^2	$R^2 = 1 - \frac{SS_{res}}{SS_{tot}} = 1 - \frac{\sum_{i=1}^{N}(y_i - y_i')^2}{\sum_{i=1}^{N}(y_i - \bar{y})^2}$
MSE	$MSE = \frac{1}{N}\sum_{i=1}^{N}\lvert y_i - y_i'\rvert^2$
RMSE	$RMSE = \sqrt{MSE} = \sqrt{\frac{1}{N}\sum_{i=1}^{N}\lvert y_i - y_i'\rvert^2}$
MAE	$MAE = \frac{1}{N}\sum_{i=1}^{N}\lvert y_i - y_i'\rvert$
MRE	$MRE = \frac{1}{N}\sum_{i=1}^{N}\left\lvert\frac{y_i - y_i'}{y_i}\right\rvert$

Table 4
The initial structural tension of the optimal solution (kN)

Cases	Types	CG01	CG02	CG03	XS01	XS02	XS03	HS01	HS02	HS03
1	NSGA-III-FEA	-1475	-507	-272	2059	739	545	2584	1371	323
	NSGA-III-SBO	-526	-379	-740	2779	834	404	1859	1455	387
2	NSGA-III-FEA	-1428	-683	-735	1037	807	710	3142	697	382
	NSGA-III-SBO	-1392	-510	-423	626	893	692	3147	1023	329

4.3. Prestress optimization

Section 3.1 introduces three neural network architectures used to build surrogate models. According to the process detailed in Section 3.2, multi-objective optimization is performed using the established surrogate models. After completing the optimization, a Pareto frontier of non-dominated solutions is obtained. Finally, the multi-criteria decision-making method described in Section 2.3 is used to select the optimal solution from the set of non-dominated solutions. Table 4 presents the prestress data for the cable-strut system obtained using both the finite element analysis software and the surrogate model.

4.4. Results and discussions

Figs. 10 to 13 present the performance evaluation metrics of the three machine learning algorithms. Specifically, Figs. 10 to 12 illustrate the evolution of evaluation metrics during training for the surrogate models constructed using DBN, Seq2Seq, and BPNN, respectively. It can be observed that the MSE, MAE, MAPE, and RMSE of the dataset exhibit similar declining trends across all models, indicating substantial reductions in prediction errors as training progresses. Fig. 13 shows the model fitting performance after training. All models demonstrate high coefficients of determination (R^2), with the BPNN model achieving a value close to 1, suggesting excellent prediction accuracy.

Among the three algorithms, the BPNN-based surrogate model outperforms the others in terms of R^2, MSE, RMSE, MAE, and MAPE, indicating superior predictive capability. The R^2 values of the BPNN model on both the testing and prediction sets are close to 1, demonstrating its high reliability and effectiveness in capturing complex data relationships. This makes it particularly suitable for engineering applications with stringent accuracy requirements, such as prestress optimization in structural engineering. Therefore, the BPNN model is selected as the surrogate model for the subsequent prestress optimization study. Its optimization results are further compared with those obtained from the FEA model to validate its effectiveness.

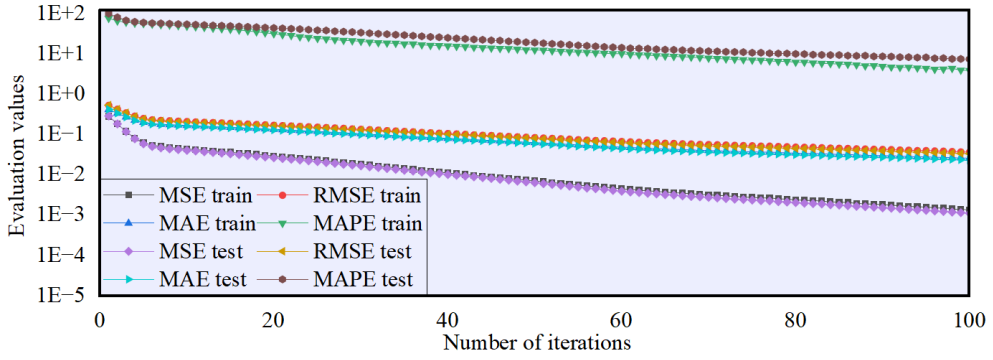

(a) The four evaluation curve of Model 1

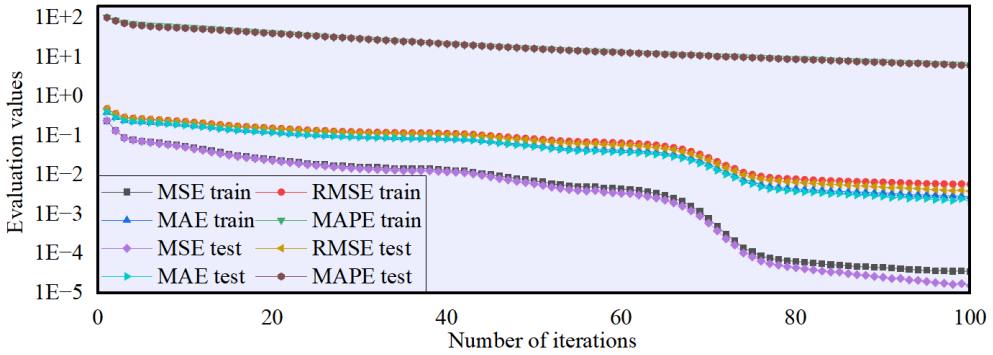

(b) The four evaluation curve of Model 2

Fig. 10 Evaluation curves of the DBN machine learning model during training and testing

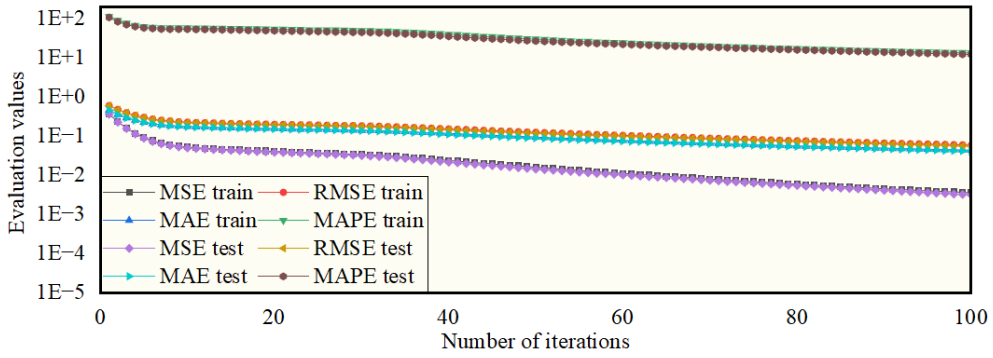

(a) The four evaluation curve of Model 1

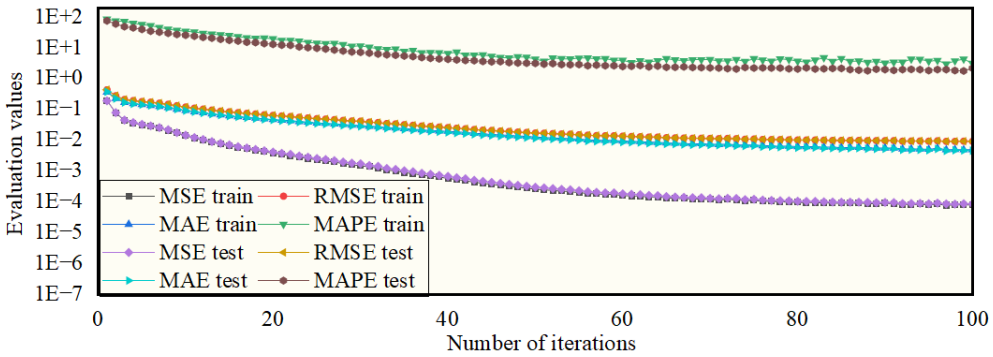

(b) The four evaluation curve of Model 2

Fig. 11 Evaluation curves of the Seq2Seq machine learning model during training and testing

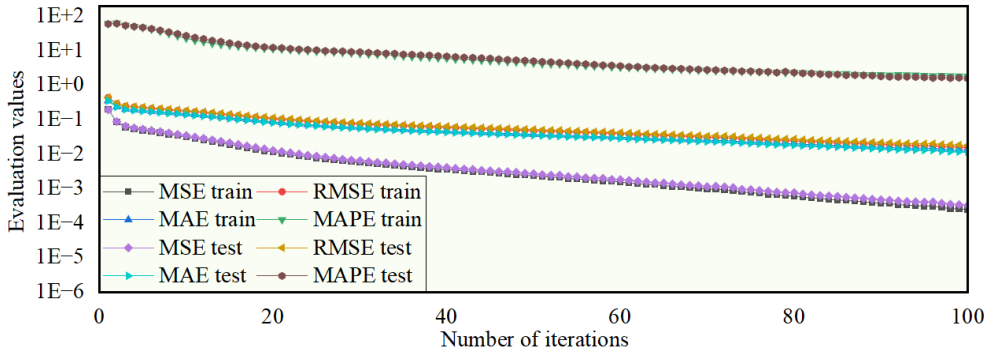

(a) The four evaluation curve of Model 1

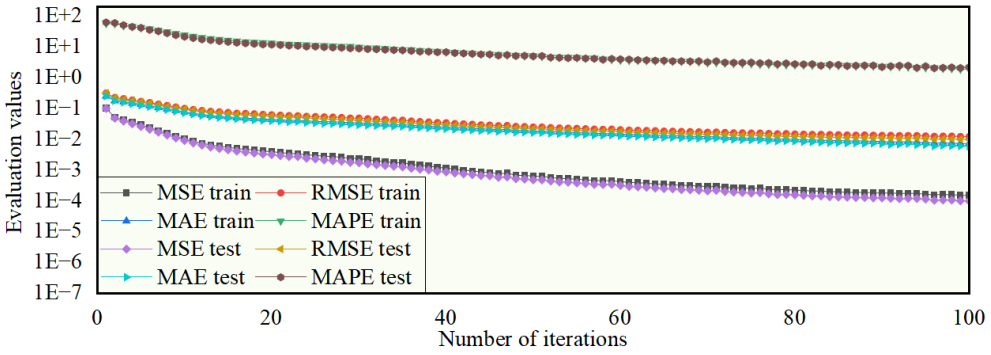

(b) The four evaluation curve of Model 2

Fig. 12 Evaluation curves of the BPNN machine learning model during training and testing

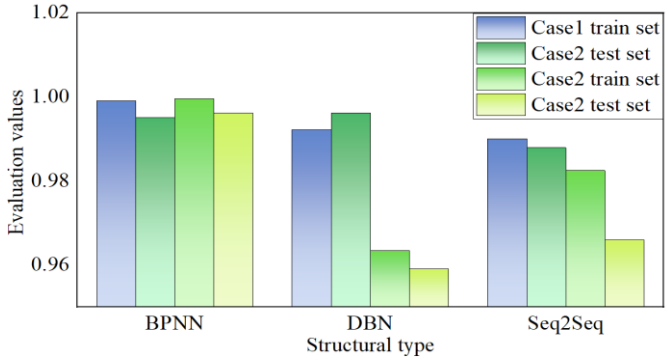

Fig. 13 The coefficient of determination (R^2) values for three different machine learning models during training and testing

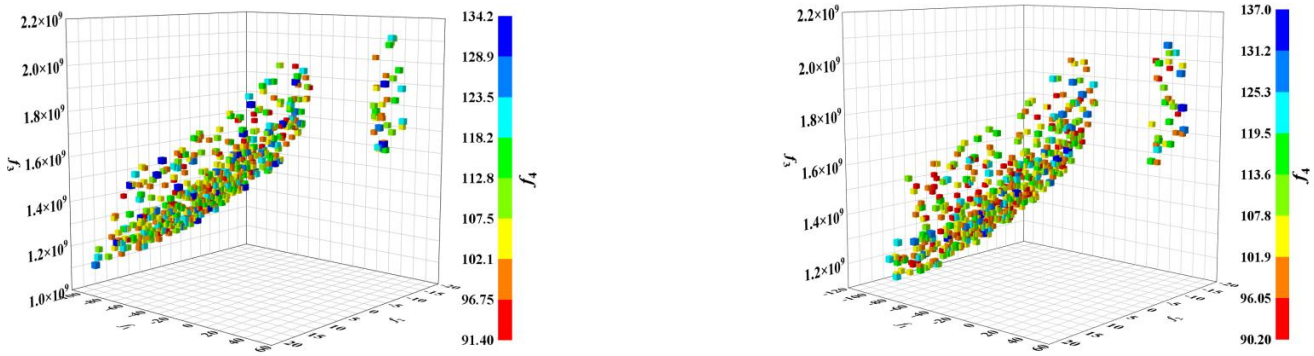

(a) NSGA-III-SBO

(b) NSGA-III-FEA

Fig. 14 The pareto front of the optimized structure in Model 01

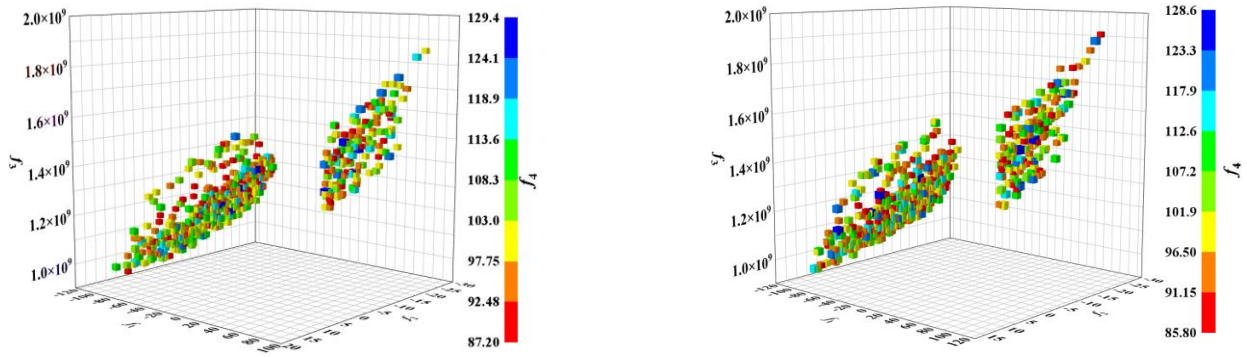

(a) NSGA-III-SBO (b) NSGA-III-FEA

Fig. 15 The pareto front of the optimized structure in Model 02

Table 5
Comparison of the best solution of various optimization algorithms

Cases	Types	$f_1(mm)$	$f_2(mm)$	f_3(J)	$f_4(t)$	Time(s)	Total time(s)
1	NSGA-III-FEA	-28.7	-6.8	1.28E9	98.5	26581	26581
	NSGA-III-SBO	-36.1	4.3	1.34E9	96.3	237	1515
2	NSGA-III-FEA	-34.7	-7.6	1.37E9	99.05	25689	25689
	NSGA-III-SBO	-31.6	-10.2	1.32E9	91.4	247	1525

Fig. 14 and Fig. 15 show multi-objective optimization results, with (a) representing optimization based on finite element analysis and (b) showing the results based on the BPNN surrogate model. In all four figures, the x, y, and z axes represent the maximum deflection of the structure (mm), the radial displacement at the supports (mm), and the minimum strain energy (J), respectively. The color scale indicates the amount of steel used in the lower cable-strut system.

Table 5 compares the optimal solutions obtained using the two methods, calculated through the AHP method for multi-criteria decision-making outlined in Section 2.3. For the surrogate model approach, the total optimization time is calculated by adding the data training time (t = 1278s) to the optimization time, resulting in $Total\ time = Time + t$. By observing Figures 10 and 11, the following conclusions can be drawn:

(1) There is a distinct linear relationship between the maximum deflection of the structure, the radial displacement at the supports, and the strain energy of the structure. The non-dominated relationships among these objectives are apparent. Strain energy and maximum vertical displacement, as well as radial displacement at the supports, show linear variation: as the support transitions from tension to compression and the maximum vertical displacement changes from negative to positive, strain energy increases.

(2) The maximum vertical displacement cannot be optimized to zero and can only reach a relatively small displacement, as the vertex of the dome structure cannot be controlled.

(3) There is no apparent relationship between the amount of steel used and the other three optimization objectives, meaning it is possible to achieve the minimum steel usage while still achieving favorable outcomes for the remaining objectives.

4.5. Limitations and future developments of the research work

This study integrates multi-objective optimization with surrogate modeling, significantly improving optimization efficiency while substantially reducing computational resource consumption. However, the proposed approach still has certain limitations, and there remains considerable room for improvement in future research:

(1) Data Dependence and Generalization: The data-driven models rely heavily on existing datasets for training and lack an understanding of underlying physical principles. As a result, their predictions can be unreliable in regions outside the training data distribution, and a large amount of data is typically required to achieve acceptable accuracy.

(2) Black-box Nature and Limited Interpretability: The adopted approach is essentially a black-box model, making it difficult to interpret the mechanisms behind the optimization results. Incorporating physical equations or domain knowledge could improve the model's transparency and interpretability.

(3) Physically Infeasible Solutions: During the optimization process, the surrogate-based model may produce solutions that violate physical constraints, such as inadequate structural strength or energy imbalance. Embedding physical boundary conditions and constraints into the model could help ensure the feasibility of the generated solutions.

(4) Lack of Sensitivity Analysis in AHP: Although the Analytic Hierarchy Process (AHP) provides a structured and logical framework for weight assignment, no sensitivity or robustness analysis was conducted in this study. Future work could address this limitation to enhance the reliability of the decision-making process.

5. Conclusion

This paper employs three different machine learning algorithms to forecast the respond of the suspen-dome structure. By inputting the initial tension, the displacement and internal force distribution of the structure were successfully predicted. Subsequently, four objective functions were constructed based on data analysis, and a multi-objective surrogate model was successfully established. On this basis, the NSGA-III algorithm was further utilized for multi-objective optimization, resulting in a set of Pareto front solutions. Finally, multi-criteria decision-making was performed using the AHP to select the optimal solution from the Pareto front.

(1) The construction of surrogate models and the options of multi-objective optimization algorithms should take into consideration both the complexity of the model and the optimization costs. Compared to other neural networks, BPNN has superior performance.

(2) The multi-objective prestress optimization method is grounded on the surrogate model not only significantly improves optimization efficiency but also more effectively coordinates the relationships among objectives, resulting in higher-quality solutions.

(3) Using the AHP to determine the best solution can effectively obtain the optimal solution from the Pareto front.

(4) This study is based on data-driven machine learning models, which inherently suffer from limited interpretability and data dependency. In addition, no sensitivity or robustness analysis was conducted on the determined weights. These limitations suggest valuable directions for future research, such as enhancing model interpretability and conducting systematic sensitivity analysis to improve the reliability of the decision-making process.

Acknowledgements

This work was supported by the National Natural Science Foundation of China (Grant Nos. 51308105, 52278190) and the Fundamental Research Funds for the Central Universities (Grant No. 2242022k30030).

References

[1] Kawaguchi M, Abe M, Tatemichi I. Design, tests and realization of suspen-dome system. Journal of the International Association for Shell and Spatial Structures 1999;40:179–92.
[2] Liu X. Introduction of structures of some stadiums and gymnasiums for Beijing 2008 Olympic Games. Fourth International Conference on Advances in Steel Structures, vol. I,

Elsevier; 2005, p. 361–8. https://doi.org/10.1016/B978-008044637-0/50052-4.
[3] Li Z Q, Zhang Z H, Dong S L, et al. Construction sequence simulation of a practical suspen-dome in Jinan Olympic Center. Advanced Steel Construction, 2012, 8(1): 38-53.
[4] Nie G, Fan F, Zhi X. Test on the Suspended Dome Structure and Joints of Dalian Gymnasium. Adv Struct Eng 2013;16:467–85. https://doi.org/10.1260/1369-4332.16.3.467.
[5] Gong S. The research of suspen-dome structure. IOP Conf Ser: Mater Sci Eng 2017;242:012050. https://doi.org/10.1088/1757-899X/242/1/012050.
[6] Yuan XF, Dong SL. Integral feasible prestress of cable domes. Comput Struct 2003;81:2111–9. https://doi.org/10.1016/S0045-7949(03)00254-2.
[7] Optimal Design of Cable-domes with Multi-overall Selfstress Modes-All Databases n.d. https://webofscience.clarivate.cn/wos/alldb/full-record/CSCD:3389260 (accessed September 2, 2024).
[8] Kitipornchai S, Kang W, Lam H-F, Albermani F. Factors affecting the design and construction of Lamella suspen-dome systems. Journal of Constructional Steel Research 2005;61:764–85. https://doi.org/10.1016/j.jcsr.2004.12.007.
[9] Zhang Z, Zhi X, Li Q, Fan F. Simlating the Stability and Pre-stressed Tension of a Single-Layer Spherical Reticulated Shell Supported by Cable. Int J Steel Struct 2019;19:618–34. https://doi.org/10.1007/s13296-018-0151-6.
[10] Kang W, Chen Z, Lam H-F, Zuo C. Analysis and design of the general and outmost-ring stiffened suspen-dome structures. Engineering Structures 2003;25:1685–95. https://doi.org/10.1016/S0141-0296(03)00149-4.
[11] Liang H Q, Dong S L, Miao F. Multi-objective optimization analysis of cable dome structures prestress based on niche genetric algorithm. J. Build. Struct, 2016, 37: 92-99.(in Chinese)
[12] Kaveh A, Rezaei M. Optimal Design of Double-Layer Domes Considering Different Mechanical Systems via ECBO. Iran J Sci Technol Trans Civ Eng 2018;42:333–44. https://doi.org/10.1007/s40996-018-0123-2.
[13] Olofin I, Liu R. Suspen-Dome System: A Fascinating Space Structure. TOCIEJ 2017;11:131–42. https://doi.org/10.2174/1874149501711010131.
[14] Lygoe RJ, Cary M, Fleming PJ. A Real-World Application of a Many-Objective Optimisation Complexity Reduction Process. In: Purshouse RC, Fleming PJ, Fonseca CM, Greco S, Shaw J, editors. Evolutionary Multi-Criterion Optimization, vol. 7811, Berlin, Heidelberg: Springer Berlin Heidelberg; 2013, p. 641–55. https://doi.org/10.1007/978-3-642-37140-0_48.
[15] Deb K, Jain H. An evolutionary many-objective optimization algorithm using reference-point-based nondominated sorting approach, part I: solving problems with box constraints. IEEE Transactions on Evolutionary Computation 2013;18:577–601. https://doi.org/10.1109/TEVC.2013.2281535.
[16] Hisao Ishibuchi, Noritaka Tsukamoto, Yusuke Nojima. Evolutionary many-objective optimization: A short review. 2008 IEEE Congress on Evolutionary Computation (IEEE World Congress on Computational Intelligence), Hong Kong, China: IEEE; 2008, p. 2419–26. https://doi.org/10.1109/CEC.2008.4631121.
[17] Ma Q, Ohsaki M, Chen Z, Yan X. Multi-objective optimization for prestress design of cable-strut structures. International Journal of Solids and Structures 2019;165:137–47. https://doi.org/10.1016/j.ijsolstr.2019.01.035.
[18] Chen Y, Yan J, Sareh P, Feng J. Feasible Prestress Modes for Cable-Strut Structures with Multiple Self-Stress States Using Particle Swarm Optimization. J Comput Civ Eng 2020;34:04020003. https://doi.org/10.1061/(ASCE)CP.1943-5487.0000882.
[19] Deb K, Pratap A, Agarwal S, Meyarivan T. A fast and elitist multiobjective genetic algorithm: NSGA-II. IEEE Trans Evol Computat 2002;6:182–97. https://doi.org/10.1109/4235.996017.
[20] Zitzler E, Laumanns M, Thiele L. SPEA2: Improving the strength Pareto evolutionary algorithm. TIK Report 2001;103.
[21] Purshouse RC, Fleming PJ. Evolutionary many-objective optimisation: An exploratory analysis. The 2003 Congress on Evolutionary Computation, 2003. CEC'03., vol. 3, IEEE; 2003, p. 2066–73. https://doi.org/10.1109/CEC.2003.1299927.
[22] Hughes EJ. Evolutionary many-objective optimisation: many once or one many? 2005 IEEE congress on evolutionary computation, vol. 1, IEEE; 2005, p. 222–7. https://doi.org/10.1109/CEC.2005.1554688.
[23] Deb K, Mohan M, Mishra S. Evaluating the ϵ-domination based multi-objective evolutionary algorithm for a quick computation of Pareto-optimal solutions. Evolutionary Computation 2005;13:501–25. https://doi.org/10.1162/106365605774666895.
[24] Yang S, Li M, Liu X, Zheng J. A grid-based evolutionary algorithm for many-objective optimization. IEEE Transactions on Evolutionary Computation 2013;17:721–36. https://doi.org/10.1109/TEVC.2012.2227145.
[25] He Z, Yen GG, Zhang J. Fuzzy-based Pareto optimality for many-objective evolutionary algorithms. IEEE Transactions on Evolutionary Computation 2013;18:269–85. https://doi.org/10.1109/TEVC.2013.2258025.
[26] Carleo G, Cirac I, Cranmer K, Daudet L, Schuld M, Tishby N, et al. Machine learning and the physical sciences. Rev Mod Phys 2019;91:045002. https://doi.org/10.1103/RevModPhys.91.045002.
[27] Chang C-M, Lin T-K, Chang C-W. Applications of neural network models for structural health monitoring based on derived modal properties. Measurement 2018;129:457–70. https://doi.org/10.1016/j.measurement.2018.07.051.
[28] Amini K, Jalalpour M, Delatte N. Advancing concrete strength prediction using non-destructive testing: Development and verification of a generalizable model. Construction and Building Materials 2016;102:762–8. https://doi.org/10.1016/j.conbuildmat.2015.10.131.
[29] Zoph B. Neural architecture search with reinforcement learning. arXiv preprint arXiv: 1611.01578, 2016.
[30] Goodfellow IJ, Pouget-Abadie J, Mirza M, Xu B, Warde-Farley D, Ozair S, et al. Generative Adversarial Networks. Communications of the ACM, 2020, 63(11): 139-144.
[31] Tai L, Zhang J, Liu M, Boedecker J, Burgard W. A Survey of Deep Network Solutions for Learning Control in Robotics: From Reinforcement to Imitation. arXiv preprint arXiv:1612.07139, 2016.
[32] Li Y, Hariri-Ardebili MA, Deng T, Wei Q, Cao M. A surrogate-assisted stochastic optimization inversion algorithm: Parameter identification of dams. Adv Eng Inform 2023;55:101853. https://doi.org/10.1016/j.aei.2022.101853.
[33] Zhou Y, Zheng S, Zhang G. Machine learning-based optimal design of a phase change material integrated renewable system with on-site PV, radiative cooling and hybrid ventilations—study of modelling and application in five climatic regions. Energy 2020;192:116608. https://doi.org/10.1016/j.energy.2019.116608.
[34] JGJ 7-2010. Technical Specification for Space Grid Structures, 2010.(in Chinese)
[35] Hinton GE, Osindero S, Teh Y-W. A Fast Learning Algorithm for Deep Belief Nets. Neural Computation 2006;18:1527–54. https://doi.org/10.1162/neco.2006.18.7.1527.
[36] Vinyals O, Le Q. A neural conversational model. arXiv preprint arXiv:1506.05869, 2015.
[37] Rumelhart DE, Hinton GE, Williams RJ. Learning representations by back-propagating errors. Nature 1986;323:533–6. https://doi.org/10.1038/323533a0.
[38] Gu Q, Wang R, Xie H, Li X, Jiang S, Xiong N. Modified non-dominated sorting genetic algorithm III with fine final level selection. Appl Intell 2021;51:4236–69. https://doi.org/10.1007/s10489-020-02053-z.
[39] Deb K, Jain H. An Evolutionary Many-Objective Optimization Algorithm Using Reference-Point-Based Nondominated Sorting Approach, Part I: Solving Problems With Box Constraints. IEEE Trans Evol Computat 2014;18:577–601. https://doi.org/10.1109/TEVC.2013.2281535.

Advanced Steel Construction – Vol. 22 No. 1 (2026) 116–129
DOI:10.18057/IJASC.2026.22.1.10

EFFICIENT CROSS-SECTIONAL ANALYSIS TECHNIQUE FOR ARBITRARY-SHAPED STEEL SECTIONS USING GAUSSIAN SEGMENTAL ELEMENTS

Wen-Long Gao [1], Liang Chen [1, *], A.H.A. Abdelrahman [2] and Si-Wei Liu [1]

[1] *Department of Civil and Environmental Engineering, The Hong Kong Polytechnic University, Hung Hom, Kowloon, Hong Kong, China*

[2] *Department of Structural Engineering, Faculty of Engineering, Mansoura University, Egypt*

** (Corresponding author: E-mail: liang17.chen@connect.polyu.hk)*

ABSTRACT

This research introduces an efficient cross-sectional analysis algorithm utilizing innovative Gaussian segmental elements for arbitrary-shaped steel sections. Steel members with arbitrary-shaped sections are gradually widely employed in engineering due to their mechanical benefits. Achieving accuracy in cross-sectional analysis remains crucial for the understanding of their comprehensive structural behavior and enhancing design optimization. Traditional fiber-based cross-sectional analysis methods prioritize accuracy but often compromise computational efficiency. The proposed algorithm leverages the Gaussian quadrature method, renowned for its precise approximation of definite integrals, to address complex cross-sectional geometries. In addition, a refined line-segment model is introduced to solve the overlapping problem by configuring eccentricities at the ends of segments. The paper elaborates on the derivation of the novel Gaussian segmental element designed for modeling the arbitrary-shaped section, determining the section properties, generating full yield surfaces, and calculating the moment-thrust-curvature relationships. Notably, the algorithm balances accuracy and computational efficiency by strategically selecting integration Gauss points and weights across thicknesses. Three groups of examples are provided to demonstrate the accuracy and efficiency of the proposed method for the cross-sectional analysis of arbitrary-shaped steel sections.

ARTICLE HISTORY

Received: 06 November 2025
Revised: 26 January 2026
Accepted: 6 February 2026

KEYWORDS

Arbitrary-shaped steel sections;
Cross-sectional analysis;
Yield surface;
Moment-thrust-curvature;
Gauss integration

1. Introduction

Steel members with arbitrary-shaped sections are gradually widely used in contemporary steel constructions due to their elevated flexibility forms and structural efficacy. In addition, robotic welding machines and building information modeling eliminate the constraints of fabricating such sections. Accurate and efficient cross-sectional analysis of the arbitrary-shaped sections is crucial in understanding their mechanical behavior and optimizing their design for practice design. One widely employed approach is the fiber-based method, which facilitates the analysis of complex cross-sectional geometries and material properties, allowing for a comprehensive investigation of essential parameters like cross-section properties [1-5], full yield surface [6-8], and moment-curvature relationships [9-11].

Accurate calculations of cross-sectional properties are vital for analyzing and designing members with arbitrary-shaped steel sections. Researchers have thoroughly explored various techniques for calculating cross-sectional properties encompassing torsional, shear, and nonsymmetrical section properties [12-14]. For example, Waldron [1] introduced the sectorial method of analysis, emphasizing its potential to incorporate warping restraint effects for torsional analysis in thin-walled beams. However, complexities in calculating sectorial functions hindered its applicability. Expanding this discourse, Chai Hong and Acra [2] delved into torsional and flexural properties of multicellular cross-sections, proposing an algorithm to tackle indeterminate shear flows and thus analyze sections with complex geometries. Li et al. [3] introduced a numerical procedure for analyzing arbitrary beam-columns, accounting for residual stresses and geometric imperfections, crucial in designing high-strength steel structures. Shortly after, Bourihane et al. [15] developed a beam-column element for stability analyses of beams comprising thin-walled open sections under various loading conditions. Elkaimbillah et al. [16] extended this research and proposed a refined beam-column element for the nonlinear dynamic behavior of thin-walled open-section composite beams. Hancock and Rasmussen [17, 18] further analyzed members with nonsymmetrical cross-sections accounting for the misalignment between the cross-sectional centroid and shear center. More recently, Chen et al. [19] introduced an efficient line-element method for second-order analysis of steel members with nonsymmetrical thick-walled sections, addressing twisting effects and warping degrees of freedom alongside a two-dimensional finite-element cross-section analysis method implemented in the educational software MASTAN2 [20]. While these studies offer significant insights, limitations persist. Challenges remain in analyzing sections with complex geometries or substantial torsion.

Notably, cross-sectional analysis for arbitrary-shaped steel sections has seen notable advancements, particularly in understanding their yield capacity and section properties. The concept of the yield surface, encompassing axial force and bending responses, plays a pivotal role in determining section behavior [21-24]. While conventional methodologies, such as the one proposed by McGuire et al. [6], have provided valuable insights for symmetric sections, addressing nonsymmetrical shapes remains challenging. Nonsymmetrical sections are extensively used for their structural efficiency, necessitating accurate analysis techniques. In this context, the approach proposed by Liu et al. [7] introduces a cross-section analysis method that calculates yield surfaces for both symmetric and nonsymmetrical sections. This method harnesses the Quasi-Newton divergence-free algorithm and integrates the fiber-based model. More recently, Chen et al. [8] developed an improved line-element formulation to model nonsymmetrical sections' geometric and material nonlinear behaviors. The proposed methodology not only generates yield surfaces of arbitrary steel sections but also employs gradients for effective plastic flow control. However, it is acknowledged that the complexities associated with generating the fiber model may introduce challenges in terms of applicability for complex geometries and computational efficiency.

The moment-thrust-curvature relationships of steel sections offer crucial insights into their structural behavior under bending. These relationships illuminate how the sections respond to axial load and bending moments, thereby effectively guiding engineers in designing and analyzing these components [25-30]. Duan et al. [9] examined the moment-curvature relationships for dented tubular sections under combined biaxial bending and axial load. Their work introduced closed-form moment-thrust-curvature expressions for dented and undented tubular sections. Additionally, Liew et al. [10] extended the concept of moment-thrust-curvature relationships to address inelastic and geometrically non-linear structural problems involving elements subjected to combined axial load and bending. Their numerical discretized cross-section method yielded moment-thrust-curvature relationships for I-sections, rectangular box-sections, and circular or elliptical hollow sections. Exploring moment-thrust-curvature relationships enriches the broader investigation into the cross-sectional analysis, complementing the studies on yield surfaces, cross-sectional properties, and section capacity checks.

Generally, the previous studies predominantly focused on symmetric sections and often implemented the time-consuming fiber-based models. To fill the research gap, this paper presents a novel algorithm for precisely determining cross-section properties, the full yield surface, and the moment-thrust-curvature of the cross-sections. The proposed algorithm leverages the Gaussian quadrature method, renowned for its precise approximation of definite integrals [31-36], to address complex cross-sectional geometries. Additionally, a refined Coordinate Method was introduced to eliminate the interaction between the adjacent elements in the line-segment model by configuring eccentricities at the ends of segments. The paper elaborates on the derivation of the novel Gaussian segmental element (GSE) and provides three groups of examples to demonstrate the accuracy and efficiency of the proposed GSE for the cross-sectional analysis of arbitrary-shaped steel sections.

2. Cross-section modeling using gaussian segmental element

The fiber-based approach is widely used for cross-sectional analysis [3, 7, 8, 11, 19], where full section meshing or excessive fiber generation is required to obtain the accurate section properties, yield surfaces, or the moment-curvature. Despite its utility, the fiber-based approach introduces its own set of challenges, notably the intricate fiber mesh generation algorithm. This algorithm necessitates extensive effort to ascertain the number of fibers and their geometric details, such as center coordinates and area, thus complicating the process of building and meshing sections. Addressing these challenges, an innovative cross-sectional modeling and analysis methodology using GSE is developed in this paper, offering an efficient alternative to conventional fiber-based models.

2.1. Gaussian segmental element

This study introduces a novel method employing the GSE based on the line finite element method, aiming to enhance the efficiency and accuracy of cross-sectional analysis. The Gaussian integration strategy is applied for area integration in the cross-sectional plane, offering a better balance between computational cost and accuracy compared to the classical 2D finite element method, which uses a fiber section obtained from meshing the geometric model. The cross-sectional configuration is generated using a line-segment approach, consisting of a series of segments and points, as illustrated in Fig. 1(b). Each segment is aligned with the central axis of the section plate and is defined by two points representing its start and end. These segments are not only defined by the two points but are also associated with the thickness of the section plate.

Furthermore, the initially established global axis system, denoted as *Z-O-Y*, determines each point's coordinates, with Gaussian points systematically distributed along the section's thickness and length based on the integral range (Fig. 1c). In this research, a GSE has three columns of Gauss integral points along the section plate thickness and seven rows of Gauss integral points along its length.

The distribution of Gauss points directly governs the integration accuracy of the proposed GSE. With Gauss–Legendre quadrature, increasing the number of Gauss points enhances the order of accuracy for evaluating sectional integrals, allowing accurate results with far fewer sampling points than uniform fiber partitioning. In the present study, three Gauss points through the thickness and seven Gauss points along the segment length are adopted as a practical balance between accuracy and efficiency for thin-walled steel sections, where the through-thickness stress variation is typically mild under the adopted sectional assumptions. For problems involving sharper stress gradients (e.g., locally thick regions, pronounced nonlinearity localization, or refined residual-stress patterns), accuracy can be further improved by increasing the Gauss points and/or refining the line-segment representation, analogous to mesh refinement in fiber-based models.

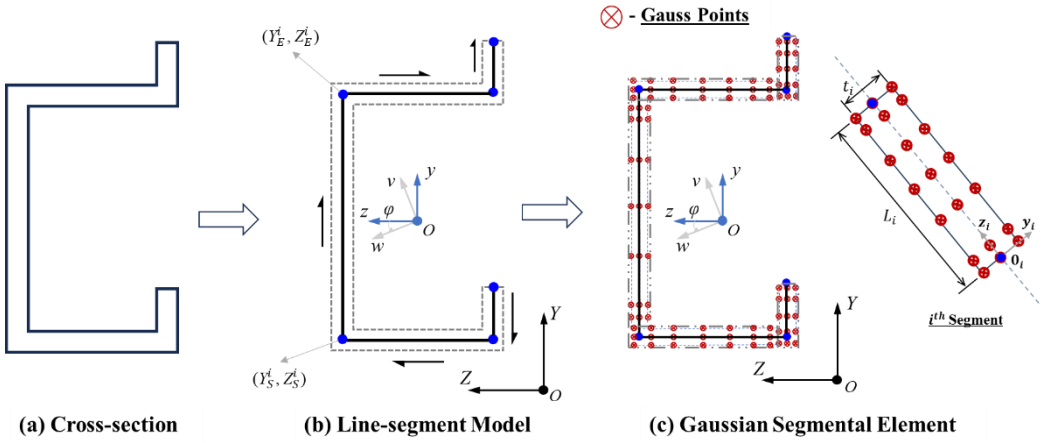

Fig. 1 Cross-section modeling using the Gaussian line-segment approach

A local axis system denoted as *zi-oi-yi* is established to obtain the distribution of Gauss points in each segment, as depicted in Fig. 1 (c), in which three Gauss points are distributed along the thickness, and seven Gauss points along the length of each segment. This distribution configuration of Gauss points in a segment is both efficient and sufficient for most common cases. In extreme cases, such as when the segment is too thin or too thick, the distribution of Gauss points can be automatically adjusted based on the width-to-thickness ratio. The coordinates of each Gauss integration point within its respective local axis system are determined by the following equations:

$$y^i_{m,n} = \xi^i_{m,n} t_i \qquad (m = 1 \sim 3, n = 1 \sim 7) \tag{1}$$

$$z^i_{m,n} = \zeta^i_{m,n} L_i \qquad (m = 1 \sim 3, n = 1 \sim 7) \tag{2}$$

where the subscripts m and n represent the m^{th} and n^{th} Gauss points in the section plate's thickness and length directions. The coefficients, $\xi^i_{m,n}$ and $\zeta^i_{m,n}$, representing the location of Gauss points distributed on each segment in two directions, should vary for each segment due to its length-to-thickness ratio. t_i and L_i denote the thickness and length of the i^{th} segment in the line-segment model, respectively. The locations and the weight factors for the Gauss points used in this research are given in Tables 1 and 2.

Table 1
The locations and weight factors of Gauss points in the thickness direction

Gauss point m	1	2	3
$\xi^i_{m,n}$	-0.387298	0	0.387298
H_m	0.277778	0.444444	0.277778

Table 2
The location and weight factors of Gauss points in the length direction

Gauss point n	1	2	3	4	5	6	7
$\zeta^i_{m,n}$	0.02545	0.12923	0.29708	0.5	0.70292	0.87077	0.97455
H_n	0.06474	0.13985	0.19092	0.20897	0.19092	0.13985	0.06474

2.2. Refined line-segment model with eccentricity at segment ends

Modeling tree-type sections like I-sections and T-sections using the line-segment approach poses a challenge in the conventional Coordinate Method [37], primarily due to overlapping areas between the flange and the web. A refined line-segment model is introduced to solve the problem by configuring eccentricities at the ends of segments as shown in Fig. 2. Eccentricities e^i_S and e^i_E, are introduced at the start and end of segment i (defined in the local z_i-o_i-y_i system) to eliminate overlap between intersecting plates (e.g., flange–web intersection). The sign of e^i_S and e^i_E follows the local axis convention (as illustrated, $e^s_i < 0$ and $e^e_i > 0$). The updated segment ending coordinates are obtained using Eqs. (3)–(6).

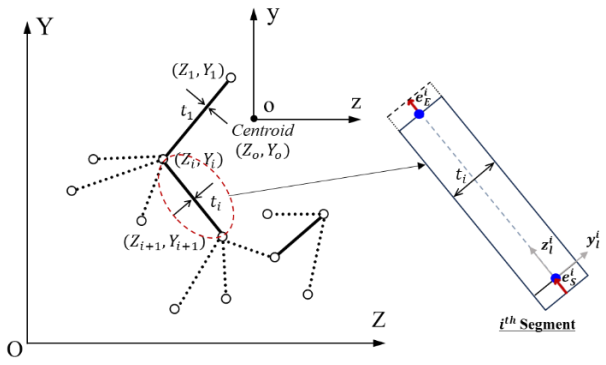

Fig. 2 Refined line-segment model with end eccentricities

The updated geometrical information of points and segments of the improved line-segment model can be obtained by following expressions.

$$Ye_E^i = \lambda_i e_E^i + Y_E^i \tag{3}$$

$$Ze_E^i = \mu_i e_E^i + Z_E^i \tag{4}$$

$$Ye_S^i = \lambda_i e_S^i + Y_S^i \tag{5}$$

$$Ze_E^i = \mu_i e_S^i + Z_S^i \tag{6}$$

where, Y_S^i, Z_S^i, Y_E^i and Z_E^i are used to define the start and end point coordinates of the i^{th} segment, as per the global axis system. These values represent the positioning of the points before considering the eccentricities. In addition, $\lambda_i = \frac{Y_E^i - Y_S^i}{L_i}$ and $\mu_i = \frac{Z_E^i - Z_S^i}{L_i}$ represent the projections of the length L_i in the horizontal and vertical directions, respectively.

2.3. Differences between the fiber-based section modeling and GSE section modeling

The proposed GSE section modeling streamlines geometry input by requiring only point coordinates, segment thickness, and relevant connection details. This simplification allows for the rapid creation of analysis models, circumventing complex modeling procedures. Conversely, the fiber-based model necessitates a more intricate approach that begins with the creation of an outline for the actual section by detailing coordinates of each corner point and loop information to form a closed geometric shape, followed by the implementation of a mesh algorithm to generate numerous fibers, each requiring the recording of centroid coordinates and cross-sectional area for analysis. The fiber-based method can be particularly cumbersome and time-consuming, especially when dealing with complex cross-sections. The proposed method eliminates the need for fiber meshing by employing a limited number of Gauss points to accelerate the procedure of the cross-sectional analysis.

From a numerical perspective, both the fiber-based model and the proposed GSE aim to evaluate the same sectional integrals (e.g., axial force, bending moments, and section properties) by sampling stress/strain over the cross-sectional area. The key difference lies in the sampling and integration strategy. The fiber-based method discretizes the cross-section into a large number of small area patches (fibers) and typically performs summation using low-order quadrature (often equivalent to midpoint/rectangular integration), such that accuracy improves primarily by increasing the number of fibers. In contrast, the proposed GSE represents each plate component by a line segment with an associated thickness and evaluates the sectional integrals using Gauss–Legendre quadrature points and weights distributed in the thickness and length directions of each segment. This strategy can achieve high integration accuracy with substantially fewer evaluation points, thereby improving computational efficiency while preserving accuracy for thin-walled steel sections.

3. Cross-sectional analysis using gse

3.1. Sectional property calculation

In arbitrary-shaped steel sections, the principal coordinate system of the cross-section, represented as the *w-o-v* axis in Fig. 1, is essential, especially for the nonsymmetrical sections [20]. This system incorporates an inclined angle, symbolized as φ, which determines the orientation between the geometric *y-o-z* coordinate system and the principal *w-o-v* coordinate system. The angle φ can be computed using the expression outlined below, which plays a crucial role in accurately defining the cross-sectional geometry.

$$\varphi = \frac{1}{2}\arctan\left(\frac{2I_{yz}}{I_y - I_z}\right) \tag{7}$$

in which, I_y, I_z and I_{yz} represent the cross-section moment of inertia along the respective axes. These values are crucial for understanding the stiffness properties of the arbitrary-shaped steel sections and can be calculated using the following equations:

$$\begin{aligned} I_z &= \int y^2 dA \\ &\doteq \frac{1}{3}\sum_{i=1}^{Ns} A_i\left(\left(Ye_S^i - Y_c\right)^2 + \left(Ye_S^i - Y_c\right)\left(Ye_E^i - Y_c\right) + \left(Ye_E^i - Y_c\right)^2\right) + \frac{1}{3}\sum_{i=1}^{Ns} A_{is}\left(\frac{t_i^2}{4}\mu_i^2\right) \\ &= \sum_{i=1}^{Ns}\frac{A_i}{3}\left(y_S^i y_S^i + y_S^i y_E^i + y_E^i y_E^i + \frac{t_i^2}{4}\mu_i^2\right) + \sum_{i=1}^{Ns}\lambda_i\frac{A_i}{3}\left(e_S^i e_S^i\lambda_i + e_E^i e_E^i\lambda_i + e_S^i e_E^i\lambda_i + 2y_S^i e_S^i + y_S^i e_E^i + y_E^i e_S^i + 2y_E^i e_E^i\right) \end{aligned} \tag{8}$$

$$\begin{aligned} I_y &= \int z^2 dA \\ &\doteq \frac{1}{3}\sum_{i=1}^{Ns} A_i\left(\left(Ze_S^i - Z_c\right)^2 + \left(Ze_S^i - Z_c\right)\left(Ze_E^i - Z_c\right) + \left(Ze_E^i - Z_c\right)^2\right) + \frac{1}{3}\sum_{i=1}^{Ns} A_i\left(\frac{t_i^2}{4}\lambda_i^2\right) \\ &= \sum_{i=1}^{Ns}\frac{A_i}{3}\left(z_S^i z_S^i + z_S^i z_E^i + z_E^i z_E^i + \frac{t_i^2}{4}\lambda_i^2\right) + \sum_{i=1}^{Ns}\lambda_i\frac{A_i}{3}\left(e_S^i e_S^i\mu_i + e_E^i e_E^i\mu_i + e_S^i e_E^i\mu_i + 2z_S^i e_S^i + z_S^i e_E^i + z_E^i e_S^i + 2z_E^i e_E^i\right) \end{aligned} \tag{9}$$

$$\begin{aligned} I_{yz} &= \int yz dA \\ &\doteq \frac{1}{6}\sum_{i=1}^{Ns} A_i\begin{pmatrix} 2\left(Ze_S^i - Z_c\right)\left(Ye_S^i - Y_c\right) + \left(Ze_S^i - Z_c\right)\left(Ye_E^i - Y_c\right) \\ + \left(Ze_E^i - Z_c\right)\left(Ye_S^i - Y_c\right) + 2\left(Ze_E^i - Z_c\right)\left(Ye_E^i - Y_c\right) \end{pmatrix} + \frac{1}{6}\sum_{i=1}^{Ns} A_i\left(\frac{t_i^2}{2}\lambda_i\mu_i\right) \\ &= \sum_{i=1}^{Ns}\frac{A_i}{6}\left(2z_S^i y_S^i + z_S^i y_E^i + z_E^i y_S^i + 2z_E^i y_E^i\right) + \sum_{i=1}^{Ns}\frac{A_i}{6}\left(\frac{t_i^2}{2}\lambda_i\mu_i\right) \\ &+ \sum_{i=1}^{Ns}\lambda_i\frac{A_i}{6}\left(2\lambda_i\mu_i\left(e_S^i + e_E^i\right)^2 + \left(\mu_i y_S^i + \lambda_i z_S^i\right)\left(2e_S^i + e_E^i\right) + \left(\mu_i y_E^i + \lambda_i z_E^i\right)\left(e_S^i + 2e_E^i\right)\right) \end{aligned} \tag{10}$$

where, N_s stands for the number of segments and A_i is the area of the i^{th} segment. Y_c and Z_c are the centroidal coordinates of the cross-section. The equations consider the eccentricities at both ends of each segment and the thickness of the section plate, overcoming the overlapping areas between the flange and the web in the conventional Coordinate Method. The inclusion of additional eccentricities in these calculations significantly improves the accuracy and

versatility in assessing the properties of various steel sections. It is important to note that the calculations for the warping constant and torsional constant in this study rely on the thin-walled assumption. Detailed expressions for these section properties can be found in the referenced literatures [20, 38].

3.2. Yield surface generation

In this research, the GSE is adapted to generate the full yield surface of the arbitrary-shaped steel sections to improve the computational efficiency. In accordance with the Euler-Bernoulli hypothesis, there is a linear strain distribution along the vertical direction of the entire section, as illustrated in Fig. 3. For strains within the elastic limit, the strain-stress relationship remains linear, permitting the use of Hooke's Law for stress determination. However, when strain exceeds the elastic limit, stress must be calculated using the material's specific strain-stress curve. The full yield surface of the arbitrary-shaped steel sections referring to the principal axis system *w-o-v* can be effectively determined using equations derived for the GSE, offering a viable alternative to the fiber model.

$$P_x = \int_A f_s(\varepsilon)dA = \int_w \int_v f_s(\varepsilon)dwdv = \sum_{i=1}^{Ns}\sum_{m=1}^{3}\sum_{n=1}^{7} H_m t_i H_n L_i f_s(\varepsilon_{m,n}^i) \tag{11}$$

$$M_w = \int_A f_s(\varepsilon)(v-v_n)dA = \int_w \int_v f_s(\varepsilon)(v-v_n)dwdv = \sum_{i=1}^{Ns}\sum_{m=1}^{3}\sum_{n=1}^{7} H_m t_i H_n L_i f_s(\varepsilon_{m,n}^i)(v_{m,n}^i - v_n) \tag{12}$$

$$M_v = \int_A f_s(\varepsilon)(w-w_n)dA = \int_w \int_v f_s(\varepsilon)(w-w_n)dwdv = \sum_{i=1}^{Ns}\sum_{m=1}^{3}\sum_{n=1}^{7} H_m t_i H_n L_i f_s(\varepsilon_{m,n}^i)(w_{m,n}^i - w_n) \tag{13}$$

in which, P_x, M_v and M_w represent the ultimate axial and bending capacities of the section, respectively; $f_s(\varepsilon)$ denotes the stress-strain relationship for the material. v_n and w_n denote the coordinates of the neutral axis in the *v-o-w* axis system; $v_{m,n}^i$ and $w_{m,n}^i$ are the coordinates of the Gauss point situated in the m^{th} row and n^{th} column on the i^{th} segment, and $\varepsilon_{m,n}^i$ represents the strain at the corresponding Gauss point, which can be determined using the following calculation:

$$\varepsilon_{m,n}^i = \varepsilon_u d_{m,n}^i / d_n \tag{14}$$

in which, ε_u represents the ultimate strain at the topmost part of the entire section; d_n is the depth of the neutral axis, as shown in Fig. 3, under a specified axial load level.

To acquire the data points of the full-yield surface, the interactive curve of M_v versus M_w under varying axial loads P_a will be calculated, ranging from minimum to maximum axial strengths. This process involves rotating the inclined angle between the principal axis and the neutral axis from 0 to 2π. In this context, the ultimate strain ε_u in the vertical direction is assumed to be the edge yield strain. The depth of the neutral axis, d_n, can be determined using the Quasi-Newton algorithm.

$$d_n^{k+1} = d_L^{k+1} + \frac{d_U^k - d_L^k}{P_U^k - P_L^k}\left(P_a - P_L^k\right) \tag{15}$$

in which, d_n^{k+1} represents the depth of the neutral axis in the subsequent iteration. d_U^k and d_L^k denote the depths of the neutral axis when the axial strengths are less than and greater than P_a, respectively. P_U^k and P_L^k denote the axial resistances calculated using d_U^k and d_L^k. Upon determining the depth of the neutral axis under a specified axial load, one data point of the full yield surface can be obtained through Eqs. (9)-(11).

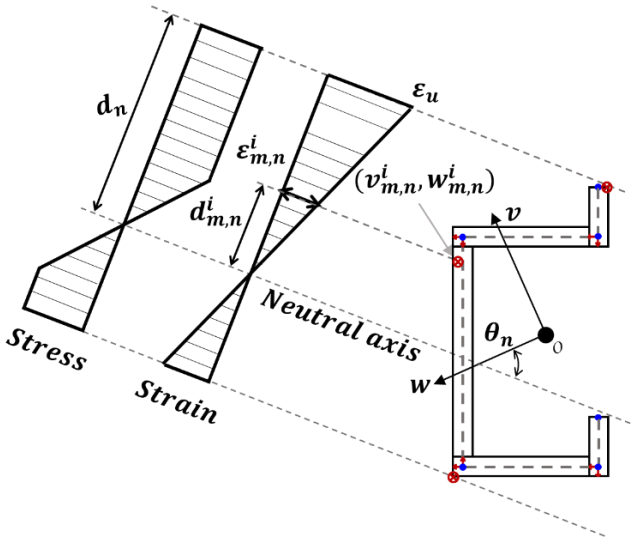

Fig. 3 Assumed strain/stress distribution for yield-surface generation

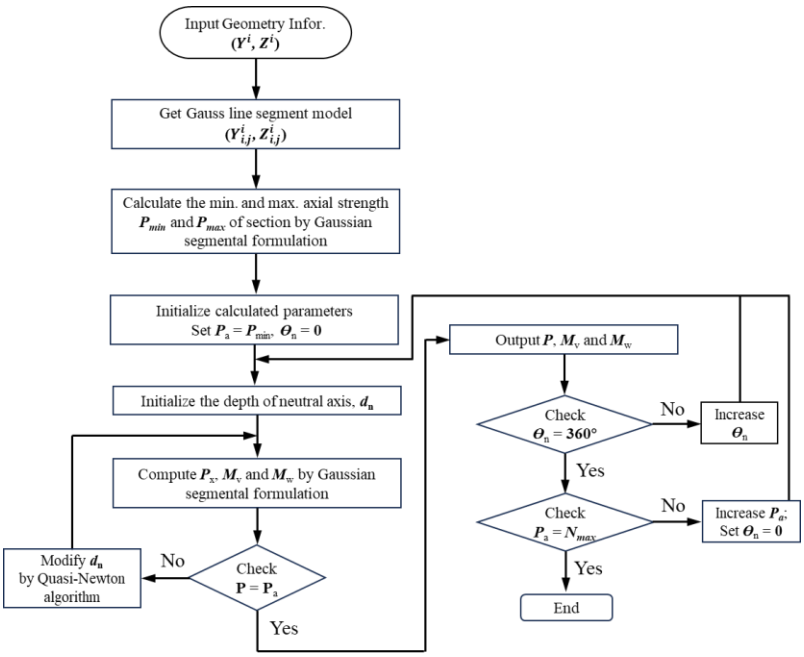

Fig. 4 Flowchart of the full-yield surface generation by Gaussian line-segment model

The analysis flowchart for generating the full yield surface using the GSE formulation is depicted in Fig. 4, successfully implemented in MSASect2 [39]. As shown in the flowchart, the analysis begins with inputting basic geometric data, such as the coordinates of points in the line-segment model. Following this, the Gaussian line-segment model, as proposed in this study, is employed, obviating the necessity for mesh generation. The minimum (tension) and maximum (compression) axial capacities of the section will be subsequently calculated.

Following this, and based on the axial load step setting, the initial axial load P_a is set as the minimum axial capacity. At this axial load level, the inclined angle of the neutral axis, θ_n changes from 0 to 2π. The section's moment capacities (M_v and M_w) are then calculated at each angle. This procedure is repeated for various axial load levels, incrementally increasing from the minimum to the maximum axial capacity. By conducting these calculations, a series of data points are generated, which collectively create the complete yield surface for the arbitrary-shaped steel sections.

3.3. Moment-thrust-curvature calculation

For the moment-thrust-curvatures analysis using the GSE formulation, a combination of the displacement-based method and the Quasi-Newton approach is utilized in the incremental and iterative procedures. The process begins by determining the axial strain of the section under a given axial load. Subsequently, the strain at the extreme Gauss point of the Gaussian line-segment model is incrementally increased until the ultimate strength is reached. Concurrently, the location of the neutral axis is ascertained at each strain increment, enabling the calculation of the corresponding curvature and moment resistance. The initial axial strain of the section under axial load P_a can be calculated using the following iterative procedure.

$$\varepsilon_n^{k+1} = \varepsilon_L^{k+1} + \frac{\varepsilon_U^k - \varepsilon_L^k}{P_U^k - P_L^k}\left(P_a - P_L^k\right) \tag{16}$$

where, ε_n^{k+1} represents the strain of the section at the next iterative step. ε_L^k and ε_U^k are the strains from the previous iterative step, with the resistances being less and more than the applied axial load P_a, respectively.

Additionally, a similar iteration algorithm can be utilized to compute the location of the neutral axis, d_n, as per Eq. (13). Following this, the moment resistance of the section can be determined using the stress integration method, as expressed in Eqs. (10) or (11), while applying the Gauss segmental formulation. The corresponding curvature of the section can be calculated using the following formula.

$$\phi^i = \varepsilon_T^i / d_n^i \tag{17}$$

in which, ε_T^i represents the strain of the section top at the i^{th} moment step, which increments from the initial strain ε_a under the applied axial load P_a to the ultimate strain of steel. Utilizing the incremental procedure, the complete moment versus curvature curve under the applied axial load P_a can be obtained.

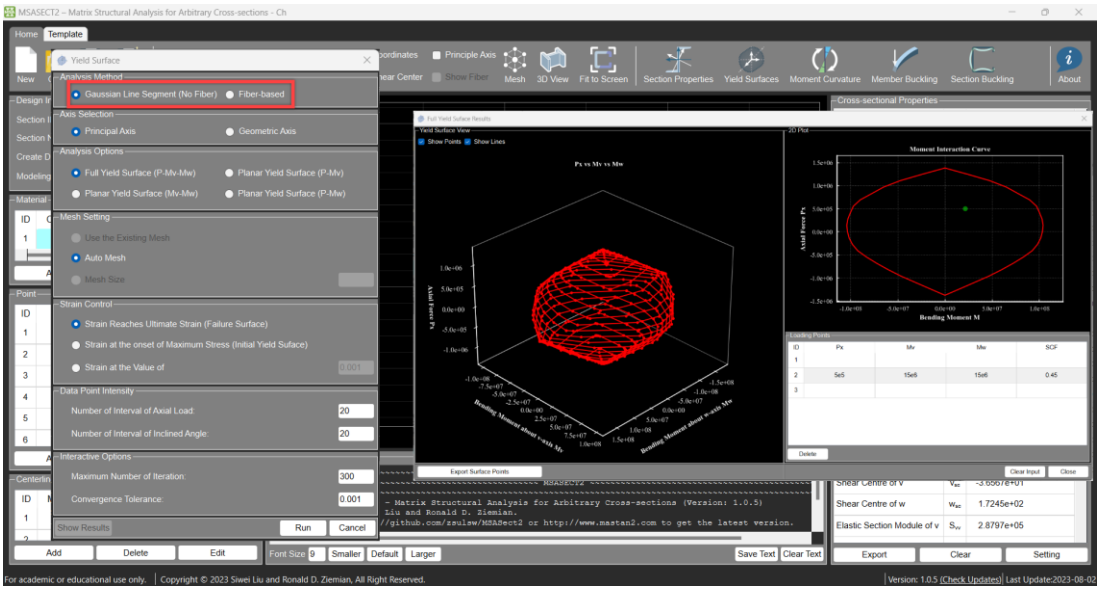

Fig. 5 Yield surface module in MSASect2 [39]

4. Numerical implementation

The cross-sectional analyses approach using the GSE has been effectively integrated into the educational cross-sectional analysis software MSASect2 [39]. Developed by the second author in collaboration with their team, this software is equipped with robust analysis features. These include assessments of cross-sectional properties, yield surfaces, moment-thrust-curvature relationships, member buckling strength, and section buckling strength. With the incorporation of the GSE formulations, MSASect2 [39] now facilitates more extensive analyses and comparative studies. Fig. 5 showcases the software's user-friendly interface, specifically designed for the yield surface function. It allows users to choose between the traditional fiber-based method and the Proposed GSE approach. This interface significantly enhances the practicality of MSASect2 [39], empowering users to efficiently compare and assess different methodologies for analyzing yield surfaces.

5. Validation examples

This section presents three sets of examples to demonstrate the accuracy and efficiency of the proposed method using GSE for the cross-sectional analysis of arbitrary-shaped steel sections. Section properties, yield surfaces, and moment-thrust-curvature curves for several arbitrary-shaped steel sections are calculated and compared with those from the fiber-based model. All computational times reported in this paper were measured on a Dell Precision 3660 workstation (Windows 11 Home, Version 10.0.22631 Build 22631; Intel Core i9-12900K, 16 cores/24 threads, 3.2 GHz base), and both the fiber-based and GSE-based models were executed under identical software settings to ensure a fair comparison.

5.1. Example 1 – Validation of section properties calculation

In this example, the proposed GSE is employed to calculate various geometrical properties for arbitrary-shaped sections with open- and closed-section shapes. While basic cross-sectional properties such as area (A), moments of inertia about geometrical axes (I_y and I_z), warping constant (I_ω), and torsional rigidity (J), are usually straightforward to be calculated, advanced geometrical properties mainly related to nonsymmetrical sections (i.e., Wagner coefficients, β_v, β_w and β_ω as well as the shear center coordinates Y_S and Z_S) are crucial and require further consideration. Accordingly, four sectional shapes, as shown in Fig. 6, are analyzed to show the reliability of the proposed algorithm.

Tables 3-6 present comparisons between the results obtained from the present study and those from the fiber-based model (benchmarks) and traditional Coordinate Method [37]. The proposed algorithm demonstrates

reliability and efficiency, as it yields almost identical results for all section types compared to the fiber-based model with much less computational time. In addition, the proposed method can calculate the basic cross-sectional properties such as area (A) and moments of inertia about geometrical axes (I_y and I_z) more accurately compares to the traditional Coordinate Method.

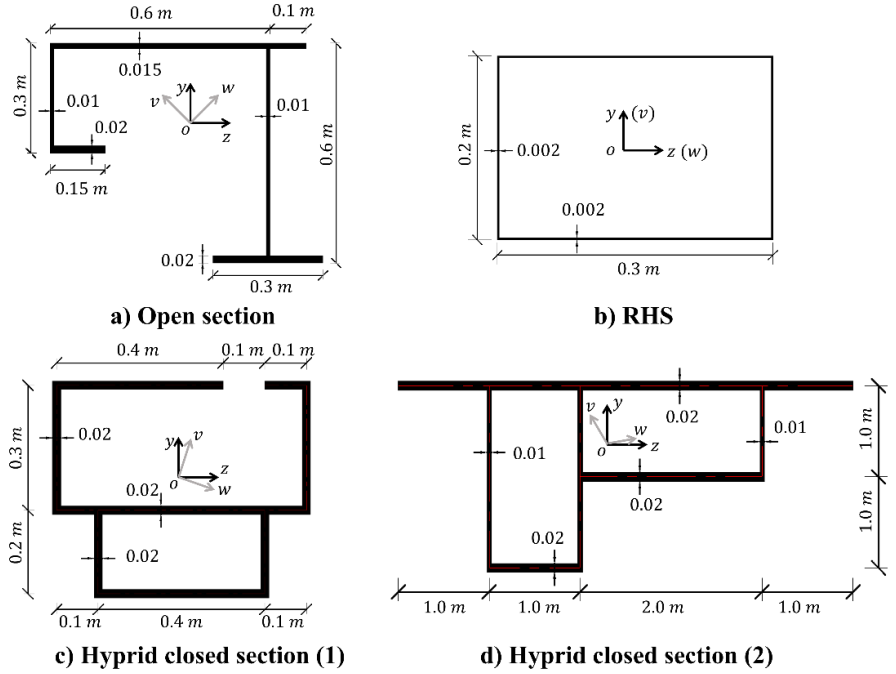

Fig. 6 Schematic diagram of cross-section shapes investigated

Table 3
Section properties for section a

Parameter	Fiber-based model	Coordinate Method	Diff.	Present Study	Diff.
Computational time (sec.)	0.91	Less than 0.01	-	Less than 0.01	-
A (m^2)	2.833E-02	2.850E-02	0.60%	2.832E-02	0.04%
I_y (m^4)	1.772E-03	1.779E-03	0.40%	1.772E-03	0.00%
I_z (m^4)	1.625E-03	1.642E-03	1.05%	1.627E-03	-0.12%
J (m^4)	2.278E-06	2.288E-06	0.44%	2.281E-06	-0.13%
I_w (m^6)	9.246E-05	9.258E-05	0.13%	9.258E-05	-0.13%
Y_s (m)	4.232E-01	4.232E-01	0.00%	4.232E-01	0.00%
Z_s (m)	-1.161E-01	-1.161E-01	0.00%	-1.162E-01	-0.09%
ϕ	4.189E+01	4.211E+01	0.53%	4.210E+01	-0.50%
β_v (m)	-4.370E-01	-4.390E-01	0.46%	-4.387E-01	-0.39%
β_w (m)	9.290E-01	9.280E-01	-0.11%	9.282E-01	0.09%
β_ω	-1.065E-01	-1.059E-01	-0.56%	-1.058E-01	0.66%

Table 4
Section properties for section b

Parameter	Fiber-based model	Coordinate Method	Diff.	Present Study	Diff.
Computational time (sec.)	0.25	Less than 0.01	-	Less than 0.01	-
A (m^2)	1.984E-03	1.984E-03	0.00%	1.984E-03	0.00%
I_y (m^4)	2.641E-05	2.640E-05	-0.04%	2.640E-05	-0.04%
I_z (m^4)	1.427E-05	1.427E-05	0.00%	1.427E-05	0.00%
J (m^4)	2.823E-05	2.808E-05	-0.53%	2.812E-05	-0.39%
I_w (m^6)	5.984E-09	5.849E-09	-2.26%	5.889E-09	-1.59%
Y_s (m)	0.0	0.0	-	0.0	-
Z_s (m)	0.0	0.0	-	0.0	-
ϕ	0.0	0.0	-	0.0	-
β_v (m)	0.0	0.0	-	0.0	-
β_w (m)	0.0	0.0	-	0.0	-
β_ω	0.0	0.0	-	0.0	-

Table 5
Section properties for section c

Parameter	Fiber-based model	Coordinate Method	Diff.	Present Study	Diff.
Computational time (sec.)	0.09	Less than 0.01	-	Less than 0.01	-
$\boldsymbol{A}$ (m^2)	4.960E-02	5.000E-02	0.81%	4.960E-02	0.00%
$\boldsymbol{I_y}$ (m^4)	2.166E-03	2.179E-03	0.60%	2.178E-03	0.55%
$\boldsymbol{I_z}$ (m^4)	1.573E-03	1.572E-03	-0.06%	1.571E-03	-0.13%
$\boldsymbol{J}$ (m^4)	4.491E-04	4.333E-04	-3.52%	4.330E-04	-3.58%
$\boldsymbol{I_w}$ (m^6)	1.823E-04	1.812E-04	-0.60%	1.812E-04	-0.60%
$\boldsymbol{Y_s}$ (m)	-2.741E-01	-2.741E-01	0.00%	-2.742E-01	0.04%
$\boldsymbol{Z_s}$ (m)	1.674E-01	1.674E-01	0.00%	1.675E-01	0.06%
$\boldsymbol{\phi}$	-7.000E+00	-7.000E+00	0.00%	-6.997E+00	-0.04%
$\boldsymbol{\beta_v}$ (m)	-2.659E-01	-2.680E-01	0.79%	-2.682E-01	0.86%
$\boldsymbol{\beta_w}$ (m)	-6.778E-01	-6.732E-01	-0.68%	-6.734E-01	-0.65%
$\boldsymbol{\beta_\omega}$	1.543E-01	1.535E-01	-0.52%	1.535E-01	-0.52%

Table 6
Section properties for section d

Parameter	Fiber-based model	Coordinate Method	Diff.	Present Study	Diff.
Computational time (sec.)	0.92	Less than 0.01	-	Less than 0.01	-
$\boldsymbol{A}$ (m^2)	2.096E-01	2.100E-01	0.19%	2.096E-01	0.00%
$\boldsymbol{I_y}$ (m^4)	3.224E-01	3.229E-01	0.16%	3.228E-01	0.12%
$\boldsymbol{I_z}$ (m^4)	1.022E-01	1.023E-01	0.10%	1.023E-01	0.10%
$\boldsymbol{J}$ (m^4)	9.265E-02	9.265E-02	0.00%	9.265E-02	0.00%
$\boldsymbol{I_w}$ (m^6)	1.333E-02	1.333E-02	0.00%	1.333E-02	0.00%
$\boldsymbol{Y_s}$ (m)	1.570E-01	1.571E-01	0.06%	1.571E-01	0.06%
$\boldsymbol{Z_s}$ (m)	-3.660E-01	-3.660E-01	0.00%	-3.660E-01	0.00%
$\boldsymbol{\phi}$	8.058E+01	8.058E+01	0.00%	8.058E+01	0.00%
$\boldsymbol{\beta_v}$ (m)	7.978E-01	7.910E-01	-0.85%	7.930E-01	-0.60%
$\boldsymbol{\beta_w}$ (m)	2.896E-01	2.935E-01	1.35%	2.932E-01	1.24%
$\boldsymbol{\beta_\omega}$	-1.762E+00	-1.775E+00	0.74%	-1.775E+00	0.74%

5.2. Example 2 – Validation of yield surface generation

This example presents an evaluation of the proposed method for generating yield surfaces for arbitrary-shaped steel sections, as illustrated in Fig. 7. Four sections are considered: an L-section, a T-section, a lipped channel section, and an irregular open section. These sections are modelled using the proposed method GSE, in which three and seven Gauss points are used along the thickness and length direction of a segment. The yield curves (i.e., p-m_y, p-m_z, m_z-m_y, p-m_v, p-m_w, and m_v-m_w) are plotted in Figs. 8-11, with y-z and v-w representing the geometric and principal axes, respectively. For comparison purposes, the results from the fiber-based cross-sectional analysis method [8] and equations given by ANSI/AISC-360-16 [30] and McGuire et al. [6] are also provided.

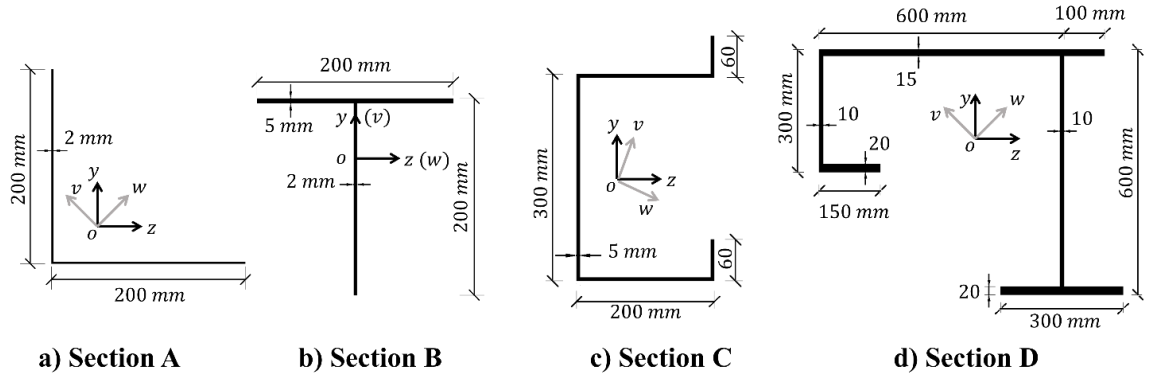

Fig. 7 Typical nonsymmetrical sections for generation of yield surface

The results presented in Figs. 8-11 show that the proposed algorithm can accurately generate yield surfaces that closely match those obtained from the advanced fiber-based model [8]. This demonstrates that the commonly used number of Gauss points for integration is sufficient and that further increasing the number of Gauss points, with additional computational effort, can yield more convergent results. Notably, the proposed method obtains these results with significantly reduced computational time compared to the fiber-based model. From a practical standpoint, reduced computational time is most beneficial when yield surfaces must be generated repeatedly, such as in parametric studies of arbitrary/built-up sections, design iterations and optimization, or when assessing multiple member types within a project. Although the time saving for a single section may appear modest in absolute terms, the computational benefit accumulates quickly when the yield surface is sampled over many axial-load levels and neutral-axis orientations. The

consistent time reductions observed in the validation studies (e.g., Table 7 for moment–thrust–curvature calculations) indicate that the proposed approach can improve analysis throughput without compromising accuracy.

Conversely, the calculation methods proposed by ANSI/AISC-360-16 [30] and McGuire et al. [6] are not suitable for analyzing nonsymmetrical sections. The former relies on conservative linear interaction curves for the yield surface, which tends to fall inside the precisely generated yield surface. Meanwhile, the equation provided by McGuire et al. [6] occasionally overestimates section capacities, as illustrated in Fig. 8 for equal leg angle sections.

Based on the findings presented in Figs. 8-11, this example provides additional evidence supporting the efficiency and reliability of the proposed method for modeling nonsymmetrical sections and accurately generating their yield surfaces. In contrast, existing calculation methods, such as those described in ANSI/AISC-360-16 [31] and McGuire et al. [6], are insufficient when dealing with arbitrary-shaped steel sections. The results obtained from the proposed method provide further evidence of its accuracy and computational efficiency over these existing methods, further highlighting the importance of employing more advanced and specialized techniques for accurate analysis of yield surfaces in such cases.

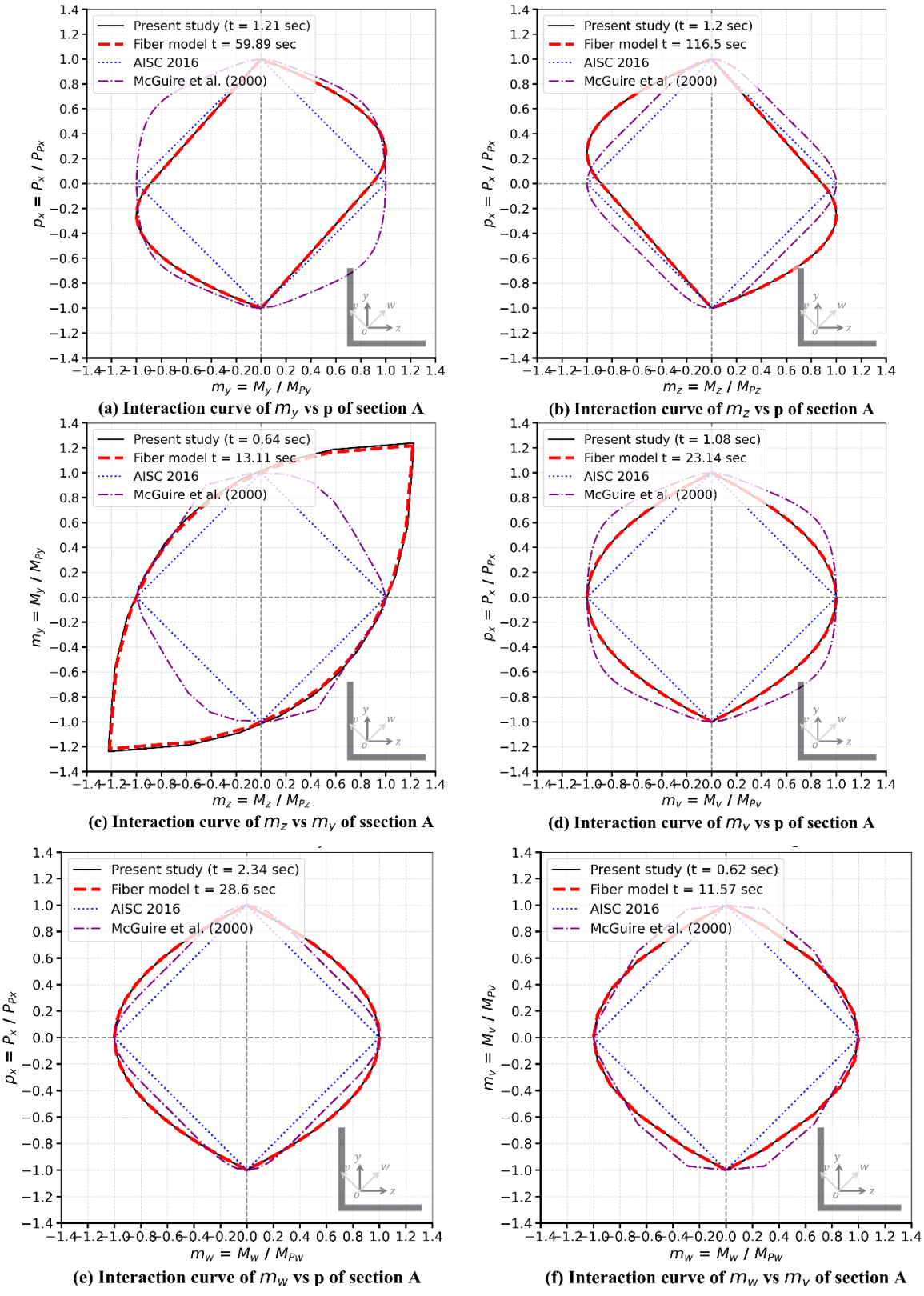

(a) Interaction curve of m_y vs p of section A

(b) Interaction curve of m_z vs p of section A

(c) Interaction curve of m_z vs m_y of ssection A

(d) Interaction curve of m_v vs p of section A

(e) Interaction curve of m_w vs p of section A

(f) Interaction curve of m_w vs m_v of section A

Fig. 8 Comparison results for the yield surface of section A

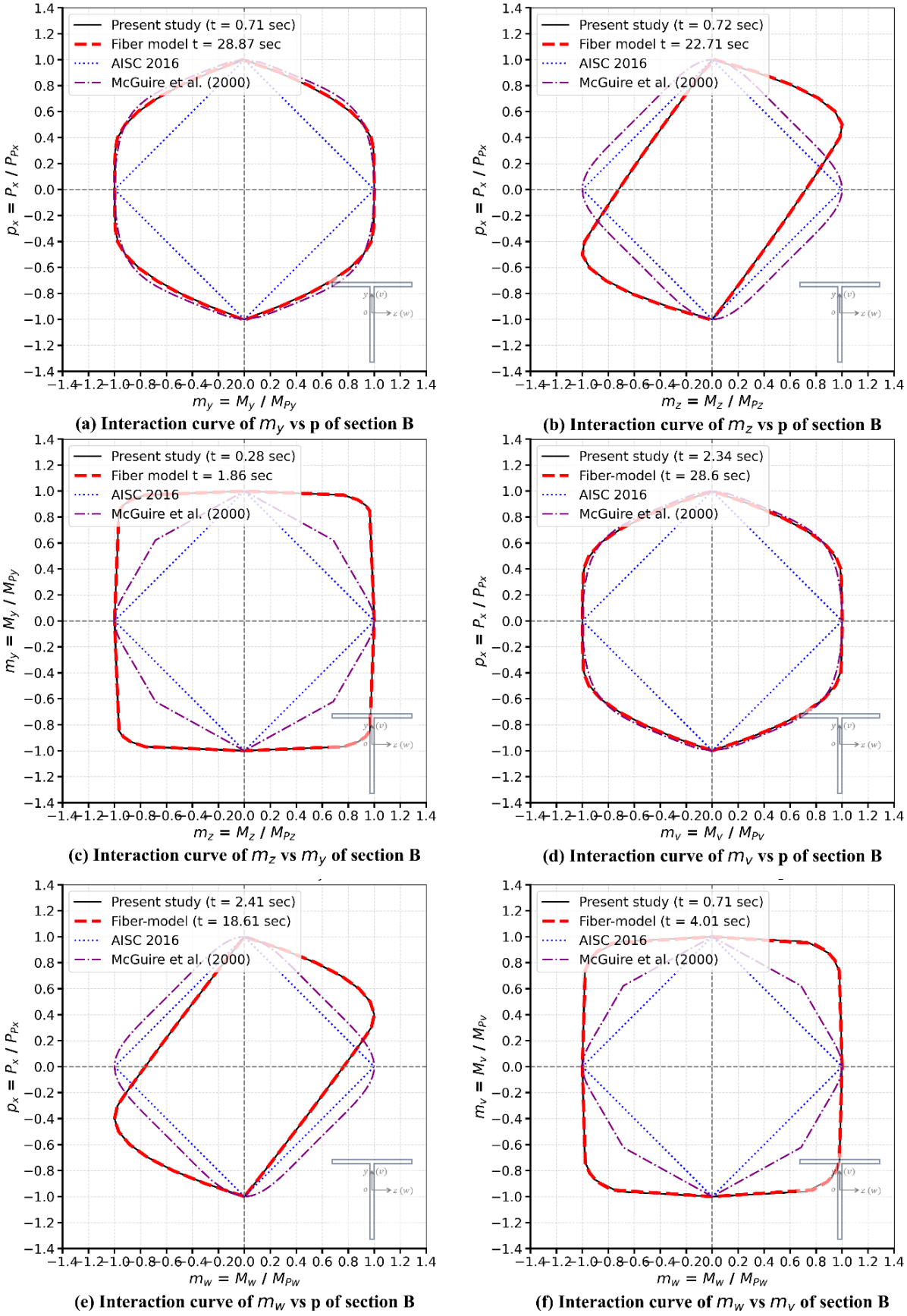

(a) Interaction curve of m_y vs p of section B

(b) Interaction curve of m_z vs p of section B

(c) Interaction curve of m_z vs m_y of section B

(d) Interaction curve of m_v vs p of section B

(e) Interaction curve of m_w vs p of section B

(f) Interaction curve of m_w vs m_v of section B

Fig. 9 Comparison results for the yield surface of section B

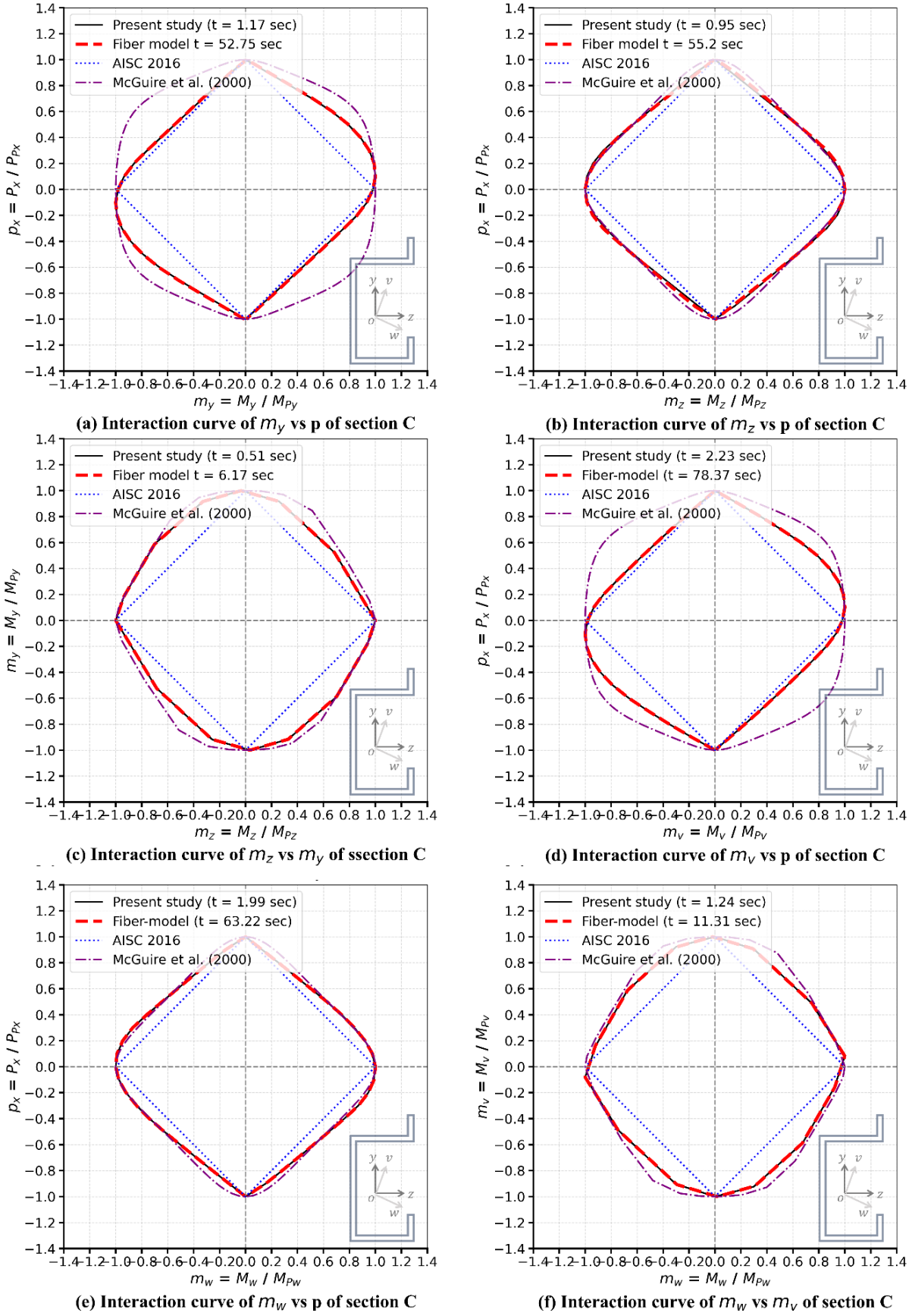

(a) Interaction curve of m_y vs p of section C

(b) Interaction curve of m_z vs p of section C

(c) Interaction curve of m_z vs m_y of ssection C

(d) Interaction curve of m_v vs p of section C

(e) Interaction curve of m_w vs p of section C

(f) Interaction curve of m_w vs m_v of section C

Fig. 10 Comparison results for the yield surface of section C

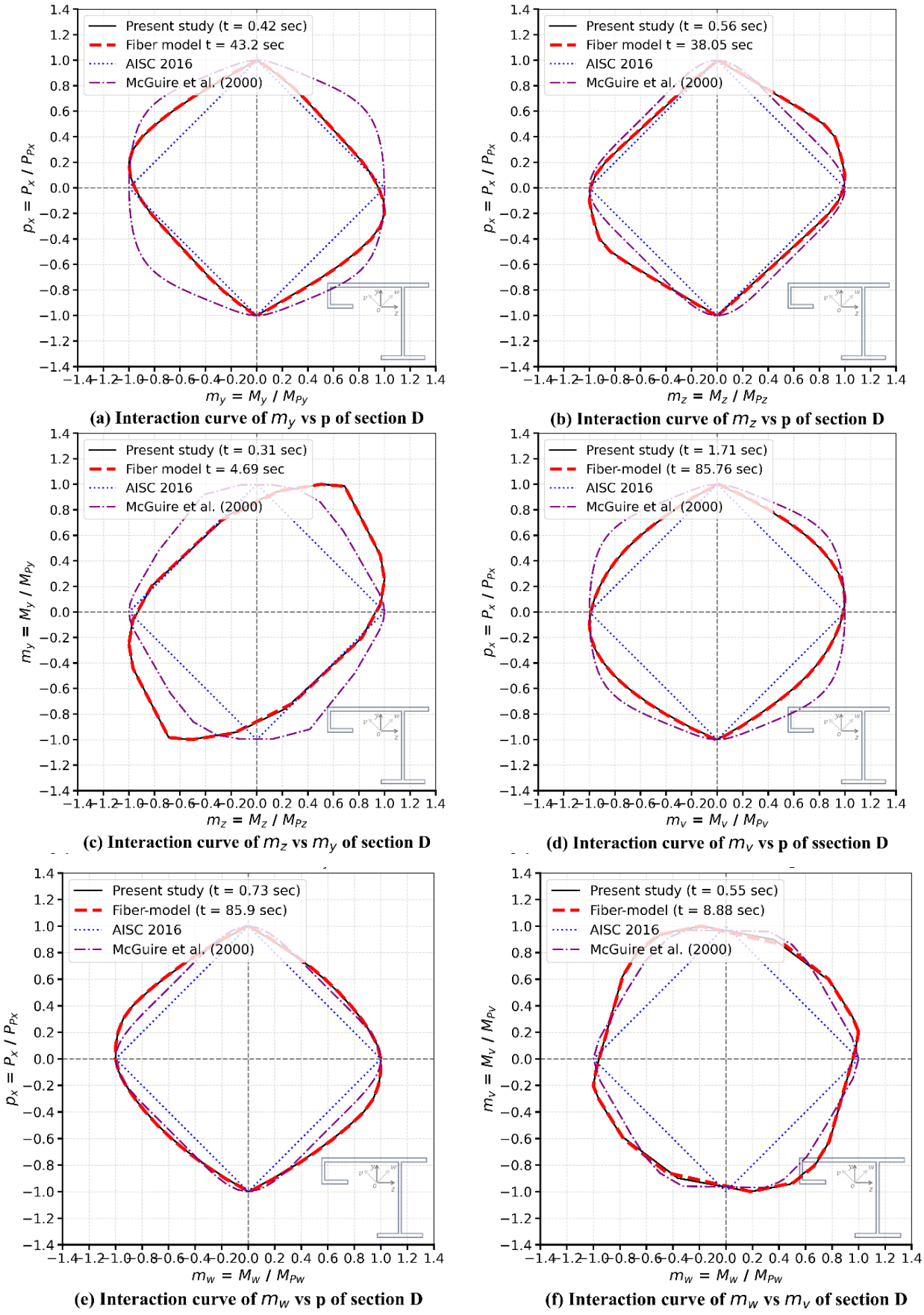

Fig. 11 Comparison results for the yield surface of section D

5.3. Example 3 – Validation of moment-thrust-curvature calculation

In this example, the moment-thrust-curvatures of three different sections (Fig. 12) are investigated to evaluate the accuracy and validity of the proposed method GSE. Similar to the previous example, three Gauss points are used along the thickness and seven along the length of each segment. The sections are analyzed using a bi-linear steel material model with Young's modulus of 200 GPa. Moment-curvature curves under different axial loads (0, 0.1Py, 0.2Py, 0.4Py, 0.6Py, and 0.8Py, with Py denoting the cross-sectional axial capacity) are provided. The comparative results are given in Figs. 13-15, where M_y and φ_y, indicate the initial yield moment and curvature, respectively. Results from the fiber-based method introduced by Chen et al. [11] and SE::MC [31] serve as the benchmark. In addition, results from the closed-form solutions introduced by Chen and Atsuta [32] for I-sections are also provided in Fig. 13.

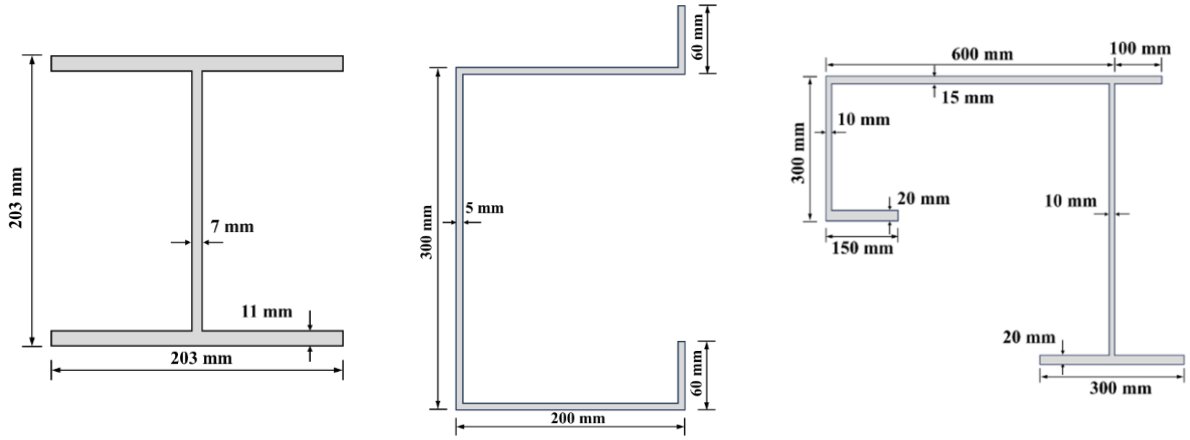

(a) W8x31 **(b) Lipped channel section** **(c) Irregular open section**

Fig. 12 The dimensions of the analyzed sections

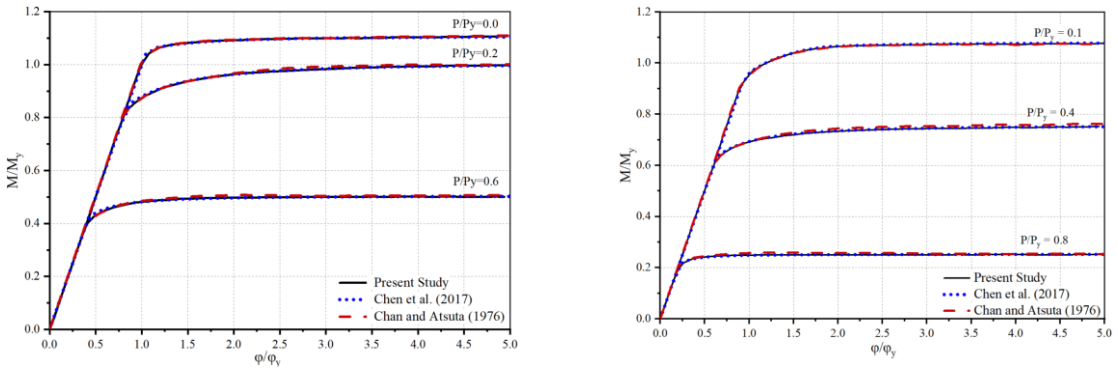

(a) P/Py = 0.0, 0.2, and 0.6 **(b) P/Py = 0.1, 0.4, and 0.8**

Fig. 13 Moment-thrust-curvatures of W8x31

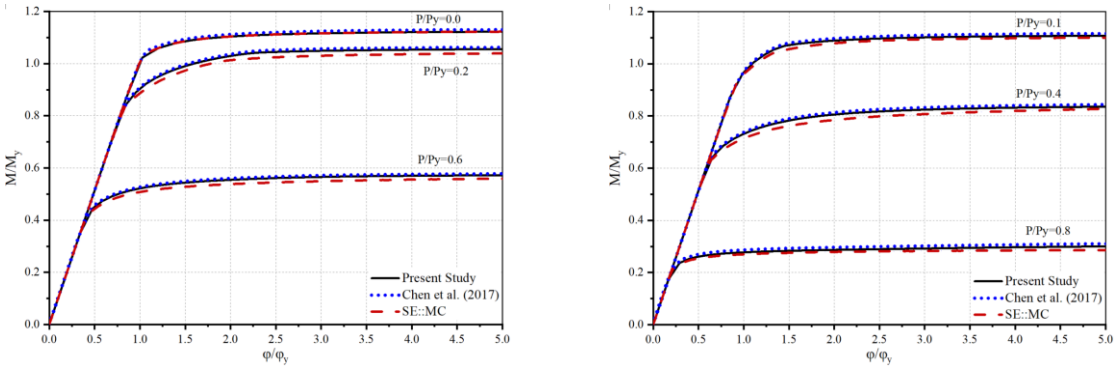

(a) P/Py = 0.0, 0.2, and 0.6 **(b) P/Py = 0.1, 0.4, and 0.8**

Fig. 14 Moment-thrust-curvatures of the lipped channel section

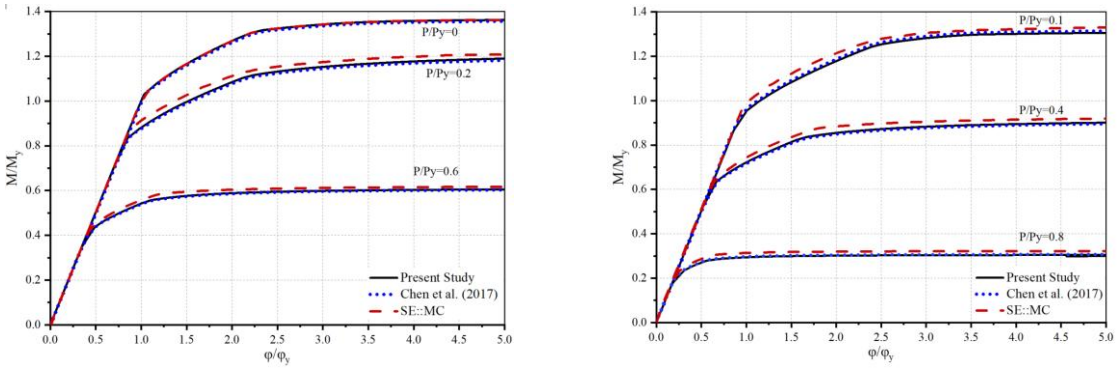

(a) P/Py = 0.0, 0.2, and 0.6 **(b) P/Py = 0.1, 0.4, and 0.8**

Fig. 15 Moment-thrust-curvatures of the irregular open section

Table 7
The computational time for fibre-based and proposed model

Section	P/Py	Fiber-based model (sec.)	Present Study (sec.)	Time reduction
(a) W8x31	0.0	2.03	0.43	78.8%
	0.1	1.58	0.46	70.9%
	0.2	2.71	0.98	63.8%
	0.4	2.17	0.72	66.8%
	0.6	3.02	1.71	43.4%
	0.8	2.86	1.21	57.7%
(b) Lipped channel section	0.0	1.93	0.51	73.6%
	0.1	1.53	0.52	66.0%
	0.2	2.39	0.96	59.8%
	0.4	2.15	0.79	63.3%
	0.6	2.89	1.61	44.3%
	0.8	2.21	1.46	33.9%
(c) Irregular open section	0.0	1.78	0.56	68.5%
	0.1	1.97	0.63	68.0%
	0.2	2.13	0.83	61.0%
	0.4	2.47	0.78	68.4%
	0.6	2.92	1.21	58.6%
	0.8	3.04	1.04	65.8%

Note: timings were obtained on the same workstation under identical software settings

The moment-thrust-curvatures obtained from the proposed method using GSE closely matched those from the fiber-based model using less computational time (Table 7). Based on these results, the proposed method using GSE has been demonstrated to be highly efficient, accurate, and reliable for the moment-thrust-curvature generation of arbitrary-shaped steel sections.

6. Conclusion

This paper proposes a Gaussian segmental element (GSE) framework for efficient cross-sectional analysis of arbitrary-shaped steel sections. This method employs a mesh-free line-segment representation with Gaussian quadrature for stress integration and introduces a refined line-segment model with end eccentricities to address overlap issues in tree-type geometries and improve geometric representation. Complete formulations and numerical procedures are presented and implemented in MSASect2, enabling the calculation of cross-section properties, full yield surfaces, and moment–thrust–curvature relationships. Validation against established benchmarks demonstrates that the proposed approach can deliver accurate sectional responses for a range of open and closed, symmetric and nonsymmetric sections, while reducing the computational effort associated with conventional fiber discretization. Future work will focus on (i) extending the geometric modeling to curved boundaries via segment refinement strategies, (ii) developing adaptive rules for segment subdivision and Gauss-point selection for highly localized response, and (iii) incorporating more general torsion/warping property evaluation for cases where thin-walled assumptions are not appropriate, together with broader validations for additional section families and material models.

Acknowledgement

The work described in this paper was partially supported by grants from the Research Grants Council of the Hong Kong Special Administrative Region through the projects "INTACT: Intelligent tropical-storm-resilient system for coastal cities (T22-501/23-R)" and " Second-order direct analysis for the design of steel members with irregular cross-sections (PolyU/21E/15203121)". Additional support was provided by the Department of Civil and Environmental Engineering at The Hong Kong Polytechnic University through the project "Development of Next-generation Sustainable Steel Construction using Built-up CFS Members (G-UAP3)", The third author is grateful for financial support from Mansoura University research unit for the project “Solar Energy Storage System Using a Medium of Sustainable Geopolymer Concrete” (MU-Eng-22-15).

References

[1] P. Waldron, "Sectorial properties of straight thin-walled beams," *Computers & Structures,* vol. 24, no. 1, pp. 147-156, 1986/01/01/ 1986. doi: https://doi.org/10.1016/0045-7949(86)90344-5

[2] Y. Chai Hong and S. V. Acra, "Cross-sectional properties of thin-walled multi-cellular section," *Computers & Structures,* vol. 22, no. 1, pp. 53-61, 1986/01/01/ 1986. doi: https://doi.org/10.1016/0045-7949(86)90084-2

[3] T. J. Li, S. W. Liu, and S. L. Chan, "Cross-sectional analysis of arbitrary sections allowing for residual stresses," *Steel and Composite Structures,* vol. 18, no. 4, pp. 985-1000, 2015.

[4] S. Abdelmageed and T. Zayed, "A study of literature in modular integrated construction - Critical review and future directions," *Journal of Cleaner Production,* vol. 277, p. 124044, 2020/12/20/ 2020. doi: https://doi.org/10.1016/j.jclepro.2020.124044

[5] X. Du and J. F. Hajjar, "Three-dimensional nonlinear mixed 6-DOF beam element for thin-walled members," *Thin-Walled Structures,* vol. 164, p. 107817, 2021/07/01/ 2021. doi: https://doi.org/10.1016/j.tws.2021.107817

[6] W. McGuire, a. R. H. Gallagher, and R. D. Ziemian, *Matrix Structural Analysis, 2nd Edition (Faculty Books. 7.)*. 2000.

[7]S.-W. Liu, Y.-P. Liu, and S.-L. Chan, "Advanced analysis of hybrid steel and concrete frames: Part 1: Cross-section analysis technique and second-order analysis," *Journal of Constructional Steel Research,* vol. 70, pp. 326-336, 2012/03/01/ 2012. doi: https://doi.org/10.1016/j.jcsr.2011.09.003

[8] L. Chen, W.-L. Gao, S.-W. Liu, R. D. Ziemian, and S.-L. Chan, "Geometric and material nonlinear analysis of steel members with nonsymmetric sections," *Journal of Constructional Steel Research,* vol. 198, p. 107537, 2022/11/01/ 2022. doi: https://doi.org/10.1016/j.jcsr.2022.107537

[9] L. Duan, J. T. Loh, and W. F. Chen, "Moment-Curvature Relationships for Dented Tubular Sections," *Journal of Structural Engineering,* vol. 119, no. 3, pp. 809-830, 1993/03/01 1993. doi: 10.1061/(ASCE)0733-9445(1993)119:3(809)

[10] A. Liew, L. Gardner, and P. Block, "Moment-Curvature-Thrust Relationships for Beam-Columns," *Structures,* vol. 11, pp. 146-154, 2017/08/01/ 2017. doi: https://doi.org/10.1016/j.istruc.2017.05.005

[11] L. Chen, S. W. Liu, and S. L. Chan, "Divergence-free algorithms for moment-thrust-curvature analysis of arbitrary sections," *Steel and Composite Structures,* vol. 25, pp. 557-569, December10 2017 2017.

[12] M. Mohareb and F. Nowzartash, "Exact Finite Element for Nonuniform Torsion of Open Sections," *Journal of Structural Engineering,* vol. 129, no. 2, pp. 215-223, 2003/02/01 2003. doi: 10.1061/(ASCE)0733-9445(2003)129:2(215)

[13] K. Saadé, B. Espion, and G. Warzée, "Discussion of “Exact Finite Element for Nonuniform Torsion of Open Sections” by Magdi Mohareb and Farhood Nowzartash," *Journal of Structural Engineering,* vol. 130, no. 9, pp. 1420-1420, 2004/09/01 2004. doi: 10.1061/(ASCE)0733-9445(2004)130:9(1420)

[14] M. Mohareb and F. Nowzartash, "Closure to “Exact Finite Element for Nonuniform Torsion of Open Sections” by Magdi Mohareb and Farhood Nowzartash," *Journal of Structural Engineering,* vol. 130, no. 9, pp. 1420-1421, 2004/09/01 2004. doi: 10.1061/(ASCE)0733-9445(2004)130:9(1420.2)

[15] O. Bourihane, A. Ed-dinari, B. Braikat, M. Jamal, F. Mohri, and N. Damil, "Stability analysis of thin-walled beams with open section subject to arbitrary loads," *Thin-Walled Structures,* vol. 105, pp. 156-171, 2016/08/01/ 2016. doi: https://doi.org/10.1016/j.tws.2016.04.008

[16] A. Elkaimbillah, B. Braikat, F. Mohri, and N. Damil, "A one-dimensional model for computing forced nonlinear vibration of thin-walled composite beams with open variable cross-sections," *Thin-Walled Structures,* vol. 159, p. 107211, 2021/02/01/ 2021. doi: https://doi.org/10.1016/j.tws.2020.107211

[17] G. J. Hancock and K. J. Rasmussen, "Formulation and Implementation of General Thin-Walled Open-Section Beam-Column Elements in Opensees (No. R961)," 2016.
[18] Rinchen, G. J. Hancock, and K. J. R. Rasmussen, "Geometric and material nonlinear analysis of thin-walled members with arbitrary open cross-section," *Thin-Walled Structures,* vol. 153, p. 106783, 2020/08/01/ 2020. doi: https://doi.org/10.1016/j.tws.2020.106783
[19] L. Chen, H.-Y. Zhang, S.-W. Liu, and D. Ziemian Ronald, "Efficient Line-Element Method for the Second-Order Analysis of Steel Members with Nonsymmetric Thick-Walled Cross Sections," *Journal of Structural Engineering,* vol. 150, no. 2, p. 04023226, 2024/02/01 2024. doi: 10.1061/JSENDH.STENG-12543
[20] S.-W. Liu, W.-L. Gao, and R. D. Ziemian, "Improved line-element formulations for the stability analysis of arbitrarily-shaped open-section beam-columns," *Thin-Walled Structures,* vol. 144, p. 106290, 2019/11/01/ 2019. doi: https://doi.org/10.1016/j.tws.2019.106290
[21] Hou, Yong, Junying Min, Nan Guo, Jianping Lin, John E. Carsley, Thomas B. Stoughton, Heinrich Traphöner, Till Clausmeyer, and A. Erman Tekkaya. "Investigation of evolving yield surfaces of dual-phase steels." *Journal of Materials Processing Technology,* vol. 287, p. 116314, 2021/01/01 2021. doi: https://doi.org/10.1016/j.jmatprotec.2019.116314
[22] Skordeli, M-AA, and C. D. Bisbos. "Limit and shakedown analysis of 3D steel frames via approximate ellipsoidal yield surfaces." *Engineering Structures*, vol. 32, no. 6, p. 1556-1567, 2010/06/01 2010. doi: https://doi.org/10.1016/j.engstruct.2010.02.004
[23] Hoang, Hieu Nghia, Quoc Anh Vu, and Manh Hien Nghiem. "An Approximation of Yield Surface for Doubly Symmetrical Sections of Steel Structures." *Periodica Polytechnica Civil Engineering,* vol. 69, no. 1, P. 321-332, 2025. doi:https://doi.org/10.3311/PPci.36589
[24] Vu, Anh Q., Nghia H. Hoang, and Hien M. Nghiem. "An efficient method for yield and failure surfaces of the steel i-section." *Advanced Steel Construction*, vol. 16, no. 3, P. 246-254, 2020/09/01 2020. doi: https://doi.org/10.18057/IJASC.2020.16.3.6
[25] Rakici, Salih, and Fatmir Menkulasi. "Moment curvature response of composite UHPC filled hollow structural steel cross-sections." *Engineering Structures*, vol. 294, P. 116728, 2023/11/01 2023. doi: https://doi.org/10.1016/j.engstruct.2023.116728
[26] Chiorean, Cosmin G. "A computer method for moment-curvature analysis of composite steel-concrete cross-sections of arbitrary shape." Engineering Structures and Technologies, vol. 9, no. 1, P. 25-40. 2017/01/02 2017, doi: https://doi.org/10.3846/2029882X.2017.1299969.
[27] Sun, Zeyang, Yang Yang, Wenlong Yan, Gang Wu, and Xiaoyuan He. "Moment-curvature behaviors of concrete beams singly reinforced by steel-FRP composite bars." *Advances in Civil Engineering*, vol. 1,P. 1309629. 2017.doi: https://doi.org/10.1155/2017/1309629
[28] Abdallah, Maha Hussein, Hamdy M. Mohamed, Radhouane Masmoudi, and Ahmed Moussa. "Analytical modeling of moment-curvature behavior of steel and CFRP RC circular confined columns." *Composite Structures*, vol. 189, p. 473-487, 2018/04/01 2018, doi: https://doi.org/10.1016/j.compstruct.2018.01.110.
[29] Montuori, Rosario, and Vincenzo Piluso. "Analysis and modelling of CFT members: moment curvature analysis." *Thin-Walled Structures*, vlo. 86, p. 157-166. 2015/01/01 2015. doi: https://doi.org/10.1016/j.tws.2014.10.010
[30] Rodriguez-Gutierrez, J. A., and J. Dario Aristizabal-Ochoa. "Bending moment-axial force-curvature interactions for metal beam-column sections." *Structures*, vol. 10, p. 139-146. 2017/05/01 2017. doi: https://doi.org/10.1016/j.istruc.2017.03.003
[31] T. J. R. Hughes and W. K. Liu, "Nonlinear finite element analysis of shells: Part I. three-dimensional shells," *Computer Methods in Applied Mechanics and Engineering,* vol. 26, no. 3, pp. 331-362, 1981/06/01/ 1981. doi: https://doi.org/10.1016/0045-7825(81)90121-3
[32] E. Spacone, F. C. Filippou, and F. F. Taucer, "FIBRE BEAM–COLUMN MODEL FOR NON-LINEAR ANALYSIS OF R/C FRAMES: PART I. FORMULATION," *Earthquake Engineering & Structural Dynamics,* vol. 25, no. 7, pp. 711-725, 1996/07/01 1996. doi: https://doi.org/10.1002/(SICI)1096-9845(199607)25:7<711::AID-EQE576>3.0.CO;2-9
[33] N. R. B. K. Raju and J. Nagabhushanam, "Nonlinear structural analysis using integrated force method," *Sadhana,* vol. 25, no. 4, pp. 353-365, 2000/08/01 2000. doi: 10.1007/BF03029720
[34] C. M. Tiago and V. M. A. Leitão, "Application of radial basis functions to linear and nonlinear structural analysis problems," *Computers & Mathematics with Applications,* vol. 51, no. 8, pp. 1311-1334, 2006/04/01/ 2006. doi: https://doi.org/10.1016/j.camwa.2006.04.008
[35] E. Parente Jr, G. V. Nogueira, M. Meireles Neto, and L. S. Moreira, "Material and geometric nonlinear analysis of reinforced concrete frames," *Revista IBRACON de Estruturas e Materiais,* vol. 7, 2014.
[36] L. Chen, A. H. A. Abdelrahman, S.-W. Liu, D. Ziemian Ronald, and S.-L. Chan, "Gaussian Beam–Column Element Formulation for Large-Deflection Analysis of Steel Members with Open Sections Subjected to Torsion," *Journal of Structural Engineering,* vol. 147, no. 12, p. 04021206, 2021/12/01 2021. doi: 10.1061/(ASCE)ST.1943-541X.0003185
[37] W.-L. Gao, A. H. A. Abdelrahman, S.-W. Liu, and R. D. Ziemian, "Second-order dynamic time-history analysis of beam-columns with nonsymmetrical thin-walled steel sections," *Thin-Walled Structures,* vol. 160, p. 107367, 2021/03/01/ 2021. doi: https://doi.org/10.1016/j.tws.2020.107367
[38] S.-W. Liu, R. D. Ziemian, L. Chen, and S.-L. Chan, "Bifurcation and large-deflection analyses of thin-walled beam-columns with non-symmetric open-sections," *Thin-Walled Structures,* vol. 132, pp. 287-301, 2018/11/01/ 2018. doi: https://doi.org/10.1016/j.tws.2018.07.044
[39] S. W. Liu and R. D. Ziemian, "MSASect2 - Matrix Structural Analysis Software for Arbitrary Cross-sections. Retrieved from http://www.msasect.com," ed, 2023.
[40] AISC, Specifications for Structural Steel Buildings ANSI/AISC 360-16, American Institute of Steel Construction, Chicago, C. American Institute of Steel Construction. 2016.
[41] Structure Express, "SE::MC – Moment Curvature Analysis (V2015.06.01)", 2024, software available at http://structurexpress.com/
[42] W. F. Chen. and and T. Atsuta, *Theory of Beam Columns: In-Plane Behavior and Design*. Ross Publishing, 1977.